Single crystal diffraction studies of gas loaded framework structures

Spencer, Elinor .

Single Crystal Diffraction Studies of Gas-Loaded Framework Structures

Elinor C. Spencer

Department of Chemistry

University of Durham

Submitted in part fulfilment of the requirements for the degree of Doctor of Philosophy at the University of Durham.

Abstract

This thesis is divided into two parts. The first part begins with a concise introduction (Chapter 1) into the crystallographic theory that underpins much of the work that is presented in later chapters. In Chapter 2, the crystal structures of eight aromatic sulphonate compounds are discussed in detail. These structures form a series, and the packing arrangements for each have been scrutinised using graph-set analysis; this allows for common structural patterns to be identified, and for conclusions to be drawn in relation to the solid-state packing behaviour for this class of compounds.

A crystallographic study of a number of phosphorus ylide compounds is reported in Chapter 3. Phosphorus ylides are of fundamental importance as reagents for a number of key synthetic reactions, and the aim of the study was to establish a deeper understanding of the modes of protonation and complexation for these materials, and the first examples of uranium(VI)-ylide complexes are reported.

Part 2 of this thesis commences with a general introduction to coordination polymer complexes and gas-storage materials (Chapter 4). The structural features and physical properties of the three-dimensional framework Zn_4O(1,4-benzenedicarboxylate) (Zn_4O(BDC)) that is central to the work presented in the following chapters are discussed. In Chapter 5, a variable temperature single crystal X-ray diffraction study of nitrogen- and argon-loaded Zn_4O(BDC) is presented. The aim of this ambitious project was to locate the absorption sites for the physically absorbed gas that are located within the cavities of the framework architecture. This work laid the foundation for the neutron Laue diffraction study of hydrogen-loaded Zn_4O(BDC) that is reported in the final chapter (Chapter 6). This neutron study represents the first example of the use of neutron diffraction for the location of physically absorbed gas within a host structure. The results given in Chapters 5 and 6 are of vital importance for the development of Zn_4O(BDC), and similar complexes, for gas-storage and purification applications.

Declaration

The work described in this thesis was carried out in the Department of Chemistry at the University of Durham, and the Institut Laue-Langevin (Grenoble, France), between September 2002 and September 2005, under the joint supervision of Prof. J. A. K. Howard and Dr. G. J. McIntyre. All the work is my own, unless otherwise stated, and has not been submitted previously for a degree at this or any other university.

Elinor C. Spencer

Durham, September 2005.

Acknowledgements

My most heartfelt thanks are proffered to Professor Judith A.K. Howard for the seminal guidance, friendship, and compassion that she has shown me throughout the time I have known her. I also wish to thank Dr. Garry J. McIntyre for his supervision and mischievous wit that kept me smiling during my time at the Institut Laue-Langevin (Grenoble, France).

I would also like to thank the members of the Durham Crystallography Group, both past and present, for creating such a fantastic and supportive environment to work in. In particular, I would like to acknowledge Drs. Victoria Money, Ivana Radosavljevic Evans, Horst Puschmann, and Dima Yufit, for their friendship, advice and sense of humour.

Finally to my parents, Edward and Ingrid Spencer, you have supported me without question, for this I am eternally grateful, and this thesis is dedicated to you.

Table of Contents

List of Tables

Chapter 2 Tables:

Chapter 3 Tables:

Chapter 5 Tables:

Chapter 6 Tables:

List of Figures

Chapter 1 Figures:

Chapter 2 Figures:

Chapter 4 Figures:

Chapter 5 Figures:

Chapter 6 Figures:

Chapter 1

Introduction to Crystallography

1.1 Introduction

Crystallography, as the name implies, is the study of crystals. Crystallographic analyses are concerned with the elucidation of the exact spatial arrangement of atoms and molecules in the crystalline state. This important and often under valued technique proves a wealth of information as to the nature of the molecular species present in the solid state, including the identification of chemical groups, the structural geometry, and the packing arrangements adopted by the molecules. Additionally, details pertaining to intermolecular interactions maybe inferred from crystallographic data.

1.2 Diffraction Theory

1.2.1 The crystal

For the purposes of this thesis a crystal is defined as an infinite three-dimensional array of a repeating molecular motif upon a lattice structure. There are only fourteen unique lattice arrays known as the 'fourteen Bravais lattices'. The smallest repeat volume of the lattice that displays the full symmetry of the crystal structure is referred to as the unit cell. The geometry of a unit cell is fully described by six parameters, namely, the length of the cell sides a, b, and c, with inter-axial angles α, β, and γ. In some cases the full symmetry of the lattice is best defined by a unit cell of larger dimensions and higher symmetry than a smaller oblique cell (the so-called primitive cell (P)). In these specialist cases additional lattice points will be included within the unit cell. Depending on the location of these additional points with respect to the faces of the unit cell, the lattice is said to be body-centred (I) or face-centred (B / C / A or F).

It is the long-range order exhibited by a crystal that enables it to act as a diffraction 'grating' for radiation possessing a wavelength comparable to inter-atomic distances (~1 Å), which is to say, neutrons, electrons or most commonly X-radiation.

1.2.2 Symmetry elements

A symmetry element is an imaginary entity about which a symmetry operation is conducted on an object, such that the final object arrangement is indistinguishable from the initial object arrangement. There are two classes of symmetry elements in crystallography, translational and non-translational elements, and these elements are used to describe the symmetry of the unit cell. Non-translational elements include inversion centres, mirror planes and rotation axes. Only 2-, 3-, 4- and 6-fold rotation axes are feasible in unit cells, as cells possessing 5-, 7- and 8-fold rotational symmetry will not translate to fill all space. Translational elements involve a translation along, or diagonal to, one of the cell axes combined with either a rotation or reflection in a mirror plane, these are known as a screw axis or glide plane, respectively.

1.2.3 Space groups

The combination of all symmetry elements with the 14 Bravais lattice systems has been shown by point group theory to give rise to 230 unique combinations, known as the 230 crystallographic space groups. These space groups provide information as to which symmetry elements are present in the unit cell. Details of the 230 space groups can be found by consulting the International Tables for Crystallography.[1] A space group symbol denotes the crystal lattice centring and the symmetry elements displayed by the unit cell. Due to element combination, certain symmetry elements are inherently present if other elements are in attendance, and as such need not be noted in the space group title. For example a mirror plane perpendicular to a 2-fold rotation axis (2/m) automatically generates an inversion centre at the point of intersection, by convention this symmetry element does not appear in the space group title (e.g. *P*2/m).

1.2.4 The asymmetric unit

The asymmetric unit is the smallest group of atoms that when the symmetry operations commanded by the space group are applied to it, the entire contents of the unit cell are generated. This may be less than, or more than, one formula unit.

It is the aim of the crystallographer to determine the both the space group and the asymmetric unit from a diffraction experiment. Equipped with this knowledge the full crystal structure can be generated.

1.2.5 Miller planes and indices

Miller planes are a conceptual contrivance to aid in the understanding of diffraction from crystals. They are parallel sets of planes that pass through the crystal at a number of different angles to the crystallographic axes. Each set of parallel planes has a characteristic plane spacing referred to as the 'd-spacing', and can be defined by set of indices, namely the Miller indices 'h k l'. The integer values of h k l for a set of planes can be determined by considering the plane that lies nearest the origin of a unit cell without passing through it. The point at which the plane crosses the *a*, *b* and *c* axes will be equal to 1/h, 1/k and 1/l respectively. Diffraction is said to occur from these so-called Miller planes.

1.2.6 Bragg's equation and reciprocal space

No introduction to diffraction would be complete without reference to Bragg's equation (Bragg's law). For a diffracted beam from a set of Miller planes to be observed the rays from individual planes must interact constructively. This will only occur when the path difference for the rays is an integer number of wavelengths. Bragg's equation stipulates the conditions for which this is true for a given Miller plane d-spacing.

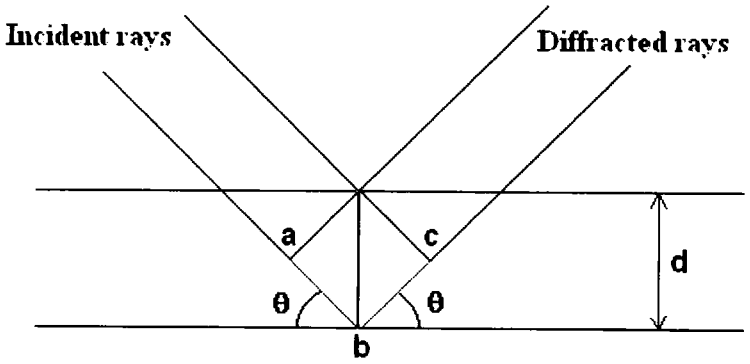

Figure 1.2.1: Schematic of diffraction from a pair of Miller planes

Figure 1.2.1 is a classical depiction of diffraction from a pair of Miller planes and will be used to show the derivation of Bragg's equation. The path difference between the two rays is highlighted in red in Figure 1.2.1, where the distances ab and bc are equal and can calculated using trigonometry:

$$ab = d \sin \theta$$

Equation 1.2.1

The path difference must be equal to nλ, where n is an integer value, to allow constructive interference to occur. Therefore nλ = 2ab, substituting this into equation 1.2.1 gives Bragg's equation:

$$n\lambda = 2d\sin\theta \qquad \textbf{Equation 1.2.2}$$

Bragg's law dictates that for a given wavelength there is an angle θ for which constructive interference can be observed from a set of Miller planes with a inter-plane spacing, d. However, Bragg's law gives no indication as to the amplitude of the diffracted ray.

Equation 1.2.2 also shows the reciprocal relationship between sinθ and d; hence a diffraction pattern is constructed in reciprocal space. For every set of planes in real space there results a point in reciprocal space, collectively these points comprise the reciprocal lattice.

In diffraction experiments the intensity and position of spots in reciprocal space are measured, and information relating to the crystal in real space deduced. The position of the spots in the diffraction pattern allows for the Miller planes from which they originate to be determined, and subsequently each spot is assigned an h k l label corresponding the h k l planes in real space to which it is associated, a process known as indexing.

1.2.7 The Ewald construction

A convenient representation of the diffraction phenomenon that elegantly combines the concepts of Bragg's law and the reciprocal lattice is provided by the Ewald construction that is shown in Figure 1.2.2 (the three-dimensional analogue is known as the Ewald sphere). The Ewald construction enables the prediction of which reflections will be at present at a given angle θ.

Rearranging Bragg's equation (Eq.1.2.2) for a first order reflection (n = 1) gives Equation 1.2.3, where the diffraction vector 'd*' equates to 1/d, and lies perpendicular to its associated Miller planes in real space.

$$\sin\theta = \frac{d^*/2}{1/\lambda} \qquad \textbf{Equation 1.2.3}$$

It can be inferred from Equation 1.2.3 that at a given value of θ, reciprocal lattices points with a diffraction vector d* will intersect a circle drawn about the crystal with a radius of 1/λ; as such these reciprocal lattice points will be in diffracting condition, and subsequently will be observed in the diffraction pattern. During a diffraction experiment the reciprocal lattice points are bought into diffracting condition (i.e. are made to intersect the Edwald sphere) by rotation of lattice about the origin,[†] in practise this is achieved by rotating the crystal, as the reciprocal lattice planes lie parallel to the Miller planes in real space (Fig.1.2.2).

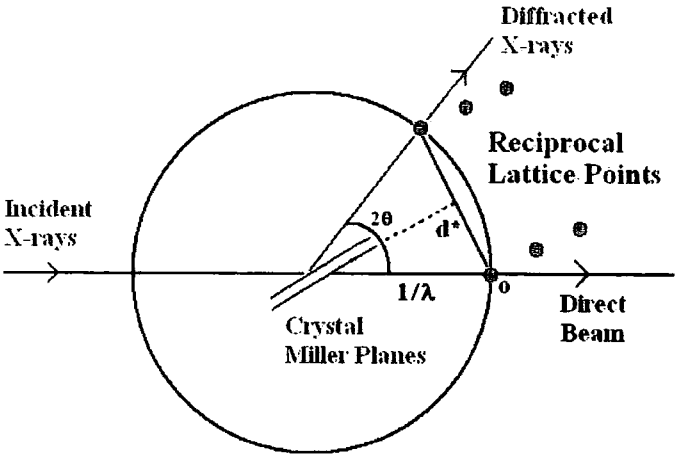

Figure 1.2.2: Schematic showing the Ewald construction (not drawn to scale). The label 'O' denotes the location of the origin of the reciprocal lattice.

1.2.8 Structure factors and atomic scattering factors

During data analysis the intensities of the spots on a given diffraction pattern (the reciprocal lattice points) are measured. The observed intensity, once corrected for background, Lorentz-polarisation and absorption effects, is equal to the square of the structure factor for the associated Miller index:

$$I_{hkl}^{corr} = \left(F_{hkl}^{obs}\right)^2 \qquad \textbf{Equation 1.2.4}$$

The structure factor, F_{hkl}, contains information regarding the position of all atoms in the unit cell, in accordance with Equation 1.2.5, where 'n' equals the number of atoms in the unit cell.

[†] The reciprocal lattice point at the origin corresponds to F(000) which is equal in magnitude to the total number of electrons in the unit cell.

The symmetry equivalent positions of the asymmetric unit within the unit cell can be obtained from the space-group, therefore it is only necessary for the structure factor of the asymmetric unit at the coordinates x, y, z to be calculated in the knowledge that the remaining electron density in the unit cell is symmetry related.

$$F_{hkl}^{calc} = \sum_{j=1}^{j=n} f_j \cos 2\pi\left(hx_j + ky_j + lz_j\right) + i\sum_{j=1}^{j=n} f_j \sin 2\pi\left(hx_j + ky_j + lz_j\right)$$

Equation 1.2.5

'Scattering' of the X-rays in a diffraction experiment is due to the interaction of the electric component of the electromagnetic radiation with the electron density of atoms present in the unit cell. Clearly as different elements possess different levels of electron density, it is not surprising that they have diverse scattering abilities. Information on the scattering power of an atom is contained in the atomic scattering factor (a.k.a. 'atomic form factor'). For atom *j* the atomic scattering factor has the symbol f_j, it is angular dependent and falls off at higher diffraction angles (the same is not true for neutron diffraction, where the atomic scattering factor is not angle dependent).

1.2.9 Absences

By definition, an absence in the data set is a reciprocal lattice point with zero intensity, such that it is not observed in the diffraction pattern with intensity much greater than its associated error value. There are two classes of absences:

(i) General Absences – observed across the complete data set, these absences result from lattice centring.

(ii) Systematic Absences – these arise due to translational symmetry elements being present in crystal structure. They affect small subsets of reflections in the dataset e.g. zones of reflections such as h k 0 or h 0 l.

From Equation 1.2.4 it can seen that zero intensity will result when the structure factor is equal to zero. To demonstrate how absences occur, let us consider the case of a centrosymmetric I-centred unit cell, where the lattice point environment comprises a single atom of type 'j'.

In a centrosymmetric cell there will be an atom at position x, y, z and -x, -y, -z. As sin(-x) = -sin(x) Equation 1.2.5 simplifies to:

$$F_{hkl}^{calc} = \sum_{j=1}^{j=n} f_j \cos 2\pi\left(hx_j + ky_j + lz_j\right) \qquad \textbf{Equation 1.2.6}$$

For an I-type centred cell there are lattice points situated at the corners of the unit cell, contributing ⅛th of a lattice point to the cell, and a lattice point in the centre of the cell at co-ordinates ½, ½, ½ that contributes a whole lattice point to the cell. As the lattice points on the corners are all equivalent is only necessary to consider one. For simplicity let us select the point at co-ordinates 0,0,0.

Substituting this information into Equation 1.2.6 gives the following:

$$F_{hkl}^{calc} = f_j \cos 2\pi(0) + f_j \cos 2\pi\left(\frac{1}{2}h + \frac{1}{2}k + \frac{1}{2}l\right)$$

$$F_{hkl}^{calc} = f_j + f_j \cos \pi(h + k + l)$$

For the structure factor to have a value of zero, then cosπ (h + k +l) must be negative, this will only occur when h + k +l = 2n + 1 (i.e. is odd). In summary, for an I-type lattice when h + k +l = 2n + 1 the reflection will be absent from the dataset. This simplistic example can be extended to more complex environments to explain absences due to other centring types or translational symmetry.

It can therefore be concluded that by careful consideration of the observed reflections corresponding to the h k l planes and their relative intensities, the symmetry of the unit cell can be established, and the space group can be deduced.

1.2.10 The phase problem in crystallography

It has now been demonstrated how the space group can be inferred from the symmetry of the diffraction pattern. The next stage in solving a crystal structure is the determination of the contents of the asymmetric unit.

To do this a Fourier series is assembled to represent the electron density in the unit cell, equivalent to a three-dimensional electron density map (ρ_{xyz}). Such as series is given in Equation 1.2.7.

$$\rho_{xyz} = \frac{1}{V}\sum_{h}\sum_{k}\sum_{l} F_{hkl}^{calc} \exp[-2\pi i(hx + ky + lz)]$$

Equation 1.2.7

As the unit cell dimensions are also known, the volume (V) of the cell can be calculated. However, although the magnitude of the structure factors can be calculated using Equation 1.2.4, the phases cannot. This is known as the 'phase problem in crystallography'.

1.2.11 Structure solution

There are two methods that have been developed to overcome the phase problem, the aim of these methods to develop a trial structure that can be improved upon by means of an iterative process termed 'refinement'.

For structures that contain relatively heavy atoms e.g. organometallic complexes, Patterson methods may be an appropriate means of structural solution. The Patterson function is

$$p_{uvw} = \frac{1}{V}\sum_{h}\sum_{k}\sum_{l} (F_{hkl})^2 \cos 2\pi(hu + kv + lw)$$

Equation 1.2.8

It should be noted that the coordinate system used in Patterson space is u, v, w. Although they refer to the same unit cell, the coordinates u, v, w are not directly related to the atomic co-ordinates x, y, z. By using the square of the structure factor, the phase problem is eliminated. The resultant Patterson map consists a number of peaks corresponding to the interatomic vectors, and the intensity of a peak is equal to the product of the number of electrons for the atoms contributing to it. Prominent peaks[§] will be vectors between the heaviest atoms in the structure,

[§] The highest Patterson peak is located at origin of the unit cell. This is because at this point every atom is a distance zero from itself. The intensity of this peak is proportional to the sum of the squares of all the atoms in the unit cell. It is usual for this peak to be scaled to 999 and for all other peaks to be normalised accordingly.

and as such their atomic positions can be deduced, providing an initial model for structural refinement.

'Direct methods' is the second method of structure solution, although more versatile than Patterson methods, it is primarily used for light atom structures with less than ~300 atoms e.g. small organics. The Sayre equation (Eq. 1.2.9) is based on two assumptions: (i) the electron density in a structure can never be negative; (ii) the electron density is concentrated into well-defined maxima.

$$F_{hkl} = k\sum_{h'k'l'}\left(F_{h'k'l'}\right)\cdot\left(F_{h-h',k-k',l-l'}\right) \qquad \textbf{Equation 1.2.9}$$

The term 'k' is a scale factor. From Equation 1.2.9 it can be deduced that for a triplet of strong reflections the sign relationship (Σ_2-relationship) for a centrosymmetric structure is:

$$S_{hkl} \approx \left(S_{h'k'l'}\right)\cdot\left(S_{h-h',k-k',l-l'}\right) \qquad \textbf{Equation1.2.10}$$

For structure solution, the strongest reflections in a dataset are assigned a positive phase, and by applying the Σ_2-relationship the signs of other reflections can be elucidated, in this manner the phase problem is overcome. The probability, '*P*', that a phase has been correctly assigned as positive is given by Equation 1.2.11.

$$P = \frac{1}{2} + \frac{1}{2}\tanh\left(N^{-\frac{1}{2}}\left[E_{hkl}\right]\cdot\left[E_{h'k'l'}\right]\cdot\left[E_{h-h',k-k',l-l'}\right]\right)$$

Equation 1.2.11

Where 'N' is the number of atoms in the asymmetric unit, and 'E' is the normalised structure factor. In practice, many different sign combinations are investigated and combination that generates the most realistic initial structural model is selected. For non-centrosymmetric structures, a phase-relationship between strong reflections that is analogous to Equation 1.2.10 is applied, this leads to the tangent formula (Eq.1.2.12), where $\chi = N^{-1/2}[E_{hkl}][E_{h'k'l'}][E_{h-h',k-k',l-l'}]$.

$$\tan\phi_{hkl} = \frac{\sum_{h'k'l'} \chi \cdot \sin\left(\phi_{hkl} + \phi_{h-h',k-k',l-l'}\right)}{\sum_{h'k'l'} \chi \cdot \cos\left(\phi_{hkl} + \phi_{h-h',k-k',l-l'}\right)}$$

Equation 1.2.12

1.2.12 Structure refinement

Once an initial model has been established it is then refined. The purpose of refinement is to optimise the atomic parameters so that the errors in the determined structure are reduced to an acceptable level. The refinement method used for all structures presented in this report is one of the most common methods employed, namely least squares. Refinements of all the structures discussed in this Thesis were based on $(F_o)^2$, the corrected intensities. Least squares based on $(F_o)^2$ is an iterative process concerned with the minimisation of the parameter $\sum_{hkl} w\Delta^2$ given in Equation 1.2.13.

$$\sum_{hkl} w\Delta^2 = \sum_{hkl} w\left(F_o^2 - F_c^2\right)^2 \qquad \textbf{Equation 1.2.13}$$

Where $(F_o)^2$ and $(F_c)^2$ are the observed and calculated intensities respectively. A weight, w, is applied to each reflection which may, in the simplest case, be equal to the reciprocal of the error in the measured intensity for that particular reflection (σ) squared. The weighting influences the overall contribution of that reflection to $\sum_{hkl} w\Delta^2$. After each adjustment to the structural model, F_c is recalculated and a new value of $\sum_{hkl} w\Delta^2$ generated.

1.2.13 Atomic displacement parameters & the occupancy value

In Chapters 5 and 6 the refinements of variable temperature data for a gas-loaded framework structure are discussed. In these studies, the refinement of the atomic displacement parameters (ADPs) and the occupancy values was of major significance; therefore, in this section the theory underpinning the refinement of these parameters will be discussed.

The occupancy value and ADPs for a given atom *i* modify the atomic scattering factor for that atom (f_i) which is inputted into the equation for the structure factor (Eq. 1.2.5). The equation for

the modified atomic scattering factor (f_i') is given as Equation 1.2.14, in which 'g_i' is the fractional occupancy for atom *i*, and U_{iso} is the isotropic displacement parameter ($U_{iso} = u^2$, where u is the displacement of the atom from its mean position). The initial independent refinement of the ADPs and atomic occupancy is of importance as they are both strongly correlated; thus under estimating one will lead to the other compensating for the deficiency, the extent of this occurrence is difficult to detect. On a practical level this means that only limited confidence in the occupancies of the atoms (or indeed, in the ADPs) is possible unless the two parameters are refined individually. Ultimately it is desirable to refine jointly the ADPs and occupancies to account for the correlation effects, as this will allow the values to 'balance' giving a more realistic model.

$$f_i^{'} = g_i \cdot f_i \cdot \exp\left\{-2\pi^2 U_{iso} d^{*2}\right\} \qquad \textbf{Equation 1.2.14}$$

A visual representation of the effects of the atom occupancy and isotropic thermal vibration on the atomic scattering factor (in this case for argon) is given in Figure 1.2.3.

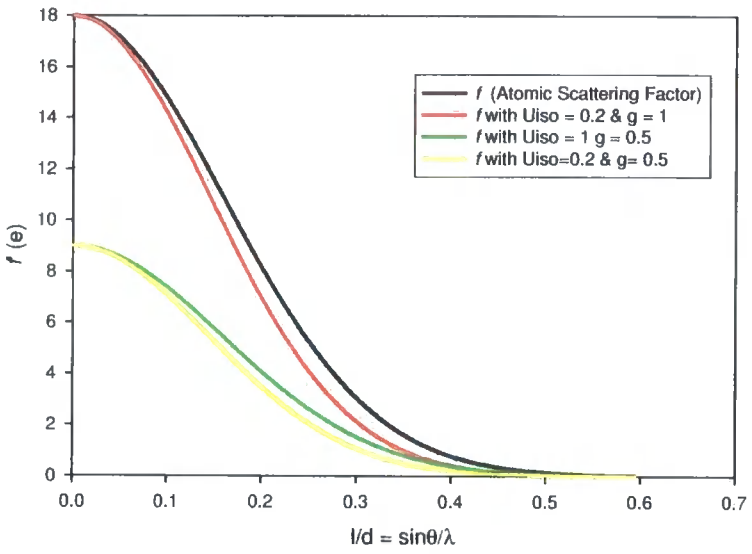

Figure 1.2.3: Plots showing the effects of g_i and U_{iso} on the atomic scattering factor of argon.

It can be seen from Figure 1.2.3 that U_{iso} has a subtle influence on *f*, and the effect is more pronounced at higher angles. However, *f* is directly proportional to the occupancy factor, g_i, such that g_i can be considered as being a scaling factor.

The effect on *f* of the atomic anisotropy requires a much more multifaceted mathematical description (Eq.1.2.15) with the scattering vector, d^*, being replaced by the reciprocal lattice

components; however the principles are essentially the same as in the isotropic case discussed above. Equation 1.2.15 expresses the thermal motion using a second-order tensor. This results in the vibrational motion being represented by an ellipsoid. The magnitude and orientation of this so-called thermal ellipsoid with respect to reciprocal axes is given by the U_{ii} and U_{ij} parameters. It is possible to incorporate further terms into this equation[‡] i.e. to apply higher-order tensors, if the data allow. This can enable a more realistic model of the thermal motion of an atom to be generated.[2-4]

$$f_i^{'} = g_i \cdot f_i \cdot \exp -2\pi\left(U_{11}h^2a^{*2} + U_{22}k^2b^{*2} + U_{33}l^2c^{*2} + 2U_{23}klb^*c^* + 2U_{13}hla^*c^* + 2U_{12}hka^*b^*\right)$$

Equation 1.2.15

A thermal ellipsoid is an equal-probability surface and is an illustrative means of representing the thermal motion of an atom. It contains a predefined fraction (usually 50%) of the Gaussian probability density function (PDF) for that atom. With this mind, it can be seen that it is perfectly reasonable to model static disorder anisotropically, and indeed this is to be expected if the data allow for it. However, it is *not* legitimate to model dynamic disorder in the same way as the ellipsoid representation is virtually meaningless. The result of modelling dynamically disordered atoms anisotropically is to lower the residual factors falsely (see Section 1.2.14).

1.2.14 Refinement statistics

The R-value, or residual value, provides an indication as to the progress of the refinement i.e. how well the proposed model conforms to reality. Two R-factors are calculated throughout the course of the refinement the first of these is given in Equation 1.2.16. However, no allowance is made for the weighting in the calculation of R_1 and it is based on F_o, which is often not the factor upon which the refinement has been based. A more meaningful value, the weighed residual (wR_2) is given by Equation 1.2.17, and is based on the square of the corrected intensities and does include a weighting term.

$$R_1 = \frac{\sum_{hkl}\left||F_o| - |F_c|\right|}{\sum_{hkl}|F_o|} \quad \textbf{Equation 1.2.16}$$

$$wR_2 = \sqrt{\frac{\sum_{hkl} w\left(F_o^2 - F_c^2\right)^2}{\sum_{hkl} w\left(F_o^2\right)^2}} \quad \textbf{Equation 1.2.17}$$

[‡] The tensor applied to model the PDF must reflect the site symmetry of the atom.

1.3 Instrumentation

1.3.1 X-ray generation

The X-rays employed in an X-ray diffraction experiment are generated by means of a high-vacuum X-ray tube. A beam of electrons is directed towards a target of high purity metal, usually either copper or molybdenum, known as the anode, which is continuously cooled by circulated water. For fine-focus tubes the target has an area of approximately 0.4 x 8 mm. The electron beam is generated from a cathode source under an applied voltage of between 40-60 kV.

The X-rays are produced in two ways; firstly, the deceleration of the electrons as they approach and enter the metal target results in the generation of 'white' radiation – electromagnetic radiation containing a range of wavelengths. The minimum wavelength radiation created by this process is inversely proportional to the applied voltage on the cathode. The second method of X-ray generation is of primary importance and produces the radiation used in the diffraction experiment. The electron beam ionises the metal target, ejecting electrons from the K-shell. Electrons from a higher energy orbital, the L-shell, relax in the lower energy K-shell emitting X-rays of two distinct wavelengths ($k_{\alpha 1}$ and $k_{\alpha 2}$) that are characteristic of the metal used as the target. As these two wavelengths are very similar ($k_{\alpha 1}$ = 0.70926Å and $k_{\alpha 2}$ = 0.713543 Å for Mo targets) it is not necessary for the purposes of routine diffraction experiments to separate the $k_{\alpha 1}$/ $k_{\alpha 2}$ doublet. In addition to the $k_{\alpha 1}$/ $k_{\alpha 2}$ doublet, higher energy radiation referred to as K_β radiation is also emitted when electrons for the M-shell as opposed to the L-shell relax into the vacancy created in the K-shell.

The radiation leaves the tube by means of beryllium windows built into the side of the X-ray tube. Both the white radiation and K_β radiation are filtered out to give a monochromatic beam of K_α radiation, for Mo-radiation a zirconium metal filter is suitable for this purpose

1.3.2 The single crystal diffractometer

The X-ray crystallographic analyses reported in this thesis were performed with a standard 3-circle diffractometer (of Eulerian geometry), a typical example of which is shown in Figure 1.2.4. The 3-circles, ϕ, ω, and θ, are shown in red. The ϕ-circle allows rotation of the crystal about a circle on which the goniometer (**B** in Figure 1.2.4) is mounted. The ω-circle lies in the

horizontal plane, and enables the vertical rotation to the goniometer mount; the θ-circle is concentric with the ω-circle and carries the detector. The key components of the diffractometer are labelled A-E in green:

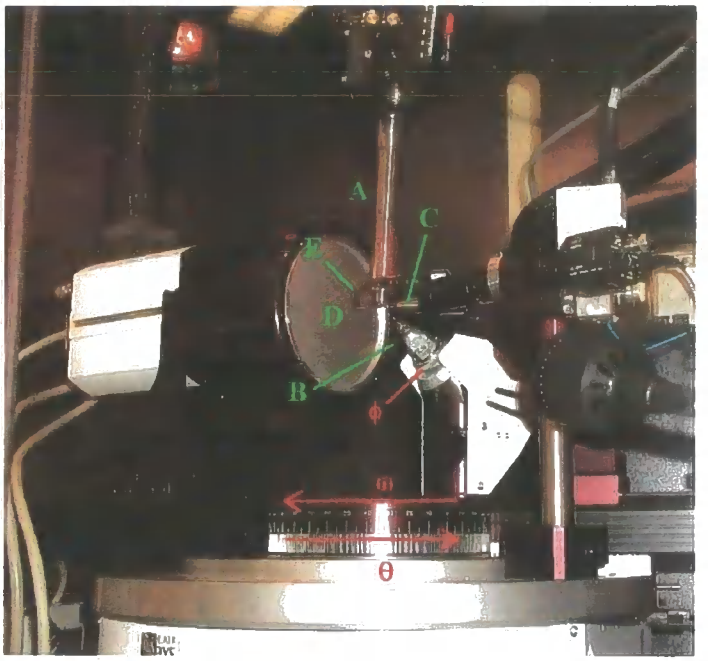

Figure 1.2.4: Bruker SMART 6K. See main text for label definitions.

(A) *Cryo-stream* – this temperature-controlling device directs a flow of dry nitrogen gas at the required temperate over the crystal, and it is capable of accurately operating in a temperature range of 90 –350K. 'Routine' structure analyses are preformed at low-temperature (typically 120K) to reduce the thermal motion of the molecules in the crystal, subsequently giving data of a higher quality, and ultimately more accurate atomic parameters. The main flow of nitrogen gas that bathes the crystal is encased within a secondary flow of nitrogen gas that shields it from small perturbations created by the surrounding air atmosphere.

(B) *Goniometer* – the crystal is mounted on a fibre (glass or hair) that is attached via a brass pip to the goniometer head. The goniometer comprises two mutually perpendicular slides that enable the crystal to be centred accurately in the X-ray beam. To further aid the correct positioning of the crystal, the goniometer also allows a height adjustment to be performed.

(C) *Collimator* – the X-rays that exit the generator are diffracted from a single crystal graphite monochromator (111 'reflection') which produces a highly focused and coherent

X-ray beam that then pass into the collimator. The collimator then directs the beam towards the crystal.

(D) *Area detector* – the detector in this case is a charged-coupled device (CCD). The X-rays incident on the detector fall on an X-ray sensitive film that then fluoresces in the visible region. These secondary photons activate the CCD chip, and the intensity is recorded (the intensity of the visible fluorescence is proportional to the intensity of the incident X-ray beam). The chip is continually cooled (to -54°C) to reduce the background noise level. During a data collection the detector moves through the θ angle in small increments (0.3°) to ensure that the required angular range is covered so that a sufficient proportion of reciprocal space investigated.

(E) *Beam-stop* – the beam-stop is designed to absorb the intense direct beam of X-rays, to prevent them from damaging the detector. This produces the traditional beam-stop shadow in each collected data frame.

1.3.3 The sample

The single crystal used in an X-ray diffraction experiment should have dimensions less than 0.5 x 0.5 x 0.5 mm^3 to ensure it is completely bathed in the X-ray beam. The crystal is mounted on fibre on the end of the goniometer head. The crystal should be as free from defects as possible, and single such that while being observed with a microscope using plane-polarised light, it will be seen to 'extinguish' when rotated. There are a number of ways to mount a crystal, but the two main ways for attaching to a fibre are either glue (epoxy resin) for high temperature work (< 200K) or using inert oil that will freeze to a glass when placed under the nitrogen cold-stream below 200K. Care should be taken to include as little of the fibre as possible in the X-ray beam, and to prevent the axes (a, b, c) of the crystal aligning perpendicular to the beam (particularly in the case of crystals that exhibit needle morphology). For air-sensitive crystals, or for mounting the crystal in the mother-liquor, a Lindermann capillary maybe used (see Chapter 5).

1.3.4 Data manipulation

Much of the theory behind diffraction data manipulation has been provided in Section 1.2 of this chapter. In practice, experimental data processing is computationally demanding and requires the use of several programs that perform automatically the analysis and calculations introduced in Section 1.2. The software is supplied by instrument manufacture (Bruker) for use with their diffractometers and each of the programs dovetail, writing files that are inter-program

compatible.[5] All structures reported in this thesis were analysed with this software, unless otherwise stated. The program SADABS was used to perform the absorption corrections reported in this thesis (unless otherwise stated).[6] As well as correcting for absorption by the crystal and crystal support, SADABS also corrects for inhomogeneity in the incident beam and crystal decay.

1.4 References

[1] Hahn T, '*International Tables for Crystallography, Volume A, Space-Group Symmetry*'. (1983).

[2] Johnson CK, *Acta Cryst.*, **A25**, 187 (1969).

[3] Dunitz JD, Schomaker V, Trueblood KN, *J. Phys. Chem.*, **92**, 856 (1988).

[4] Kuhs WF, *Acta Cryst.*, **A48**, 80 (1992).

[5] Bruker **1998**, SMART-NT version 5.0 (Data collection and indexing), SAINT version 6.04 (Data processing), and SHELXTL version 6.1 (Structure solution, refinement & graphics), Bruker AXS Inc., Madison, Wisconsin, USA.

[6] Sheldrick GM, SADABS version 2.03, University of Göttingen, Germany 1998.

The crystallographic theory presented in Section 1.2 was taken from the following secondary sources:

[7] Glusker JP, Lewis M, Rossi M, '*Crystal Structure Analysis for Chemists and Biologists*', Wiley-VCH 1994.

[8] Glusker JP, Trueblood KN, '*Crystal Structure Analysis A Primer*', 2nd Ed., Oxford University Press 1985.

[9] Massa W, 'Crystal Structure Determination', 2nd Ed., Springer-Verlag 2000.

[10] Hammond C, '*The Basics of Crystallography and Diffraction*', 2nd Ed., Oxford University Press 2001.

Chapter 2

Crystallographic Study of Aromatic Sulphonates

2.1 Introduction

Much of the work presented in this chapter was conducted in collaboration with Nagarajan Vembu of Bharathidasan University, India. The purpose of this research was the elucidation of the crystal structures of several different organic compounds that have potential use in commercially exploitable applications; namely, aromatic sulphonates for use in biomedical science. Appendix 2 is associated with this chapter, and is an introduction to the theory that underpins the study of secondary interactions and additionally, the key principles of graph-set analysis are highlighted therein.

2.1.1 Aromatic sulphonates for biomedical applications

Aromatic sulphonates have long been associated with environmental pollution. Their presence in ground water results from the biotic degradation of the most abundantly used surfactant, linear alkylbenzene sulphonate, and from their use in the production of optical brighteners. Both applications result in aromatic sulphonate species being regularly discharged into the watercourse via domestic and industrial waste effluent.[1,2] However, despite this negative history, aromatic sulphonates have begun to attract interest in the field of biomedical science.

Matulis *et al.* have conducted an extensive investigation into the protection of enzymes by azoaromatic sulphonate anions from deactivation by acid and elevated temperatures.[3] It would be of considerable benefit to be able to protect enzymes from deactivation by heat and acid, greatly simplifying methods for enzyme isolation and purification from crude and dilute sources. The authors compared the ability of twenty-nine azoaromatic sulphonate anions to protect six different proteases.

The pivotal role performed by the aromatic sulphonate groups of the protecting compound during complex formation with the protein is of particular interest. The binding of the protecting ligand to the protein is via ion-pair formation; the interaction being primarily between the negatively charged sulphonate groups of the ligand and the positive charged protein groups. The total negative charge on the ligand ideally should balance the positive charge held by the protein; the location and number of sulphonate groups on the protecting ligand is therefore of great importance.

Aromatic sulphonates have been used to aid the binding of photosensitizer species to antibody molecules.[4] In their study Jiang *et al.* used aromatic sulphonates to chemically modify polyvinyl alcohol (PVA) to enable it to be used as a linker molecule between the photosensitizer and the antibody. Such complexes are of interest in cancer research for the targeted destruction of malignant tumours.

Spungin *et al.* have successfully employed aromatic sulphonates in the study of merging of lipid membranes.[5] The purpose of this work was to improve scientific understanding of the mammalian fertilisation mechanism. The authors used a variety of different aromatic sulphonate solutions to aid in the separation of the membranes from their respective cells, and to monitor the merging the separated membranes.

The examples presented above provide a succinct introduction into the importance of aromatic sulphonates in biomedical research. The next section introduces the aromatic sulphonates that have been central to this study.

2.1.2 The aromatic sulphonate compounds

Table 2.1.1 lists the aromatic sulphonate compounds that have been investigated in this study. The chemical structure of each compound is given in Figure 2.1.1. Nagarajan Vembu supplied all compounds in a crystalline form and no further sample preparation was deemed necessary.

All the compounds shown in Figure 2.1.1 clearly posses a sulphonyl link, except for compound **1**. Compound **1** is the precursor to compounds **2 – 6** and has been included in this study for completeness.

Table 2.1.1: Names of the compounds central to this study.

Compound Number	Compound Name
1	3-Nitrobenzenesulphonyl Chloride
2	Phenyl 3-nitrobenzenesulphonate
3	2-Nitrophenyl 3-nitrobenzenesulphonate
4	2,4-Dinitrophenyl 3-nitrobenzenesulphonate
5	8-Quinolyl 3-nitrobenzenesulphonate
6	Methyl 4-(3-nitrobenzenesulphonyloxy)benzoate
7	Methyl 4-tosyloxybenzoate
8	4-Naphthyl 4-toluenesulphonate

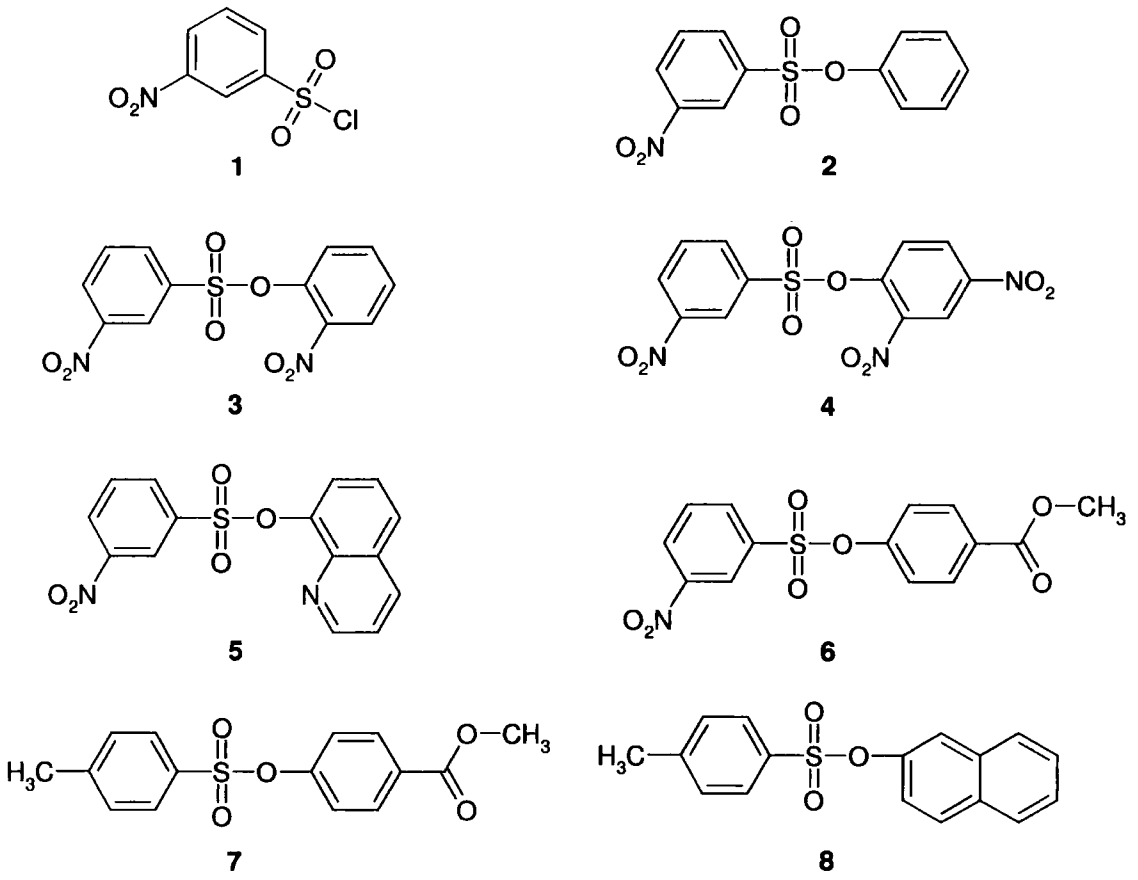

Figure 2.1.1: The above compounds are the subjects of this study. The name of each compound is recorded in Table 2.1.1.

2.2 Experimental

All crystallographic data for compounds **1-8** were collected at 120K, using graphite-monochromated MoK_α X-radiation ($\lambda = 0.71073$ Å). Data for compounds **1**, **3**, **7** and **8** were collected on a Bruker 6K CCD diffractometer; the remaining samples (**2**, **4**, **5**, and **6**) were analysed using a Bruker Proteum M diffractometer. All data processing was performed using standard Bruker software; structure solutions were via Direct Methods (See Chapter 1). Further experimental and refinement details can be found in the supplementary data tables and in Table 2.2.1.

Table 2.2.1: Crystallographic data and refinement details for compounds **1-8**.

	1	**2**	**3**	**4**	**5**	**6**	**7**	**8**
Crystal size (mm^3)	0.39x0.24 x0.13	0.16x0.14x0.09	0.14x0.12x0.08	0.28x0.25x0.11	0.20x0.19x0.11	0.22x0.13x0.12	0.28x0.24x 0.15	0.51x0.45x026
Crystal system	Monoclinic	Orthorhombic	Orthorhombic	Orthorhombic	Monoclinic	Monoclinic	Monoclinic	Monoclinic
Space group	$P2_1/n$	$Pna2_1$	$Pna2_1$	$Pca2_1$	$P2_1/c$	$P2_1/c$	$P2_1/c$	Pc
a (Å)	7.8868(4)	17.458(4)	19.9671(8)	27.730(2)	8.6001(6)	11.125(2)	8.292(1)	7.9315(6)
b (Å)	9.4298(4)	12.287(4)	12.7083(5)	4.7374(3)	23.068(2)	9.643(2)	12.280(2)	29.130(2)
c (Å)	11.8789(5)	5.489(1)	5.1306(2)	10.7800(8)	13.9192(3)	13.236(3)	14.275(2)	6.1111(5)
α (°)	90	90	90	90	90	90	90	90
β (°)	107.318(2)	90	90	90	100.132(2)	90.257(5)	101.229(3)	92.383(3)
γ (°)	90	90	90	90	90	90	90	90
Volume ($Å^3$) / Z	843.40(7) / 4	1177.4(5) / 4	1301.88(9) / 4	1416.2(2) / 4	2718.3(3) / 8	1419.9(5) / 4	1425.7(3) / 4	1410.7(2) / 4
μ (mm^{-1})	0.679	0.291	0.291	0.290	0.269	0.267	0.246	0.236
Unique Reflections	1928	2392	2832	2952	6011	3150	3289	6450
R(int)	0.0278	0.0589	0.0594	0.0332	0.0503	0.0303	0.0371	0.0449
Gof (on F^2)	1.080	0.913	0.962	0.967	0.904	0.952	1.037	1.039
R1/ wR2 (all data)	0.0452 / 0.1057	0.0647 / 0.0598	0.0458 / 0.0699	0.0362 / 0.0592	0.0666 / 0.0783	0.0541 / 0.0823	0.0552 / 0.1159	0.0519 / 0.1122

2.3 Results & Discussion

2.3.1 3-Nitrobenzenesulphonyl chloride

Figure 2.3.1 shows the intramolecular hydrogen bond interactions present in 3-nitrobenzenesulphonyl chloride (**1**).[6] The graph-set notation [7,8] S(5) can be assigned to each of the hydrogen bond motifs involving atoms O1, O2, O4 and O3. The H-bond parameters are given in Table 2.3.1.

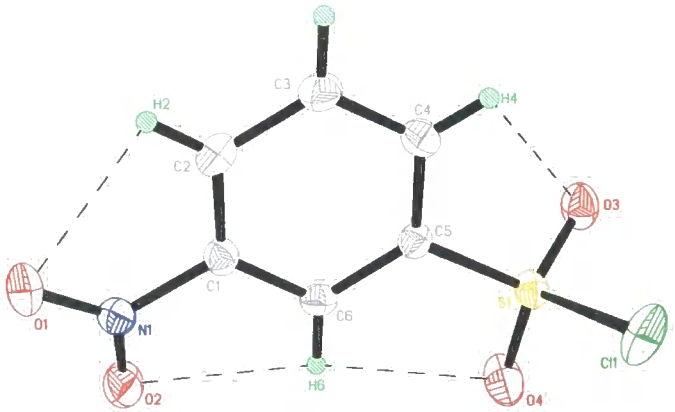

Figure 2.3.1: 50% Thermal-ellipsoid plot of compound **1** displaying intramolecular hydrogen bonds.

Table 2.3.1: Geometric bond parameters for hydrogen bonds exhibited in compound **1**.

D-A···A (Å)	D-H (Å)	H···A (Å)	D···A (Å)	D-H···A (°)
C6-H6···O4	0.95(3)	2.55(3)	2.897(3)	101.9(18)
C6-H6···O2	0.95(3)	2.42(3)	2.712(3)	97.1(18)
C4-H4···O3	0.91(3)	2.79(3)	3.051(3)	97.8(18)
C2-H2···O1	0.90(3)	2.48(3)	2.725(3)	96.0(19)
C4-H4···O4^{i}	0.91(3)	2.38(3)	3.116(3)	138(2)
C6-H6···O1^{ii}	0.95(3)	2.52(3)	3.251(3)	134(2)
C3-H3···O2^{iii}	0.93(3)	2.97(3)	3.504(3)	118(2)
C2-H2···O2^{iii}	0.90(3)	2.71(3)	3.387(3)	133(2)
C3-H3···O3^{iv}	0.93(3)	2.54(3)	3.412(3)	156(3)

Symmetry codes: (i) ½ + x, ½ - y, ½ + z; (ii) ½ - x, ½ + y, ½ - z;
(iii) ½ + x, - ½ - y, ½ + z; (iv) ½ - x, y - ½, $^{3}/_{2}$ – z.

Also listed in Table 2.3.1 are the intermolecular hydrogen bonds present in the crystal structure of compound **1** as displayed in Figure 2.3.2. All these bonds are C-H···O interactions in which the donor is not activated, and as such, all these bonds can be considered as typical weak hydrogen bond interactions (as defined by Desiraju and Steiner [9]). Both C2-H2 and C3-H3 donate to acceptor atom O2^{iii} to form a bifurcated hydrogen bond creating a pattern of binary graph-set $R_2^1(5)$ (see Table 2.3.1 for symmetry codes).

Figure 2.3.2 indicates the possibility of π···π interactions in the crystal structure of **1.** The centroid-centroid distance to the symmetry generated molecule at 1-x, -y, 1-z is 3.824 Å. Although no precise cut-off criterion has been assigned to π···π interactions this maybe regarded as a π···π bond.

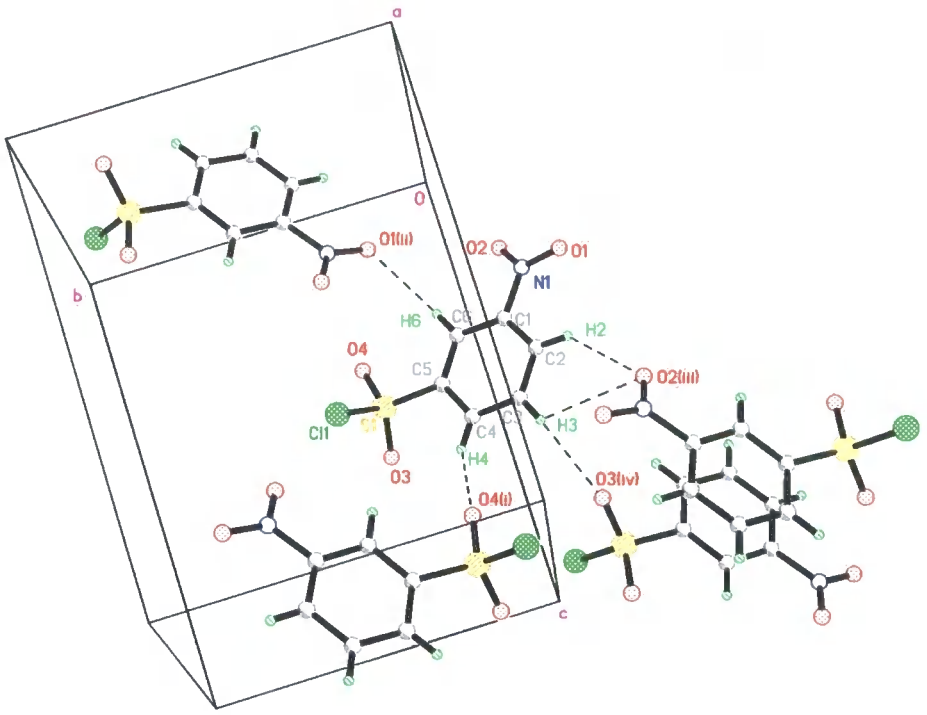

Figure 2.3.2: Diagram displaying intermolecular interactions present in compound **1**. See Table 2.3.1 for symmetry codes.

Table 2.3.2 lists selected bond geometries observed in the crystal structure of **1**. The N-O bond distances are as expected for a nitro group bonded to an aromatic carbon atom.[10] The bond lengths and angles surrounding the S1 atom are comparable to those found for a similar aromatic sulphonyl chloride compound.[11]

The deviations of atoms N1, O1, and O2 from the plane formed by atoms C1-C6 are -0.051(2) Å, 0.165(2) Å and -0.317(2) Å respectively. These values suggest that the nitro group is twisted away from the ring plane, this may occur to aid the formation of intermolecular interactions. Alternatively, the intermolecular interactions may force the nitro groups to adopt this geometry.

Table 2.3.2: Selected bond parameters for compound **1**

Bond	Length (Å)	Atoms	Angle (°)
S1-O3	1.418(2)	O3-S1-O4	120.9(1)
S1-O4	1.419(2)	O3-S1-C5	109.4(1)
S1-C5	1.761(2)	O4-S1-C5	109.4(1)
S1-Cl1	2.0198(8)	O3-S1-Cl1	105.20(8)
N1-O1	1.222(3)	O4-S1-Cl1	108.0(1)
N1-O2	1.224(3)	C5-S1-Cl1	102.24(7)
N1-C1	1.472(3)	O1-N1-O2	124.2(2)
		O1-N1-C1	117.9(2)
		O2-N1-C1	117.8(2)

2.3.2 Phenyl 3-nitrobenzenesulphonate

Figure 2.3.3 shows the weak intramolecular C-H···O interactions present in phenyl 3-nitrobenzenesulphonate (**2**).[12] The geometric parameters for these hydrogen bonds are given in Table 2.3.3. The intramolecular interactions involving H2, H6, and H4 generate motifs of graph-set S(5). The remaining intramolecular hydrogen bond motif involving H12 is of graph-set S(6).

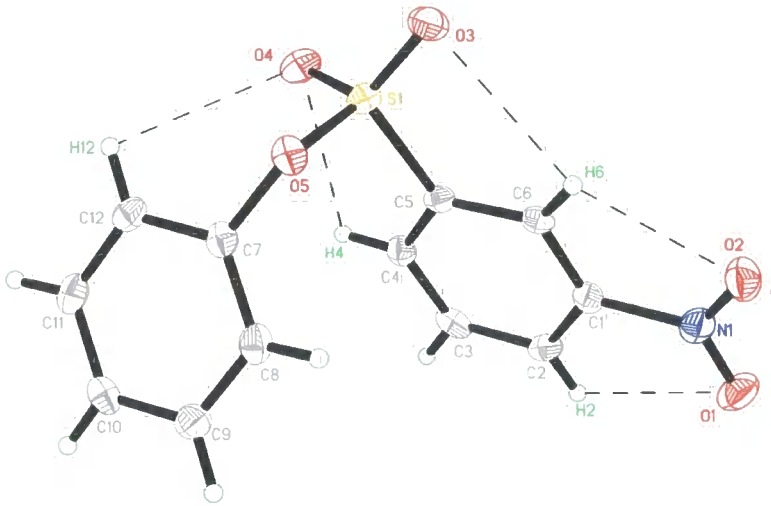

Figure 2.3.3: 50% Thermal-ellipsoid plot of compound **2**, displaying intramolecular C-H···O bonds.

The crystal structure of compound **2** is stabilised by an intricate network of weak intermolecular hydrogen bonds, all of which are listed in Table 2.3.3. Cg2 is the centroid of the phenyl ring C7-C12. Figure 2.3.4 is a diagrammatic representation of the network of intermolecular interactions that are present in the crystalline state of compound **2**. C3-H3 forms a bifurcated hydrogen bond with atoms $O3^{i}$ and $O5^{i}$ of the graph-set N_2: $R_1^2(4)$ (see Table 2.3.3 for symmetry codes). Atom $O3^{i}$ is a bifurcated hydrogen bond acceptor. Bonds C3-H3···$O3^{i}$ and C4-H4···$O3^{i}$ form a N_2: $R_2^1(5)$ chelate pattern. A large ring pattern of the basic binary graph-set $R_2^2(13)$ (complex binary sets $R_2^2(15)$ and $R_2^2(17)$) is formed by bonds C3-H3···$O4^{ii}$ and C9-H9···$O3^{ii}$.

The stacking of the molecules, as seen in Figure 2.3.5 indicates the possibility of π···π bonding, however the distance between the ring centroids of neighbouring molecules is 5.489 Å, which is too long to be considered as a π···π interaction. The C10-H10···$O1^{iv}$ interaction links the molecules parallel to the *a*-axis into infinite chains that can be assigned the extended basic graph-set notation C(12)[D] (complex graph-set C(14)[D]).

Table 2.3.3: Geometric bond parameters for hydrogen bonds exhibited in compound **2**.

D-A···A (Å)	D-H (Å)	H···A (Å)	D···A (Å)	D-H···A (°)
C2-H2···O1	0.89(2)	2.42(3)	2.707(4)	98.8(18)
C4-H4···O4	0.90(2)	2.57(2)	2.932(3)	104.5(17)
C6-H6···O2	0.94(2)	2.39(2)	2.715(4)	100.2(15)
C6-H6···O3	0.94(2)	2.69(2)	2.968(3)	97.7(16)
C12-H12···O4	0.90(3)	2.80(2)	3.095(3)	100.4(18)
C3-H3···O3^{i}	1.00(2)	2.80(3)	3.426(4)	121.2(17)
C3-H3···O5^{i}	1.00(2)	2.67(3)	3.647(3)	165(2)
C9-H9···O2^{i}	0.93(3)	2.87(2)	3.399(4)	117(2)
C10-H10···O2^{i}	0.94(2)	2.58(2)	3.260(3)	129.6(19)
C4-H4···O3^{i}	0.90(2)	2.75(2)	3.364(4)	127.0(18)
C9-H9···O3^{ii}	0.93(3)	2.78(3)	3.366(4)	121.7(19)
C3-H3···O4^{ii}	1.00(2)	2.65(2)	3.170(3)	112.2(19)
C6-H6···O4^{iii}	0.94(2)	2.84(2)	3.317(3)	112.9(15)
C10-H10···O1^{iv}	0.94(2)	2.48(3)	3.219(4)	135(2)
C4-H4···Cg2	0.90(2)	3.38	3.72	105
C12-H12···Cg^{v}	0.90(3)	3.13	3.71	124

Symmetry codes: (i) ½ - x, ½ + y, z - ½; (ii) ½ - x, ½ + y, ½ + z; (iii) x, y, 1 + z; (iv) ½ + x, ½ - y, z - 1; (v) 1 - x, -y, z - ½.

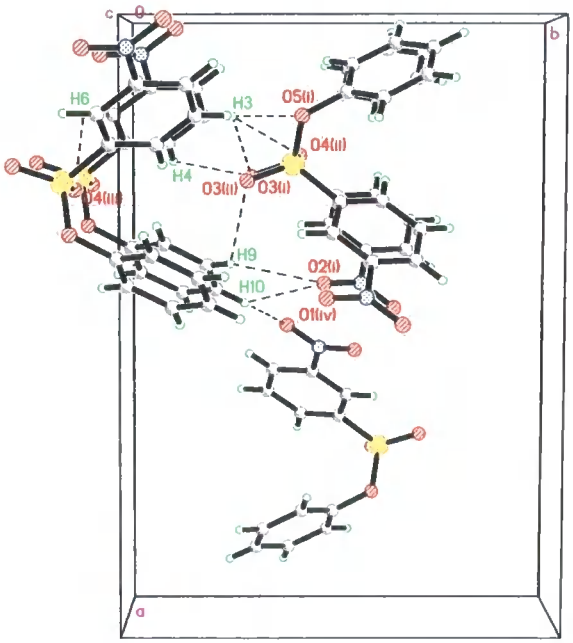

Figure 2.3.4: Diagram of intermolecular interactions in compound **2** as viewed along the *c*-axis. For symmetry codes see Table 2.3.3.

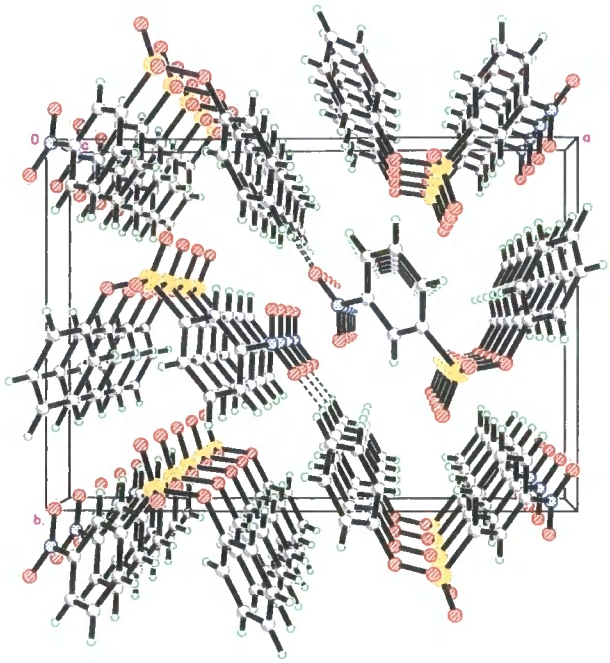

Figure 2.3.5: Packing diagram for compound **2** as viewed along the *c*-axis. The dashed lines indicate the C10-H10···O1^{iv} interaction.

Table 2.3.4: Selected bond parameters for compound **2**.

Bond	Length (Å)	Atoms	Angle (°)
S1-O3	1.418(2)	O3-S1-O4	120.8(1)
S1-O4	1.418(2)	O3-S1-O5	103.7(1)
S1-O5	1.600(2)	O4-S1-O5	108.9(1)
S1-C5	1.763(3)	O3-S1-C5	110.7(1)
N1-O1	1.230(3)	O4-S1-C5	108.0(1)
N1-O2	1.226(3)	O5-S1-C5	103.3(1)
N1-C1	1.480(4)	C7-O5-S1	117.4(2)
		O1-N1-O2	124.3(3)
		O1-N1-C1	117.6(2)
		O2-N1-C1	118.1(2)

The dihedral angle between the aromatic rings is 38.76(8)°. This clearly indicates that the molecule is non-planar. Atoms N1, O1 and O2 lie in the plane given by atoms C1-C6; the deviations of these atoms from this plane are -0.021(2) Å, -0.049(2) Å and 0.005(2) Å respectively. Table 2.3.4 provides information about selected bonds in the structure of **2**. To allow for easy comparison with the experimental obtained values, Table 2.3.5 gives the expected

bond lengths for the major functional groups present in compounds **2** - **8**. The reported bond lengths for **2** (Table 2.3.4) are in agreement with the expected literature values. The sulphur atom possesses highly distorted tetrahedral geometry.

Table 2.3.5: Selected bond parameters listed in the International Tables Vol. C.[10]

Bond Type	Bond Environment	Average Bond Length (Å)
O-S	C-**O**-SO_2-C	1.577
O-S	C-**O**-SO_2-C_{ar} †	1.580
O=S	C-SO_2-O-C	1.423
C-S	C_{ar}-SO_2-O-X ††	1.752
N-O	C_{ar}-NO_2	1.217
N-C	C_{ar}-NO_2	1.468
C-O	CH_3-C-O-C(=O)-C	1.448
C=O	C_{ar}-C(=O)-O-C	1.202

† No average bond length for C_{ar}-**O**-SO_2-C_{ar} was reported. †† 'X' denotes any atom.

2.3.3 2-Nitrophenyl 3-nitrobenzenesulphonate

Figure 2.3.6 displays the weak intramolecular hydrogen bonds present in the crystal structure of 2-nitrophenyl 3-nitrobenzenesulphonate (**3**).[13] The geometric parameters for these interactions are given in Table 2.3.6. Each intramolecular bond forms an S(5) pattern.

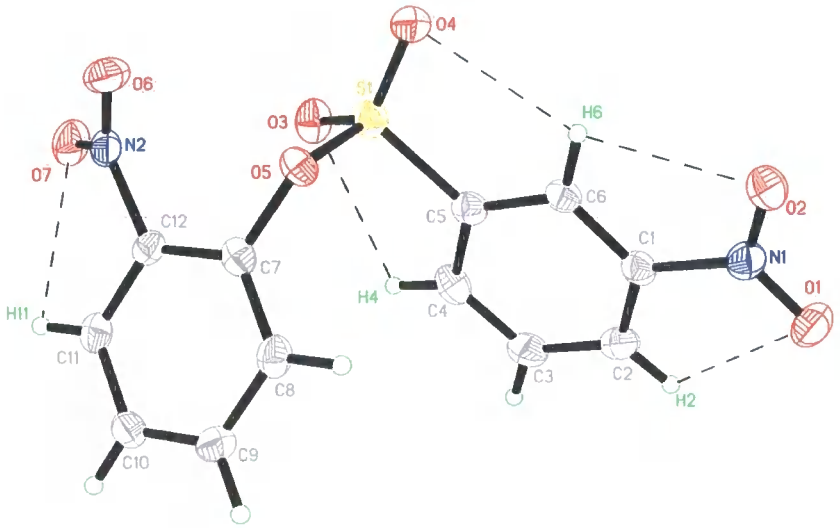

Figure 2.3.6: 50% Thermal-ellipsoid plot of compound **3**, displaying intramolecular C-H···O bonds.

A complex network of C-H···O hydrogen bonds exists in the crystal structure of compound **3** (Table 2.3.6); this network is shown in Figure 2.3.7. Atom $O4^{i}$ is a bifurcated hydrogen acceptor to which both C8-H8 and C9-H9 donate (see Table 2.3.6 for symmetry codes). The pattern generated by these interactions is of the binary graph-set $R_2^1(5)$. Atom $O4^{ii}$ is also a bifurcated hydrogen acceptor, and forms hydrogen bonds with C3-H3 and C4-H4 to give a pattern with the binary graph-set $R_2^1(5)$.

Table 2.3.6: Geometric bond parameters for hydrogen bonds exhibited in compound **3**.

D-A···A (Å)	D-H (Å)	H···A (Å)	D···A (Å)	D-H···A (°)
C2-H2···O1	0.93(2)	2.40(3)	2.708(4)	99.2(18)
C4-H4···O3	0.94(2)	2.57(2)	2.948(3)	104.5(17)
C6-H6···O2	1.03(2)	2.43(2)	2.711(3)	94.2(14)
C6-H6···O4	1.03(2)	2.58(2)	2.944(3)	100.4(16)
C11-H11···O7	0.91(2)	2.57(2)	2.788(3)	94.4(16)
C8-H8···$O4^{i}$	0.97(2)	2.72(2)	3.359(3)	123.8(17)
C9-H9···$O4^{i}$	0.95(3)	2.73(3)	3.374(3)	125.3(18)
C2-H2···$O6^{i}$	0.93(3)	2.48(2)	3.092(3)	123.5(18)
C3-H3···$O6^{ii}$	0.98(2)	2.98(3)	3.836(3)	147.1(19)
C3-H3···$O4^{ii}$	0.98(3)	2.78(3)	3.409(3)	122.5(18)
C9-H9···$O2^{ii}$	0.95(3)	2.88(2)	3.398(3)	115.6(18)
C4-H4···$O4^{ii}$	0.94(3)	2.86(2)	3.401(3)	117.31(18)
C10-H10···$O2^{ii}$	0.93(2)	2.54(2)	3.236(3)	131.4(18)
C3-H3···$O5^{ii}$	0.98(2)	2.93(2)	3.842(3)	156(2)
C10-H10···$O1^{iii}$	0.93(2)	2.51(2)	3.177(3)	129.2(19)
C11-H11···$O1^{iii}$	0.91(2)	2.79(2)	3.300(3)	116.2(17)
C11-H11···$O6^{iv}$	0.91(2)	2.60(2)	3.484(3)	163.5(19)

Symmetry codes: (i) ½ - x, ½ + y, ½ +z; (ii) ½ - x, ½ + y, z - ½; (iii) ½ + x, $^{3}/_{2}$ – y, 1 - z; (iv) 1 + x, 1 - y, z - ½.

Table 2.3.7: Higher-level graph-set analysis for C3-H3···O bond patterns.

	C3-H3···O6^{ii}	C3-H3···O5^{ii}	C3-H3···O4^{ii}
C3-H3···O6^{ii}	D	-	-
C3-H3···O5^{ii}	N_2: $R_1^2(6)$	D	-
C3-H3···O4^{ii}	N_2: $R_1^2(8)$	N_2: $R_1^2(4)$	D

Symmetry code: (ii) ½ - x, ½ + y, z - ½.

C3-H3 is a trifurcated hydrogen bond donor, and the resultant pattern is assigned the 'unitary' graph-set DDD. Higher-level graph-set analysis of the C3-H3 hydrogen bond patterns can be found in Table 2.3.7. The C9-H9···O2^{ii} and C10-H10···O2^{ii} interactions constitute a bifurcated hydrogen bond of the N_2: $R_2^1(5)$ graph-set. Bonds C10-H10···O1^{iii} and C11-H11···O1^{iii} together constitute a bifurcated hydrogen bond of the N_2: $R_2^1(5)$ set.

The overlaying of the nitrobenzene rings in the packing arrangement indicates the possible of π···π interactions (Figure 2.3.8). However the distance between centroids of neighbouring molecules is 5.131 Å. This is too long to be considered as an intermolecular π···π bond.

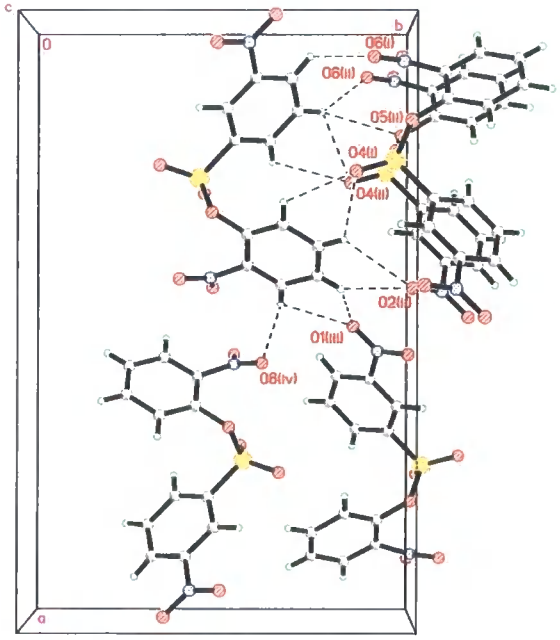

Figure 2.3.7: Diagram of intermolecular interactions in compound **3** as viewed along the *c*-axis. For symmetry codes see Table 2.3.6

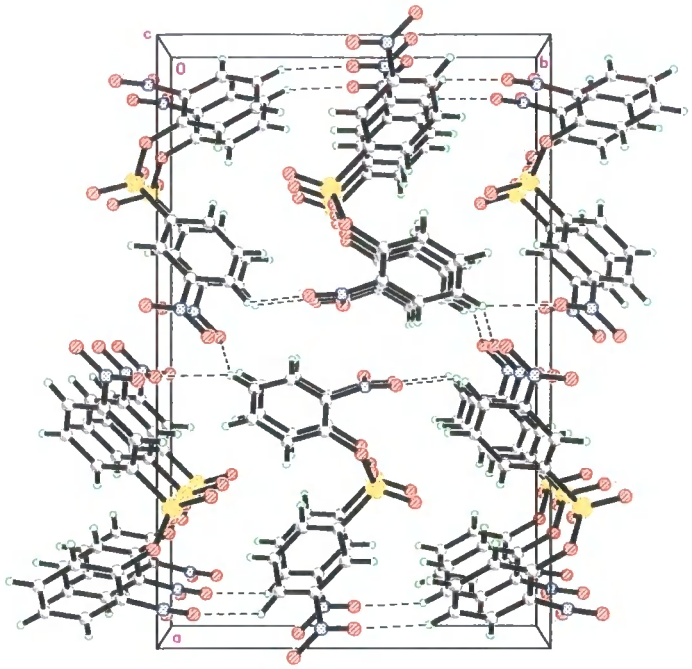

Figure 2.3.8: Packing diagram for compound **3** as viewed along the *c*-axis.

In the crystal structure of compound **3** molecular chains parallel to the *b*-axis are present (Figure 2.3.8). These chains are linked via C11-H11···O6^{iv} interactions and run in alternating directions. The apparent ring patterns in Figure 2.3.8 are a feature of the diagram orientation and not, as might be interpreted, a 'true' hydrogen bond ring.

The bond lengths for compound **3** are given in Table 2.3.8, they are in reasonable agreement with the expected values given in Table 2.3.5. The dihedral angle between the aromatic rings is 39.68(8)°. The deviations of atoms N1, O1, and O2 from the plane formed by atoms C7-C12 are 0.031(3) Å, 0.015(4) Å and 0.085(4) Å respectively, implying that this nitro group lies in the plane formed by the ring. Conversely, the deviations of atoms N2, O6 and O7 from the plane formed by atoms C1-C6 are 0.146(3) Å, 0.874(4) Å and 0.456(4) Å respectively, these values suggests that this nitro group is twisted with respect to the ring plane.

Table 2.3.8: Selected bond parameters for compound **3**.

Bond	Length (Å)	Atoms	Angle (°)
S1-O3	1.425(2)	O3-S1-O4	121.3(1)
S1-O4	1.420(2)	O3-S1-O5	108.83(9)
S1-O5	1.599(2)	O4-S1-O5	103.53(9)
S1-C5	1.765(2)	O3-S1-C5	108.2(1)
N1-O1	1.227(2)	O4-S1-C5	109.93(9)
N1-O2	1.228(3)	O5-S1-C5	103.59(9)
N1-C1	1.471(3)	C7-O5- S1	118.1(1)
N2-O6	1.226(2)	O1-N1-O2	124.0(2)
N2-O7	1.229(3)	O1-N1-C1	117.7(2)
N2-C12	1.469(3)	O2-N1-C1	118.3(2)
		O6-N2-O7	124.8(2)
		O6-N1-C12	117.5(2)
		O7-N1-C12	117.7(2)

2.3.4 2,4-Dinitrophenyl 3-nitrobenzenesulphonate

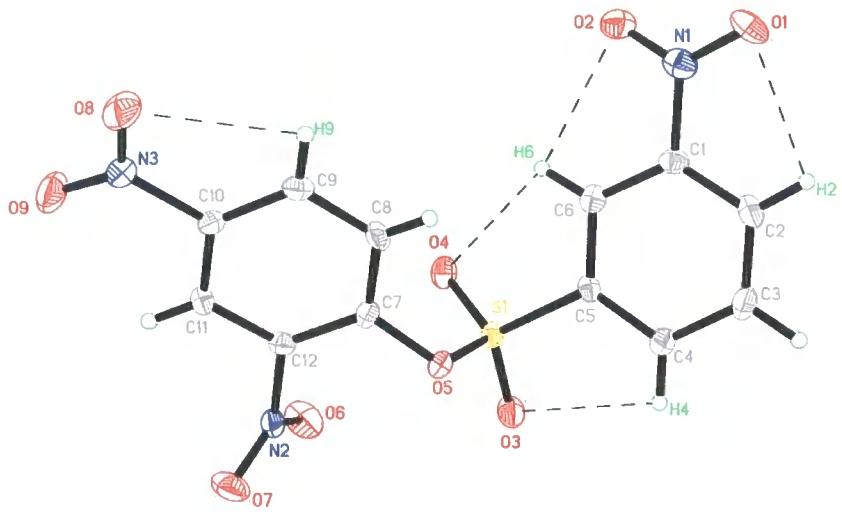

Figure 2.3.9: 50% Thermal-ellipsoid representation of compound **4** displaying intermolecular C-H···O hydrogen bonds.

All intramolecular hydrogen motifs in 2,4-dinitrophenyl 3-nitrobenzenesulphonate (**4**) [14] (Figure 2.3.9), namely those involving atoms O1, O2, O3, O4, and O8, are of graph-set S(5). All intra- and inter-molecular hydrogen bonds that are present in the crystal structure of compound **4** are recorded in Table 2.3.9.

The intermolecular hydrogen bond network within the crystal structure of **4** is elaborate and comprises many weak C-H···O interactions. C3-H3 acts as a bifurcated donor forming hydrogen bonds with both $O3^{ii}$ and $O6^{ii}$ this gives a N_2: $R_1^2(8)$ pattern (see Table 2.3.9 for symmetry codes). C6-H6 is a trifurcated donor forming weak hydrogen bonds with atoms $N3^{iv}$, $O8^{iv}$, and $O9^{iv}$. A higher-level graph-set analysis for the hydrogen bond patterns generated by C6-H6 interactions with the symmetry-generated molecule 1 – x, 1 – y, z - ½ is given in Table 2.3.10.

The C8-H8···$O4^{v}$ and C8-H8···$O8^{vi}$ interactions constitute a bifurcated hydrogen bond. Likewise, the C11-H11···$O1^{viii}$ and C11-H11···$O2^{ix}$ interactions when considered together give a bifurcated hydrogen bond. The hydrogen bond network is completed by several other contacts listed in Table 2.3.9 all of which are of the graph-set D. The intermolecular interactions listed in Table 2.3.9 are displayed diagrammatically in Figure 2.3.10. The complex molecular packing of compound **4** in the crystalline state is shown in Figure 2.3.11.

The bond lengths in Table 2.3.11 are in reasonable agreement with the expected values given in Table 2.3.5. The dihedral angle between the aromatic rings is 36.10(7)°. The deviations of atoms N1, O1 and O2 from the plane formed by atoms C1-C6 are 0.005(3) Å, -0.248(4) Å and 0.267(4) Å respectively; the deviations of atoms N2, O6, O7, N3, O8, and O9 from the plane defined by atoms C7-C12 are 0.069(3) Å, -0.849(3) Å, 1.051(3) Å, 0.026(3) Å, 0.341(4) Å and -0.277(4) Å respectively. These figures indicate that all the nitro groups are tilted with respect to the plane of the aromatic ring to which they are bound.

Table 2.3.9: Geometric bond parameters for C-H···O bonds in compound **4**.

D-A···A (Å)	D-H (Å)	H···A (Å)	D···A (Å)	D-H···A (°)
C2-H2···O1	0.95(2)	2.43(2)	2.742(3)	99.0(15)
C4-H4···O3	0.94(2)	2.63(2)	2.944(3)	100.4(15)
C6-H6···O2	0.95(2)	2.50(2)	2.715(3)	92.7(15)
C6-H6···O4	0.95(2)	2.49(2)	2.898(2)	106.4(16)
C9-H9···O8	0.86(2)	2.53(2)	2.745(3)	94.9(18)
C11-H11···O9	0.90(2)	2.46(2)	2.699(3)	95.3(16)
C2-H2···O7^{i}	0.95(2)	2.45(2)	3.374(3)	166.2(19)
C3-H3···O3^{ii}	0.97(2)	2.43(2)	3.208(3)	137.0(18)
C3-H3···O6^{ii}	0.97(2)	2.47(2)	3.263(3)	138.2(18)
C4-H4···O7^{iii}	0.94(2)	2.99(2)	3.781(3)	142.9(17)
C6-H6···N3^{iv}	0.95(2)	2.93(2)	3.836(3)	161.2(18)
C6-H6···O8^{iv}	0.95(2)	2.77(2)	3.652(3)	155.7(19)
C6-H6···O9^{iv}	0.95(2)	2.70(2)	3.572(3)	153.6(17)
C8-H8···O4^{v}	0.81(2)	2.43(2)	3.008(2)	129.2(19)
C8-H8···O8^{vi}	0.81(2)	2.96(2)	3.681(3)	150.0(16)
C9-H9···O2^{vii}	0.86(2)	2.97(2)	3.726(3)	147(2)
C11-H11···O1^{viii}	0.90(2)	2.58(2)	3.362(3)	145.1(18)
C11-H11···O2^{ix}	0.90(2)	2.62(2)	3.240(3)	126.4(17)

Symmetry codes: (i) x, 1 + y, z –1; (ii) $^{3}/_{2}$ – x, 1 + y, z - ½; (iii) $^{3}/_{2}$ – x, y, z - ½; (iv) 1 – x, 1 – y, z - ½; (v) x, 1 + y, z; (vi) 1 – x, 2 – y, z - ½; (vii) 1 – x, 2 – y, z - ½; (viii) x, y – 1, 1 + z; (ix) x, y, 1 + z.

Table 2.3.10: Higher-level graph-set analysis for C6-H6···O^{iv} patterns.

	C6-H6···N3^{iv}	C6-H6···O8^{iv}	C6-H6···O9^{iv}
C6-H6···N3^{iv}	D	-	-
C6-H6···O8^{iv}	N_2: $R_1^2(3)$	D	-
C6-H6···O9^{iv}	N_2: $R_1^2(3)$	N_2: $R_1^2(4)$	D

Symmetry code: (iv) 1 – x, 1 – y, z - ½

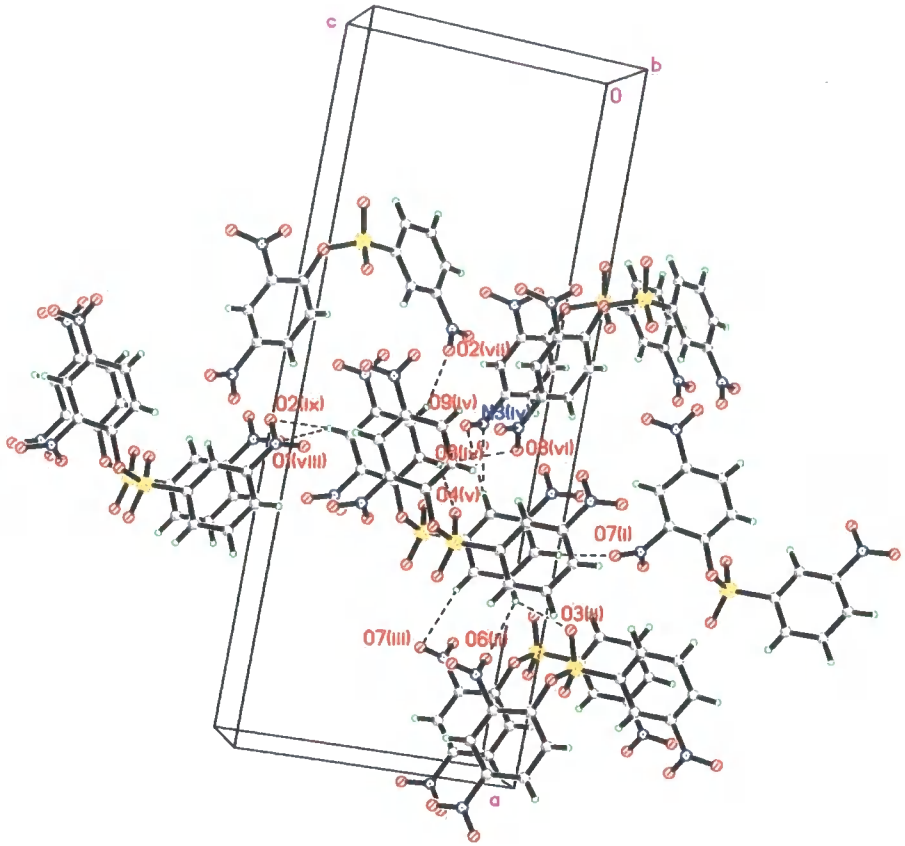

Figure 2.3.10: Diagram of intermolecular interactions in compound **4**. For symmetry codes see Table 2.3.9.

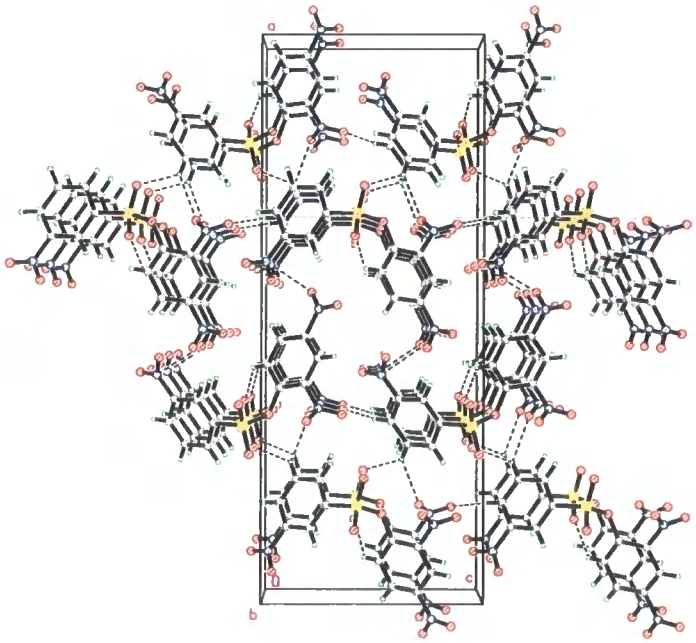

Figure 2.3.11: Packing diagram of compound **4** as viewed along the *a*-axis.

Table 2.3.11: Selected bond parameters for compound **4**.

Bond	Length (Å)	Atoms	Angle (°)
S1-O3	1.415(2)	O3-S1-O4	122.42(8)
S1-O4	1.418(1)	O3-S1-O5	104.06(8)
S1-O5	1.622(2)	O4-S1-O5	107.75(8)
S1-C5	1.753(2)	O3-S1-C5	108.77(9)
N1-O1	1.225(2)	O4-S1-C5	108.5(1)
N1-O2	1.227(3)	O5-S1-C5	103.71(8)
N1-C1	1.473(3)	C7-O5- S1	120.2(1)
N2-O6	1.211(2)	O1-N1-O2	124.0(2)
N2-O7	1.224(2)	O1-N1-C1	118.1(2)
N2-C12	1.477(2)	O2-N1-C1	117.9(2)
N3-O8	1.216(2)	O6-N2-O7	125.8(2)
N3-O9	1.216(2)	O6-N1-C12	118.1(2)
		O7-N1-C12	116.1(2)
		O8-N3-O9	124.4(2)
		O8-N3-C10	118.2(2)
		O9-N3-C10	117.4(2)

2.3.5 8-Quinolyl 3-nitrobenzenesulphonate

The intramolecular hydrogen bonds for 8-quinolyl 3-nitrobenzenesulphonate (**5**) [15] are shown in Figure 2.3.12 are listed in Table 2.3.12. C2-H2 is a trifurcated hydrogen bond donor; the C2-H2···O2 and C2-H2···O3 interactions generate ring patterns of graph-set S(5). The C2-H2···N2 bond gives a larger ring motif of S(8). The C4-H4···O4 and C6-H6···O1 contacts both create ring patterns of graph-set S(5). The donor group C17-H17 forms a trifurcated hydrogen bond to acceptor atoms N4, O7 and O10. The weak C17-H17···N4 interactions results in the formation of a ring pattern of the graph-set S(8). The remaining two C17-H17 intramolecular interactions both form S(5) motifs. The intramolecular bonding in compound **5** is completed by the C19-H19···O9 and C21-H21···O6 bonds, both of which form ring patterns that can be assigned the graph-set S(5).

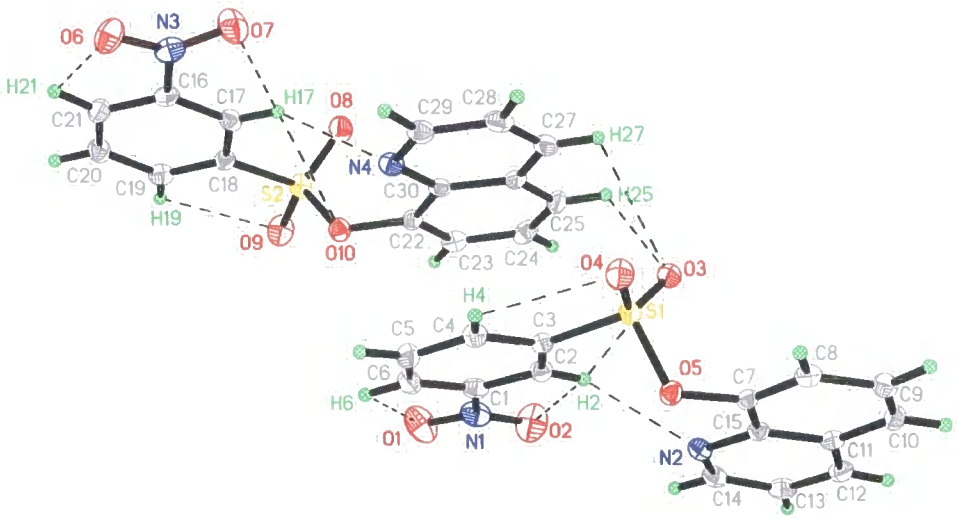

Figure 2.3.12: 50% Thermal-ellipsoid representation of compound **5**, displaying intramolecular hydrogen bonds.

The O3 atom acts as a bifurcated hydrogen bond acceptor forming bonds with both C25-H25 and C27-H27 donors. These intermolecular interactions link the two molecules of the asymmetric unit, and give a hydrogen bond pattern of the binary graph-set $R_2^1(6)$. Figure 2.3.13 is a partial representation of the hydrogen bond network present in compound **5**, for clarity only selected bonds are shown.

From Table 2.3.12, and by consideration of the molecular structure it can be seen that the C4-H4···O8^{i} and C5-H5···O9^{i} bonds produce a ring pattern of the graph-set N_2: $R_2^2(7)$. It can also be seen that C8-H8 is a trifurcated hydrogen bond donor forming intermolecular bonds with the N3, O6 and O7 atoms of a symmetry equivalent molecule at 2 – x, 1 - y, 1 – z. The two latter bonds create a ring pattern of the binary graph-set $R_1^2(4)$. In addition to forming an interaction with C8-H8, O6^{iii} forms a hydrogen bond to C9-H9; this makes O6^{iii} a bifurcated hydrogen bond acceptor (see Table 2.3.12 for symmetry codes). The combination of the C9-H9···O6^{iii} and C8-H8···O6^{iii} interactions creates a ring pattern of the binary graph-set $R_2^1(5)$. A large ring pattern of set N_2: $R_2^2(7)$ is generated by bonds C9-H9···O6^{iii} and C8-H8···O7^{iii}.

A combination of the C9-H9···O10^{iv} and C10-H10···N4^{iv} interactions give rise to a ring pattern of the binary graph-set $R_2^2(8)$. The donor group C10-H10 is bifurcated and also forms a bond with atom O8^{v}. This interaction and the C12-H12···O8^{v} interaction give an $R_2^1(6)$ pattern. Bonds C12-H12···O4^{vi} and C13-H13···O3^{vi} form a chelate pattern of graph-set N_2: $R_2^2(7)$. Bonds C14-H14···O9^{vii} and C13-H13···O9^{vii} constitute a pair of bifurcated acceptor bonds generating an N_2: $R_2^1(5)$ pattern. Bonds C24-H24···O1^{vii} and C23-H23···O2^{vii} creates a N_2: $R_2^2(7)$ pattern. A large ring pattern is formed by the hydrogen bonds C28-H28···O8^{xi} and C25-H25···O7^{xi} ; this can be assigned the binary graph-set $R_2^2(13)$.

In addition to these weak hydrogen bonds, the crystal structure of compound **5** is further stabilised by weak intermolecular π···π bonds; these interactions are listed in Table 2.3.13. The identities of the individual centroids are given in Table 2.3.14.

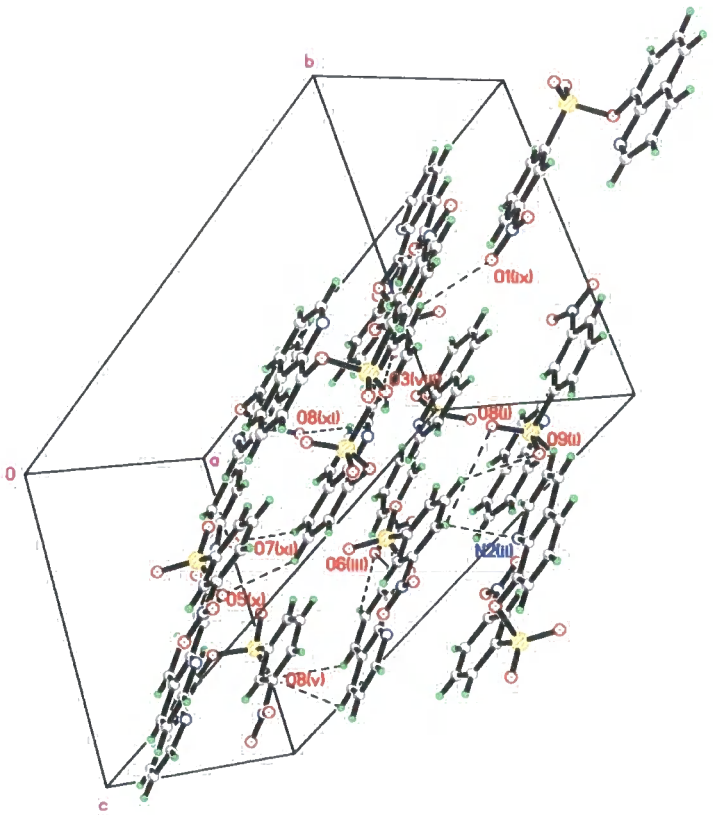

Figure 2.3.13: Diagram displaying selected hydrogen bonds in compound **5** as dashed lines. For symmetry codes refer to Table 2.3.12.

Table 2.3.12: Geometric bond parameters for weak hydrogen bonds in compound **5**.

D-A···A (Å)	D-H (Å)	H···A (Å)	D···A (Å)	D-H···A (°)
C2-H2···N2	0.949(19)	2.51(2)	3.281(3)	138.2(15)
C2-H2···O2	0.949(19)	2.379(18)	2.691(2)	98.7(13)
C2-H2···O3	0.949(19)	2.808(18)	3.023(2)	93.8(12)
C4-H4···O4	0.960(19)	2.568(19)	2.926(2)	102.3(13)
C6-H6···O1	0.98(2)	2.427(19)	2.734(2)	97.6(13)
C17-H17···N4	0.953(19)	2.49(2)	3.336(3)	147.6(15)
C17-H17···O7	0.953(19)	2.438(18)	2.704(2)	95.7(13)
C17-H17···O10	0.953(19)	2.833(18)	3.056(2)	94.3(12)
C19-H19···O9	0.926(19)	2.526(19)	2.911(2)	105.3(14)
C21-H21···O6	0.93(2)	2.45(2)	2.726(2)	96.6(14)
C25-H25···O3	0.95(2)	2.968(19)	3.382(2)	107.9(14)
C27-H27···O3	0.95(2)	2.810(19)	3.249(2)	109.2(14)
C4-H4···O8^{i}	0.96(2)	2.977(19)	3.665(2)	129.7(14)
C5-H5···O9^{i}	0.96(2)	2.96(2)	3.749(3)	140.2(15)
C6-H6···N2^{ii}	0.98(2)	2.68(2)	3.377(3)	128.6(15)
C9-H9···O6^{iii}	0.96(2)	2.661(19)	3.344(2)	128.4(15)
C8-H8···N3^{iii}	0.952(19)	2.970(19)	3.807(2)	147.4(14)
C8-H8···O6^{iii}	0.952(19)	2.761(19)	3.380(2)	123.4(14)
C8-H8···O7^{iii}	0.952(19)	2.506(19)	3.444(2)	168.3(16)
C29-H29···O4^{iii}	0.96(2)	2.495(19)	3.305(2)	141.8(16)
C9-H9···O10^{iv}	0.96(2)	2.82(2)	3.566(2)	134.9(15)
C10-H10···N4^{iv}	0.963(19)	2.67(2)	3.346(2)	127.7(15)
C10-H10···O8^{v}	0.963(19)	2.99(2)	3.391(2)	106.5(13)
C12-H12···O8^{v}	0.94(2)	2.94(2)	3.313(2)	105.3(14)
C12-H12···O4^{vi}	0.94(2)	2.71(2)	3.547(2)	147.9(16)
C13-H13···O3^{vi}	0.98(2)	2.79(2)	3.509(2)	130.6(15)
C24-H24···O1^{vii}	0.96(2)	2.78(2)	3.517(3)	133.8(15)
C14-H14···O9^{vii}	0.99(2)	2.491(19)	3.217(2)	129.9(15)
C13-H13···O9^{vii}	0.98(2)	2.77(2)	3.336(2)	117.5(14)
C23-H23···O2^{vii}	0.993(19)	2.479(19)	3.412(2)	156.3(15)

C19-H19···O3^{viii}	0.926(19)	2.76(2)	3.435(2)	130.6(15)
C21-H21···O1^{ix}	0.93(2)	2.87(2)	3.694(3)	147.2(16)
C24-H24···O5^{x}	0.96(2)	2.81(2)	3.651(2)	146.8(16)
C28-H28···O8^{xi}	0.91(2)	2.78(2)	3.387(2)	125.9(16)
C25-H25···O7^{xi}	0.95(2)	2.68(2)	3.543(3)	151.7(16)

Symmetry codes: (i) 1 + x, y, z; (ii) 2 – x, 1 - y, 2 - z; (iii) 2 – x, 1 - y, 1 - z; (iv) 2 – x, y - ½, $^{3}/_{2}$ - z; (v) 1 - x, y - ½, $^{3}/_{2}$ - z; (vi) x, ½ – y, ½ + z; (vii) 1 – x, 1 – y, 2 - z; (viii) 1 - x, ½ - y, $^{3}/_{2}$ - z; (ix) x, $^{3}/_{2}$ - y, z - ½; (x) x – 1, y, z; (xi) 1 - x, 1 – y, 1 – z.

Interaction	Centroid - Centroid Distance (Å)
Cg1···Cg5^{v}	3.604
Cg2···Cg2^{xi}	3.450
Cg2···Cg3	3.786
Cg3···Cg6	3.596
Cg4···Cg5^{iv}	3.781

Symmetry codes: Refer to Table 2.3.12

Table 2.3.13: Bond lengths for π···π interactions present in the structure of compound **5**.

Centroid	Associated Ring
Cg1	N2, C11-C15
Cg2	N4, C26-C30
Cg3	C1-C6
Cg4	C15, C7-C11
Cg5	C16-C21
Cg6	C30, C22-C26

Table 2.3.14: Identities of the individual centroids reported in Table 2.3.13.

Selected bond lengths and angles for compound **5** are provided in Table 2.3.15, the values reported are in agreement with the expected values. The dihedral angles between the quinoline rings and the nitrobenzene ring are 8.28(5)° and 5.18(5)° for molecules 1 (contains S1) and 2 (contains S2) respectively implying that the molecules are nearly planar. Atoms N1, O1 and O2

deviate from the plane given by atoms C1-C6 by -0.005(2) Å, -0.099(2) Å, and 0.091(2) Å respectively. Atoms N3, O6 and O7 deviate from the plane defined by atoms C16-C21 by -0.002(2) Å, 0.220(1) Å, and -0.218(2) Å respectively.

Table 2.3.15: Selected bond parameters for compound **5**.

Bond	Length (Å)	Atoms	Angle (°)
S1-O3	1.427(1)	O3-S1-O4	119.43(8)
S1-O4	1.424(1)	O3-S1-O5	108.56(7)
S1-O5	1.591(1)	O4-S1-O5	108.26(8)
S1-C3	1.756(2)	O3-S1-C3	109.91(8)
N1-O1	1.223(2)	O4-S1-C3	108.84(9)
N1-O2	1.221(3)	O5-S1-C3	100.10(8)
N1-C1	1.483(2)	C7-O5- S1	117.1(1)
		O1-N1-O2	124.5(2)
		O1-N1-C1	117.8(2)
		O2-N1-C1	117.7(2)
S2-O8	1.428(1)	O8-S2-O9	119.27(9)
S2-O9	1.421(1)	O8-S2-O10	108.40(8)
S2-O10	1.594(1)	O9-S2-O10	108.09(8)
S2-C18	1.761(2)	O8-S2-C18	110.24(9)
N3-O6	1.223(2)	O9-S2-C18	108.59(9)
N3-O7	1.228(2)	O10-S2-C18	100.62(8)
N3-C16	1.475(2)	C22-O10-S2	118.2(1)
		O6-N3-O7	124.3(2)
		O6-N3-C16	118.2(2)
		O7-N3-C16	117.6(2)

2.3.6 *Methyl 4-(3-nitrobenzenesulphonyloxy)benzoate*

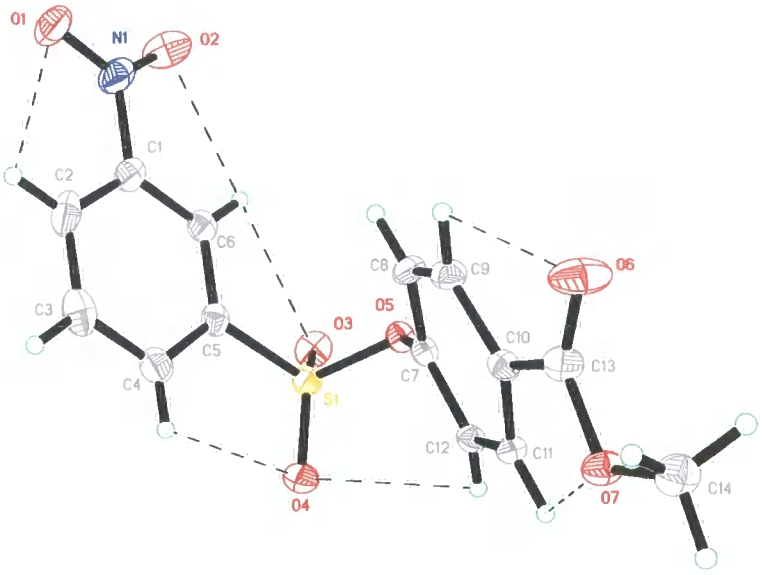

Figure 2.3.14: 50% Thermal-ellipsoid representation of compound **6**. Dashed lines indicate intramolecular C-H···O bonds.

A diagrammatic representation of the intramolecular interactions present in methyl 4-(3-nitrobenzenesulphonyloxy)benzoate (**6**) [16] is provided in Figure 2.3.14. The hydrogen bond ring motifs involving atoms O1, O2, O3, O6, and O7 are all of the graph-set S(5). Atom O4 is a bifurcated hydrogen bond acceptor forming two intramolecular C-H···O bonds. The C4-H4···O4 contact generates an additional S(5) motif, while the C12-H12···O4 interaction gives an S(6) motif.

Table 2.3.16 lists all the hydrogen bonds present in the crystal structure of compound **6**; the intermolecular interactions are shown in Figure 2.3.15. A combination of bonds C9-H9···O3^{iv} and C8-H8···O4^{iv} creates a ring pattern of graph-set N_2: $R_2^2(7)$ (see Table 2.3.16 for symmetry codes). Atom O6^{v} is a bifurcated hydrogen bond acceptor forming bonds with both C11-H11 and C12-H12 donor groups; the resulting pattern is of the binary graph-set $R_2^1(5)$.

Table 2.3.16: Geometric bond parameters C-H···O bonds in compound **6**.

D-A···A (Å)	D-H (Å)	H···A (Å)	D···A (Å)	D-H···A (°)
C2-H2···O1	0.93(2)	2.438(19)	2.717(3)	97.2(13)
C4-H4···O4	0.886(19)	2.571(18)	2.938(2)	105.8(13)
C6-H6···O2	0.920(18)	2.422(18)	2.702(2)	97.6(13)
C6-H6···O3	0.920(18)	2.696(18)	2.996(2)	100.0(13)
C9-H9···O6	0.946(18)	2.543(17)	2.816(2)	96.8(11)
C11-H11···O7	0.928(16)	2.479(16)	2.771(2)	98.4(11)
C12-H12···O4	0.915(18)	2.855(16)	3.184(2)	102.7(12)
C2-H2···O2^{i}	0.93(2)	2.796(19)	3.309(3)	115.7(14)
C4-H4···O1^{ii}	0.886(19)	2.596(19)	3.454(3)	163.2(15)
C6-H6···O7^{iii}	0.920(18)	2.707(19)	3.599(2)	163.5(15)
C9-H9···O3^{iv}	0.946(18)	2.401(18)	3.198(2)	141.6(13)
C8-H8···O4^{iv}	0.932(18)	2.998(18)	3.870(2)	156.4(14)
C12-H12···O6^{v}	0.915(18)	2.489(18)	3.152(2)	129.6(13)
C11-H11···O6^{v}	0.948(16)	2.805(16)	3.324(2)	116.5(11)
C14-H14A···O4^{vi}	0.98(2)	2.74(2)	3.712(2)	173.3(15)
C14-H14B···O5^{vii}	0.953(19)	2.67(2)	3.528(2)	149.7(15)
C14-H14B···O7^{viii}	0.953(19)	2.839(19)	3.497(2)	127.1(13)
C14-H14C···O3^{ix}	0.96(2)	2.721(19)	3.536(2)	143.2(15)
C3-H3···Cg2^{x}	0.95(2)	2.85	3.70	149

Symmetry codes: (i) 1 - x, ½ + y, ½ - z; (ii) x, ½ - y, z - ½; (iii) x, y - 1, z; (iv) x, ½ - y - ½, ½ + z; (v) x, $^{3}/_{2}$ – y, z - ½; (vi) x, $^{3}/_{2}$ – y, ½ + z; (vii) x, 1 + y, z; (viii) - x, 2 - y, - z; (ix) - x, 1 - y, - z; (x) 1 - x, - y, - z.

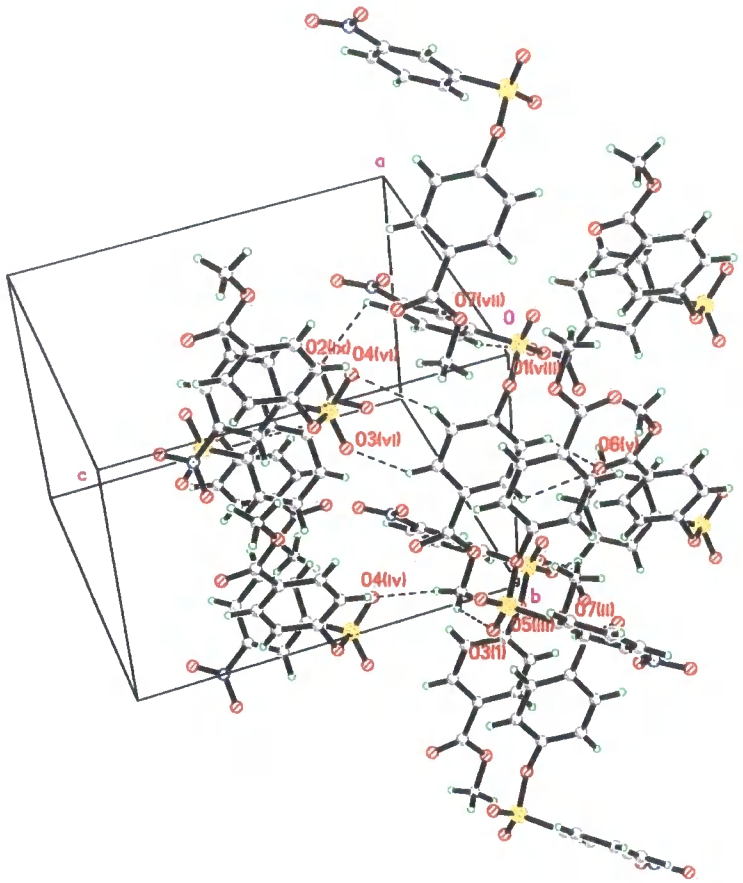

Figure 2.3.15: Diagram showing intermolecular interactions in compound **6**. Symmetry codes are given in Table 2.3.16.

Additional stabilisation of the crystal structure is achieved by the presence of a weak C-H···π interaction (Table 2.3.16); the C-H···Cg2^{x} angle is 149°. Cg2 is the centroid of the ring formed by atoms C7-C12. A weak π···π bond completes the network of intermolecular contacts. This interaction is between Cg2 and Cg2^{x}, and has a centroid-centroid separation of 3.663 Å.

The experimental values reported in Table 2.3.17 concord with the expected values given in Table 2.3.5. The dihedral angle between the phenyl rings is 58.4(5)°. The ester group atoms C13, O6, O7 and C14 deviate from the plane given by atoms C7-C12 by -0.189(3) Å, -0.512(3) Å, 0.015(3) Å, and -0.229(4) Å respectively. The nitro-group atoms, N1, O1 and O2 deviate from the C1-C6 plane by 0.003(2) Å, 0.085(1) Å, and -0.077 (1) Å respectively.

Table 2.3.17: Selected bond parameters for compound **6**.

Bond	Length (Å)	Atoms	Angle (°)
S1-O3	1.416(1)	O3-S1-O4	120.90(8)
S1-O4	1.421(1)	O3-S1-O5	102.93(7)
S1-O5	1.589(1)	O4-S1-O5	109.67(7)
S1-C5	1.757(2)	O3-S1-C5	109.59(8)
N1-O1	1.225(2)	O4-S1-C5	109.51(8)
N1-O2	1.225(2)	O5-S1-C5	102.53(7)
N1-C1	1.474(2)	C7-O5- S1	120.64(9)
C13-O6	1.205(2)	O1-N1-O2	124.6(2)
C13-O7	1.338(2)	O1-N1-C1	117.6(2)
C14-O7	1.447(2)	O2-N1-C1	117.8(2)
C10-C13	1.488(2)	C10-C13-O6	123.9(2)
		C10-C13-O7	112.5(1)
		O6-C13-O7	123.9(2)
		C13-O7-C14	114.9(1)

2.3.7 Methyl 4-tosyloxybenzoate

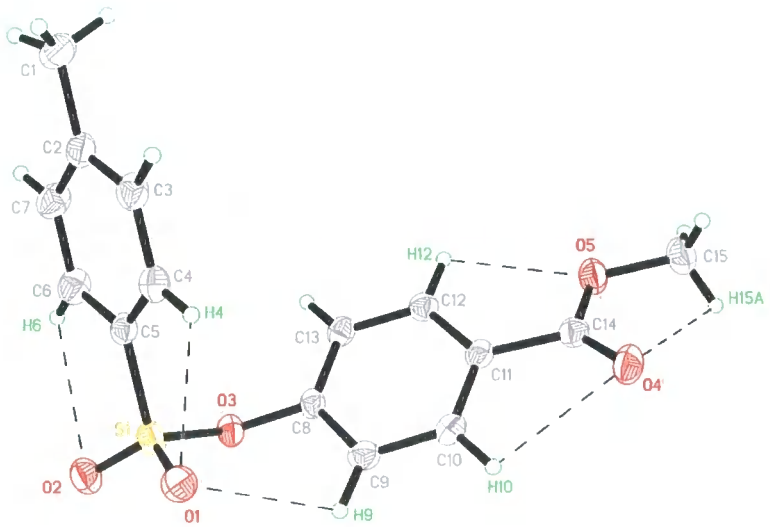

Figure 2.3.16: 50% Thermal-ellipsoid plot of compound **7** showing intramolecular C-H···O bonds.

The geometric parameters for the intramolecular C-H···O bonds displayed in methyl 4-tosyloxybenzoate (**7**) [17] are shown in Figure 2.3.16 are listed in Table 2.3.18.The intramolecular contacts involving atoms O2, O5 and O4, all give ring motifs of graph-set S(5). Atom O1 is a bifurcated hydrogen bond acceptor. Bond C9-H9···O1 forms a S(6) motif, and bond C4-H4···O1 forms a S(5) pattern.

Also included in Table 2.3.18 is a list of the inter-molecular secondary interactions that are present in the crystal structure of compound **7**. The weak intermolecular C-H···O bonds are shown in Figure 2.3.17. A combination of the C10-H10···O2^{ii} and C9-H9···O2^{ii} interactions gives a ring pattern of the binary graph-set $R_2^1(5)$ (see Table 2.3.18 for symmetry codes). Equally, bonds C1-H1C···O4^{iv} and C7-H7···O4^{iv} when considered together create a N_2: $R_2^1(6)$ pattern. The hydrogen bond donor group C15-H15A forms a bifurcated hydrogen bond to atoms O3^{vi} and O2^{vi}; this generates a pattern of the binary graph-set $R_1^2(4)$.

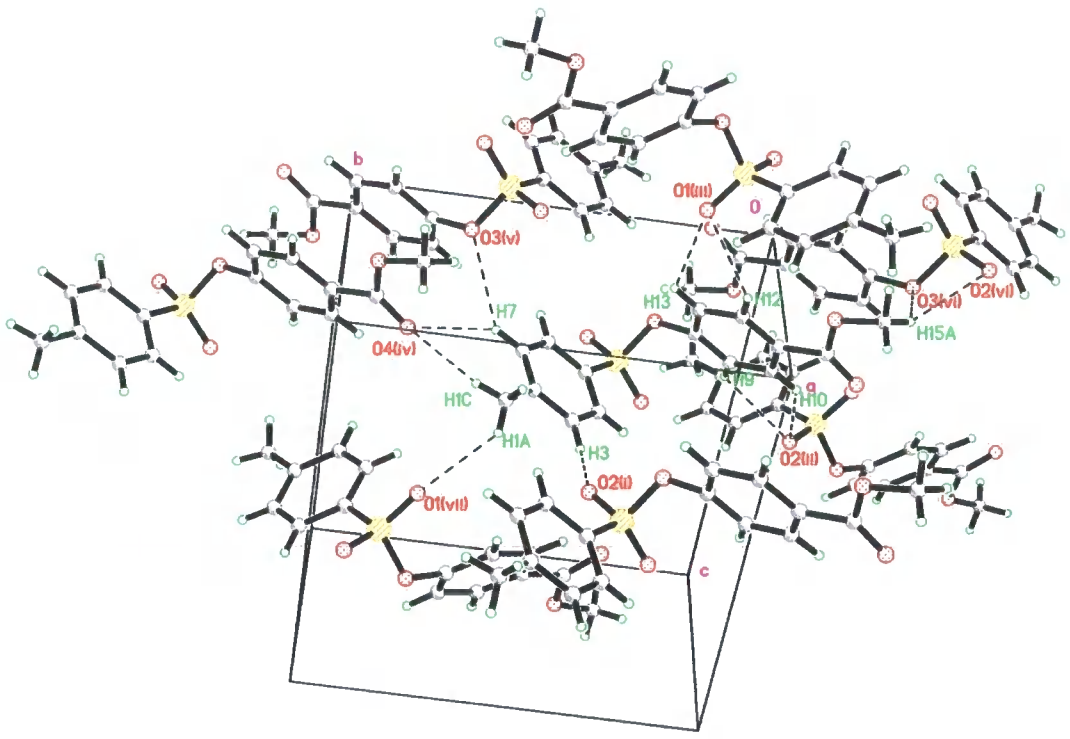

Figure 2.3.17: Diagram showing intermolecular interactions in compound **7**. Symmetry codes are given in Table 2.3.18.

Also listed in Table 2.3.18 are several C-H···π interactions. Cg1 and Cg2 denote the centroids of rings C2-C7 and C8-C13 respectively. The secondary interaction network in compound **7** is completed by the presence of a weak π···π contact of 3.659 Å (β = 21.47°) between Cg2 and $Cg2^{vi}$.

Table 2.3.18: Geometric parameters for the secondary interactions in compound **7**.

D-A···A (Å)	D-H (Å)	H···A (Å)	D···A (Å)	D-H···A (°)
C9-H9···O1	0.964(18)	2.495(19)	2.948(2)	108.6(14)
C12-H12···O5	0.98(2)	2.43(2)	2.735(2)	97.3(13)
C10-H10···O4	0.97(2)	2.54(2)	2.834(2)	97.3(13)
C6-H6···O2	0.97(2)	2.62(3)	2.971(2)	101.6(18)
C4-H4···O1	0.94(2)	2.60(2)	2.942(2)	102.2(14)
C15-H15A···O4	0.96(3)	2.55(3)	2.656(3)	85.5(17)
C3-H3···$O2^{i}$	0.94(2)	2.54(2)	3.392(2)	150.3(19)
C10-H10···$O2^{ii}$	0.97(2)	2.64(2)	3.314(2)	126.6(16)
C9-H9···$O2^{ii}$	0.964(18)	2.807(19)	3.371(2)	118.2(14)
C13-H13···$O1^{iii}$	0.95(2)	2.652(19)	3.174(2)	115.0(14)
C12-H12···$O1^{iii}$	0.98(2)	2.61(2)	3.166(2)	115.7(14)
C1-H1C···$O4^{iv}$	0.90(3)	2.58()	3.403(3)	153(3)
C7-H7···$O4^{iv}$	0.95(2)	2.52(2)	3.355(2)	145.7(18)
C7-H7···$O3^{v}$	0.95(2)	2.84(2)	3.585(2)	135.6(18)
C15-H15A···$O3^{vi}$	0.96(3)	2.82(3)	3.540(3)	132(2)
C15-H15A···$O2^{vi}$	0.96(3)	2.96(3)	3.824(3)	151(2)
C15-H1A···$O1^{vii}$	0.91(4)	2.83(4)	3.560(3)	139(3)
C15-H1B···$Cg1^{viii}$	0.94(4)	3.09(4)	3.982(3)	160(3)
C15-H15B···$Cg2^{ix}$	0.91(3)	2.84(3)	3.693(3)	156(2)
C15-H15C···$Cg1^{iii}$	0.95(3)	3.09(3)	3.844(2)	138(2)

Symmetry codes: (i) 1 + x, y, z; (ii) 1 - x, y - ½, ½ - z; (iii) x, ½ - y, z - ½; (iv) x, 1 + y, z; (v) 1 - x, 1 – y, - z; (vi) 1 - x, - y, - z; (vii) 2 - x, ½ + y, ½ - z; (viii) 2 - x, 1 - y, - z; (ix) 2 - x, - y, - z.

With reference to Table 2.3.5 it can be seen the bond lengths for **7** (Table 2.3.19) concur with the expected values. The dihedral angle between the two phenyl rings is 58.74(8)°. The ester group atoms, C14, O4, O5 and C15 deviate from the plane given by atoms C8-C13 by -0.0078(3) Å, 0.113(3) Å, -0.410 Å and -0.591(4) Å respectively.

Table 2.3.19: Selected bond parameters for compound **7**.

Bond	Length (Å)	Atoms	Angle (°)
S1-O1	1.421(1)	O1-S1-O2	120.51(8)
S1-O2	1.424(1)	O1-S1-O3	108.83(7)
S1-O3	1.598(1)	O2-S1-O3	102.52(7)
S1-C5	1.746(2)	O1-S1-C5	109.63(8)
C14-O4	1.202(2)	O2-S1-C5	109.80(8)
C14-O5	1.339(2)	O3-S1-C5	104.13(7)
C15-O5	1.445(2)	C8-O3- S1	120.2(1)
C11-C14	1.489(2)	C11-C14-O4	124.3(2)
		C11-C14-O5	111.8(1)
		O4-C14-O5	123.9(2)
		C14-O5-C15	115.8(2)

2.3.8 2-Naphthyl 4-toluenesulphonate

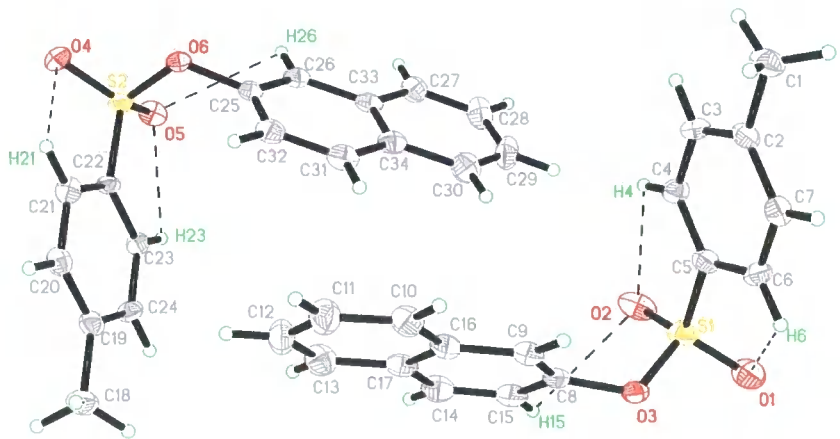

Figure 2.3.18: 50% Thermal-ellipsoid representation of compound **8**. Dashed lines signify intramolecular C-H···O contacts.

All intra- and inter-molecular interactions that are exhibited in the crystal structure of 2-naphthyl 4-toluenesulphonate (**8**) [18] are listed in Table 2.3.20. The weak intramolecular C-H···O bonds in which atoms O1 and O4 are engaged produce S(5) ring motifs (Figure 2.3.18). Both atoms O2 and O5 are bifurcated hydrogen bond acceptors. The former forms a bond with C4-H4 giving an S(5) motif, and also bonds with the donor group C15-H15 giving an S(6) ring motif. Equally, the C23-H23···O5 interaction results in an S(5) motif, and the C26-H26···O5 gives an S(6) pattern.

The bifurcated hydrogen bond donor group C24-H24 forms bonds to atoms $O4^{i}$ and $O6^{i}$, this gives an N_2: $R_1^2(4)$ pattern. Atom $O5^{iv}$ accepts hydrogen bonds from the donor groups C21-H21 and C32-H32 forming a ring pattern of the binary graph-set $R_2^1(9)$ (See Table 2.3.20 for symmetry codes). Atom $O3^{vii}$ is also a bifurcated hydrogen bond acceptor. Consideration of the C1-H1A···$O3^{vii}$ and C3-H3···$O3^{vii}$ interactions together give a ring pattern of the binary graph-set $R_2^1(6)$. The C3-H3 group forms a second weak hydrogen bond with atom $O1^{vii}$. The C3-H3···$O3^{vii}$ and C3-H3···$O1^{vii}$ bonds form an N_2: $R_1^2(4)$ pattern, likewise the C1-H1A···$O3^{vii}$ and C3-H3···$O1^{vii}$ bonds together give an N_2: $R_2^2(8)$ design. The secondary interaction network in compound **8** is completed by several C-H···π contacts; these are listed in Table 2.3.20. The identities of the centroids are given in Table 2.3.21.

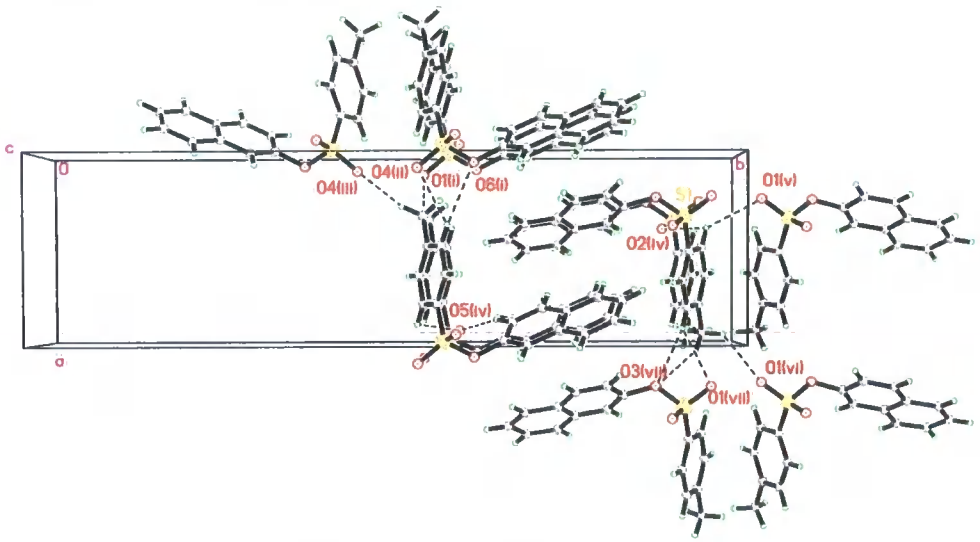

Figure 2.3.19: Diagram displaying the intermolecular C-H···O bonds (dashed lines) that are present in compound **8**, as viewed along the *c*-axis.

Table 2.3.20: Geometric parameters for the secondary interactions in compound **8**.

D-A···A (Å)	D-H (Å)	H···A (Å)	D···A (Å)	D-H···A (°)
C4-H4···O2	0.95	2.51	2.895(4)	104
C6-H6···O1	0.95	2.81	3.061(4)	96
C15-H15···O2	0.95	2.78	3.012(4)	95
C21-H21···O4	0.95	2.77	3.054(4)	98
C23-H23···O5	0.95	2.51	2.900(3)	104
C26-H26···O5	0.95	2.80	3.111(3)	100
C24-H24···O6^{i}	0.95	2.77	3.663(3)	157
C24-H24···O4^{i}	0.95	2.70	3.458(4)	138
C18-H18A···O4^{ii}	0.98	2.86	3.495(4)	124
C18-H18C···O4^{iii}	0.98	2.38	3.298(4)	156
C32-H32···O5^{iv}	0.95	2.63	3.549(4)	163
C21-H21···O5^{iv}	0.95	2.90	3.273(3)	105
C6-H6···O2^{iv}	0.95	2.88	3.138(3)	97
C6-H6···O1^{v}	0.95	2.82	3.138(3)	135
C1-H1B···O1^{vi}	0.98	2.66	3.386(4)	131
C1-H1A···O3^{vii}	0.98	2.85	3.753(4)	153
C3-H3···O3^{vii}	0.95	2.69	3.554(3)	152
C3-H3···O1^{vii}	0.95	2.73	3.521(4)	142
C10-H10···Cg6	0.95	2.74	3.383	121
C11-H11···Cg5	0.95	3.14	3.835	121
C7-H7···Cg1^{viii}	0.95	2.84	3.578	133
C14-H14···Cg5^{ix}	0.95	2.74	3.430	128
C15-H15···Cg6^{ix}	0.95	3.05	3.744	123
C20-H20···Cg4^{x}	0.95	2.82	3.574	138
C26-H26···Cg3^{vii}	0.95	3.15	3.806	128
C27-H27···Cg2^{vii}	0.95	2.63	3.415	132
C30-H30···Cg2^{iv}	0.95	3.23	3.956	138
C31-H31···Cg3^{iv}	0.95	2.84	3.582	132

Symmetry codes: (i) x -1, y, z; (ii) x - 1, y - 1, z - 1; (iii) x -1, 1 - y, z - ½; (iv) x, y, z -1; (v) x, 2 – y, z - ½; (vi) 1+ x, 2- y, z - ½; (vii) 1 + x, y, z; (viii) x, - y, z - ½; (ix) x - 1, y, 1 + z; (x) x, 1 – y, z - ½.

Centroid	Associated Ring
Cg1	C2-C7
Cg2	C8-C9, C14-C17
Cg3	C10-C13, C16-C17
Cg4	C19-C24
Cg5	C25-C26, C31-C34
Cg6	C27-C30, C33-C34

Table 2.3.21: Identities of the individual centroids reported in Table 2.3.20.

Figure 2.3.19 is suggestive of the possibility of π···π interactions. However, the shortest centroid-centroid distance in the crystal structure of compound **8** is 4.5063 Å between Cg6 and Cg3. This is too long to be deemed a π···π bond.

Table 2.3.22: Selected bond parameters for compound **8**.

Bond	Length (Å)	Atoms	Angle (°)
S1-O1	1.421(2)	O1-S1-O2	120.9(2)
S1-O2	1.426(2)	O1-S1-O3	102.8(1)
S1-O3	1.608(2)	O2-S1-O3	108.9(1)
S1-C5	1.755(3)	O1-S1-C5	109.6(1)
		O2-S1-C5	103.9(1)
		O3-S1-C5	103.9(1)
		C8-O3-S1	118.4(2)
S2-O4	1.422(2)	O4-S2-O5	120.5(1)
S2-O5	1.424(2)	O4-S2-O6	102.8(1)
S2-O6	1.608(2)	O5-S2-O6	108.9(1)
S2-C22	1.747(3)	O4-S2-C22	110.52(1)
		O5-S2-C22	109.4(1)
		O6-S2-C22	103.2(1)
		C25-O6-S2	118.5(2)

Table 2.3.22 lists selected bond parameters for compound **8**; comparison of these figures with those provided in Table 2.3.5 indicates that the observed and expected bond length values are in agreement. The dihedral angles between the naphthyl and phenyl rings in molecules 1 (containing S1) and 2 (containing S2) are 65.10(7)° and 55.11(7)° respectively.

2.3.9 Evaluation of the structures of aromatic sulphonates.

A literature survey, and a search of the Cambridge Structural Database (version 5.25),[19] highlighted a total of fourteen structures that are closely related to structures reported in Section 2.3. [20-31] The searches were limited to consideration of structures possessing the structural moieties shown in Figure 2.3.20. Structures containing **A** with relatively small substituent groups on the phenyl rings were also accepted (e.g. Methyl, methoxy, nitro, amino, and short-chain ester groups). Structures with heterocycle variations on the naphthyl group of **B** were also reviewed.

The first point of note is that all the sulphonyl bond lengths for the literature reported structures and compounds **2** - **8** concur. The O-S bond lengths are in the range of 1.576-1.628 Å, and the S=O bond lengths are consistently in the range of 1.412-1.446 Å. The C-S bond lengths lie in the range of 1.743-1.777 Å.

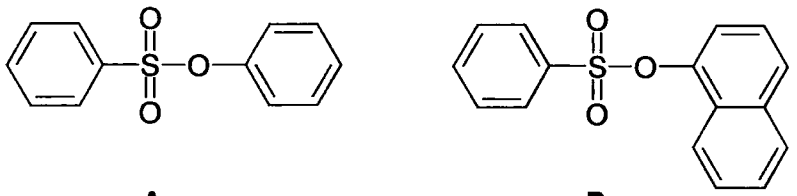

Figure 2.3.20: Basic structural moieties used as criterion for CSD and literature searches.

Of particular interest, is the significant variation in the dihedral angles observed in these structures, ranging from 5.18(5)° for compound **5** to 80.39° for 4-methoxyphenyl-2-cyanobenzene sulphonate.[23] There appears to be no pattern to the variation, with very similar compounds exhibiting widely dissimilar values. For example, compound **5** and 8-tosyloxyquinoline[25] (Figure 2.3.21a) differ only in the type and location of substituent group on the phenyl ring, but the dihedral angles are 8.28(5)°, 5.18(5)° and 47.53(6)°, respectively. Yet the same alteration in the case of compounds **6** and **7** had a minimal affect on the dihedral angle

(58.4(4)° and 58.74(8)° respectively). Compound **3** possesses a single nitro groups on one of the phenyl rings, whereas compound **4** has two nitro groups on the same ring. Due to the greater steric bulk on **4**, this structure would be expected to have a greater dihedral angle then **3**, however the dihedral angles for these two structures are 39.69(8)° and 36.10(7)° respectively. This unexpected result is also found for 2-Chlorophenyl-4-toluenesulphonate [21] (Figure 2.3.21b) and 2,4-Dichlorophenyl-4-toluenesulphonate [22] (Figure 2.3.21c) where the dihedral angles are 51.47(9)° and 43.92(4)° respectively.

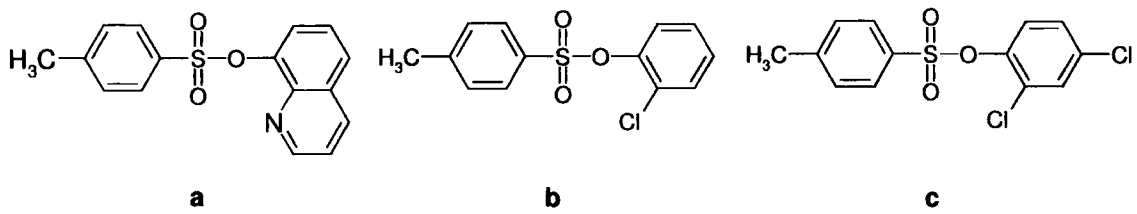

Figure 2.3.21: (a) 8-tosyloxyquinoline;[25] (b) 2-Chlorophenyl-4-toluenesulphonate;[21] (c) 2,4-Dichlorophenyl-4-toluenesulphonate.[22]

The above examples suggest that simple steric considerations are insufficient to explain the differences in the dihedral angles observed in this class of compound. Any rationalisation for the wide range of dihedral angles displayed by aromatic sulphonates would be expected to indicate a subtle balance between the steric requirements of subsistuent groups, the molecular orientations required to maximise the secondary interaction energetics, and the crystallisation methods employed during sample preparation.

The preponderance of weak C-H···O hydrogen bonds observed in the crystal structures of compounds **1** - **8** can be attributed to the lack of more favourable hydrogen bond donor groups (i.e. N-H and O-H groups) to satisfy the many potential hydrogen bond acceptor atoms (either oxygen or nitrogen atoms) that are present in all these compounds.[9,32] Similar situations are found in other aromatic sulphonates.[20-22, 24-29] If more favourable hydrogen bond donors were present, these would be expected to preferentially form hydrogen bonds with any available acceptor groups, as is the case with m-(p-Tolysulphonyloxy) aniline.[30]

Hydrogen bond motifs common to compounds **1** - **8** are the intramolecular S(5) and/or S(6) rings formed by the O=S groups of the sulphonyl with hydrogen atoms on the adjacent phenyl rings. The oxygen atoms of the sulphonyl groups routinely act as intermolecular hydrogen bond acceptors. Three distinct patterns involving theses atoms can be identified from compounds **2** - **8** and these are shown in Figure 2.3.22.

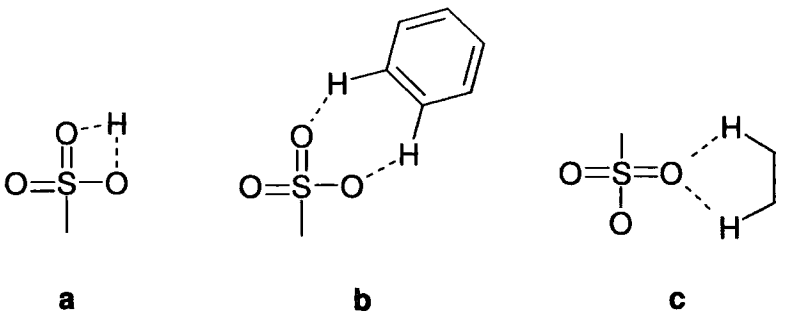

Figure 2.3.22: Hydrogen bond patterns involving sulphonyl group atoms as observed in compounds **2** - **8**; (a) bifurcated hydrogen bond of the graph-set N_2: $R_1^2(4)$; (b) Ring pattern of the graph-set N_2: $R_2^2(7)$; (c) bifurcated hydrogen bond of the graph-set N_2: $R_2^1(5)$.

Pattern **a** is seen only in structure **8**, but a similar pattern of the same graph-set is observed in 2-Chlorophenyl-4-toluenesulphonate [21] (Figure 2.3.21b). In this compound the acceptor atoms of the bifurcated hydrogen bond are the two S=O oxygen atoms of the sulphonyl group. Pattern **b** is seen in the structure of compound **2** only. Compounds **3**, **5** and **7** all display the **c** pattern in their packing arrangements, indeed in **7** both S=O oxygen atoms participate in the formation of this type of hydrogen bonding pattern. This pattern is also observed in 2,4-Dinitrophenyl-4-toluenesulphonate [27], and the structure of m-(p-Tolysulphonyloxy) aniline [30] displays a modified form of pattern **c** with one of the hydrogen bond donor groups being an N-H group.

However, it should be noted that the hydrogen patterns shown in Figure 2.3.22 are by no means common in aromatic sulphonate compounds. In the majority of the structures considered, none of these patterns were present; in these materials the oxygen atoms of the sulphonyl groups favour the formation of multiple discrete hydrogen bonds.

Aromatic sulphonates may be expected to form many weak π-interactions [33,34] due to the presence of the aromatic groups, and a plethora of potential C-H donor groups. However, only

compounds **2**, **6** and **7** display C-H···π interactions, and π···π bonds are observed in compounds **5**, **6**, and **7** only. The small number of π-interactions observed in compounds **1** - **8** may be due to the conformation of the molecules preventing the aromatic groups from forming close contacts. It is of interest to note that in the structure of **5**, in which the molecules are nearly planar, five different π···π bonds are present (Table 2.3.13).

2.4 Conclusion

In this chapter the low-temperature crystallographic analysis of eight aromatic sulphonates has been reported. This analysis entailed the accurate determination of the crystal structures of these compounds and the network of secondary interactions displayed by each structure being fully described. In addition to these eight compounds, a further fourteen structures were identified from searches of the CSD and literature as being of interest to this study. All twenty-two structures were evaluated in an attempt to identify any pattern to the preferred molecular conformations and packing arrangements exhibited by this class of compounds. The results from this investigation are given above (Section 2.3.9).

The packing arrangement adopted by any given aromatic sulphonate will be influenced by a number of factors, such as the steric requirements of any substituent groups, the maximisation of the number of favourable secondary interactions, and the crystallisation method used. All these factors will interplay to direct the molecular orientation and packing within the crystal, and with this in mind it is not surprising that there is little consistency in the molecular conformations and hydrogen bond patterns seen in the crystal structures of the aromatic sulphonates investigated.

From this study it can be concluded that the prediction of the crystal structures of aromatic sulphonate compounds is exceptionally difficult, if not impossible. This will limit the feasibility of customising the crystal form adopted by these materials i.e. crystal engineering is virtually impossible for this class of compounds.

2.5 References

The analysis of secondary interactions reported in Section 2.3 was aided by the *PLATON* software (Spek AL, *PLATON*, Utrecht University, The Netherlands.).

[1] Eichhorn P, Knepper TP, Ventura F, Diaz A, *Water Res.*, **36**, 2179 (2002).

[2] Lange TL, Wenz M, Brauch HJ, *J. High Resol. Chromatogr.*, **18**, 243 (1995).

[3] Matulis D, Wu C, Pham TV, Guy C, Lovrien R, *J. Mol. Cat. B: Enzymatic*, **7**, 21 (1999).

[4] Jiang FN, Jiang S, Lui D, Richter A, Levy JG, *J. Immun. Met.*, **134**, 139 (1990).

[5] Spungin B, Levinshal T, Rubinstien S, Breitbart H, *FEBS*, **311**, 155 (1992).

[6] Vembu N, Nallu M, Spencer EC, Howard JAK, *Acta. Cryst.*, **E59**, o1036 (2003).

[7] Etter MC, *Acc. Chem. Res.*, **23**, 120 (1990).

[8] Bernstein J, Davis RE, Shimoni L, Chang NL, *Angew. Chem. Int. Ed. Engl.*, **34**, 1555 (1995).

[9] Desiraju GR, Steiner T, '*The Weak Hydrogen Bond in Structural Chemistry and Biology*', IUCr Monograph, Oxford University Press 1999.

[10] Wilson AJC, *International Tables for Crystallography, Volume C.*, IUCr. (1992).

[11] Zimer B, Sauer E, *Acta. Cryst.* **C55**, IUC9800074 (1999).

[12] Vembu N, Nallu M, Spencer EC, Howard JAK, *Acta. Cryst.*, **E59**, o1213 (2003).

[13] Vembu N, Nallu M, Spencer EC, Howard JAK, *Acta. Cryst.*, **E59**, o1390 (2003).

[14] Vembu N, Nallu M, Spencer EC, Howard JAK, *Acta. Cryst.*, **E59**, o1387 (2003).

[15] Vembu N, Nallu M, Spencer EC, Howard JAK, *Acta. Cryst.*, **E59**, o1379 (2003).

[16] Vembu N, Nallu M, Spencer EC, Howard JAK, *Acta. Cryst.*, **E59**, o1216 (2003).

[17] Vembu N, Nallu M, Spencer EC, Howard JAK, *Acta. Cryst.*, **E59**, o1009 (2003).

[18] Vembu N, Nallu M, Spencer EC, Howard JAK, *Acta. Cryst.*, **E59**, o1033 (2003).

[19] Allen FH, *Acta. Cryst.*, **B58**, 380 (2002).

[20] Vembu N, Nallu M, Garrison J, Youngs WJ, *Acta. Cryst.*, **E59**, o936 (2003).

[21] Vembu N, Nallu M, Garrison J, Youngs WJ, *Acta. Cryst.*, **E59**, o503 (2003).

[22] Vembu N, Nallu M, Garrison J, Youngs WJ, *Acta. Cryst.*, **E59**, o939 (2003).

[23] Brigas AF, Fonseca CSC, Johnson RAW, *J. Chem. Res. (S)*, 299 (2002).

[24] Vembu N, Nallu M, Garrison J, Hindi K, Youngs WJ, *Acta. Cryst.*, **E59**, o830 (2003).

[25] Vembu N, Nallu M, Garrison J, Youngs WJ, *Acta. Cryst.*, **E59**, o776 (2003).

[26] Vembu N, Nallu M, Durmus S, Pazner M, Garrison J, Youngs WJ, *Acta. Cryst.*, **E60**, o1 (2004).

[27] Vembu N, Nallu M, Garrison J, Youngs WJ, *Acta. Cryst.*, **E59**, o378 (2003).

[28] Vembu N, Nallu M, Durmus S, Pazner M, Garrison J, Youngs WJ, *Acta. Cryst.*, **C60**, o248 (2004).

[29] Vembu N, Nallu M, Durmus S, Pazner M, Garrison J, Youngs WJ, *Acta. Cryst.*, **C60**, o65 (2004).

[30] Goswami S, Mahapatra AK, Nigam GD, Chinnakali K, Razak A, Fun H-K, *Acta. Cryst.*, **C54**, 954 (1998).

[31] Niestroj AJ, Bruhn C, Maier ME, *J. prakt. Chem.*, **340**, 175 (1998).

[32] Desiraju GR, *Acc. Chem. Res.*, **24**, 290 (1991).

[33] Hunter CA, Lawson KR, Perkins J, Urch CJ, *J. Chem. Soc., Perkin Trans.* **2**, 651 (2001).

[34] Umezawa Y, Tsuboyama S, Honda K, Uzawa J, Nishio M, *Bull. Chem. Soc. Jpn.*, **71**, 1207 (1998).

Chapter 3

Crystallographic Study of Phosphorus Ylides

3.1 Introduction

This study arose from collaboration with Dr. K. Panchanatheswaran of Bharathidasan University, India. The purpose of this work was to characterise, using single-crystal X-ray diffraction, the structural features of several complexes and co-crystals of three different phosphorus ylide materials.

3.1.1 Phosphorus ylides

The IUPAC definition of the term 'ylide' is given below;[1] a phosphorus ylide is a species in which 'Y' is a carbon atom (α-carbon) and 'X' is a phosphorus atom:

'Compounds in which an anionic site Y^- is attached directly to a heteroatom X^+ carrying a formal positive charge. They are thus 1,2-dipolar species of the of the type R_mX^+-Y^-R_n.'

The chemistry related to phosphorus ylides is vast, and a full appraisal of the field is outside of the scope of this chapter, however, Kolodiazhnyi has written an excellent review article on the chemistry of phosphorus ylide materials, and the interested reader is referred to this article and the references within.[2] Suffice it to say that the popularity of ylides as reagents for chemical reactions arises due the possibly of chemically tailoring the reactivity of the ylide to suit a particular application.

3.1.2 α-carbon stabilised phosphorus ylides

The presence of either a carbonyl or cyano group bound to the α-carbon provides additional stability to the ylide compound. This is achieved by resonance delocalisation of the ylidic electron density (Fig. 3.1.1). Such compounds are of practical use, because in contrast to non-

stablised ylide compounds, so-called α-stabilised ylides can be easily isolated and are stable in air and are not moisture sensitive.

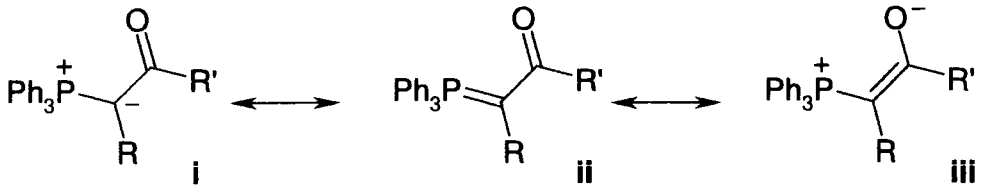

Figure 3.1.1: Canonical forms of a keto-stabilised phosphorus ylide.

The resonance delocalisation of the electron density in a carbonyl-stabilised ylide increases the number of coordination modes accessible to the ylide molecule. This gives rise to the possibility of linkage isomerism when the ylide molecule binds to a metal centre; bonding via either the ylide form (i), or enolate form (iii), gives C- and O-isomeric forms respectively. Moreover, *E/Z* isomerism is introduced into the ylide molecule, if it binds via the carbonyl oxygen (iii).

3.1.3 Ylides containing metals at the α-carbon atom

Several metal-ylide complexes have been investigated as part of this study and for this reason a brief explanation as to the effect of metallation on the reactivity of ylide species is appropriate.

The bonding of metal atoms to the α-carbon can have either a positive or detrimental effect on the nucleophilicity of the resulting ylide complex. If the metal has a propensity to be a σ-donor (as is the case with mercury and cadmium) this can activate the ylide species by means of positive induction effects increasing the electron density situated on the ylide carbon. However if the metal atom has available orbitals of the correct energy that can interact with the filled p-orbtials on the ylide carbon (for example the valence p-orbitals of silicon and tin), π-back bonding will result and this will effectively reduce the electron density on the ylide carbon, subsequently lowering the ylide reactivity by stabilising the carbanion. Due to the interest in the development of new ylide reagents, in Section 3.3.4 the structures of three mercury(II)-ylide complexes are discussed. To compliment this work, a study of the bonding modes adopted by uranium(VI)-ylide complexes was performed. Information pertaining to the chemistry of uranium is of interest to the nuclear waste industry, and the results of this study are discussed in Section 3.3.3.

The focus of this introduction will now be directed towards a discussion of the ylide materials that have been central to this study.

3.1.4 Benzoylmethylenetriphenylphosphorane (BPPY)

Benzoylmethylenetriphenylphosphorane (BPPY) (Figure 3.1.2) is one of the most widely studied phosphorus ylides. The crystal structure of this material was reported in 1994,[3] however an earlier structural report of the C-protonated form of BPPY appeared in 1984.[4]

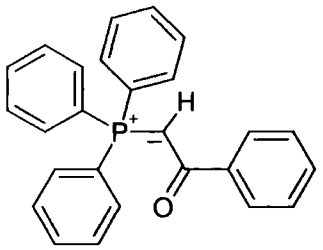

Figure 3.1.2: Schematic of BPPY

A search of the Cambridge Structural Database (version 5.25) (CSD)[5] yielded several examples of structures in which BPPY features. Mariyatra *et al.* have reported on the synthesis of iodide and nitrate salts of the H-BPPY$^+$ cation (C-protonated BPPY).[6,7] In both cases the salt crystallised in the orthorhombic space group P*bca*. The same authors have also reported the $[Cd_2Br_6]^{2-}$ salt of BPPY.[8] The authors attribute the stability of these salts to the formation of secondary interactions; in particular they refer to the presence of C-H···C_{ylide} interactions.

The main supporting evidence for such carbanion interactions in ylides has been limited to theoretical studies.[9,10] Batsanov *et al.* proposed experimental evidence for the presence of C-H···C_{ylide} contacts in triphenylphosphonium benzylide, a material structurally similar to BPPY.[11] The decision to classify a short contact between a phenyl hydrogen atom and the ylide carbon as a hydrogen bond was based on geometric criteria. However a charge density study conducted by Yufit *et al.* using the same ylide, failed to find evidence for the existence of this elusive C-H···C_{ylide} interaction.[12] Due to lack of experimental evidence pertaining the existence of C-H···C_{ylide} contacts, no discussion of such 'interactions' in relation to the structures to be presented in Section 3.3 will be offered.

Two other BPPY salts containing metallic anions, namely $[H\text{-}BPPY]_2^+.[CoCl_4]^{2-}$ and $[H\text{-}BPPY]_2^+.[NiCl_4]^{2-}$, have been reported by Albanese *et al.*[13] Both salts crystallise in the triclinic space group P-1, and in both cases the BPPY molecules exhibit C-protonation. To ensure the

neutrality of the materials the stoichiometric ratio between the phosphonium cations and relevant anion is 2:1, with each anion displaying subtlety distorted tetrahedral geometry. Falvello *et al.* have prepared several palladium (II) BPPY complexes each of which the authors have characterised using spectroscopic methods.[14] Vicente *et al.* have synthesised and elucidated the crystal structure of the $[Ag\{BPPY\}_2].X$ salt (where X = ClO_4, NO_3).[15] This material is a 2:1 molecular complex with the C-coordinated silver atom bridging two BPPY molecules.

Perhaps the most interesting BPPY containing materials reported, at least in the context of this study, are the mercury halide complexes synthesised by Kalyanasundari *et al.*[16] These C-coordinated complexes form molecular dimer units as illustrated in Figure 3.1.3a. The same authors have prepared and characterised the tri-mercury complex shown in Figure 3.1.3b.[17] The mercury halide complexes of BPPY will be discussed further in Section 3.3 in conjunction with the mercury halide complexes of the phosphorus ylide carbethoxymethylenetriphenylphosphorane (EPPY).

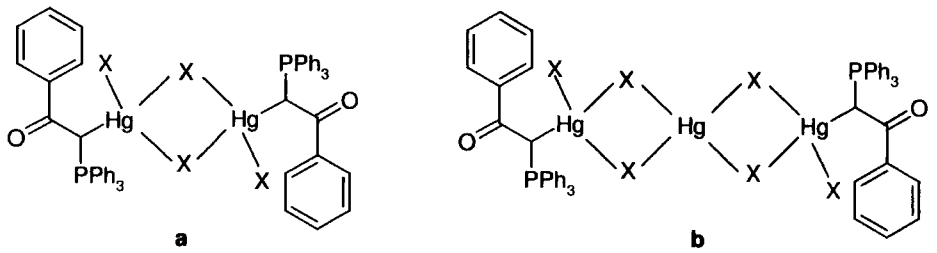

Figure 3.1.3: (a) Structure of $[BPPY.\ HgX_2]_2$ where X = Br, Cl, I; (b) Structure of $[Hg\{HgI(BPPY)(\mu\text{-}I)_2\}_2]$.

In Section 3.3 the crystal structures of dimer species $[UO_2(NO_3)_2(BPPY)_2]$ and the salt $[H\text{-}BPPY^+]_2.[UO_2(OH)_2(NO_3)_4]^{2-}$ will be presented. To complement this work, the crystal structures of the salts and co-crystals of BPPY with four organic acids will also be reported; the impetus for investigating these materials has been provided by Hon and Lee.[18] These authors have demonstrated that the reactivity of phosphorus ylides is counterion dependent. They have concluded that the stronger the Brønsted basicity of the carboxylate counterion, the greater the alkene yield from the Wittig reaction.

These findings can be rationalised by considering that the Wittig reaction is catalysed by addition of small amounts of acid that activates the reacting aldehyde by protonation of the carbonyl oxygen atom. The greater the Brønsted basicity of the anion, the higher the likelihood that proton transfer from the phosphonium cation to the carboxylate anion will occur, generating a protonated acid that can subsequently act as a catalyst (Figure 3.1.4).

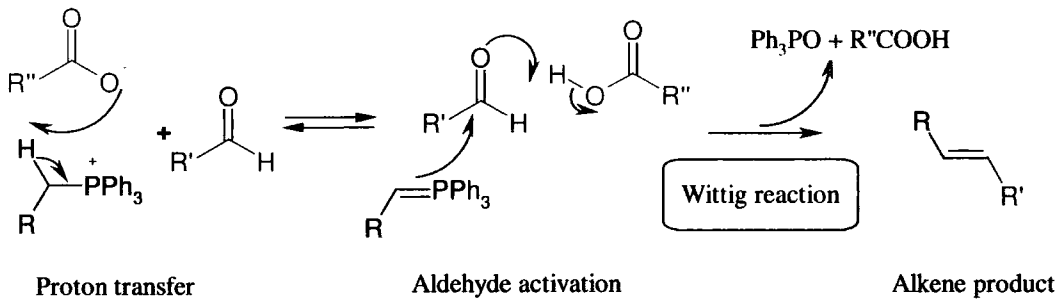

Figure 3.1.4: Mechanism of aldehyde activation by an acid catalysis. The species in red and blue are the ylide counterion and aldehyde respectively. Diagram adapted from Hon *et al.*[18]

$$BPPY + HA \rightleftharpoons H\text{-}BPPY^{+} + A^{-} \qquad \textbf{Equation 3.1.1}$$

The organic acids investigated in this work are picric, maleic, fumaric and terephthalic acid. The pKa values for these acids are 0.38, 1.83/6.07, 3.03/3.51 and 4.44/4.82 respectively;[19] all of these acids would be expected to protonate BPPY (pKa of 6.0).[20] Both fumaric and terephthalic acid have values that are high enough to shift the equilibrium position of the reaction shown in Equation 3.1.1 to the left, thus facilitating the formation of the catalytic acid (HA). Conversely, the pKa values of picric and maleic acid would suggest that the equilibrium position for the reaction (Eq. 3.1.1) involving these acids would lie to the right, reducing the production of AH. Inclusion of these acids in this study is to allow for structural comparison of these materials with the fumaric and terephthalic acid co-crystals of BPPY.

3.1.5 α-acetyl-α-benzoylmethylenetriphenylphosphorane (ABPPY)

Antipin *et al.* have synthesised and characterised the chloride and boron tetrafluoride salts of O(Me)-protonated ABPPY.[21,22] To date, the O-coordinated mercury species of ABPPY are the only organometallic structures containing ABPPY (Figure 3.1.5) that have been reported.[23] Both mercury bromide and iodide complex to ABPPY to form dimer species in an analogous manner to the mercury halide complexes of BPPY (Figure 3.1.3a). The primary difference being,

that in the [ABPPY. $HgX_2]_2$ (where X = Br or I) complexes, the mercury is coordinated to the ylide via the oxygen atom of the acetyl groups. The reaction of mercury chloride with ABPPY does not afford the same dimer species that is observed with $HgBr_2$ and HgI_2. The chloride forms a dimer unit with a single bridging $HgCl_2$ group O-coordinated to two ABPPY ligands. These materials will be discussed further in Section 3.3.

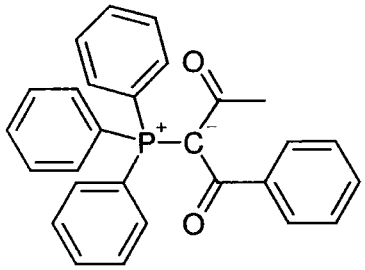

Figure 3.1.5: Schematic of ABPPY

In Section 3.3 the crystal structures of the free ylide will be reported along side the uranium(VI) complex $[UO_2(NO_3)_2(ABPPY)_2]$.

3.1.6 Carbethoxymethylenetriphenylphosphorane (EPPY)

Figure 3.1.6 is a diagrammatic representation of carbethoxymethylenetriphenylphosphorane (EPPY). EPPY is a commercially available ester ylide, although to date only a few crystal structures incorporating this material have been reported. These include the silver salt [Ag{EPPY}$_2$]. X (where X = ClO_4, NO_3) a structure that is comparable to the BPPY complex [15], and the hexa- and octa-molybdate salts synthesised by Arzoumanian *et al.*[24] Several tetrahaloaryltellurate (IV) salts,[25] and a dichloropalladium(II) complex of EPPY [26] have also been prepared, however, the structural analysis of these materials has been limited to spectroscopic methods.

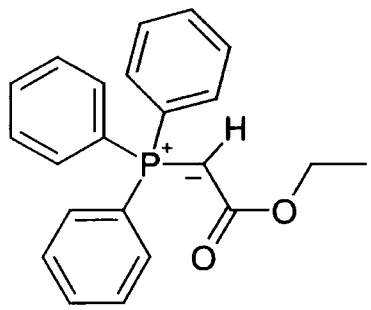

Figure 3.1.6: Schematic of EPPY

In Section 3.3 the crystal structure of the free ylide will be discussed, as will several metal-EPPY complexes. These will include the dimeric molecular species [EPPY. $HgX_2]_2$ where X = Br, Cl,

I, which are analogous to the mercury halide complexes of BPPY, and the [EPPY.$UO_2(CH_3COO)_3$] salt.

3.2 Experimental

Crystallographic data for all compounds were collected at 120K, using graphite-monochromated MoK_α X-radiation (0.71073 Å). Data were collected on a Bruker 6K CCD diffractometer; the exception was compound **3**, which was analysed with a Bruker Proteum M diffractometer. All data processing was performed using standard Bruker software; structure solutions were by Direct Methods (See Chapter 1). Data for compounds **1** - **7** and **9** - **13** were corrected for absorption using SADABS. Data for compound **8** were corrected using psi-scan techniques. Further experimental and refinement details can be found in Tables 3.3.1, 3.3.13, 3.3.16, and 3.3.21.

3.3 Results & Discussion

3.3.1 The co-crystals and salts of BPPY with organic dicarboxylic acids.

Table 3.3.1: Crystallographic data and refinement details for compounds **1-4**.

	1	**2**	**3**	**4**
Crystal size (mm^3)	0.30 x 0.25 x 0.12	0.39 x 0.27 x 0.22	0.23 x 0.15 x 0.13	0.34 x 0.29 x 0.17
Crystal system	Monoclinic	Monoclinic	Monoclinic	Orthorhombic
Space group	$P2_1/n$	$P2_1/c$	$P2_1/n$	Pbca
a (Å)	10.0900(6)	13.0883(6)	7.531(1)	10.5582(5)
b (Å)	17.9737(9)	9.7883(5)	25.241(3)	19.5961(8)
c (Å)	13.1613(7)	17.9970(9)	14.490(2)	24.003(1)
α (°)	90	90	90	90
β (°)	92.048(2)	102.500(2)	98.639(3)	90
γ (°)	90	90	90	90
Volume ($Å^3$) / Z	2385.3(2) / 4	2251.0(2) / 4	2722.9(6) / 4	4966.2(4) / 8
μ (mm^{-1})	0.145	0.150	0.163	0.150
Unique reflections	5465	5164	6344	5704
R(int)	0.0467	0.0325	0.0463	0.0508
Gof (on F^2)	0.950	0.990	1.013	1.014
R1 / wR2 ($I>2\sigma(I)$)	0.0405 / 0.0984	0.0382 / 0.0995	0.0410 / 0.1009	0.0407 / 0.0936

In this section the structures of co-crystals of BPPY with terephthalic (**1**) and fumaric acid (**2**) will be presented. In these materials the BPPY molecules remain un-protonated. In contrast, the ylide molecules are protonated in the pricrate (**3**) and maleate (**4**) salts of BPPY affording the benzoylmethylenetriphenylphosphonium cation.[27-29] Table 3.3.1 provides crystallographic details and refinement information for all these compounds.

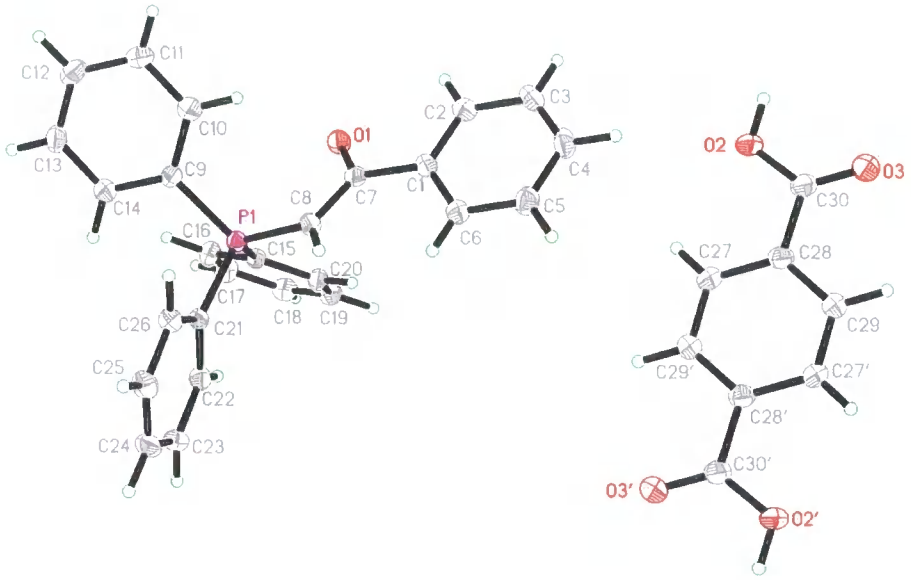

Figure 3.3.1: Molecular structure of BPPY with terephthalic acid (**1**). Thermal displacement ellipsoids are drawn at the 50% probability level. Symmetry equivalent atoms (primed) are included for completeness (sym. code: 1-x, -y, -z).

The molecular structure of **1** is given is Figure 3.3.1. Table 3.3.2 lists the secondary contacts for this compound, and selected interactions are shown diagrammatically in Figure 3.3.2. The strong hydrogen bond O2-H1···O1^{v} and its symmetry equivalent O2^{x}-H1^{x}···O1^{ix} generate a unit comprising a single terephthalic acid molecule and two BPPY molecules (see Table 3.3.2 for symmetry codes). A combination of the C2-H2···O3^{iv} and O2^{iv}-H1^{iv}···O1 interactions generates a ring pattern of the binary graph-set $R_2^2(9)$. Bonds C4-H4···O2, O2-H1···O1^{v}, C2-H2···O3^{iv} and C17^{v}-H17^{v}···O3^{iv} create a distorted ring motif of the quaternary graph-set $R_4^3(16)$. Contacts C4-H4···O2, C17-H17···O3^{ii} and their inversion related equivalents C4^{vi}-H4^{vi}···O2^{vi} and C17^{vi}-H17^{vi}···O3^{x} create a large ring pattern of the binary graph-set $R_4^4(40)$.

The crystal structure of **1** is further stabilised by several short C-H···π contacts, details of which are provided in Table 3.3.8. Cg1 is the centroid of the ring defined by atoms C9-C14, Cg2 by atoms C15-C20, Cg3 by atoms C21-C26, and Cg4 is the centroid of the ring formed by atoms C1-C6.

Table 3.3.2: Geometric parameters for the secondary interactions displayed in the crystal structure of BPPY with terephthalic acid (**1**).

Contact	D-H (Å)	H···A (Å)	D···A (Å)	D-H···A (°)
C10-H10···O1	0.97(2)	2.50(2)	3.163(2)	125.5(14)
C27-H27···O2	0.94(2)	2.42(2)	2.745(2)	100.2(13)
C4-H4···O2	0.99(2)	2.75(2)	3.592(2)	143.4(15)
C25-H25···O1^{i}	0.94(2)	2.60(2)	3.460(2)	152.1(17)
C17-H17···O3^{ii}	0.94(2)	2.49(2)	3.218(2)	134.9(16)
C25-H25···O2^{iii}	0.94(2)	2.60(2)	3.440(2)	149.1(17)
C2-H2···O3^{iv}	0.96(2)	2.62(2)	3.217(2)	120.8(13)
O2-H1···O1^{v}	0.92(3)	1.64(3)	2.526(2)	161(3)
C3-H3···Cg1^{v}	0.96(2)	2.844	3.589	135.15
C6-H6···Cg2^{vi}	0.92(2)	3.233	3.982	139.98
C19-H19···Cg3^{vi}	0.99(2)	2.995	3.785	137.46
C23-H23···Cg4^{vi}	0.99(2)	3.018	3.816	138.77
C13-H13···Cg3^{vii}	0.93(2)	2.731	3.594	155.59
C18-H18···Cg4^{viii}	0.94(2)	2.705	3.526	145.61

Symmetry Codes: (i) ½ - x, -½ + y, 1.5 - z; (ii) –1 + x, y, 1 + z; (iii) 1 - x, -y, 1 - z; (iv) –½ + x, ½ -y, ½ + z; (v) ½ + x, ½ - y, -½ + z; (vi) -x, -y, 1-z; (vii) -x, -y, 2-z; (viii) –1 + x, y, z (ix) ½ - x, -½ + y, ½ - z; (x) 1–x, -y, -z.

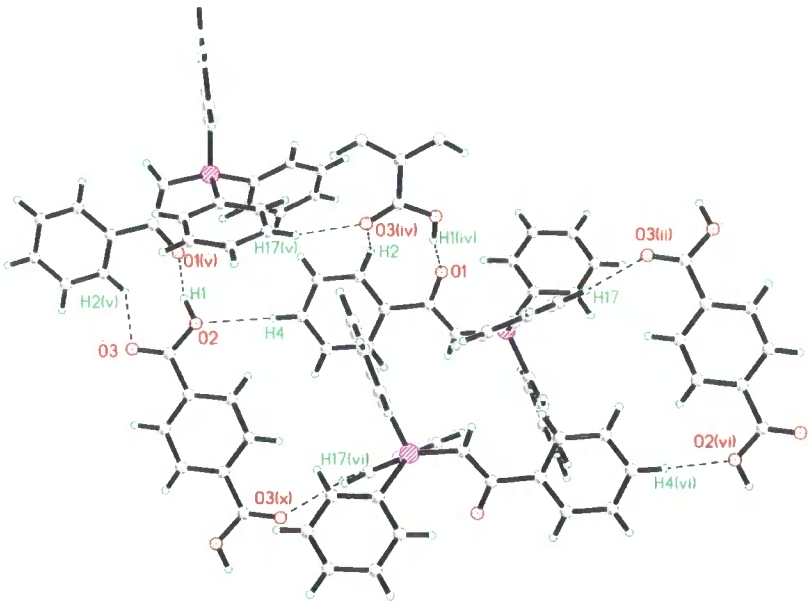

Figure 3.3.2: Intermolecular interactions present in the crystal structure of **1**. See Table 3.3.2 for symmetry codes.

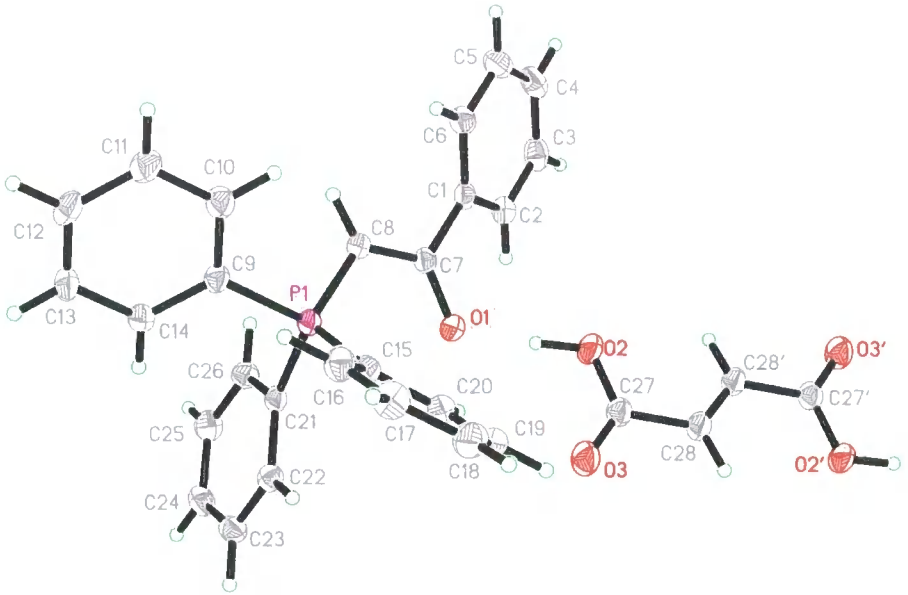

Figure 3.3.3: Molecular structure of BPPY with fumaric acid (**2**). Thermal displacement ellipsoids are drawn at the 50% probability level. Symmetry equivalent atoms (primed) are included for completeness (sym. code: 1-x, 1-y, 1-z).

Figure 3.3.3 shows the molecular structure of compound **2** and Table 3.3.3 lists the secondary interactions observed within its crystal structure; these are shown pictorially in Figure 3.3.4. Both the C11-H11···O2^{i} or C11-H11···O3^{i} interactions when considered in conjunction with the C5-H5···O2^{iii} bond generate a ring pattern of the basic binary graph-set $R_2^2(17)$ (see Table 3.3.3 for symmetry codes). Oxygen atom O1 is a bifurcated hydrogen bond acceptor. The intra-molecular hydrogen bond C20-H20···O1 forms an S(7) motif. This bond along with the O2-H2A···O1 and C20-H20···O3 contacts creates a pattern that can be assigned the graph-set N_3: $R_2^2(6)$. The C2-H2···O2 and O2-H2A···O1 contacts create a ring pattern of the graph-set $R_2^2(7)$. The fumaric acid and ylide molecules are linked into 'trimeric' units by the O2-H2A···O1 bond and its symmetry equivalent at 1-x, 1-y, 1-z.

Table 3.3.3: Geometric parameters for the secondary interactions displayed in the crystal structure of compound **2**.

Contact	D-H (Å)	H···A (Å)	D···A (Å)	D-H···A (°)
O2-H2A···O1	0.99(3)	1.52(3)	2.509(1)	176(3)
C20-H20···O1	0.96(2)	2.33(2)	3.094(2)	135.8(14)
C2-H2···O2	0.93(2)	2.67(2)	3.136(2)	111.8(12)
C20-H20···O3	0.96(2)	2.62(2)	3.345(2)	132.4(13)
C11-H11···O1^{i}	0.96(2)	2.57(2)	3.213(2)	124.1(14)
C11-H11···O2^{i}	0.96(2)	2.75(2)	3.440(2)	128.9(14)
C11-H11···O3^{i}	0.96(2)	2.63(2)	3.521(2)	154.4(15)
C25-H25···O3^{ii}	0.98(2)	2.75(2)	3.348(2)	120.3(13)
C5-H5···O2^{iii}	0.96(2)	2.80(2)	3.591(2)	141.0(15)
C14-H14···Cg1	0.92(2)	2.995	3.716	136.44
C12-H12···Cg1^{i}	0.98(2)	2.607	3.502	151.78
C13-H13···Cg2^{iv}	0.98(2)	2.955	3.694	133.30
C24-H24···Cg3^{v}	0.96(2)	2.981	3.869	155.42

Symmetry Codes: (i) x, ½ - y, -½ + z; (ii) –x, -½ + y, ½ - z; (iii) 1 - x, -½ + y, ½ - z; (iv) -x,1-y,-z; (v) –x, ½ + y, ½ - z.

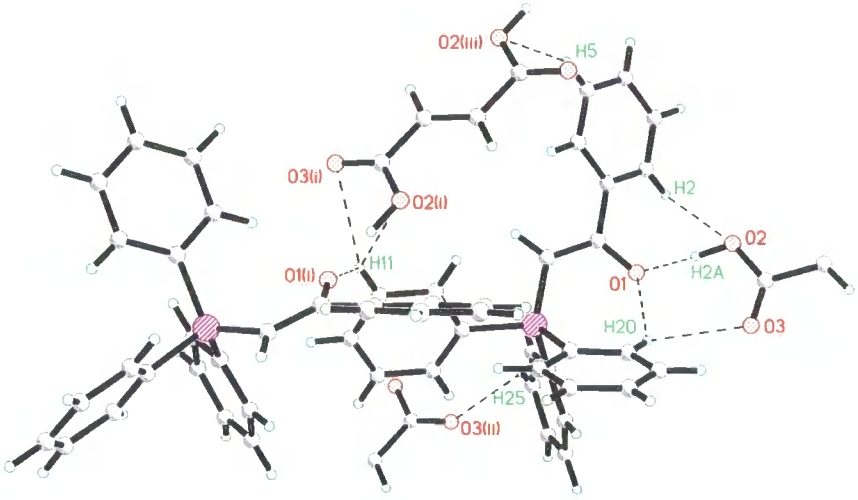

Figure 3.3.4: Intermolecular hydrogen bond interactions present in the crystal structure of **2**. See Table 3.3.3 for symmetry codes.

The secondary interactions for structure **2** include several short C-H···π contacts, the details of which have been included in Table 3.3.3. Cg1 is the centroid of the ring defined by atoms C1-C6, Cg2 by atoms C15-C20 and Cg3 of the ring given by atoms C1-C6. Two π···π interactions complete the complex network of secondary interactions present in the crystal packing of **2**, namely Cg3···Cg2^{iii} and Cg2···Cg3^{v}; both interactions are 3.994 Å in length.

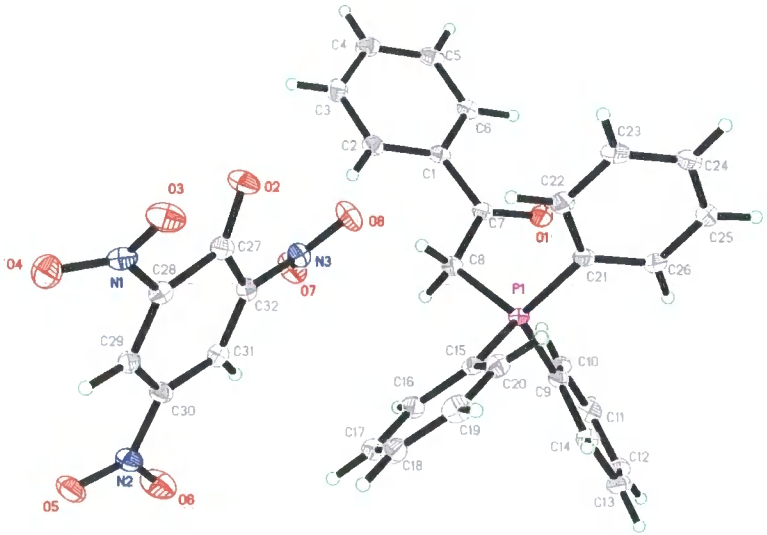

Figure 3.3.5: Molecular structure of benzoylmethylenetriphenylphosphonium picrate (**3**). Thermal displacement ellipsoids are drawn at the 50% probability level.

Figure 3.3.5 shows the molecular structure of benzoylmethylenetriphenylphosphonium picrate (**3**). Table 3.3.4 provides details of the secondary interactions that stabilise the crystal structure of **3**. These interactions are displayed in Figure 3.3.6.

Table 3.3.4: Geometric bond parameters for hydrogen bonds exhibited in **3**.

Contact	D-H (Å)	H···A (Å)	D···A (Å)	D-H···A (°)
C2-H2···O7	0.92(2)	2.51(2)	3.428(2)	174(2)
C8-H8A···O7	0.97(2)	2.52(2)	3.222(2)	129(1)
C8-H8A···O8	0.97(2)	2.45(2)	3.401(2)	167(2)
C10-H10···O1	0.94(2)	2.38(2)	3.057(2)	129(2)
C19-H19···O8^{i}	0.96(2)	2.55(2)	3.510(2)	171(2)
C23-H23···O2^{ii}	0.91(2)	2.59(2)	3.240(2)	129(2)
C24-H24···O3^{ii}	0.94(2)	2.59(2)	3.223(2)	125(2)
C6-H6···Cg1^{iii}	0.99(2)	2.79	3.5059	129
C16-H16···Cg2^{v}	0.95(2)	2.53	3.3872	150

Symmetry codes: (i) 1 - x, -y, -z; (ii) -x, -y, 1 - z; (iii) x - 1, y, z; (iv) 1 + x, y, z.

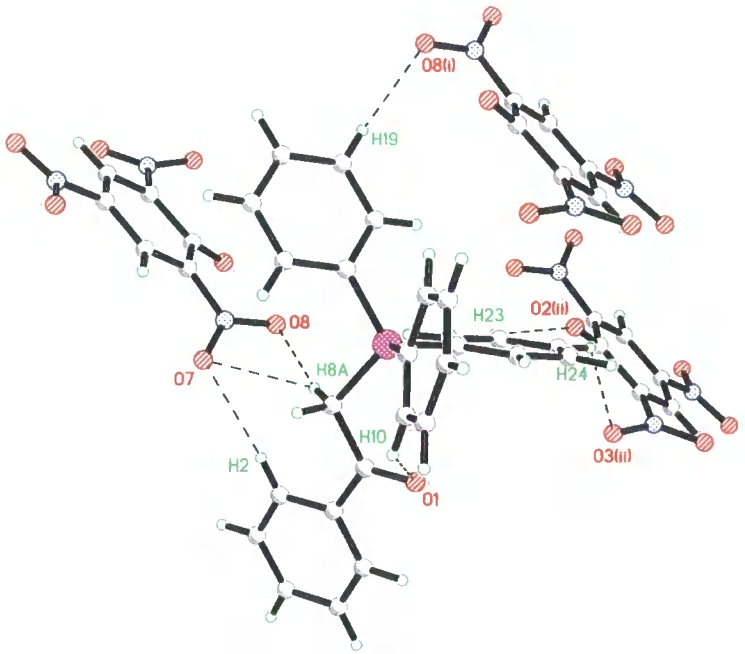

Figure 3.3.6: Diagram displaying intermolecular interactions observed in the crystal structure of **3**. Refer to Table 3.3.4 for symmetry codes.

The intramolecular C10-H10···O1 hydrogen bond produces an S(7) motif. The C2-H2···O7 and C8-H8A···O8 contacts form a ring motif of the graph-set N_2: $R_2^2(8)$. The bifurcated donor C8-H8A generates a smaller ring pattern N_2: $R_1^2(4)$ with atoms O7 and O8. The C2-H2···O7 and C8-H8A···O7 bonds give a N_2: $R_2^1(7)$ ring pattern. Contacts C23-H23···O2^{ii} and C24-H24···O3^{ii} create a ring motif of the binary graph-set $R_2^2(9)$ (see Table 3.3.4 for symmetry codes). The crystal structure of **3** is further stabilised by two C-H···π interactions (see Table 3.3.4). Cg1 is the centroid of the phenyl ring defined by atoms C9-C14, and Cg2 of the ring given by atoms C1-C6.

The structure of benzoylmethylenetriphenylphosphonium maleate (**4**) is shown in Figure 3.3.7. The secondary interactions for this compound are listed in Table 3.3.5; these are shown in Figure 3.3.8.

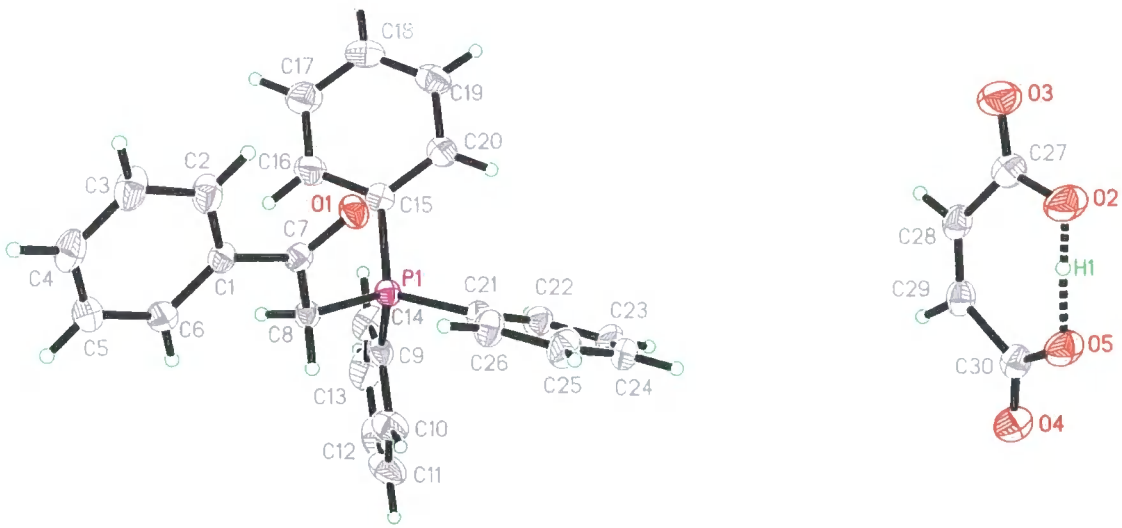

Figure 3.3.7: Molecular structure of benzoylmethylenetriphenylphosphonium maleate (**4**). Thermal displacement ellipsoids are drawn at the 50% probability level.

Table 3.3.5: Geometric bond parameters for hydrogen bonds exhibited in **4**.

Contact	D-H (Å)	H···A (Å)	D···A (Å)	D-H···A (°)
O2-H1···O5	1.05(3)	1.35(3)	2.420(2)	176(3)
C26-H26···O1	0.98(2)	2.47(2)	3.042(2)	117.1(14)
C3-H3···O2^{i}	0.94(2)	2.44(2)	3.243(2)	143.0(16)
C4-H4···O3^{ii}	0.98(2)	2.36(2)	3.277(2)	156.8(16)
C8-H8A···O1^{iii}	0.98(2)	2.40(2)	3.371(2)	170.3(15)
C8-H8B···O4^{iv}	1.00(2)	2.42(2)	3.184(2)	132.9(16)
C8-H8B···O5^{iv}	1.00(2)	2.28(2)	3.270(2)	171.0(17)
C26-H26···O4^{iv}	0.98(2)	2.49(2)	3.267(2)	135.4(15)
C19-H19···O4^{v}	0.93(2)	2.49(2)	3.210(2)	134.8(19)
C25-H25···Cg1^{iv}	0.95(2)	2.79(2)	3.6319	149

Symmetry codes: (i) 1.5 - x, - y, ½ +z; (ii) 1 - x, y - ½, 1.5 - z; (iii) x - ½, y, 1.5 - z; (iv) 1 - x, - y, 1 - z; (v) x - ½, ½ -y, 1 - z.

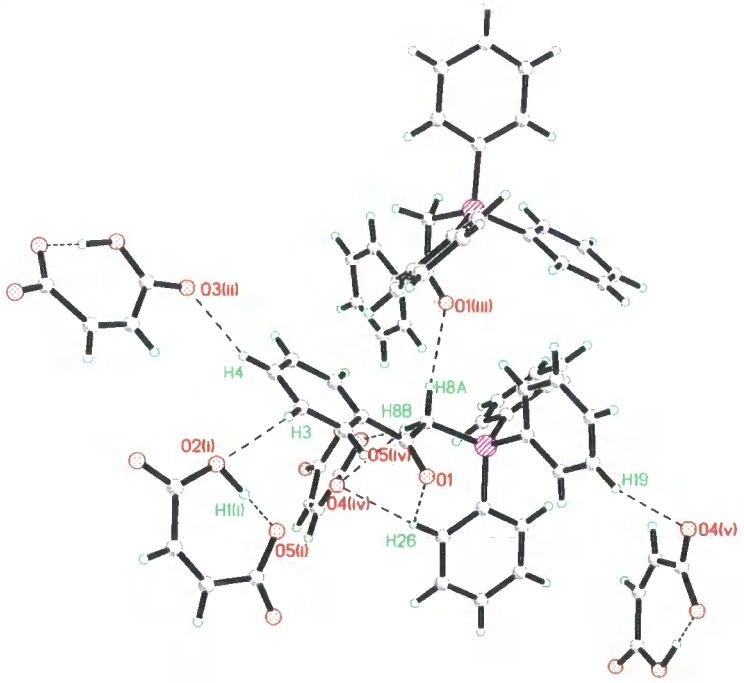

Figure 3.3.8: Diagram showing the hydrogen bonds present in compound **4**. See Table 3.3.5 for symmetry codes.

The intramolecular O2-H1···O5 contact forms a ring motif of the graph-set S(7); likewise the C26-H26···O1 bond also creates an S(7) motif. The C8-H8B group is a bifurcated hydrogen bond donor forming contacts with atoms $O4^{iv}$ and $O5^{iv}$ giving an N_2: $R_1^2(4)$ pattern. The $O4^{iv}$ atom is a bifurcated hydrogen bond acceptor and the C8-H8B···$O4^{iv}$ and C26-H26···$O4^{iv}$ bonds produce an N_2: $R_2^1(7)$ motif. The secondary interactions for compound **4** are completed by a C-H···π interaction (see Table 3.3.5). Cg1 is the centroid of the phenyl ring defined by atoms C1-C6.

Tables 3.3.6, 3.3.7, 3.3.8 and 3.3.9 list principal bonds lengths and angles for compounds **1**, **2**, **3** and **4**, respectively. For the purposes of comparison Table 3.3.10 listed the expected bond lengths for a number of key bonds.

Table 3.3.6: Selected bond geometries for the co-crystal of BPPY with terephthalic acid (**1**).

Bond	Length (Å)	Atoms	Angle (°)
P1-C8	1.729(2)	C8-P1-C9	114.72(8)
P1-C9	1.806(2)	C8-P1-C15	112.28(7)
P1-C15	1.810(2)	C8-P1-C21	107.02(7)
P1-C21	1.810(2)	P1-C8-C7	118.4(1)
O1-C7	1.277(2)	O1-C7-C8	121.1(1)
C7-C8	1.388(2)	C7-C8-H8	124(1)
O2-C30	1.319(2)	P1-C8-H8	118(1)
O3-C30	1.205(2)		

Table 3.3.7: Selected bond geometries for the co-crystal of BPPY with fumaric acid (**2**).

Bond	Length (Å)	Atoms	Angle (°)
P1-C8	1.738(1)	C8-P1-C9	105.92(6)
P1-C9	1.805(1)	C8-P1-C15	114.82(6)
P1-C15	1.807(1)	C8-P1-C21	114.40(7)
P1-C21	1.802(1)	P1-C8-C7	121.1(1)
O1-C7	1.280(2)	O1-C7-C8	122.1(1)
C7-C8	1.386(2)	C7-C8-H8	124(1)
O2-C27	1.311(2)	P1-C8-H8	115(1)
O3-C27	1.214(2)		

Table 3.3.8: Selective bond parameters for H-BPPY$^+$ picrate (**3**).

Bond	Length (Å)	Atoms	Angle (°)
P1-C8	1.816(2)	C9-P1-C8	112.68(8)
P1-C9	1.792(2)	C15-P1-C8	106.21(7)
P1-C15	1.801(2)	C21-P1-C8	108.41(7)
P1-C21	1.791(2)	C7-C8-P1	112.9(1)
C7-C8	1.524(2)	O1-C7-C8	120.2(1)
C7-O1	1.217(2)	O1-C7-C1	121.8(2)
C27-O2	1.232(2)		
C28-N1	1.456(2)		
C30-N2	1.437(2)	P1-C8-H8A	106(1)
C32-N3	1.447(2)	P1-C8-H8B	109(1)
N1-O3	1.231(2)	H8A-C8-H8B	110(2)
N1-O4	1.231(2)		
N2-O5	1.232(2)	O3-N1-O4	123.5(1)
N2-O6	1.237(2)	O5-N2-O6	122.6(1)
N3-O7	1.236(2)	O7-N3-O8	122.5(1)
N3-O8	1.233(2)		

Table 3.3.9: Selective bond parameters for H-BPPY$^+$ maleate (**4**).

Bond	Length (Å)	Atoms	Angle (°)
P1-C8	1.802(2)	C9-P1-C8	107.36(7)
P1-C9	1.797(2)	C15-P1-C8	107.81(8)
P1-C15	1.799(2)	C21-P1-C8	112.41(8)
P1-C21	1.795(2)	C7-C8-P1	112.3(1)
C7-C8	1.516(2)	O1-C7-C8	119.7(1)
C7-O1	1.220(2)	O1-C7-C1	122.1(1)
C27-O2	1.299(2)	P1-C8-H8A	107(1)
C27-O3	1.221(2)	P1-C8-H8B	109(1)
C30-O4	1.233(2)	H8A-C8-H8B	106(2)
C30-O5	1.288(2)		
C28-C29	1.331(3)		

Table 3.3.10: Selected bond parameters taken from the International Tables Vol. C.[30]

Bond Type	Bond Environment	Average Bond Length (Å)
P^+-C_{ar}	C_3-$\mathbf{P^+}$-$\mathbf{C_{ar}}$	1.793
P^+-C	C_3-$\mathbf{P^+}$-**C**	1.800
C-C	$(\mathbf{C})_2$-**C**=O (ketones)	1.511
C=C	**C**=**C**-C=O†	1.331
C=O	C_{ar}-**C**=**O**	1.221
C=O	$(C)_2$-**C**=**O**	1.210
C=O	C-**C**(=**O**)-O-C (esters)	1.196
C=O	C=C-**C**(=**O**)-**OH**	1.229
C-O	C=C-C(=O)-**OH**	1.293
C-N	$\mathbf{C_{ar}}$-$\mathbf{NO_2}$	1.468
N-O	C_{ar}-$\mathbf{NO_2}$	1.217
C-O	C_{ar}-**OH**	1.362

† Unconjugated

The O1-C7 and the C7-C8 distances in compounds **1** and **2** (Tables 3.3.6 and 3.3.7) are longer than the expected distances (Table 3.3.10) this implies that the electron density of the carbanion is resonance delocalised with in the ylide molecules. The sum of the angles surrounding the C8 atoms, 360.4° (**1**) and 360.1° (**2**), signifies that the environment about these carbanions is trigonal planar. These bond lengths and angles provide conclusive evidence pertaining to the existence of BPPY in the un-protonated form in structures **1** and **2**.

The inequality of the O2-C30 and O3-C30 bond lengths in **1**, and the O2-C27 and O3-C27 bond lengths in **2**, suggests that the dicarboxylic acid molecules exist in the un-ionised form in both these compounds.

Comparison of the figures in Tables 3.3.8, 3.3.9 and 3.3.10 indicates that the observed bond lengths determined from the crystal structures of **3** and **4** are in agreement with the expected values for protonated BPPY in which the resonance delocalisation has been lost. The bond lengths associated with the nitro groups of the picric acid (**3**) are not as expected, the C-N bonds are markedly shorter, and the N-O bonds somewhat longer than predicted. These anomalies will be due to the resonance affect introduced by the oxygen anion (O2).

Table 3.3.11 lists the deviations of substituent atoms from the plane of the ring defined by atoms C27-C32 in the crystal structure of **3**. It is clear that all the nitro groups and the oxygen anion are twisted out of the plane of the ring; presumably this is to facilitate the formation of the inter-molecular contacts these groups participate in.

Table 3.3.11: Deviation of atoms from the plane defined by atoms C27-C32

Atom	N1	O3	O4	N2	O5	O6	N3	O7	O8	O2
Deviation (Å)	0.028	-0.562	0.642	0.061	0.219	-0.001	0.079	0.680	-0.454	0.130

The difference between the C=O bonds of the same -COOH group in the maleate molecule of compound **4** suggest that the carboxylic acid groups are not delocalised. The variation in the C-O and C=O bond lengths between the two -COOH groups will be due to the formation of the strong non-symmetrical intra-molecular hydrogen bond O2-H1···O5 (see Table 3.3.9).

The phosphorus atoms in compounds **1** - **4** possess distorted tetrahedral geometry. The non-bonded distance between the phosphorus and carbonyl oxygen atoms of the ylide molecules are given in Table 3.3.12. These values are considerably shorter than the sum of the van der Waals radii of 3.3 Å for phosphorus and oxygen.[31] This suggests that significant non-bonding interactions exist between these two atoms in all the compounds. It is likely that the formation of such a strong contact will account for the eclipsing orientation about the C7-C8 bond that is observed in these materials. The presence of P···O interactions is a well-known feature of ylide chemistry, and these interactions have been predicted to play a significant role in determining the molecular conformation adopted by the ylide molecule.[32,33]

Table 3.3.12: Geometric data for P/O interactions.

	1	**2**	**3**	**4**
P···O Distance (Å)	2.907(1)	2.991(1)	2.954(1)	2.880(1)
P1-C8-C7-O1 Torsion Angle (°)	8.3(2)	4.3(3)	22.0(2)	-11.8(2)

It was expected that the P···O interactions in compounds **1** and **2** would be stronger, and as such the inter-atomic distances shorter, than for compounds **3** and **4**. This is because, compared to compounds **3** and **4**, the resonance delocalisation of the ylidic electron density is not lost in compounds **1** and **2** and therefore the phosphorus and oxygen atoms in these compounds possess partial positive and negative charges, respectively, (see Fig. 3.1.1) which would increase the force of attraction between these centres. Yet, the figures in Table 3.3.12 indicate that this is not the case, and the deviation from expected behaviour maybe due to un-quantified crystal packing effects.

Returning to the discussion of the counter-ion dependence of the reactivity of phosphorus ylides begun in the introduction Section 3.1. It can be hypothesised that the terephthalic (**1**) and fumaric (**2**) co-crystals of BPPY would display enhance reactivity with respect to the pricrate and maleate salts (compounds **3** and **4** respectively), at least in terms of the Wittig reaction. The structural results presented here, have shown that the BPPY molecules remain un-protonated in **1** and **2**, and thus retains its ylide status in these compounds, this is not the case for **3** and **4**. It is unfortunate that these crystallographic analyses have not confirmed the proton transfer mechanism proposed by Hon et al (Fig. 3.1.4).[18]

The co-crystals of BPPY with fumaric or terephthalic acid could have potential applications as 'all-in-one' reagents, with greater reactivity than conventional free ylide materials due to the inclusion of the catalytic acid. Furthermore, the crystal structures of **1** and **2** both have short, strong O-H···O hydrogen bonds forming between the un-ionised dicarboxylic acid molecules and the carbonyl oxygen atom of the ylide molecules, and a complex network of weaker interactions, which help to stabilise the ylide materials substantially reducing their sensitivity to air and moisture.

3.3.2 The free ylides ABPPY and EPPY.

In this section the structures of the free ylides ABPPY (**5**) and EPPY (**6**) will be reported. These materials have been included in this project as organometallic structures containing these particular ylides will be presented latter in this chapter (see Sections 3.3.3 and 3.3.4). Table 3.3.13 lists crystallographic data and refinement details for these two ylides.

Table 3.3.13: Crystallographic data and refinement details for compounds **5** and **6**.

	5	**6**
Crystal size (mm^3)	0.12 x 0.10 x 0.09	0.29 x 0.20 x 0.18
Crystal system	Monoclinic	Monoclinic
Space group	$P2_1$	$P2_1/n$
a (Å)	9.408(3)	9.8513(3)
b (Å)	27.494(2)	14.5488(4)
c (Å)	9.8621(2)	12.8581(4)
α (°)	90	90
β (°)	114.142(2)	101.443(1)
γ (°)	90	90
Volume ($Å^3$) / Z	2132.5(2)	1806.25(9) / 4
μ (mm^{-1})	0.152	0.164
Unique reflections	8058	3994
R(int)	0.0532	0.0356
Gof (on F^2)	1.047	1.038
R1 / wR2 (I>2σ(I))	0.0584 / 0.1226	0.0358 / 0.0910

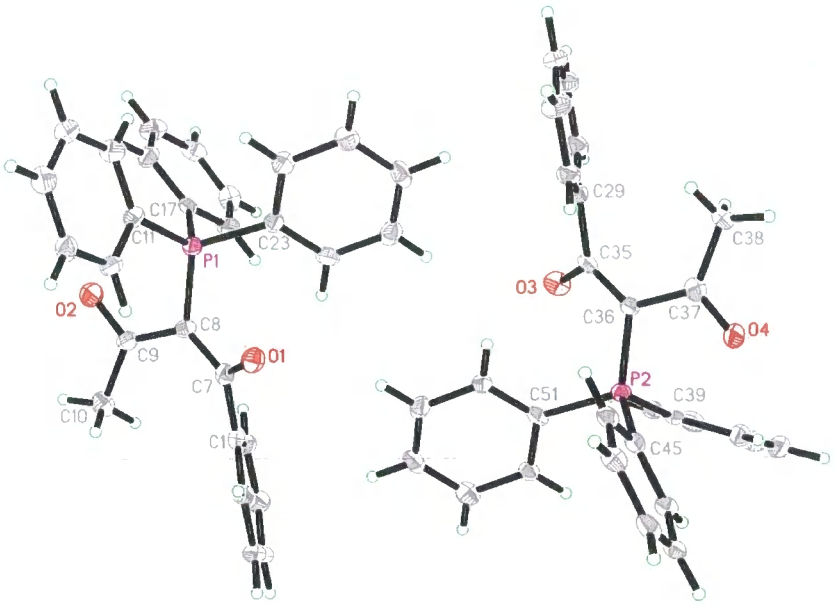

Figure 3.3.9: Molecular structure of ABPPY (**5**). Thermal displacement ellipsoids are drawn at the 50% probability level.

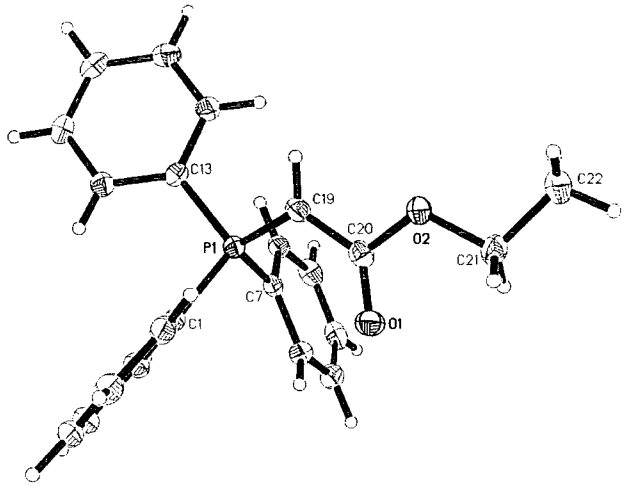

Figure 3.3.10: Molecular structure of EPPY (**6**). Thermal displacement ellipsoids are drawn at the 50% probability level.

The molecular structures of ABPPY (**5**) and EPPY (**6**) are given in Figures 3.3.9 and 3.3.10 respectively. Key bond parameters for these compounds are listed in Tables 3.3.14 and 3.3.15.

Table 3.3.14: Selected bond geometries for ABPPY (**5**).

Bond	Length (Å)	Bond	Length (Å)	Atoms	Angle (°)
P1-C8	1.751(4)	P2-C36	1.770(4)	P1-C8-C9	109.6(3)
P1-C11	1.810(4)	P2-C39	1.801(4)	P1-C8-C7	120.0(3)
P1-C17	1.811(4)	P2-C45	1.801(4)	C9-C8-C7	127.2(4)
P1-C23	1.813(4)	P2-C51	1.812(4)	O1-C7-C8	121.9(4)
C8-C9	1.430(5)	C36-C37	1.440(5)	O1-C7-C1	118.4(3)
C8-C7	1.453(5)	C36-C35	1.435(5)	O2-C9-C8	117.8(4)
C7-O1	1.232(5)	C35-O3	1.251(5)	O2-C9-C10	116.6(4)
C1-C7	1.502(6)	C29-C35	1.496(5)	P2-C36-C37	111.7(3)
C9-O2	1.268(5)	C37-O4	1.249(5)	P2-C36-C35	117.7(3)
C9-C10	1.507(6)	C37-C38	1.498(6)	C37-C36-C35	126.4(4)
				O4-C37-C36	119.7(4)
				O4-C37-C38	118.4(3)
				O3-C35-C36	122.8(4)
				O3-C35-C29	117.6(4)

Table 3.3.15: Selected bond geometries for EPPY (**6**).

Bond	Length (Å)	Atoms	Angle (°)
P1-C1	1.809(1)	P1-C19-C20	119.5(1)
P1-C7	1.811(2)	P1-C19-H19	118(1)
P1-C13	1.809(2)	C20-C19-H19	122(1)
P1-C19	1.706(2)	O1-C20-C19	126.9(1)
C19-C20	1.408(2)	O1-C20-O2	120.9(1)
C19-H19	0.95(2)	C19-C20-O2	112.2(1)
O1-C20	1.23(2)	C20-O2-C21	116.5(1)
O2-C20	1.380(2)		
O2-C21	1.443(2)		
C21-C22	1.504(2)		

There are two symmetry independent ABPPY molecules in the asymmetric unit of **5**. The discrepancies in the bond geometries between the two ylide molecules will be due to differences in the packing environments of the two molecules within the crystal structure. The asymmetric unit of **6** is composed of a single EPPY molecule.

The bond angles surrounding the carbanions in **5** and **6** signify that the environment about these centres is distorted trigonal planar, this confirms that the ylide molecule remains un-protonated at these sites. The lengthening of the C-O bonds and the intermediate single/double bond length of the $C_{(ylide)}$-C bonds in **5** is strongly suggestive of resonance delocalisation with in the ylide molecules. The degree of delocalisation manifest in the bond lengths appears to differ between the two independent ylide molecules of the asymmetric unit. Furthermore, the delocalisation is not equally distributed between the two carbonyl groups, although it is not clear which is the dominant centre. Likewise, the C20-O1 bond length in **6** is significantly longer than expected for an ester carbonyl group (1.196 Å, see Table 3.3.10), and the C19-C20 bond distance is typical for partial double bond, it can be surmised that the free ylide EPPY (**6**) also exhibits resonance delocalisation of the ylidic electron density.

In compound **5**, The torsion angles about atoms P1, C8, C9, O2 and P1, C8, C7, O1 are 0.2(5)° and 17.8(5)° respectively. The torsion angles assumed by atoms P2, C36, C37, O4 and P2, C36, C35, O3 are –11.5(5)° and –14.1(5)°, respectively. The non-bonding distances between the P^+

and O^- centres are: P1···O2, 2.661(3) Å; P1···O1, 3.046(3) Å; P2···O4, 2.785(3) Å; P2···O3, 2.997(3) Å. These distances are significantly less than the sum of the van der Waals atomic radii for phosphorus and oxygen (3.3 Å), and are suggestive of strong interactions between the P and O atoms, accounting for their eclipsing orientation. A similar interaction is observed in the crystal structure of **6** where the non-bonding distance between the phosphorus and oxygen centres is 3.039(1) Å. Equally, the torsion angle about atoms P1, C19, C20 and O1 in **6** is -10.7(2)°, which as in the case of **5**, indicates the near *cis* orientation about the C19-C20 partial double bond.

3.3.3 The uranium salts and complexes of BPPY, ABPPY and EPPY.

In this section the uranium (VI) complexes of BPPY (**7**) and ABPPY (**8**) will be discussed. These two bis(ylide) complexes are structurally similar and are of the form $[UO_2(NO_3)_2(ylide)_2]$. In addition to these complexes, the results of the X-ray analysis of the salts $[H\text{-}EPPY]^+[UO_2(CH_3COO)_3]^-$ (**9**) and $[H\text{-}BPPY]_2^+[UO_2(NO_3)_4(OH)_2]^{2-}$ (**10**) will be reported, the latter of which contains the relatively rare di-μ-hydroxo-bis[dinitratodioxouranate(VI)] anion.

Table 3.3.16: Crystallographic data and refinement details for compounds **7-10**.

	7	**8**	**9**	**10**
Crystal size (mm^3)	0.37 x 0.28 x 0.20	0.22 x 0.19 x 0.17	0.16 x 0.12 x 0.04	0.20 x 0.17 x 0.14
Crystal system	Triclinic	Monoclinic	Monoclinic	Monoclinic
Space group	P-1	$P2_1/n$	$P2_1$	$P2_1/n$
a (Å)	13.1276(6)	11.2237(3)	9.5596(5)	18.5771(8)
b (Å)	14.5793(7)	17.2428(4)	14.1265(7)	14.0779(6)
c (Å)	16.1758(8)	16.0559(5)	10.9521(5)	20.8976(9)
α (°)	80.677(2)	90	90	90
β (°)	67.458(2)	90.446(1)	93.183(2)	93.496(2)
γ (°)	75.911(2)	90	90	90
Volume ($Å^3$) / Z	2765.2(2) / 2	3107.2(2) / 2	1476.7(1) / 2	5455.1(4) / 4
μ (mm^{-1})	3.342	2.727	5.604	6.070
Unique reflections	9821	5476	9051	9642
R(int)	0.0257	0.0736	0.0293	0.0405
Gof (on F^2)	1.059	0.929	0.795	1.029
R1 / wR2 (I>2σ(I))	0.0373 / 0.0981	0.0274 / 0.0694	0.0246 / 0.0525	0.0212 / 0.0504

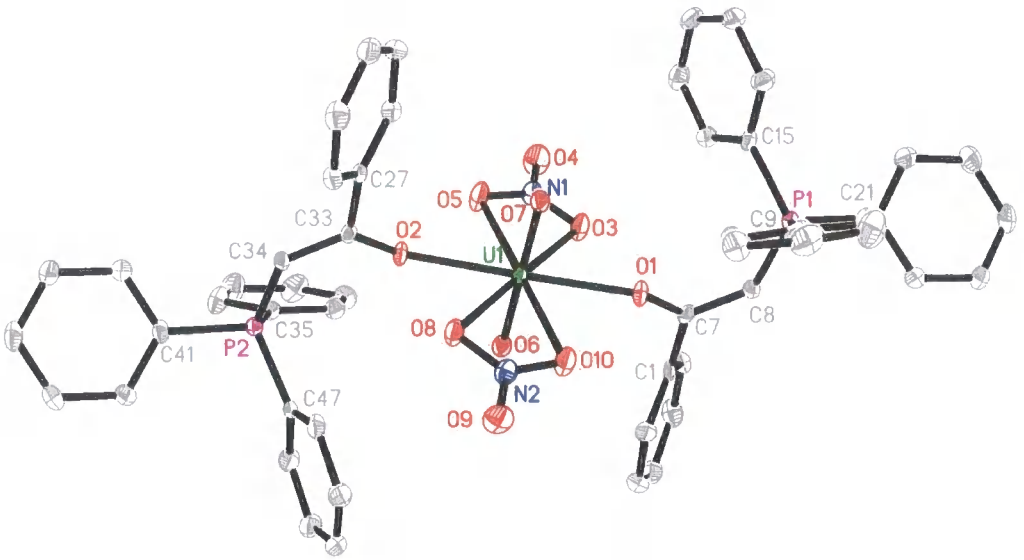

Figure 3.3.11: Molecular structure of $[UO_2(NO_3)_2(BPPY)_2]$ (**7**). Hydrogen atoms and solvent molecules have been omitted for clarity. Thermal displacement ellipsoids are drawn at the 50% probability level.

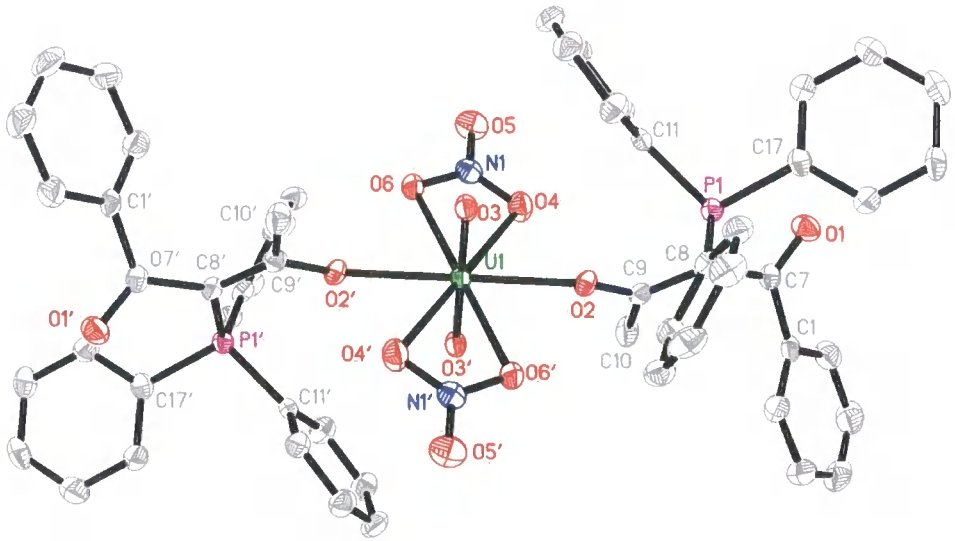

Figure 3.3.12: Molecular structure of $[UO_2(NO_3)_2(ABPPY)_2]$ (**8**). Hydrogen atoms and solvent molecules have been omitted for clarity. Symmetry equivalent atoms (primed) have been shown for completeness (sym. code: -x, -y, 1-z). Thermal displacement ellipsoids are drawn at the 50% probability level.

The molecular structures of complexes **7** and **8** are shown in Figures 3.3.11 and 3.3.12 respectively. The similarity between the two structures is immediately apparent. In both cases the ylide ligands are O-coordinated to the uranium metal. Such a coordination mode can be predicted by considering the HASB effect, that is to say, hard acids bind to hard bases, and soft acids bind to soft bases.[34] This theory would suggest that the ylide would bind preferentially to the hard UO_2^{2+} ion via the hard carbonyl oxygen as opposed to via the softer carbanion centre. Moreover, the oxygen as opposed to carbon coordination of the ylide molecules gives rise to the less sterically demanding complex configuration, and this will also have influenced the bonding mode.[35, 36] This is particularly true in the case of the bulky ABPPY ligands in compound **8**, which binds via the oxygen atom of the COMe group in a monodentate fashion.

The uranium metal in complexes **7** and **8** resides in a distorted dodecahedral environment, in which the ylide molecules are *trans*-coordinated. In complexes **7**, the dihedral angle between the two planes defined by atoms U1, O1, O2, O6, O7 and U1, O3, O5, O8, O10, respectively, is 90.0(1)°. The corresponding dihedral angle in **8** between the two planes defined by atoms U1, O4, N1, O6 and U1, O2, O3, respectively, is 88.8(1)°.

Table 3.3.17: Selected bond geometries for **7**.

Bond	Length (Å)	Bond	Length (Å)	Atoms	Angle (°)
U1-O1	2.358(3)	N2-O8	1.269(5)	O1-UI-O2	178.74(9)
U1-O2	2.358(3)	N2-O9	1.224(5)	O3-U1-O5	49.9(1)
U1-O3	2.549(3)	N2-O10	1.269(5)	O3-N1-O5	115.7(4)
U1-O5	2.524(3)	P1-C8	1.749(5)	O6-U1-O7	179.8(1)
U1-06	1.777(3)	C8-C7	1.377(6)	O8-U1-O10	50.2(1)
U1-O7	1.774(3)	C7-O1	1.287(5)	O8-N2-O10	115.5(4)
U1-O8	2.535(3)	P2-C34	1.739(5)	P1-C8-C7	127.9(4)
U1-O10	2.525(3)	C34-C33	1.377(6)	O1-C7-C8	124.9(4)
N1-O3	1.268(5)	C33-O2	1.287(5)	O1-C7-C1	119.3(4)
N1-O4	1.225(5)			P2-C34-C33	127.2(4)
N1-O5	1.261(5)			O2-C33-C34	124.4(4)
				O2-C33-C27	119.6(4)

Table 3.3.18: Selected bond geometries for **8**.

Bond	Length (Å)	Bond	Length (Å)	Atoms	Angle (°)
U1-O2	2.340(2)	P1-C8	1.771(4)	O2-U1-O3	87.8(1)
U1-O3	1.768(3)	C7-O1	1.223(4)	O4-U1-O6	50.04(8)
U1-O4	2.563(3)	C8-C7	1.490(5)	O4-N1-O6	115.3(3)
U1-O6	2.511(2)	C9-C8	1.383(5)	P1-C8-C7	119.9(3)
N1-O4	1.267(4)	C9-C10	1.512(5)	O1-C7-C8	122.1(3)
N1-O5	1.219(4)	C9-O2	1.283(4)	O1-C7-C1	119.2(3)
N1-O6	1.274(4)			P1-C8-C9	116.2(3)
				C10-C9-C8	122.8(3)
				C10-C9-O2	116.9(3)

Tables 3.3.17 and 3.3.18 list key bond parameters for compounds **7** and **8**, respectively. The U-O bond lengths in both complexes are similar to those found for complexes in which the uranium atom possesses the same triangulated dodecahedron geometry. The variation in the U-O bond lengths and small bite angles for the bidentate nitrate groups are characteristic of this type of uranyl complex.[37-40]

The P-C bonds in complex **7** are marginally longer than in the free ylide (1.716(5) Å, 1.725(4) Å; two molecules in the asymmetric unit) [3]. The C7-C8 and C33-C34 bonds lengths are consistent with the partial double bond character of these bonds. The bond lengths for the ylide components of **8** are similar to those reported for O-coordinated mercury (II) complexes of ABPPY.[23] Comparison of the ylide bond lengths with those of the parent ylide (**5**) show that, like the BPPY ligands in complex **7**, ABPPY looses its resonance stabilisation when bound to the uranium metal.

The torsion angles about atoms P1, C7, C8, O1 and P2, C34, C33, O2 of complex **7** are –3.5(7)° and 1.6(7)° respectively. Similarly, the angles about atoms P1, C8, C7, O1 and P1, C8, C9, O2 in **8** are –46.3(5)° and –4.3(5)°, respectively. These angles demonstrate the eclipsing orientation of the P1/O1 and P2/O2 atoms in **7**, and the P1/O2 atoms in **8**. The formation of strong non-bonding interactions between the phosphorus and oxygen atoms of the ylide molecules will account for these sterically unfavourable arrangements. The distances between these atom pairs are: P1···O1: 3.206(3) Å (**7**); P2···O2: 3.172(3) Å (**7**); P1···O1: 3.219(3) Å (**8**);

P1···O2: 2.851(3) Å(**8**). These distances are all markedly less than the sum of the van der Waals atomic radii for phosphorus and oxygen (3.3 Å).

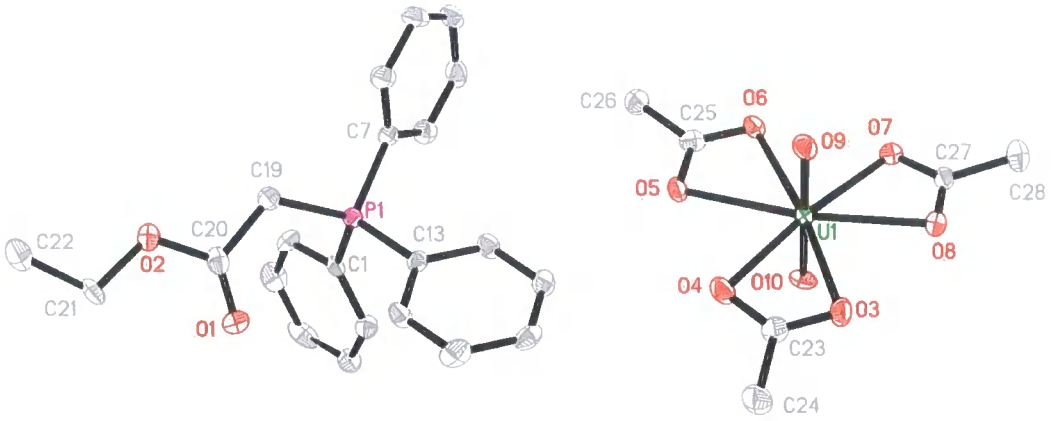

Figure 3.3.13: Molecular structure of the salt $[H\text{-}EPPY]^{+}[UO_2(CH_3COO)_3]^{-}$ (**9**). Thermal displacement ellipsoids are drawn at the 50% probability level.

Table 3.3.19: Selected bond geometries for **9**.

Bond	Length (Å)	Bond	Length (Å)	Atoms	Angle (°)
U1-O3	2.457(4)	O5-C25	1.272(7)	O9-U1-O10	179.4(2)
U1-O4	2.458(4)	O6-C25	1.259(7)	O3-C23-O4	119.8(5)
U1-O5	2.495(3)	C25-C26	1.501(8)	O5-C25-O6	119.4(5)
U1-O6	2.491(4)	O7-C27	1.271(7)	O7-C27-O8	119.8(5)
U1-O7	2.458(4)	O8-C27	1.258(7)	P1-C19-C20	115.8(4)
U1-O8	2.451(4)	C27-C28	1.511(8)	O1-C20-C19	125.0(5)
U1-O9	1.775(3)	P1-C19	1.810(5)	O1-C20-O2	125.3(5)
U1-O10	1.777(3)	C19-C20	1.508(7)	O2-C20-C19	109.7(4)
O3-C23	1.254(7)	O1-C20	1.196(2)	C20-O2-C21	114.7(4)
O4-C23	1.263(7)	O2-C20	1.337(6)		
C23-C24	1.498(7)	O2-C21	1.466(8)		

The structure of the salt $[H\text{-}EPPY]^{+}[UO_2(CH_3COO)_3]^{-}$ (**9**) is shown in Figure 3.3.13, and important bond information is given in Table 3.3.19.

In compound **9** the EPPY entity is C-protonated and as such is deprived of its ylide character. The protonation of the C19 site is reflected in the differences in the bond angles surrounding this atom when compared with the parent ylide (**6**). The significant shortening of the C20-O1 bond and lengthening of the C19-C20 bond in **9** with respect to **6**, is symptomatic of the loss of resonance stabilisation that accompanies the protonation of EPPY.

The triacetatouranylate (VI) anion possesses triangulated dodecahedron geometry. Due to lack of bulky molecules ligating to the uranium atom, the dodecahedron is notably less distorted than in the case of bis(ylide) complexes **7** and **8**. The acetate ligands are bidentate and positioned equatorially with respect to the linear O=U=O unit, the dihedral angle between the two planes defined by atoms O9, U1, O10 and U1, C23, C25, C27, respectively is 87.1(1)°. The acetate bite angles are similar to those seen for nitrate ligands. The U-O(acetate) bonds are shorter than the U-O(nitrate) bonds observed in **7** and **8**; this can be attributed to the reduced steric crowding surrounding the metal centre. The structure of the triacetatouranylate (VI) anion in **9** is consistent with the structure reported by Navaza et *al.* for sodium triacetatouranylate.[41]

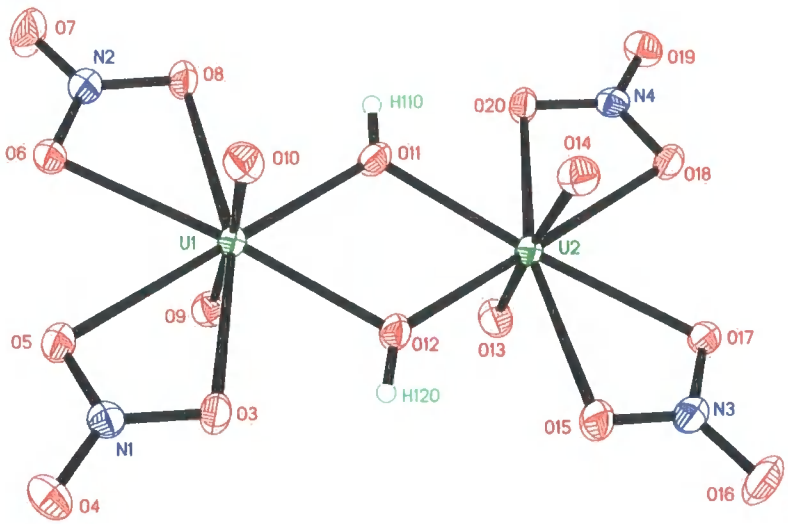

Figure 3.3.14: $[UO_2(NO_3)_4(OH)_2]^{2-}$ anion observed in the structure of **10**. Thermal displacement ellipsoids are drawn at the 50% probability level.

The asymmetric unit of **10** comprises two protonated BPPY ylide molecules and a single di-μ-hydroxo-bis[dinitratodioxouranate(VI)] anion. The H-BPPY$^+$ cations exhibit no unusual structural features and are equivalent to the structure of H-BPPY$^+$ reported by Antipin and Struchkov.[4] Both H-BPPY$^+$ cations have the expected short P···O contacts of 2.980(1) Å, and 2.922(2) Å, respectively. The uranate(VI) anion is shown in Figure 3.3.14. Key bond lengths and angles are listed in Table 3.3.20, these agree with the values previously reported for this comparatively rare anion.[42]

Table 3.3.20: Selected bond geometries for the di-μ-hydroxo-bis[dinitratodioxouranate(VI)] anion in **10**.

Bond	Length (Å)	Bond	Length (Å)	Atoms	Angle (°)
U1-O3	2.558(2)	U2-O13	1.772(2)	O3-U1-O5	49.45(7)
U1-O5	2.563(2)	U2-O14	1.773(2)	O3-N1-O5	114.9(3)
U1-O6	2.541(2)	U2-O15	2.544(2)	O6-U1-O8	49.99(7)
U1-O8	2.546(2)	U2-O17	2.534(2)	O6-N2-O8	115.4(3)
U1-O9	1.773(2)	U2-O18	2.568(2)	O9-U1-O10	175.0(1)
U1-O10	1.774(2)	U2-O20	2.564(2)	O11-U1-O12	65.68(9)
U1-O11	2.307(3)	U2-O11	2.331(3)	O11-U2-O12	65.68(9)
U1-O12	2.332(2)	U2-O12	2.309(2)	O13-U2-O14	174.9(1)
N1-O3	1.270(3)	N3-O15	1.269(4)	O15-U2-O17	50.01(7)
N1-O4	1.216(3)	N3-O16	1.209(4)	O15-N3-O17	115.1(3)
N1-O5	1.272(3)	N3-O17	1.274(4)	O18-U2-O20	49.32(7)
N2-O6	1.280(3)	N4-O18	1.274(3)	O18-N4-O20	115.1(3)
N2-O7	1.212(4)	N4-O19	1.218(3)		
N2-O8	1.263(3)	N4-O20	1.263(3)		

3.3.4 The mercury (II) complexes of EPPY.

In this section the structures of the mercury(II) halide complexes of EPPY will be discussed. These complexes are isostructural dimeric species of the form $[(EPPY)(HgX_2)]_2$ were X is either bromine (**11**), chlorine (**12**) or iodine (**13**). All structures crystallise in the centrosymmetric space group P-1, and the dimeric unit straddles the crystallographic inversion centre. Relevant crystallographic data are provided in Table 3.3.21.

Table 3.3.21: Crystallographic data and refinement details for complexes **11-13**.

	11	**12**	**13**
Crystal size (mm^3)	0.39 x 0.33 x 0.32	0.17 x 0.15 x 0.14	0.19 x 0.17 x 0.16
Crystal system	Triclinic	Triclinic	Triclinic
Space group	P-1	P-1	P-1
a (Å)	10.6974(4)	11.2465(6)	10.7970(5)
b (Å)	11.1019(4)	11.8297(7)	11.0485(5)
c (Å)	12.5683(4)	12.0170(7)	11.3649(5)
α (°)	76.161(2)	82.602(2)	67.813(2)
β (°)	68.698(2)	80.642(2)	81.098(2)
γ (°)	81.658(2)	78.368(2)	69.550(2)
Volume ($Å^3$) / Z	1347.49(8) / 1	1537.5(2) / 1	1175.82(9) /1
μ (mm^{-1})	9.052	5.774	9.253
Unique reflections	5257	5361	6922
R(int)	0.0204	0.0478	0.0204
Gof (on F^2)	1.039	1.037	1.021
R1 / wR2 (I>2σ(I))	0.0349 / 0.0837	0.0536 / 0.1226	0.0314 / 0.0638

The structures of complexes **11, 12** and **13** are shown in Figures 3.3.15, 3.3.16 and 3.3.17 respectively. Considerable disorder is observed in the crystal structures of **12** and **13**. In compound **12**, monomer material was found to be present with approximately 5% occupancy. The monomer is of the form [(EPPY)(HgCl)] in which the ylide molecule is C-coordinated to the mercury atom (see Figure 3.3.16). The second chlorine atom of the monomer component could not be resolved from a disordered $CHCl_3$ solvent molecule. In the case of complex **13** approximately 5% of un-reacted $[HgI_2]_2$ was found to be present in the sample (Figure 3.3.17). In both structures the positional and thermal parameters of the disordered components were refined freely. The occupancy values were fixed at 0.05 for the final round of least-squares refinement. Further discussion of complexes **12** and **13** will be confined to consideration of the principle dimer components only.

The dimeric structure adopted by the Hg(II)-EPPY complexes is in contrast to the C-coordinated trinuclear mercury(II) complex of BPPY,[17] but comparable to the C-coordinated dinuclear mercury(II) halide complexes of BPPY,[16] and the structure of *trans*-Di-μ-iodo-diiodobis(triphenylphosphoniumcyclopentadienylide)dimercury(II) reported by Baenziger *et*

al.[43] The mercury complexes **11** - **13** are isostructural with the dichloropalladium(II) complex of EPPY, which has been characterised using spectroscopic techniques.[25]

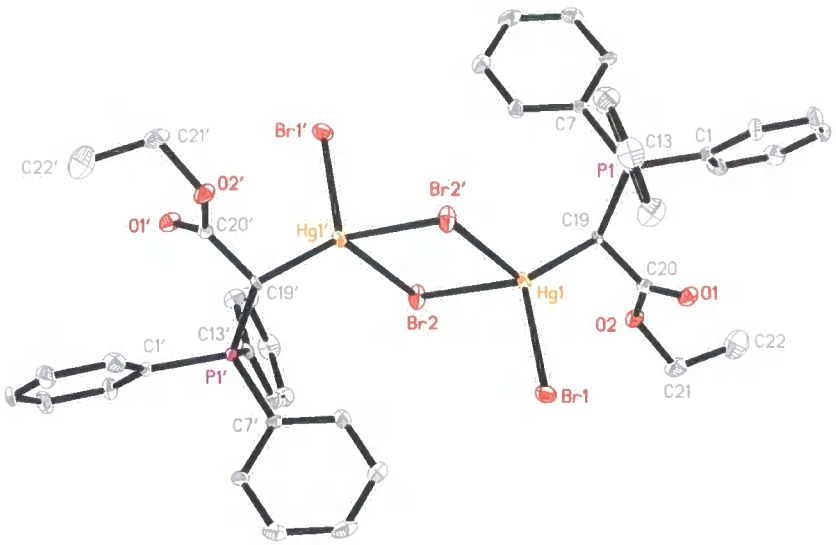

Figure 3.3.15: Structure of $[(EPPY)(HgBr_2)]_2$ (**11**). Hydrogen atoms and solvent molecules have been omitted for clarity. Thermal ellipsoids are drawn at the 50% probability level. Symmetry equivalent atoms (primed) are included for completeness (sym. code: -x, 1-y, 2-z).

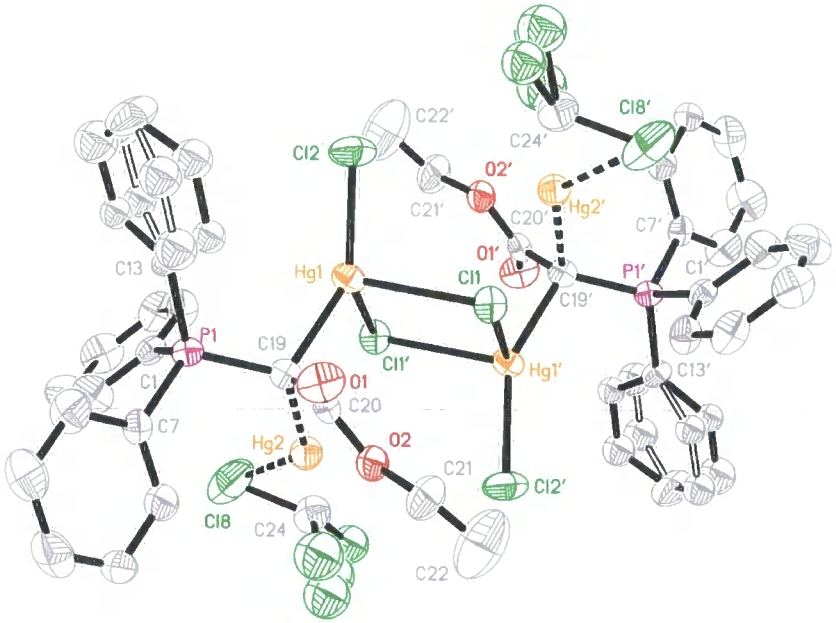

Figure 3.3.16: Structure of $[(EPPY)(HgCl_2)]_2$ (**12**). Hydrogen atoms and the second solvent molecule have been omitted for clarity. Thermal ellipsoids are drawn at the 50% probability

level. Symmetry equivalent atoms (primed) are included for completeness (sym. code: 1-x, 1-y, -z). The 5% monomer component is displayed with dashed-solid bonds.

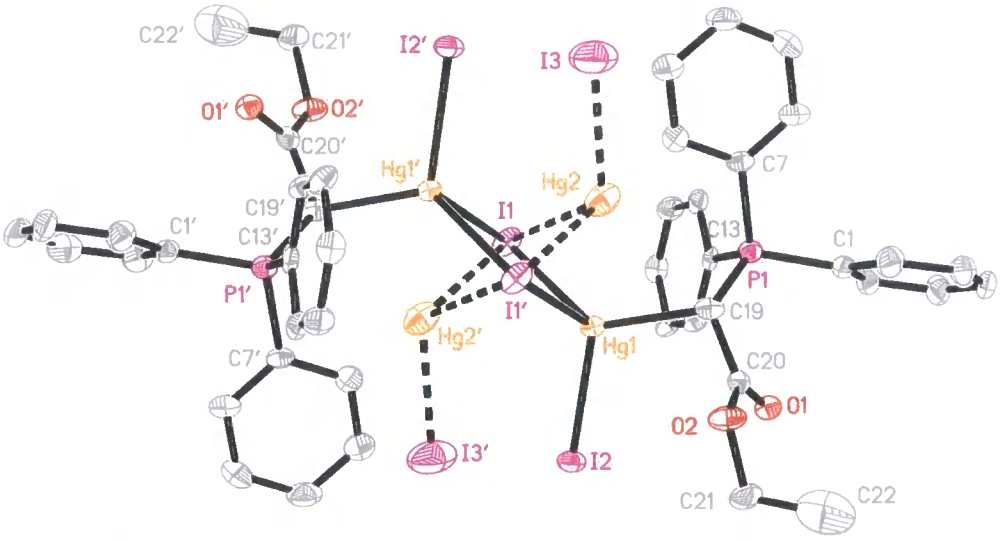

Figure 3.3.17: Structure of $[(EPPY)(HgI_2)]_2$ (**13**). Hydrogen atoms have been excluded for clarity. Thermal displacement ellipsoids are drawn at the 50% probability level. Symmetry equivalent atoms (primed) are included for completeness (sym. code: 1-x, 1-y, -z). The 5% of un-reacted $[HgI_2]_2$ is shown with dashed bonds.

The EPPY molecules are C-coordinated to the mercury atoms in **11-13**, this can be rationalised by the HASB effect. The electron density of the mercury atoms is polarisable and as such the Hg^{2+} ion can be regarded as a soft metal centre. It is therefore unsurprising that the ylide molecules bind via the soft carbanion centre as opposed to via the hard carbonyl oxygen. The ylide molecules are arranged *trans* to each other. By bonding via the ylide carbon, chirality is introduced at this site. This chiral centre and the inversion symmetry intrinsic to the complexes mean that all three mercury complexes are diasteroisomeric.

The P1-C19 and C19-C20 bonds in all the complexes are significantly longer than in the free ylide (**6**) (see Table 3.3.15), this is consistent with the loss of resonance delocalisation within the ylide molecules that occurs upon complexation. The non-bonding distance between the phosphorus and oxygen atoms of the ylide molecules are 3.048(4) Å (**11**), 3.155(8) Å (**12**), and 3.013(5) Å (**13**). These values imply that in all three complexes there is a significant non-bonding interaction between these two atoms.

Table 3.3.22: Selected bond geometries for complex **11** (Sym. code: -x, 1-y, 2-z).

Bond	Length (Å)	Atoms	Angle (°)
P1-C1	1.806(6)	P1-C19-C20	113.5(4)
P1-C7	1.796(5)	C19-C20-O1	124.5(5)
P1-C13	1.798(5)	C19-C20-O2	111.8(5)
P1-C19	1.788(5)	O1-C20-O2	123.8(5)
C19-C20	1.482(7)	O2-C21-C22	111.9(5)
O1-C20	1.207(7)	P1-C19-Hg1	111.2(2)
O2-C20	1.344(7)	Hg1-C19-C20	104.5(3)
O2-C21	1.455(7)	C19-Hg1-Br1	117.8(1)
C21-C22	1.52(1)	C19-Hg1-Br2	110(1)
Hg1-C19	2.224(5)	Br2-Hg1-Br2'	87.85(2)
Hg1-Br1	2.5784(6)	P1-C19-C20-O1	35.3(7)
Hg1-Br2	2.8088(6)		

Table 3.3.23: Selected bond geometries for complex **12** (Sym. code: 1-x, 1-y, -z).

Bond	Length (Å)	Atoms	Angle (°)
P1-C1	1.787(9)	P1-C19-C20	115.7(7)
P1-C7	1.79(1)	C19-C20-O1	124.6(9)
P1-C13	1.796(9)	C19-C20-O2	111.2(8)
P1-C19	1.78(1)	O1-C20-O2	124.1(9)
C19-C20	1.49(1)	O2-C21-C22	111(1)
O1-C20	1.22(1)	P1-C19-Hg1	111.2(5)
O2-C20	1.32(1)	Hg1-C19-C20	107.2(6)
O2-C21	1.47(1)	C19-Hg1-Cl1	104.4(3)
C21-C22	1.38(2)	C19-Hg1-Cl2	148.2(3)
Hg1-C19	2.159(9)	Cl1-Hg1-Cl1'	90.08(7)
Hg1-Cl1	2.648(2)	P1-C19-C20-O1	-44(1)
Hg1-Cl2	2.352(3)		
		P1-C19-Hg2	113.5(5)
Hg2-C19	2.25(1)	C19-Hg2-Cl8	130.8(4)
Hg2-Cl8	2.569(9)	C20-C19-Hg2	105.5(7)

Table 3.3.24: Selected bond geometries for complex **13** (Sym. code: 1-x, 1-y, -z).

Bond	Length (Å)	Atoms	Angle (°)
P1-C1	1.805(7)	P1-C19-C20	114.0(5)
P1-C7	1.811(6)	C19-C20-O1	125.0(6)
P1-C13	1.799(6)	C19-C20-O2	111.4(6)
P1-C19	1.786(6)	O1-C20-O2	123.6(6)
C19-C20	1.472(9)	O2-C21-C22	114.1(7)
O1-C20	1.216(8)	P1-C19-Hg1	111.3(3)
O2-C20	1.348(7)	Hg1-C19-C20	102.3(4)
O2-C21	1.460(8)	C19-Hg1-I1	128.8(2)
C21-C22	1.45(1)	C19-Hg1-I2	110.8(2)
Hg1-C19	2.275(7)	I1-Hg1-I1'	90.46(1)
Hg1-I1	2.8030(5)	P1-C19-C20-O1	-24.0(8)
Hg1-I2	2.7349(5)		
Hg2-I1	2.820(7)	I1-Hg2-I3	110.3(3)
Hg2-I3	2.70(1)	I1-Hg2-I1'	91.2(2)

Tables 3.3.22, 3.3.23, 3.3.24 list key bond parameters for complexes **11**, **12** and **13**, respectively. The mercury atoms in complexes **11-13** are sp^3 hybridised and as such exhibit tetrahedral geometry. In all cases the distance between the mercury atoms of the dimer unit is greater than twice the ionic radii for a 4-coordinate Hg^{2+} ion (2.20 Å),[44] indicating that no bond between the mercury atoms is present.

The Hg-C, Hg-Cl bond lengths are markedly shorter in **12** when compared with the corresponding BPPY complex (Hg-C, 2.208(8) Å, Hg-Cl(μ), 2.710(2) Å, and Hg-Cl, 2.417(3) Å). A similar situation is found for complex **13** and the equivalent BPPY-Hg(II) dimer, with the exception being the terminal Hg-I bond (Hg-C, 2.31(1) Å, Hg-I(μ), 3.010(1) Å, and Hg-I, 2.705(1) Å). These disparities can be attributed to the greater electron withdrawing properties the EPPY ligand with respect to BPPY.

The C-coordination of EPPY to Hg(II) is in stark contrast to the O-coordination of ABPPY to mercury.[23] The difference in coordination mode between ABPPY and EPPY to Hg(II) can be rationalised in terms of the electronic properties and steric requirements of the ylides. The nucleophilicity of the carbanion in ABPPY is less than for EPPY, this is due to the additional delocalisation of the ylide electron density in ABPPY which is facilitated by the second carbonyl group. This will reduce the propensity of ABPPY to bind via the ylidic carbon. The preferred coordination mode of the ylide molecules to mercury is via the ylidic carbon,[32, 34] but steric hindrance around the metal centre or the ylidic carbon will necessitate O-coordination. Indeed, this trend is reflected here, both BPPY and EPPY are marginally less sterically demanding than ABPPY and are both C-coordinated to Hg(II).

3.4 Conclusion

In this chapter the crystal structures of selected salts and complexes of three phosphorus ylide compounds have been discussed. The phosphorus ylides in question include the popular benzoylmethylenetriphenylphosphorane (BPPY), α-acetyl-α-benzoylmethylenetriphenylphosphorane (ABPPY), and the not so well known ylide carbethoxymethylenetriphenylphosphorane (EPPY). Each of these ylides is α-stabilised by a carbonyl group positioned next to the carbanion, enabling resonance delocalisation of the ylidic electron density.

The crystallographic study of the dicarboxylic salts and co-crystals of BPPY highlighted that the fumaric and terephthalic acid co-crystals could have potential applications as reagents for the Wittig reaction. These materials have considerable advantages over conventional reagents, in that they are easily handled and are expected to demonstrate enhanced reactivity. The stability of these materials can be attributed to the α-stabilisation of the ylide, and the complex network of strong and weak interaction that support the crystal structure.

The ylides BPPY and ABPPY have been shown to form stable O-coordinated complexes with uranium(VI), these complexes represent the first examples of uranium-ylide complexes in which the uranium metal is present in the (VI) oxidation state. The coordination chemistry of uranium

is diverse, and understanding the bonding behaviour of the various oxidation states of this metal is of paramount importance to the nuclear waste industry.

The C-coordinated EPPY mercury(II) halide complexes have also been presented herein. This study is complementary to work already present in the literature. The interest in mercury-ylide complexes has been primarily driven by the search for ylide materials with improved reactivity and stability; mercury-ylide compounds promise to fulfil both these requirements.

The ylide materials that have been central to the work reported in this chapter have the potential to interact and bind with metal centres via several coordination modes. It may have been expected that the nucleophilicity the carbanion would encourage the ylide to always bind via the ylidic carbon; yet, for most of the examples investigated the well-established HASB effect is found to hold true. It can been seen from this study, and from previously published work, that the bonding mode favoured will be dictated by a subtle balance between the electronic requirements and the steric demands of both the ylide and metal atom.

3.5 References

[1] McNaught AD, Wilkinson A, *IUPAC Compendium of Chemical Terminology*, 2nd Ed. (1997)

[2] Kolodiazhnyi OI, *Tetrahedron*, Report Number 389, **52**, 1855 (1996)

[3] Kalyanasundari M, Panchanatheswaran K, *Acta. Cryst.* **C50**, 1738 (1994)

[4] Antipin M Yu, Struchkov Yu T, *Zh. Struckt. Khim. (Russ.)(J.Struct.Chem)*, **25**, 122 (1984)

[5] Allen FH, *Acta. Cryst.* **B58**, 380 (2002)

[6] Mariyatra BM, Panchanatheswaran K, Goeta AE, *Acta. Cryst.* **E58**, o807 (2002)

[7] Mariyatra BM, Kalyanasundari B, Panchanatheswaran K, Goeta AE, *Acta. Cryst.* **E59**, o255 (2003)

[8] Mariyatra BM, Panchanatheswaran K, Goeta AE, *Acta. Cryst.* **E58**, m694 (2002)

[9] Platts JA, Howard ST, Woźniak K, *J. Chem Soc., Chem. Commun.* 63 (1996)

[10] Platts JA, Howard ST, *J. Chem Soc., Perkin Trans. 2,* 2241 (1997)

[11] Batsanov AS, Davidson MG, Howard JAK, Lamb S, Lustig C, *J. Chem Soc., Chem. Commun.* 1791 (1996)

[12] Yufit DS, Howard JAK, Davidson MG, *J. Chem Soc., Perkin Trans. 2,* 249 (2000)

[13] Albanese JA, Staley DL, Rheingold AL, Burmeister JL, *Acta. Cryst.* **C45**, 1128 (1989)

[14] Falvello LR, Fernández S, Navarro R, Pascual I, Urriolabeitia EP, *J. Chem Soc., Dalton Trans.* 763 (1997)

[15] Vicente J, Chicote MT, Fernandez-Baeza J, Martin J, Saura-Liamas I, Turpin J, Jones PG, *J. Organomet. Chem.* **331**, 409 (1987)

[16] Kalyanasundari M, Panchanatheswaran K, Robinson WT, Wen H, *J. Organomet. Chem.* **491**, 103 (1995)

[17] Kalyanasundari B, Panchanatheswaran K, Parthasarathi V, Robinson WT, *Bull. Chem. Soc. Jpn.* **72**, 33 (1999)

[18] Hon Y-S, Lee C-F, *Tetrahedron*, **56**, 7893 (2000)

[19] Lide DR, *CRC Handbook of Chemistry and Physics*, 74th Ed., (1994)

[20] Speziale AJ, Ratts KW, *J. Am. Chem. Soc.*, **85**, 2790 (1963)

[21] Antipin M. Yu, Sal'nikova TN, Kalinin AE, Struchkov Yu.T, Aladzheva IM, Mastryukova TA, Kabachnik MI, *Zh.Strukt.Khim.* **19**, 873 (1978)

[22] Antipin M. Yu, Kalinin AE, Struchkov Yu.T, Aladzheva IM, Mastryukova TA, Kabachnik MI, *Zh.Strukt.Khim.* **20**, 473 (1979)

[23] Laavanya P, Venkatasubramanian U, Panchanatheswaran K, Krause Bauer JA, *J. Chem Soc., Chem. Commun.* 1660 (2001)

[24] Arzoumanian H, Baldy A, Lai R, Odreman A, Metzger J, Pierrot M, *J. Organomet. Chem.* **295**, 343 (1985)

[25] Nishitama H, Itoh K, Ishii Y, *J. Organomet. Chem.*, **87**, 129 (1974)

[26] Petragnani N, Castellanos LT, Wynne, KJ, Maxwell W, *J. Organomet. Chem.*, **55**, 295 (1973)

[27] Spencer EC, Mahimaidoss BM, Howard JAK, Panchanatheswaran K, *Acta. Cryst.* **C60**, o839 (2004)

[28] Mahimaidoss BM, Spencer EC, Panchanatheswaran K, Howard JAK, *Acta. Cryst.* **E60**, o162 (2004)

[29] Mahimaidoss BM, Spencer EC, Panchanatheswaran K, Howard JAK, *Acta. Cryst.* **E60**, o123 (2004)

[30] Wilson AJC, *International Tables for Crystallography, Volume C.*, IUCr. (1992)

[31] Dunitz JD, *X-ray Analysis and the Structure of Organic Molecules*, p339, Ithaca: Cornell Univ. Press. (1979).

[32] Lledós A, Carbó JJ, Urriolabeitia EP, *Inorg. Chem.* **40**, 4913 (2001)

[33] Lledós A, Carbó JJ, Navarro R, Urriolabeitia EP, *Inorg. Chim. Acta*, **357**, 1444 (2004)

[34] Pearson RG, *J. Am. Chem. Soc.*, **85**, 3533 (1963)

[35] Navarro R, Urriolabeitia EP, *J. Chem Soc., Dalton Trans.* 4111 (1999)

[36] Belluco U, Michelin RA, Bertani R, Facchin G, Pace G, Zanotto L, Mozzon M, Furlan M, Zangrando E, *Inorg. Chim. Acta*, 355 (1996)

[37] Alcock NW, Roberts MM, *Acta Cryst.*, **C34**, 476 (1987)

[38] Rickard CEF, *Acta Cryst.*, **E57**, m446 (2001)

[39] Russell AA, Meline RL, Duesler EN, Paine RT, *Inorg. Chim. Acta*, **231**, 1 (1995)

[40] Ruikar PB, Nagar MS, *Polyhedron*, **14**, 3125 (1995)

[41] Navaza A, Charpin P, Vigner D, Heger G, *Acta Cryst.*, C47, 1842 (1991).

[42] Alcock NW, Flanders DJ, *Acta Cryst.*, **C43**, 1267 (1987)

[43] Baenziger NC, Flynn RM, Swenson DC, *Acta Cryst.*, **B34**, 2300 (1978)

[44] Shannon RD, *Acta Cryst.*, **A32**, 751 (1976)

Chapter 4

Literature Evaluation: Coordination Polymers and Gas Storage Materials

---

4.1 Introduction

The second part of this thesis is concerned with crystallographic structural studies of gas-loaded Zn_4O(1,4-benzenedicarboxylate) (Zn_4O(BDC)). As an introduction to this work, an evaluation of the relevant literature is presented in this chapter.

The compound Zn_4O(BDC) possesses an infinite three-dimensional framework structure and is a member of a class of materials popularly known to as coordination polymers (3-D structures are occasionally referred to as metal organic frameworks (MOFs)). This introductory chapter is sub-divided into several sections, the first of which (Section 4.1.1) provides the reader with a brief insight into the nature of coordination polymers focusing on their structural features rather than their preparation; for the interested reader several articles providing excellent reviews of the more recent developments in the field of coordination polymer chemistry have been published.[1-4]

The possible applications for coordination polymers will be discussed in Section 4.1.2, providing a prelude to a more detailed review of gas-storage materials, a role for which coordination polymers, such as Zn_4O(BDC), can be considered as viable candidates (Section 4.1.3). The structural attributes and gas absorption properties of Zn_4O(BDC) are highlighted in Section 4.1.4, and this precedes the more general discussion of metal-BDC coordination polymers that is offered in Section 4.1.5. Finally, in Section 4.1.6, techniques used to identify absorption sites in gas-loaded coordination polymers will be reviewed. In particular, examples of X-ray diffraction work that complements the research reported in later chapters will be presented.

4.1.1 Coordination polymers

To date no precise definition[§] of the term 'coordination polymer' has been agreed, so in the context of this thesis it will be assumed to encompass inorganic compounds that comprise repeat units of metal complexes, covalently linked by one or more organic species, into macromolecules of infinite length that extend in one or more dimension(s). Of particular interest are coordination polymers that extend in three-dimensions to form framework, or net, structures. The first examples of 3-D framework structures were reported by Abrahams, Hoskins, Robson and co-workers in the early 90s, and were composed of transition metal nodes (zinc, cadmium or copper) with either cyanide or organic-nitrile links.[5-8] This pioneering work laid the foundations for research into the preparation and characterisation of 3-D coordination polymers, and paved the way to the development of more elaborate structures.

Since then, a large number of framework systems exhibiting a variety of structural features have been reported. The diversity in these structures has been introduced, purposely or serendipitously, by modification of the following framework properties:

(i) *Type and oxidation state of the metal species* – the vast majority of molecular frameworks incorporate transition metals at the nodal points, however a select number of lanthanide based systems have been created.[9-13] The oxidation state of the metal can be adjusted to alter the electronic proprieties, or the topology, of the framework. Hybrid systems containing metal centres in different oxidation states have also been prepared.[14]

(ii) *Type of organic linker molecules* – the selection of organic linker available for the construction of framework systems is limited only by the chemist's imagination. By prudent choice of the organic component(s), the required physical and chemical properties can be imparted to the framework. For this reason, an assortment of different ligands have been employed in the preparation of molecular frameworks, such as carboxylates,[15] pyridyl bases,[16-18] silanes,[19] phosphanes,[20] porphyrins,[21] and amines.[22]

(iii) *Pillaring* – framework structures that comprise more than one type of organic liker maybe pillared. In this case, two-dimensional sheets formed exclusively by one organic ligand and the metal ions are connected in the third dimension by a second organic linker acting as a 'pillar'.[23-25]

[§] *Id est.* a definition accepted by the International Union of Pure and Applied Chemistry (IUPAC).

(iv) *Framework topology* – the topology of a framework can be defined as the geometric configuration of the linker molecules and metal ions/clusters (nodes). The topology is influenced by the type of metal ions (and their oxidation state, as this affects the metal's coordination geometry) and organic ligands used, and by the reaction conditions employed during synthesis.[26]

(v) *Catenation (interpenetration and interweaving)* – framework structures possessing large cavities and relatively small nodes can inter-grow during synthesis. [27-30] Hypothetically speaking, the frameworks can only be separated by the breaking of covalent bonds. In the case of interpenetration two or more frameworks are inter-locked in such away as to be maximally displaced from each other. Conversely, interweaved frameworks are infinitely enmeshed in a manner such that nets are minimally displaced from each other. Batten and Robson have published a comprehensive review of catenation in nets, and this article provides a superb introduction to the subject.[31]

Perhaps the most fundamentally important property of a framework structure is the degree of porosity that it exhibits. A structure is said to be porous if the framework can be evacuated yet retain its structural integrity. The porosity is controlled by a subtle balance between a number of factors such as the framework charge and topology, the degree of catenation, and the size and structural stability of the nodal and linker components.

A number of design strategies that involve alterations to the size, shape, and chemical functionality of the framework cavities, have been implemented in an attempt to tailor-make structures with desirable properties. Although there are some examples of small molecules such as anions and solvent influencing the final topology of framework structures,[32-32] their practical use as tools for designing network materials is limited. This limitation arises because the way in which these molecules control the growth of frameworks is poorly understood and not easily controlled. There have also been reports of the cavities being modified *post* framework construction,[35,36] however, this method of design has not been widely exploited.

The most logical design approach is based on the principles of supramolecular chemistry. In this strategy, the required framework architecture is conceptually broken down into its constituent parts and suitable chemical motifs are then identified as 'building blocks' from which the

framework can be synthesised[‡] (Fig.4.1.1). This approach differs from supramolecular chemistry in that only the formation of *covalent* bonds is considered in the design strategy (i.e. intermolecular interactions are not included), it also different from retrosynthesis in that the molecular synthons retain their individual structures during the synthesis of the framework.[26,37-43]

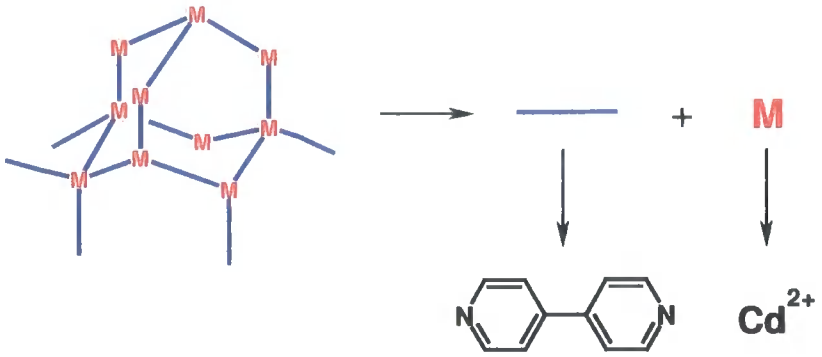

Figure 4.1.1: Simplistic representation of the design strategy for a framework with a diamond topology (left). The structure can be regarded as being composed of linear linker molecules (—) coordinated to metal ions (M) with tetrahedral coordination geometry. The chemical precursors for this structure may be the linear 4,4'-bipyridine ligand and a metal species that typically adopts a tetrahedral geometry such as Cd(II) or Zn(II).

Much emphasis has been placed on developing coordination polymers that have a ridged non-flexible structure in the belief that this is necessary for framework stability in the absence of adsorbed guests/solvent (i.e. porosity). More recently there has been growing interest in deliberately developing framework structures that exhibit structural flexibility and undergo some form of deformation/expansion,[44-49] or structural rearrangement [50,51] in response to a guest species. The most successful materials in this respect have taken advantage of the intrinsic flexibility of intermolecular contacts such as hydrogen bonds. In these cases, the covalently bonded coordination polymer only extends in 1- or 2-dimensions and a 3-dimensional structure is constructed through weaker interaction between the polymer entities (normally 1-D 'chains' or 2-D 'sheets').[44-47,52]

[‡] This design strategy has been termed 'reticular synthesis' by Yaghi and co-workers (see references given in the main text). However, as this terminology has not been widely accepted it will not be use here.

4.1.2 Applications

In this section a range of possible applications for coordination polymers will be reviewed. Many of the practical uses highlighted stem from the exceptional porosity and chemical variations that can be incorporated into these materials allowing them to be customised to fulfil specific functions.[53,54]

Catalysis

Coordination polymers are well suited as catalysts for reactions that occur under mild conditions (< 300°C), unfortunately they tend to lack the thermal stability to enable their use under harsh reaction conditions. It has been suggested that these materials may be suitable as enantioselective catalysts. Although several chiral polymer materials have been reported,[55-58] very few practical examples of their use have been published; Seo and co-workers demonstrated that a chiral metal dicarboxylate polymer could successfully catalyse a transesterification reaction within the framework cavities with a low enantiomeric excess of ~8%, with the dominant isomer being dictated by the handedness of the framework.[59]

Perhaps a more profitable future for coordination polymers is as conventional catalysts. Indeed, various metal dicarboxylate polymers have been shown to catalyse the hydrogenation of olefins exceptionally well.[60-62] Moreover, Cu(II) dicarboxylate polymers have been identified as the catalytically active species in the Cu(II)-catalysed oxidation of carboxylic acids.[63] It has also been reported that lanthanide phosphate polymers can catalyse the cyanosilylation of aldehydes and the ring opening of carboxylic anhydrides.[64]

Separation & purification of Gases and Solvents

Coordination polymers can be optimised chemically and electronically to enable them to act as efficient molecular sieves. The size selectivity of the 2-D network formed by Cd(II) and 4,4'-bipyridine has been exploited to separate dibromobeneze isomers, a procedure that is difficult using conventionally means (e.g. fractional distillation) due to similar chemical and physical properties of the ortho-, meta- and para- isomers.[65]

Guest selectivity can be enhanced further by incorporating unsaturated metal centres (USCs) into a coordination polymer. 3-D frameworks containing USCs have been created, and have been shown to display electronic, as well as size, selectivity towards guest species.[66] Such materials have been used to separate solvents by selective uptake mechanisms.[67-70] The USCs can be

generated by including labile ligands in the coordination sphere of the metal centres during the synthesis of the coordination polymer. These ligands can then be removed from the final framework architecture by controlled heating.

Titanium silicates are well-known molecular sieving materials that are being used by industry for methane purification on a multi-ton scale.[71] The reason these materials are so successful is because the pores of their framework structures can be tuned to the ideal size to efficiently 'filter' contaminants such as nitrogen and water from the methane gas stream. This would suggest that metal organic coordination polymers would be suitable candidates for gas purification/separation, as the size and shape of their channel systems can be adapted with relative ease.[72,73] One of the most extensive studies has been conducted using Cu(II) benzene-1,3,5-tricarboxylate.[72] This highly porous material can synthesised on a large scale and is exceptionally good at selectively absorbing various gases in the presence of others, and as such may find practical use in cleansing industrial waste streams or in air purification systems.

Sensors

Coordination polymers display a diverse range of physical properties such as magnetism,[74-76] and guest-dependant spin crossover,[77] that may indicate their suitability as sensor materials, but perhaps the most attractive contenders for use as chemical sensors are coordination polymers constructed using lanthanide metals.

The preparation of lanthanide coordination polymers is notoriously difficult as the high coordination numbers adopted by f-block metals inhibits directional control of the polymer growth; nevertheless, a few lanthanide-based polymers have been reported.[9-13] Investigations into the properties of lanthanide framework polymers have demonstrated that these materials are capable of generating guest-dependent luminescence. Hitherto work has been limited to studying the influence of small organic guest molecules on the quantum yield and lifetime of the emitted radiation, rather than the host-guest interactions.[78,79] Nonetheless, these initial studies have shown that there is scope for the development of these materials for sensor applications.

The viability of coordination polymers for use as gas-storage materials has been the subject of debate in recent years, and it is this issue that is of specific interest to the work to be presented in the following chapters. For this reason, a brief review of the challenges and achievements in this thriving field of research is deemed appropriate and is the subject of the next section.

4.1.3 A review of gas-storage media

The technology exists, in the form of fuel cells, to convert stored chemical energy directly into electrical energy with high efficiency.[80] The majority of these extraordinary cells generate electrical energy by the oxidation of hydrogen, or in some specialist cases, carbon monoxide. The by-product of this reaction is pure water, meaning that fuel cells have a significant environmental advantage over the more conventional combustion engine, or batteries. Moreover, gravimetrically speaking, hydrogen gas (at 20 MPa) has an energy density approximately three times that of petrol, and forty times that of a lead-acid battery.[81]

One can envisage such lightweight fuel cells being commercial available in portable electronic devices such as mobile phones, laptop computers and power tools. Yet, for the many manufactures and researchers developing fuel cell technology, the primary objective is to create a fuel cell system that would be of practical, and economic benefit, to the vehicle industry.[82] The two principal factors that are hindering progress towards this goal are (i) the cheap and ecologically sound production of hydrogen, and (ii) the storage of the fuel gas.

Hydrogen is the most abundant element in the Universe and on Earth. The vast majority of hydrogen on Earth is chemically bound in water, and considerable effort has been directed towards liberating elemental hydrogen gas from this readily available and cheap resource. Thermal dissociation of water requires harsh conditions, 2,000 °C with a Pt/Ru catalysis; an alternative is the steam reformation of hydrocarbons, which produces CO_2 as a by-product. Neither of these methods is environmentally desirable, and negates the benefit of using fuel cells in the first place. However, there has been considerable success in developing photovoltaic cells that use sunlight to split water photochemically, and this advancing technology is offering a way to meet the future demands of the fuel cell and vehicular industries.[83]

It is the second of these two problems, the fuel storage issue, which is of key interest to the project work to be presented in this thesis. For an electric car with a fuel cell approximately 4kg of hydrogen is required to cover the same range as a car with a conventional combustion engine that uses petrol. Conventionally, hydrogen is stored under higher pressure, ~200 bar, but due to its low-density 4 kg of hydrogen gas, even at this pressure, would occupy 225 litres.[84] It is obvious that this creates a considerable problem for the automobile industry – where do you place the heavy and bulky container necessary to contain this volume of gas? In addition to this, carrying compressed gas onboard a car raises serious safety issues, particularly if that gas

happens to be highly flammable like hydrogen. Indeed, in some countries such as Japan, vehicles using such technology are prohibited on the public highways.

Attempts have been made to eliminate this gas-storage problem by using liquid alcohol or hydrocarbon fuels as a hydrogen source for fuel cell use, but the significant disadvantage is that these fuels require some form of pre-processing system to be incorporated into the fuel cell arrangement in order to liberate the chemically bound hydrogen. This increases the expense and bulk of the device, as well as lowering its efficiency. The most promising solution to this fundamental problem is to store the fuel gas in an absorbent material, and hence increase the mass of gas that can be stored per unit volume of the storage container (i.e. to increase the gas density).

The US Department of Energy (USDoE) has set targets for on-board hydrogen storage systems that must be achieved if hydrogen is to be considered as a feasible fuel for cars.[85] The most important, but also the most challenging of these goals, is to obtain a gravimetric capacity of 4.5 wt.% for the gas-storage system (to rise to 9 wt.% by 2015), volumetrically this equates to 720 ml H_2 (STP)/g. For methane, the working target is determined by the 'delivery' (the volume of gas that is released from the absorbent when the pressure is reduced from the storage pressure to 1.0 bar). The USDoE has set a delivery target figure of 150 v/v for a system working at 35 bar and 25 °C.

Many materials have been investigated as potential gas-storage media, and a brief review of the most promising candidates will now be presented. As the development of materials for hydrogen storage has been running concurrently with research into methane storage, also for use as an 'alterative fuel', materials for storing both gases will be discussed.

Activated carbonaceous materials (ACMs)

Activated carbon materials have received considerable attention as potential methane storage media,[86,87] and to a lesser extent for hydrogen storage.[88,89] These absorbents are carbon materials that have undergone some form of activation process, either chemical or physical, to remove some of the carbon atoms, to produce a porous material. A variety of different carbon sources have been investigated as precursors for ACMs with varying degrees of success, these include carbonised peach pits,[90] waste tires,[91] coconut shells, pinewood,[92] and coals (both

anthracite and bituminous forms).[93] Several factors have been found to influence the gas-storage suitability of a given ACM and these are briefly discussed below†:

(i) *The micro-porosity of the material* – there is a linear relationship between the degree of micro-porosity (pores < 20 Å) of the ACM and amount of gas absorbed. The development of meso-pores (20-500 Å) and macro-pores (> 500 Å) should be avoided, as these pores do not absorb gases.

(ii) *The pore size distribution (PSD)* – it has been determined experimentally that to optimise the gas uptake the ACM should have a narrow pore size distribution centred on the ideal pore size for the gas in question. For methane this ideal value is ~8 Å and for hydrogen is it <7 Å (precise value unknown).[88,94]

(iii) *Minimum pore size* – although micro-porosity is to be encouraged in ACMs, decreasing the pore size much below the ideal value can reduce the delivery value as the gas becomes too tightly bound in the pores and is retained when the pressure is reduced to 1.0 bar.[86]

(vi) *Density* – to optimise the delivery value for a given ACM the density should be as high as possible without causing gas diffusion problems.

(v) *Heat of absorption* – a notable amount of heat is produced when gas is absorbed by an ACM (i.e. exothermic process). Equally, desorption is an endothermic process and energy is required to release the absorbed gas. ACMs with low isosteric heat of absorption would be preferable.[86]

(vi) *Heat Capacity/thermal conductivity* – this is closely related to point (iv) above. The absorption capabilities of an ACM is reduced as the temperature rises, it is therefore necessary for an ACM to have a high heat capacity and good thermal conductivity.[86]

(vii) *Hydrophilicity* – the absorption of water by an ACM drastically reduces its gas absorption capacity. Therefore this parameter should be minimised.

There is little that can be done to improve the heat of absorption, heat capacity, thermal conductivity and hydrophilicity of an ACM, as these properties are intrinsic to carbon. However, the properties noted in points (i) to (iv) can be altered by adjusting the activation procedure and the physical form of the final ACM.

† Note: The gas interaction within ACMs is physical absorption only.

The activation of the carbon in the manufacture of ACMs is usually by chemical treatment either with phosphoric acid or potassium hydroxide followed by pyrolysis and washing. Detailed investigations into the nature and effects of the activation procedure on the final ACM product have been performed, and are well-documented elsewhere.[87,94] Suffice it to say that fine-tuning of the activation procedure is necessary to achieve the highest possible micro-porosity, without substantially increasing the macro- and meso-porosity and the PSD. Equally, a balance must be attained between the degree of micro-porosity and the density, for which an inverse relationship exists (i.e. increased micro-pore volume decreases the density).

The most popular method for increasing the density and improving the mechanical properties of a given ACM without impinging on the micro-porosity is compression of the ACM into monoliths in the presence of a binder, usually some form of polymer material, to help agglomerate the powdered material and minimising useless void space.[95] Again, a balance must be reached to ensure that the binder concentration is high enough to improve sufficiently the density of the ACM, but not too high so as to notably block the pores. Additionally, a low concentration is preferable as the binder does not actively store gas (although one exception to this has been reported [96]), but it does contribute to the volume of the absorbent, thus lowering the delivery value of the ACM. It is worth noting that good delivery values have been achieved using activated carbon fibres (ACFs) that have a naturally higher density than normal ACMs. However the higher micro-porosity and lower PSD of the ACMs counteract this advantage, resulting in both materials having similar delivery values of ~145 v/v.[93] Furthermore, ACFs are markedly more expensive to manufacture than ACMs.

Notwithstanding the complexity associated with optimising ACMs for gas-storage purposes, these materials have shown remarkably high storage capabilities, and realistically the USDoE targets for methane storage can be met using ACMs. The highest delivery value reported to date is ~145 v/v representing 97% of the USDoE target.[87] Interestingly, the best binder-ACM composite has a delivery of only 126 v/v.[95] In terms of hydrogen storage, the potential of ACMs is less promising, with the maximum uptake reported being only 238ml (STP)/g, ~33% of the USDoE target.[89]

Nanostructures

Single- and multi-walled carbon nanotubes (SWCNTs and MWCNTs) have attracted much interest as potential hydrogen storage media.[97] SWCNTs are hollow tubular carbon structures

with typical diameters in the nanometer range (~1-20nm) and lengths in the range of ~100nm to several microns. The surface of the tube has a graphitic hexagon structure.[98] MWCNTs are similar to SWCNTs, but as the name suggests, there are several hexagon sheets wrapped around the tube in concentric layers to give a 'multi-walled' nanotubular structure.[99] Both forms may be 'capped' at the tips, by hemispheres of carbon hexagons and pentagons, or they may remain 'open'. Capped tubes can be opened by treatment with a strong mineral acid, or by oxidation processes.

The impetus for investigating carbon nanotubes (CNTs) for gas-storage applications was provided by Dillon *et al.* in 1997.[100] This group reported an extraordinarily high hydrogen uptake by CNTs of ~5-10 wt.% after exposure to H_2 at pressures less than 1.0 bar and near room temperature. Since this report, the gas-storage capabilities of CNTs has become a contentious issue. The experimental findings of Dillon *et al.* are yet to be corroborated, although hydrogen uptakes of 4.2 wt.% (at RT and 10 MPa) [101] and 8 wt.% (at 80 K and 40 bar) [102] have been reported for SWCNT. Contrary to these findings, there are numerous experimental reports recording uptake values less than 2 wt.%.[103-105]

It is likely that much of the controversy surrounding CNTs stems from the diverse range of pre-treatment methods, purities and physical characteristics of the samples being used for gas uptake measurements. Physically, CNTs vary in length, diameter distribution, defects, bundle size, and orientation, all of which are difficult to control. How these different physical parameters affect the hydrogen uptake has not been systematically investigated, although some workers are attempting to rectify this oversight.[104] The purity of the sample is of particular importance. CNT samples are often contaminated with metallic particles due to their preparation and/or treatment methods, it has been suggested that these make no difference to the overall gas uptake,[101,105] but there are reports admonishing these claims.[106-108]

Chen and co-workers suggested that lithium and potassium doped CNTs could absorb an impressive 20 wt.% and 14 wt.% of hydrogen under moderate (200-400 °C) or ambient conditions respectively.[109] However this claim was later refuted by Yang, who demonstrated that the high gravimetric uptake was due to the formation of alkali hydroxides caused by moisture contamination in the hydrogen gas stream used for the measurements.[110] Using dry hydrogen gas, Yang showed that the uptakes for lithium and potassium doped CNT are actually

2.5 wt.% and 1.4 wt.%, respectively. Theoretical simulations performed by Zhu *et al.* support Yang's results.[111]

Theoretical modelling of the hydrogen absorption by CNTs has been a flourishing area of research. As with experimental researchers, the opinion among theoreticians as to the potential of CNTs as suitable gas-storage media is also divided. An optimistic view is held by Yin *et al.* who calculated that open and closed CNTs with a diameter of 6 Å can successfully hold 33 wt.% of hydrogen.[112] The hydrogen molecules ware shown to be absorbed physically in the interstitial spaces (~30 Å) between the tubes, so-called exohedral absorption. The importance of exohedral absorption has been indicated by the theoretical modelling of methane uptake by CNTs performed by Cao *et al.*[113] This group calculated that under optimum conditions (tube spacing of 8 Å, RT and 4.1 MPa), a methane storage capacity of 216 v/v could be reached, a value that is higher than for ACMs. The concept of exohedral absorption is supported by experimental work reported by Ye *et al.*[102] Open single-walled carbon nanohorns (SWCNHs), which are structurally similar to SWCNTs but with a 'pointed tip' at one end, reportedly can absorb 160 v/v of methane gas at 3.5 MPa and 303 K, and again, absorption in the interstitial channels was deemed to be important.[114] Conversely, investigations conducted by Talapatra *et al.* using Xe, CH_4 and Ne lead these authors to conclude that gases do not absorb in the interstitial channels of CNT bundles,[115] although the same authors later published additional data supporting the exohedral absorption theory.[116]

Equally positive results have been presented by Zhang and co-workers who calculated gravimetric hydrogen absorption capacities as high as 7.1 wt.% for arrays of CNT with a diameter of 27.2 Å at 77 K and 4 MPa. In this case the physical absorption was postulated to occur both within the tubes (endohedral) and within the interstitial spaces.[117] A hydrogen storage capacity of 14 wt.% for SWCNTs has been calculated Lee *et al.*[118] Surprisingly the authors have identified two chemisorption sites for the hydrogen, the first exohedral and the second endohedral. Although hydrogen chemisorption has been suggested for MWCNTs samples incorporating metallic particles,[106] it seems unlikely that such materials would not find practical application as gas-storage materials due to difficulty in releasing the absorbed gas. Gauy *et al.*[108] and Wang *et al.*,[119] have a more pessimistic view towards the gas-storage capabilities of CNTs. In their molecular simulations the calculated gravimetric hydrogen uptake values did not indicate a positive future for CNTs as gas-storage media.

Boron nitride (BN) nanostructures have also been investigated as gas-storage compounds. Theoretical studies have shown that the clusters $B_{60}H_{60}$, $B_{36}H_{36}$ and $B_{24}H_{24}$ have hydrogen storage capacities of 4.9, 4.3 and 2.9 wt.%, respectively.[120] Experimental measurements of the gravimetric hydrogen uptake by BN clusters (between 20-300 °C, and at 1.0 bar) have recorded values similar to those theoretically predicted.[121,122] BN nanotubes have been shown to absorb up to 2.6 wt.% of hydrogen at RT under 10 MPa of pressure.[123] The gas was found to chemisorb, with ~70% of the absorbed gas being retained in the structure after the pressure was reduced to 1.0 bar, and this could only be released by heating the sample to 573 K. This may limit the practical use of boron nitride nanotubes for gas-storage purposes.

Calculations by Koi and Oku suggest that carbon fullerenes could store 6.5 wt.% of hydrogen.[120] These authors only considered hydrogen encapsulated within the fullerene molecules (endohydrogen) and ignored the possibility of fullerite formation (hydrogenated fullerene molecules). Schur *et al.* have extensively reviewed fullerites and have published an excellent article on the subject.[124] It was demonstrated that fullerites could support up to 7.70 wt.% hydrogen, although accessing the stored gas is somewhat problematic, as the required thermal treatment caused decomposition of the sample followed by polymerisation of the fullerene product. Moreover, the preparation of fullerites generally involves the use of expensive metal catalysis, and is by no means a simple process.

The highest absorption claim to date has been reported using graphite nanofibres (GNFs).[125,126] Graphite nanofibres are graphitic platelets (30-500 Å) that stack in ordered arrangements forming fibres. Chambers *et al.* have stated that 1.0 gram of GNFs can absorb in excess of 20 L of hydrogen at 120 atm and 25 °C, this equates to a staggering ~68 wt.% of hydrogen.[125] However it should be noted that this claim is yet to be corroborated, and theoretical simulations executed by Wang *et al.* calculated uptake values almost twenty times less than those reported by Chambers.[119]

What is apparent from the literature is that opinion remains severely divided over the use of nanostructure materials for gas-storage, and until many of the scientific and technical questions that remain are answered satisfactorily, the prospect of these materials being of use in gas-storage applications is limited. Furthermore, considerable work still needs to be done to devise methods for the economic mass production of these materials; at present CNTs and BN materials are prepared by arc discharge methods in low yields with variable purity.[121,127]

Coordination polymers

The gas-storage capabilities of this class of materials have not been so extensively investigated as in the case of ACMs or nanometerials. Nonetheless, there have been some positive results published in this area. One advantage of coordination polymers possess over nanometerials and ACMs is the ease by which their uniform pore dimensions and chemistry can be altered to suit the desired application, allowing incorporation of properties such as size selective gas sorption,[128] or pressure dependent absorption (so-called 'gate-opening' effect).[129]

Although there are some reports of gas absorption in frameworks systems employing base ligands as linker molecules,[130-132] by far the majority of reported studies have concentrated on frameworks with dicarboxylates as linkers.[62,133] The gas-storage capabilities of a variety of Cu(II),[134,135] Mo(II),[136] Ru(II,III),[14] and Ru(II) [61] dicarboxylates with the general formula $M_2(O_2CR)_4$ have been evaluated. These structures are 2-D coordination polymers, and they typically absorb 0.6-2.2 moles of gas per mole of metal depending on the cavity size and the gas in question (data recorded at ~0.03 bar and at the temperature at which the gas liquefies). By pillaring 2-D Cu(II) dicarboxylates with triethylenediamine, a 3-D network can be generated, and it has been demonstrated that by changing the dicarboxylate component the cavity size and surface area of the framework can be optimised to store 225 v/v of methane (298 K, 3.5 MPa), which is considerably more than reported for ACMs.[137,138] Alternatively, the pillar ligand can be altered to improve the cavity properties and optimise the gas-storage capacity of a particular metal dicarboxylate framework.[139]

Other storage compounds

At present hydrogen storage for vehicle use is confined to metal hydrides. These can absorb large amounts of hydrogen reversibly. The required operating conditions are dictated by the thermodynamics of the hydride formation and this depends on the initial metal alloy employed. The major failure of metal hydrides as gas-storage compounds is due to the large mass of the component metals reducing the wt.% of hydrogen that can be stored. The most popular metal hydride, $LaNi_5H_6$ holds only 1.37 wt.% of hydrogen (2.0 bar, 298 K). Other hydrides can hold more hydrogen than this, but their operating conditions make them impractical for storage applications e.g. Mg_2NiH_4 supports 3.59 wt.% hydrogen but at 555 K (and 1.0 bar).[84]
Other materials that have been implicated as gas-storage materials include nickel phosphates,[140] calixarenes,[141-143] hydrates,[144] and solvents.[145] However, before any of these materials can be realistically considered as gas-storage candidates they need to be investigated further.

4.1.4 Zn_4O(1,4-benzenedicarboxylate) (Zn_4O(BDC))

The 3-D coordination polymer that is central to the work to be reported in the following chapters is the Zn_4O(1,4-benzenedicarboxylate) (Zn_4O(BDC)) framework. Li *et al.* first prepared this material in 1999.[146] The authors demonstrated that the Zn_4O(BDC) framework is stable up to 300°C and does not collapse on the removal of solvent from the channels. Moreover, the empty cavities account for ~80% of the crystal volume, resulting in the material possessing an exceptionally low density of 0.59 gcm^{-3}.

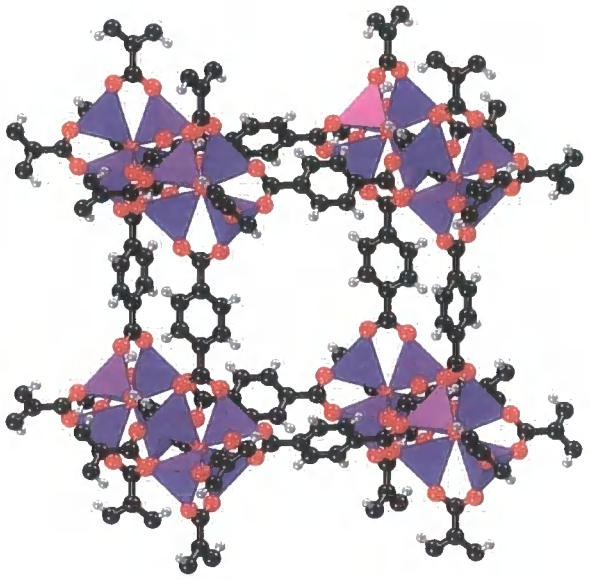

Figure 4.1.2: The Zn_4O(BDC) framework. The purple polyhedra represent ZnO_4 clusters.

The Zn_4O(BDC) framework is shown in Figure 4.1.2. The nodes of the framework structure consist of four ZnO_4 tetrahedra that share a common vertex. 1,4-benzenedicarboxylate (terephthalate) molecules act as 'struts', linking the metal clusters producing the 3-D framework. The distance between the centres of adjacent clusters is 12.94 Å. The novel ZnO_4 clusters observed in Zn_4O(BDC) have also been reported for open-framework zincophosphates and arsenates. These materials are structurally similar to Zn_4O(BDC), except that the linker molecule is either a phosphate or arsenate group.[147] These materials exhibit high thermal stability, of up to 600°C, the highest value recorded for this class of materials.

There are two types of cavity present in the Zn_4O(BDC) framework, the larger is lined with 72 carbon atoms, the smaller by 24 hydrogen atoms (Fig.4.1.3). Li *et al.* state that, after allowing for the van der Waals radii for the framework atoms, spheres with a max diameter of 15.1 Å and

11.0 Å could fit in the large and small cavities, respectively. Furthermore, a sphere with a diameter of 8.0 Å could pass freely through the window between the two cavities.

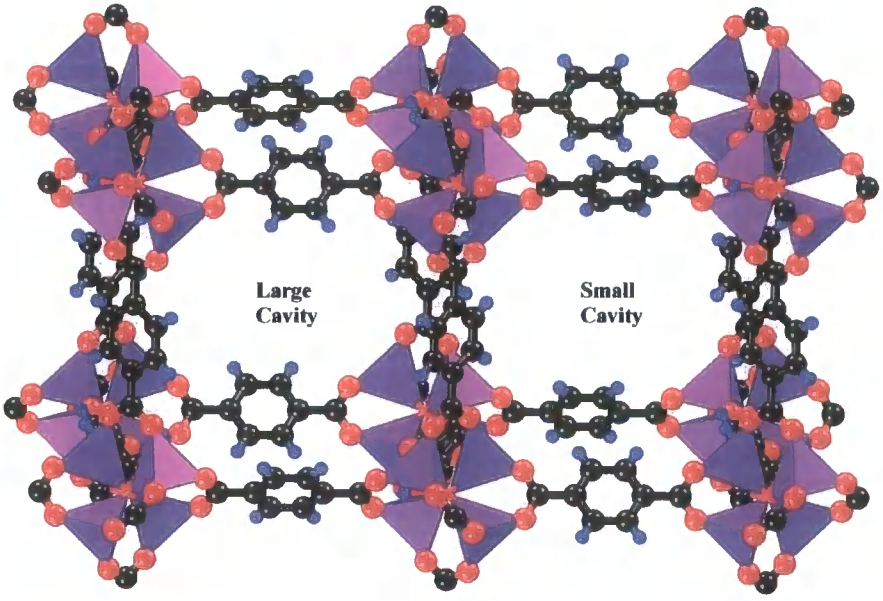

Figure 4.1.3: Diagram displaying the two cavity types present in the $Zn_4O(BDC)$ framework. For clarity the hydrogen atoms are shown in blue.

The remarkable characteristics shown by the $Zn_4O(BDC)$ framework suggest that this material has potential as a medium for gas-storage. It has been shown that $Zn_4O(BDC)$ is capable of absorbing up to 4.5 wt.% of hydrogen gas at 78 K and up to 20 bar, and this equates to ~70% of the US Department of Energy design target.[85,148] Although later, this value was revised to 1.3-1.6 wt.%.[149,150] The methane absorption capability of $Zn_4O(BDC)$ has also been evaluated by Eddaoudi *et al.* and was found to be 135 $cm^3(STP)/cm^3$ (v/v).[151] Interestingly, these authors also investigated the methane uptake by framework materials that posses the same framework topology as $Zn_4O(BDC)$, but are constructed using different dicarboxylate linker units. It was shown that by judicious choice of linker molecule the gas uptake could be optimised. This finding is of significance, as it implies that the key to the successful design of organic-metal framework materials for gas-storage applications lies in understanding the interaction of the gas with the framework structure.

4.1.5 Other metal-BDC coordination polymers

The three-dimensional α-polonium structure of $Zn_4O(BDC)$ is unique in coordination polymers, employing 1,4-benzenedicarboxylate (BDC) as the linker molecule. Several other compounds based on the combination of zinc with 1,4-benzenedicarboxylate have been synthesised, and these will be discussed in this section, along with other metal-BDC coordination polymers.[152-154] The primary aim of this section is to highlight the structural diversity that is available by using BDC as the principal organic component in metal-organic systems.

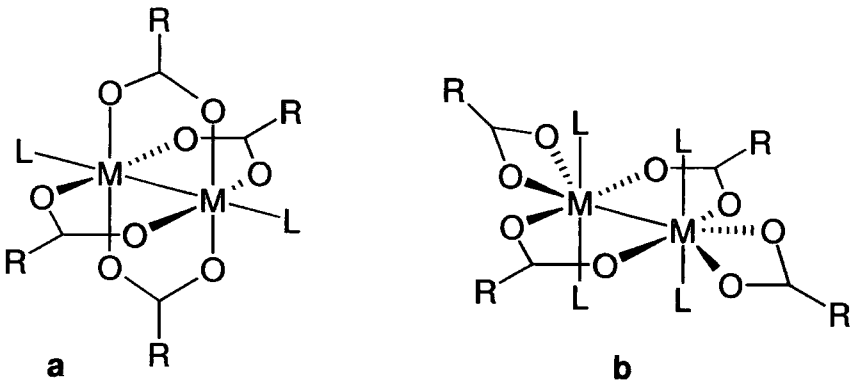

Figure 4.1.4: (a) The 'lantern-like' structure often seen in metal-BDC coordination polymers. (b) Prismatic dinuclear unit. R = benzene ring, L = additional ligand bound to the metal, M = metal site.

The most common type of metal-BDC coordination polymer contains dinuclear nodes that have been described as 'lantern-like' (Fig.4.1.4a). It is worth noting that Tao *et al.* have reported a variation on the common lantern unit for two 2-D mixed ligand coordination polymers.[155] In these complexes the dinuclear metal unit has a novel prismatic geometry (Fig. 4.1.4b).
The zinc analogue of the 'lantern' structure, Zn(BDC) (no additional ligands, 'L', are bound to the zinc), was reported by Li *et al.*[156] The dinuclear metal clusters are linked by the BDC ligands into 2-D layers that overlay each other to allow Zn···O interactions to form between adjacent layers, producing a 3-D network with 1-D channels. This material was shown to be porous with thermal stability up to 315 °C. In the same paper, the authors reported the structure of $Zn(BDC)(H_2O)\cdot(DMF)$ (where L = H_2O) which is structurally similar to Zn(BDC), but the presence of the water bound to the zinc atoms precludes the formation of Zn···O interactions between the 2-D layers. Instead, the 3-D structure is completed by hydrogen bonds between the

water molecules in one layer and the carboxylate oxygen atoms of an adjacent layer. The DMF solvent molecules reside in the framework channels.

A 2-D layer structure has been postulated as being the likely structure for Cu(BDC), Rh(BDC) and Mo(BDC).[60,136,157] The Mo(BDC) structure is thought to contain Mo-Mo quadruple bonds. Unfortunately, the structures of these materials have not been fully elucidated. In all cases the materials absorb a notable amounts of gas implying that they posses a micro-porous structure. The authors have assumed, based on magnetic data for Cu(BDC) and IR and NMR data for Mo(BDC), and the similar gas absorption behaviour of the complexes, that all these materials are isostructural with Cu(II) and Mo(II) acetate (which both have a 2-D layer structure). Whether or not this assumption is truly justified is questionable.

The structure of Ru(BDC)(Cl) is a mixed valence complex containing ruthenium atoms in both the II and III oxidation states. Again, the lantern-like dinuclear metal units and the 2-D layers are present. However, in this complex L = Cl, and the chlorine atoms form halide bridges (Ru-Cl-Ru) between adjacent layers, generating a porous covalent 3-D framework (structural determination based on Raman and far-IR data only).[14] There are examples whereby the 2-D layers comprising lantern metal-BDC units have being converted into porous covalent 3-D frameworks by the additional metal ligands ('L' in Fig.4.1.4) acting as pillar ligands between the layers.[61,137]

Perhaps the most elegant metal-BDC complex is the $Zn_3(BDC)_3{\cdot}6CH_3OH$ framework reported by Li *et al.*[67] The 'building block' for this 3-D structure is a trinuclear zinc cluster. A similar 'figure-of-eight' trinuclear zinc unit also was observed in the non-porous framework $Zn_3[(CTC)(C_5H_5N)]_2{\cdot}2(CH_3)_2NC(O)H$ where CTC = cis,cis-1,3,5-cyclohexanetricarboxylate.[158] These 'building blocks' are related to the molecular structure of the discrete $[Zn_3(crotonate)_6(quinoline)_2]$ complex reported by Clegg *et al.*[159]

One of the most unusual metal-BDC complexes synthesised to date is $InH(BDC)_2$, which adopts the chiral β-quartz structure in which each indium atom possesses triangulated dodecahedral geometry and is co-ordinated to four BDC molecules, that act as bidentate ligands. The structure contains two interpenetrating nets, and has a six-fold screw axis parallel to the *c*-axis, along which a right-handed channel runs.[160]

The isostructural Al(III) and Cr(III) BDC complexes absorb 3.8 and 3.1% w/w of hydrogen gas at 77 K and 1.6 MPa.[161] The structures comprise metal octahedra linked into chains by bridging hydroxyl groups. These chains are cross-linked by BDC to give a 3-D structure. Remarkably, the chromium analogue demonstrates an exceptionally large 'breathing' affect during the reversible transition from the hydrated to anhydrous form. In the absence of water the cavities are fully dilated to give a porous framework. When water is included in the channels, strong hydrogen bonds form between the guest water molecules and the –OH bridges of the framework, this causes the structure to deform and the cavities to 'close'. The ability of the framework to interact so strongly with guest molecule leads to the material demonstrating selective uptake of solvents that is governed by the guest's propensity to form hydrogen bonds.[162,163] A similar, 'breathing' affect had been reported previously for the isostructural V(OH)(BDC) framework.[74]

Finally, it should be noted that BDC has also been combined successfully with lanthanide metals to produce 3-D structures with varying degrees of porosity.[78,164,165]

4.1.6 The use of diffraction to locate physisorbed gas

The importance of studying the interactions between a gas guest and the host framework was alluded to in Section 4.4.4. Understanding the nature of such interactions will allow the host structure to be tailored, both topologically and chemically, to optimise the gas-storage capability of the material. However, determining the location of physisorbed gas within a framework cavity poses a considerable challenge.

Rosi and co-workers have used inelastic neutron scattering (INS) in an attempt to locate absorbed hydrogen in the cavities of the ZnO_4(BDC) structure.[148] This method identified two distinct absorption sites for the gas in the framework cavities, and the authors hypothesised that the two sites correspond to the gas interacting with the framework nodes and the linker molecules respectively. The use of INS to determine gas absorption sites within a metal-organic framework is without precedent; however, the interpretation of the data is somewhat speculative and inconclusive.

A more reliable model of the absorption sites within a framework structure can be achieved using diffraction techniques, although very few examples of such work have been reported in the literature.[166-169] One of the first studies of this kind was reported in 1987, and identified argon gas within the gas clathrate tetra-*tert*-butyltetrahedrane.[166] Later work utilised synchrotron X-

ray powder diffraction to locate oxygen molecules absorbed in the micro-channels of a 3-D Cu(II) coordination polymer.[166] Conventional single-crystal X-ray diffraction, using standard laboratory equipment, has been used to locate physisorbed argon and carbon dioxide in flexible 1-D Rh(II) coordination polymers; in both cases the host structure undergoes a phase transition upon gas inclusion.[168,169]

4.2 Summary

In this chapter, a general introduction to 3-D coordination polymers has been given, and the structural variations and possible applications for this class of materials were highlighted. An evaluation of the literature concerning gas-storage materials was then presented. This was followed by a detailed appraisal of the structural and physical properties of the 3-D polymer, $Zn_4O(BDC)$, which preceded a more general overview of other metal-benzenedicarboxylate structures reported in the literature. Finally, reported examples of the use of crystallography in locating physically absorbed gas in crystalline materials were discussed.

4.3 References

[1] Robson R, *J. Chem. Soc., Dalton Trans.*, 3735 (2000).

[2] Maeda K, *Mircopor. Mesopor. Mater.*, **73**, 47 (2004).

[3] Moulton B, Zaworotko MJ, *Chem. Rev.*, **101**, 1629 (2001).

[4] Rowsell JLC, Yaghi OM, *Mircopor. Mesopor. Mater.*, **73**, 3 (2004).

[5] Abrahams BF, Hoskins BF, Robson R, *J. Chem. Soc., Chem. Comm.*, 60 (1990).

[6] Hoskins BF, Robson R, *J. Am. Chem. Soc.*, **111**, 5962 (1989).

[7] Hoskins BF, Robson R, *J. Am. Chem. Soc.*, **112**, 1546 (1990).

[8] Abrahams BF, Hoskins BF, Lui J, Robson R, *J. Am. Chem. Soc.*, **113**, 3045 (1991).

[9] Kiritsis V, Michaelides A, Skoulika S, Golhen S, Ouahab L, *Inorg. Chem.*, **37**, 3407 (1998).

[10] Long D-L, Blake AJ, Champness NR, Wilson C, Schröder M, *Angew. Chem. Int. Ed.*, **40**, 2444 (2001).

[11] Reineke TM, Eddaoudi M, Moler D, O'Keeffe M, Yaghi OM, *J. Am. Chem. Soc.*, **122**, 4843 (2000).

[12] Long D-L, Blake AJ, Champness NR, Schröder M, *J. Chem. Soc., Chem. Comm.*, 1369 (2000).

[13] Zhao B, Cheng P, Dai Y, Cheng C, Liao D-Z, Yan S-P, Jiang Z-H, Wang G-L, *Angew. Chem. Int. Ed.*, **42**, 934 (2003).

[14] Takamizama S, Yamaguchi K, Mori W, *Inorg. Chem. Comm.*, **1**, 177 (1998).

[15] Yaghi OM, Li H, Groy TL, *J. Am. Chem. Soc.*, **118**, 9096 (1996).

[16] Yaghi OM, Li H, *J. Am. Chem. Soc.*, **118**, 295 (1996).

[17] Biradha K, Hongo Y, Fujita M, *Angew. Chem. Int. Ed.*, **39**, 3843 (2000).

[18] Kepert CJ, Rosseinsky MJ, *J. Chem. Soc., Chem. Comm.*, 375 (1999).

[19] Liu F-Q, Tilley TD, *J. Chem. Soc., Chem. Comm.*, 103 (1998).

[20] Xu X, Nieuwenhuyzen M, James SL, *Angew. Chem. Int. Ed.*, **41**, 764 (2002).

[21] Abrahams BF, Hoskins BF, Michail DM, Robson R, *Nature*, **369**, 727 (1994).

[22] Kamiyama A, Noguchi T, Kajiwara T, Ito T, *Angew. Chem. Int. Ed.*, **39**, 3130 (2000).

[23] Prior TJ, Bradshaw D, Teat SJ, Rosseinsky MJ, *J. Chem. Soc., Chem. Comm.*, 500 (2003).

[24] Rather B, Zaworotko MJ, *J. Chem. Soc., Chem. Comm.*, 830 (2003).

[25] Tao J, Tong M-L, Chen X-M, *J. Chem. Soc., Dalton Trans.*, 3669 (2000).

[26] O'Keeffe M, Eddaoudi M, Li H, Reineke T, Yaghi OM, *J. Solid State Chem.*, **152**, 3 (2000).

[27] MacGillivray LR, Subramanian S, Zaworotko MJ, *J. Chem. Soc., Chem. Comm.*, 1325 (1994).

[28] Chen B, Eddaoudi M, Hyde ST, O'Keeffe MO, Yaghi OM, *Science*, **291**, 1021 (2001).

[29] Carlucci L, Ciani G, Moret M, Proserpio DM, Rizzato S, *Angew. Chem. Int. Ed.*, **39**, 1506 (2000).

[30] Rosi NL, Eddaoudi M, Kim J, O'Keeffe MO, Yaghi OM, *Angew. Chem. Int. Ed.*, **41**, 284 (2002).

[31] Batten SR, Robson R, *Angew. Chem. Int. Ed.*, **37**, 1461 (1998).

[32] Noro S-I, Kitaura R, Kondo M, Kitagawa S, Ishii T, Matsuzaka H, Yamashita M, *J. Am. Chem. Soc.*, **124**, 2568 (2002).

[33] Lu J, Paliwala T, Lim SC, Yu C, Niu T, Jacobson AJ, *Inorg. Chem.*, **36**, 923 (1997).

[34] Vaid TP, Lobkovsky EB, Wolczanski PT, *J. Am. Chem. Soc.*, **119**, 8742 (1997).

[35] Chui SS-Y, Lo SM-F, Charmant JPH, Orpen AG, Williams ID, *Science*, **283**, 1148 (1999).

[36] Kiang Y-H, Gardner GB, Lee S, Xu Z, Lobkovsky EB, *J. Am. Chem. Soc.*, **121**, 8204 (1999).

[37] Yaghi OM, O'Keeffe M, Ockwig NW, Chae HK, Eddaoudi M, Kim J, *Nature*, **423**, 705 (2003).

[38] Rosi NL, Eddaoudi M, Kim J, O'Keeffe M, Yaghi OM, *CrystEngComm*, **4**, 401 (2002).

[39] Eddaoudi M, Moler DB, Li H, Chen B, Reineke T, O'Keeffe M, Yaghi OM, *Acc. Chem. Res.*, **34**, 319 (2001).

[40] Yaghi OM, Li H, Davis C, Richardson D, Groy TL, *Acc. Chem. Res.*, **31**, 474 (1998).

[41] Kim J, Chen B, Reineke T, Li H, Eddaoudi M, Moler DB, O'Keeffe M, Yaghi OM, *J. Am. Chem. Soc.*, **123**, 8239 (2001).

[42] Eddaoudi M, Kin J, O'Keeffe M, Yaghi OM, *J. Am. Chem. Soc.*, **124**, 376 (2002).

[43] Ferlay S, Koenig S, Hosseini MW, Pansanel J, De Cian A, Kyritsakas N, *J. Chem. Soc., Chem. Comm.*, 218 (2002).

[44] Russell VA, Evans CC, Li W, Ward MD, *Science*, **276**, 575 (1997).

[45] Mäkinen SK, Melcer NJ, Parvez M, Shimizu GKH, *Chem. Eur. J.*, **7**, 5176 (2001).

[46] Holman KT, Pivovar AM, Swift JA, Ward MD, *Acc. Chem. Res.*, **34**, 107 (2001).

[47] Kepert CJ, Prior TJ, Rosseinsky MJ, *J. Solid State Chem.*, **152**, 261 (2000).

[48] Soldatov DV, Grachev EV, Ripmeester JA, *Crystal Growth & Design*, **2**, 401 (2002).

[49] Takamizawa S, Nakata E, Yokoyama H, *Inorg. Chem. Comm.*, **6**, 763 (2003).

[50] Cussen EJ, Claridge JB, Rosseinsky MJ, Kepert CJ, *J. Am. Chem. Soc.*, **124**, 9574 (2002).

[51] Kitazawa T, Kikuyama T, Takeda M, Iwamoto T, *J. Chem. Soc., Dalton Trans.*, 3715 (1995).

[52] Aakeröy CB, Beatty AM, Leinen DS, Lorimer KR, *J. Chem. Soc., Chem. Comm.*, 935 (2000).

[53] Davis ME, *Nature*, **417**, 813 (2002).

[54] Rosseinsky MJ, *Mircopor. Mesopor. Mater.*, **73**, 15 (2004).

[55] Cui Y, Evans OR, Ngo HL, White PS, Lin W, *Angew. Chem. Int. Ed.*, **41**, 1159 (2002).

[56] Cui Y, Ngo HL, White PS, Lin W, *J. Chem. Soc., Chem. Comm.*, 994 (2003).

[57] Kepert CJ, Rosseinsky MJ, *J. Chem. Soc., Chem. Comm.*, 31 (1998).

[58] Kepert CJ, Prior TJ, Rosseinsky MJ, *J. Am. Chem. Soc.*, **122**, 5158 (2000).

[59] Seo JS, Whang D, Lee H, Jun SI, Oh J, Jeon YJ, Kim K, *Nature*, **404**, 982 (2000).

[60] Naito S, Tanibe T, Saito E, Miyao T, Mori W, *Chem. Lett.*, 1178 (2001).

[61] Ohmura, Mori W, Hiraga H, Ono M, Nishimoto Y, *Chem. Lett.*, **32**, 468 (2003).

[62] Mori W, Takamizawa S, Kato CN, Ohmura T, Sato T, *Mircopor. Mesopor. Mater.*, **73**, 31 (2004).

[63] Agterburg FPW, Provó Kluit HAJ, Driessen WL, Oevering H, Buijs W, Larkin MT, Spek AL, Reedijk J, *Inorg. Chem.*, **36**, 4321 (1997).

[64] Evan OR, Ngo HL, Lin W, *J. Am. Chem. Soc.*, **123**, 10395 (2001).

[65] Fujita M, Kwon YJ, Washizu S, Ogura K, *J. Am. Chem. Soc.*, **116**, 1151 (1994).

[66] Sharma AC, Borovik AS, *J. Am. Chem. Soc.*, **122**, 8946 (2000).

[67] Li H, Davis CE, Groy TL, Kelley DG, Yaghi OM, *J. Am. Chem. Soc.*, **120**, 2186 (1998).

[68] Chen B, Eddaoudi M, Reineke TM, Kampf JW, O'Keeffe MO, Yaghi OM, *J. Am. Chem. Soc.*, **122**, 11559 (2000).

[69] Yaghi OM, Davis CE, Li G, Li H, *J. Am. Chem. Soc.*, **119**, 2861 (1997).

[70] Yaghi OM, Li G, Li H, *Nature*, **378**, 703 (1995).

[71] Kuznicki SM, Bell VA, Nair S, Hillhouse HW, Jacubinas RM, Braunbarth CM, Toby BH, Tsapatsis M, *Nature*, **412**, 720 (2001).

[72] Wang MQ, Shen D, Bülow M, Lau ML, Deng S, Fitch FR, Lemcoff NO, Semanscin J, *Mircopor. Mesopor. Mater.*, **55**, 217 (2002).

[73] Pan L, Adams KM, Hernandez HE, Wang X, Zheng C, Hattori Y, Kaneko K, *J. Am. Chem. Soc.*, **125**, 3062 (2003).

[74] Barthelet K, Marrot J, Riou D, Férey G, *Angew. Chem. Int. Ed.*, **41**, 281 (2002).

[75] Manson JL, Campana C, Miller JS, *J. Chem. Soc., Chem. Comm.*, 251 (1998).

[76] Plater MJ, St. J. Foreman MR, Coronado E, Gómez-García C, Slawin AMZ, *J. Chem. Soc., Dalton Trans.*, 4209 (1999).

[77] Halder GJ, Kepert CJ, Moubaraki B, Murray KS, Cashion JD, *Science*, **298**, 1762 (2002).

[78] Reineke TM, Eddaoudi M, Fehr M, Kelley D, Yaghi OM, *J. Am. Chem. Soc.*, **121**, 1651 (1999).

[79] Chandler BD, Côté AP, Cramb DT, Hill JM, Shimizu KH, *J. Chem. Soc., Chem. Comm.*, 1900 (2002).

[80] Steele BCH, Heinzel A, *Nature*, **414**, 345 (2001).

[81] McEnaney B, *Chemistry in Britain*, 24 (Jan. 2003).

[82] Willcocks E, *Chemistry in Britain*, 27 (Jan. 2003).

[83] Grätzel M, *Nature*, **414**, 338 (2001).

[84] Schlapbach L, Züttel A, *Nature*, **414**, 353 (2001).

[85] US Dept. of Energy Technical Targets; http://www.eere.energy.gov/hydrogenandfuelcells

[86] Menon VC, Komarneni S, *J. Porous Mater.*, **5**, 43 (1998).

[87] Lozano-Castelló D, Alcañiz-Monge J, de la Casa-Lillo MA, Cazorla-Amorós D, Linares-Solano A, *Fuel*, **81**, 1777 (2002).

[88] Texier-Mandoki, Dentzer J, Piquero T, Saadallah S, David P, Vix-Guterl C, *Carbon*, **42**, 2735 (2004).

[89] Nijkamp MG, Raaymakers JEMJ, Van Dillen AJ, de Jong KP, *Appl. Phys. A*, **72**, 619 (2001).

[90] MacDonald JAF, Quinn DF, *Carbon*, **34**, 1103 (1996).

[91] Brady TA, Rostam-Abadi M, Rood MJ, *Gas. Sep. Purif.*, **10**, 97 (1996).

[92] Perrin A, Celzard A, Marêché JF, Furdin G, *Carbon*, **32**, 1249 (2004).

[93] Lozano-Castelló D, Cazorla-Amorós D, Linares-Solano A, *Energy & Fuels*, **16**, 1321 (2002).

[94] Lozano-Castelló D, Cazorla-Amorós D, Linares-Solano A, Quinn DF, *Carbon*, **40**, 989 (2002).

[95] Lozano-Castelló D, Cazorla-Amorós D, Linares-Solano A, *Carbon*, **40**, 2817 (2002).

[96] MacDonald JAF, Quinn DF, *Fuel*, **77**, 61 (1998).

[97] Cheng H-M, Yang Q-H, Lui C, *Carbon*, **39**, 1447 (2001).

[98] Iijima S, *Nature*, **354**, 56 (1991).

[99] Iijima S, Ichihashi T, *Nature*, **363**, 603 (1993).

[100] Dillon AC, Jones KM, Bekkedahl TA, Kiang CH, Bethune DS, Heben MJ, *Nature*, **386**, 377 (1997).

[101] Lui C, Fan YY, Lui M, Cong HT, Cheng HM, Dresselhaus MS, *Science*, **286**, 1127 (1999).

[102] Ye Y, Ahn CC, Witham C, Fultz, Lui J, Rinzler AG, Colbert D, Smith KA, Smalley RE, *Appl. Phys. A*, **74**, 2307 (1999).

[103] Ansón A, Callejas MA, Benito AM, Maser WK, Izquierdo MT, Rubio B, Jagiello J, Thommes M, Parra JB, Martínez MT, *Carbon*, **42**, 1243 (2004).

[104] Shen K, Xu H, Jiang Y, Pietraß T, *Carbon*, **42**, 2315 (2004).

[105] Sudan P, Züttel A, Mauron P, Emmenegger C, Wenger P, Schlapbach L, *Carbon*, **41**, 2377 (2003).

[106] Hou P-X, Xu S-T, Ying Z, Yang Q-H, Liu C, Cheng H-M, *Carbon*, **41**, 2471 (2003).

[107] Hischer M, Becher M, Haluska M, Dettlaff-Weglikowska U, Quintel A, Duesberg GS, Choi Y-M, Downes P, Hulman M, Roth S, Stepanek I, Bernier P, *Appl. Phys. A*, **72**,129 (2001).

[108] Gauy P, Stansfield BL, Rochefort A, *Carbon*, **42**, 2187 (2004).

[109] Chen P, Wu X, Lin J, Tan KL, *Science*, **285**, 91 (1999).

[110] Yang RT, *Carbon*, **38**, 623 (2000).

[111] Zhu ZH, Lu GQ, Smith SC, *Carbon*, **42**, 2509 (2004).

[112] Yin YF, Mays T, McEnaney B, *Langmuir*, **16**, 10521 (2000).

[113] Cao D, Zhang X, Chen J, Wang W, Yun J, *J. Phys. Chem. B*, **107**, 13286 (2003).

[114] Bekyarova E, Murata K, Yudasaka M, Kasuya D, Iijima S, Tanaka H, Kahoh H, Kaneko K, *J. Phys. Chem. B*, **107**, 4681 (2003).

[115] Talapatra S, Zambano AZ, Weber SE, Migone AD, *Phys. Rev. Lett.*, **85**, 138 (2000).

[116] Talapatra S, Migone AD, *Phys. Rev. B*, **65**, 045416 (2002).

[117] Zhang X, Cao D, Chen J, *J. Phys. Chem. B*, **107**, 4942 (2003).

[118] Lee SM, Lee YH, *Appl. Phys. Lett.*, **76**, 2877 (2000).

[119] Wang Q, Johnson JK, *J. Chem. Phys.*, **110**, 577 (1999).

[120] Koi N, Oku T, *Solid State Comm.*, **131**, 121 (2004).

[121] Oku T, Kumo M, *Diamond Rel. Mater.*, **12**, 840 (2003).

[122] Oku T, Kuno M, Narita I, *J. Phys. Chem. Solids*, **65**, 549 (2004).

[123] Ma R, Bando Y, Zhu H, Sato T, Xu C, Wu D, *J. Am. Chem. Soc.*, **124**, 7672 (2002).

[124] Schur DV, Tarasov BP, Shul'ga YM, Zaginaichenko SY, Matysina ZA, Pomytkin AP, *Carbon*, **41**, 1331 (2003).

[125] Chambers A, Park C, Baker TK, Rodriguez NM, *J. Phys. Chem. B*, **102**, 4253 (1998).

[126] Park C, Anderson PE, Chambers A, Tan CD, Hidalgo R, Rodriguez NM, *J. Phys. Chem. B*, **103**, 10572 (1999).

[127] Liu C, Cong HT, Li F, Tan PH, Cheng HM, Lu K, Zhou BL, *Carbon*, **37**, 1865 (1999).

[128] Dybtsev DN, Chun H, Yoon SH, Kim D, Kim K, *J. Am. Chem. Soc.*, **126**, 32 (2004).

[129] Kitaura R, Seki K, Akiyama, Kitagawa S, *Angew. Chem. Int. Ed.*, **42**, 428 (2003).

[130] Kondo M, Shimamura M, Noro S, Minakoshi S, Asami A, Seki K, Kitagawa S, *Chem. Mater.*, **12**, 1288 (2000).

[131] Kondo M, Yoshitomi T, Seki K, Matsuzaka H, Kitagawa S, *Angew. Chem. Int. Ed.*, **36**, 1725 (1997).

[132] Noro S, Kitagawa S, Kondo M, Seki K, *Angew. Chem. Int. Ed.*, **39**, 2082 (2000).

[133] Düren T, Sarkisov L, Yaghi OM, Snurr RQ, *Langmuir*, **20**, 2683 (2004).

[134] Seki K, Takamizawa S, Mori W, *Chem. Lett.*, 122 (2001).

[135] Mori W, Takamizawa S, *J. Solid State Chem.*, **152**, 120 (2000).

[136] Takamizama S, Mori W, Furihata M, Takeda S, Yamaguchi K, *Inorg. Chim. Acta*, **283**, 268 (1998).

[137] Seki K, Mori W, *J. Phys. Chem. B*, **106**, 1380 (2002).

[138] Seki K, *J. Chem. Soc., Chem. Comm.*, 1496 (2001).

[139] Kondo M, Okubo T, Asami A, Noro S, Yoshitomi T, Kitagawa S, Ishii T, Matsuzaka H, Seki K, *Angew. Chem. Int. Ed.*, **38**, 140 (1999).

[140] Forster PM, Eckert J, Chang J-S, Park S-E, Férey G, Cheetham AK, *J. Am. Chem. Soc.*, **125**, 1309 (2003).

[141] Enright GD, Udachin KA, Moudrakovski IL, Ripmeester JA, *J. Am. Chem. Soc.*, **125**, 9896 (2003).

[142] Atwood JL, Barbour LJ, Jerga A, *Science*, **296**, 2367 (2002).

[143] Atwood JL, Barbour LJ, Thallapally PK, Wirsig TB, *J. Chem. Soc., Chem. Comm.*, 51 (2005).

[144] Sun Z-G, Ma R-S, Wang R-Z, Guo K-H, Fa S-S, *Energy & Fuels*, **17**, 1180 (2003).

[145] Wang L, Gardeler H, Gmehling J, *Sep. Purif. Tech.*, **12**, 35 (1997).

[146] Li H, Eddaoudi M, O'Keeffe M, Yaghi OM, *Nature*, **402**, 276 (1999).

[147] Broach RW, Bedard RA, Gier TE, Bu X, Stucky GD, *Chem. Mater.*, **8**, 691 (1996).

[148] Rosi NL, Eckert J, Eddaoudi M, Vodak DT, O'Keeffe M, Yaghi OM, *Science*, **300**, 1127 (2003).

[149] Rowsell JLC, Millward AR, Park KS, Yaghi OM, *J. Am. Chem. Soc.*, **126**, 5666 (2004).

[150] Panella B, Hirscher M, *Adv. Mater.*, **17**, 538 (2005).

[151] Eddaoudi M, Kim J, Rosi NL, Vodak DT, Wachter J, O'Keeffe M, Yaghi OM, *Science*, **295**, 469 (2002).

[152] Eddaoudi M, Li H, Reineke T, Fehr M, Kelley DG, Groy TL, Yaghi OM, *Top. Catal.*, **9**, 105 (1999).

[153] Edgar M, Mitchell R, Slawin AMZ, Lightfoot P, Wright PA, *Chem. Eur. J.*, **7**, 5168 (2001).

[154] Eddaoudi M, Li H, Yaghi OM, *J. Am. Chem. Soc.*, **122**, 1391 (2000).

[155] Tao J, Chen X-M, Huang R-B, Zheng L-S, J. *Solid State Chem.*, **170**, 130 (2003).

[156] Li H, Eddaoudi M, Groy TL, Yaghi OM, *J. Am. Chem. Soc.*, **120**, 8571 (1998).

[157] Mori W, Inoue F, Yoshida K, Nakayama H, Takamizama S, Kihita M, *Chem. Lett.*, 1219 (1997).

[158] Yaghi OM, Jernigan R, Li H, Davis CE, Groy TL, *J. Chem. Soc., Dalton Trans.*, 2383 (1997).

[159] Clegg W, Little IR, Straughan BP, *J. Chem. Soc., Chem. Comm.*, 73 (1985).

[160] Sun J, Weng L, Zhou Y, Chen J, Chen Z, Liu Z, Zhao D, *Angew. Chem. Int. Ed.*, **41**, 4471 (2002).

[161] Férey G, Latroche M, Serre C, Millange F, Loiseau T, Percheron-Guégan A, *J. Chem. Soc., Chem. Comm.*, 2976 (2003).

[162] Millange F, Serre C, Férey G, *J. Chem. Soc., Chem. Comm.*, 822 (2002).

[163] Serre C, Millange F, Thouvenot C, Noguès M, Marsolier G, Louër D, Férey G, *J. Am. Chem. Soc.*, **124**, 13519 (2002).

[164] Reineke TM, Eddaoudi M, O'Keeffe M, Yaghi OM, *Angew. Chem. Int. Ed.*, **38**, 2590 (1999).

[165] Serre C, Millange F, Marrot J, Férey G, *Chem. Mater.*, **14**, 2409 (2002).

[166] Irngartinger H, Jahn R, Maier G, Emrich R, *Angew. Chem. Int. Ed.*, **26**, 356 (1987).

[167] Kitaura R, Kitagawa S, Kubota Y, Kobayashi TC, Kindo K, Mita Y, Matsuo A, Kobayashi M, Chang H-C, Ozawa TC, Suzuki M, Sakata M, Takata M, *Science*, **298**, 2358 (2002).

[168] Takamizama S, Nakata E, Yokoyama H, Mochizuki K, Mori W, *Angew. Chem. Int. Ed.*, **42**, 4331 (2003).

[169] Takamizama S, Nakata E, Saito T, Kojima K, *CrystEngComm*, **5**, 411 (2003).

Chapter 5

Single Crystal X-ray Diffraction Studies of Gas-Loaded Zn_4O(1,4-benzenedicarboxylate)

5.1 Introduction

This study was conducted in collaboration with Prof. Omar Yaghi of the University of Michigan, USA. The objective of this project was to locate the gas absorption sites within argon and nitrogen-loaded Zn_4O(1,4-benzenedicarboxylate) (Zn_4O(BDC)) using low-temperature single crystal X-ray diffraction. Chapter 4 contains a survey of the literature that is of importance to the work presented in this chapter. Of particular relevance is Section 4.1.4 in which the structural and physical attributes of the Zn_4O(BDC) framework are discussed.

5.2 Experimental

The samples used in this investigation were colourless cubic crystals of gas loaded Zn_4O(1,4-benzenedicarboxylate). The argon-loaded crystal possessed the following dimensions: 0.33 x 0.33x 0.33 cm, the nitrogen-loaded crystal was of the size 0.39 x 0.36 x 0.26 cm. The crystals were sealed in a Lindermann capillary filled with the appropriate gas at an approximate pressure of 1.0 atm. Prior to gas loading, all air had been evacuated from the crystal and capillary.

The capillary was mounted on a 'swivel' goniometer head using a magnetic capillary holder. This enabled to crystal to be mounted vertically to allow the Helix cooling system to be lowered over the crystal (Fig. 5.2.1). Care was taken to position the centroid of the crystal in the centre of the X-ray beam (monochromatic Mo-K_α radiation, λ = 0.71073 Å). A variable temperature data collection was performed in the range of 30 - 293K on a Bruker APEX 3-circle diffractometer. As the crystal was known to possess cubic symmetry (space group Fm-3m) only a partial sphere data collection was required. A total of 600, 20-second, frames were collected scanning through

ω in 0.3° steps. χ ,ϕ, and 2θ were fixed at 54.74°, 65.63° and 28°, respectively. The total runtime was approximately 4 hours. The reciprocal space coverage was checked, and determined to be 100%, using ASTRO.[†]

It should be noted that is was necessary to halt the data collection during the run sequence to clear the accumulation of ice from the Helix head and capillary. Data treatment was performed using the SHELX suite of software. A multi-scan absorption correction was applied using SADABS, no correction for extinction was performed. Structure solution was by Direct Methods and refinement was on F^2.

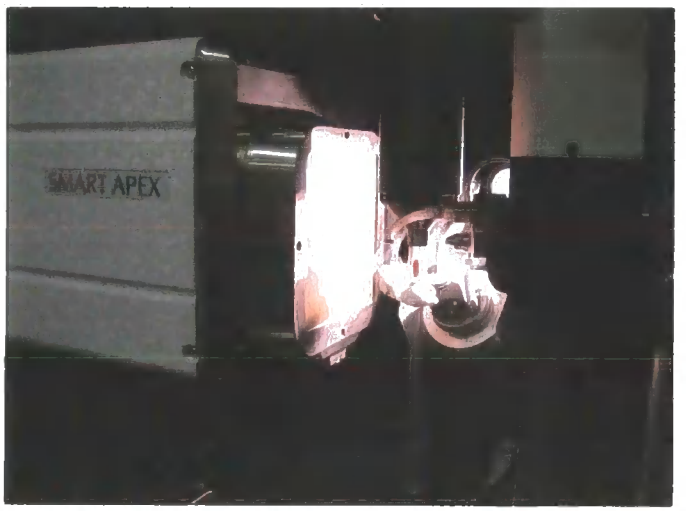

Figure 5.2.1: Photograph of the sample environment employed in this study.

5.3 Results & Discussion

For both samples the space group was established to be the expected cubic group Fm-3m (Nº 225), and no phase transitions were observed in the temperature range investigated. Tables 5.3.1 and 5.3.2 list additional refinement and crystallographic details. In both cases the framework is well defined at all temperatures with no apparent disorder. The refinement of the guest gas atoms/molecules is a noticeably more complex problem and forms the focus of this chapter. Further details regarding the final crystallographic models can be found in supplementary data for this chapter.

[†] ASTRO is part of the Bruker suite of software (1998)

Table 5.3.1: Crystallographic data and refinement details for the variable temperature datasets collected on nitrogen-loaded $Zn_4O(BDC)$.

	30K	50K	90K	120K	293K
a (Å)	25.898(4)	25.889(3)	25.872(3)	25.856(3)	25.7927(4)
Volume (Å^3) / Z	17370(4) / 8	17351(3) / 8	17318(3) / 8	17285(3) / 8	17158.9(5) / 8
μ (mm^{-1})	1.125	1.124	1.124	1.122	1.126
Unique reflections	1265	1257	1257	1255	1337
R(int)	0.0194	0.0204	0.0196	0.0218	0.0248
Gof (on F^2)	1.140	1.124	1.156	1.151	1.116
R1 / wR2 (I>2σ(I))	0.0357 / 0.1131	0.0247 / 0.0766	0.0282 / 0.0854	0.0265 / 0.0749	0.0301 / 0.0813

Table 5.3.2: Crystallographic data and refinement details for the variable temperature datasets collected on argon-loaded $Zn_4O(BDC)$.

	30K	50K	90K	293K
a (Å)	25.8821(5)	25.8824(3)	25.8878(4)	25.7947(4)
Volume (Å^3) / Z	17338.0(6) / 8	17338.6(3) / 8	17349.4(5) / 8	17162.9(5) / 8
μ (mm^{-1})	1.516	1.504	1.367	1.125
Unique reflections	1266	1318	1298	1296
R(int)	0.0296	0.0197	0.0224	0.0264
Gof (on F^2)	1.290	1.306	1.244	1.265
R1 / wR2 (I>2σ(I))	0.0866 / 0.0866	0.0656 / 0.2025	0.0433 / 0.1177	0.0328 / 0.0862

5.3.1 Negative thermal expansion of the $Zn_4O(BDC)$ framework

A plot of the unit cell length versus temperature for the nitrogen-loaded sample is shown in Figure 5.3.1. It is immediately apparent form the negative slope of the linear regression line that the $Zn_4O(BDC)$ framework undergoes negative thermal expansion (NTE).

The coefficient of thermal expansion can be calculated using the following equation (Eq.5.3.1):[1]

$$\alpha_l = (l_T - l_o) / l_o (T - T_o) \qquad \textbf{Equation 5.3.1}$$

By substituting in the values determined from the linear regression analysis into Equation 5.3.1 the coefficient of thermal expansion for the $Zn_4O(BDC)$ framework was calculated to be

$-1.54 \times 10^{-5}\ K^{-1}$. Furthermore, as the material is cubic the volume expansion coefficient (α_v) is equal to $3\alpha_l$ and is $-4.62 \times 10^{-5}\ K^{-1}$.

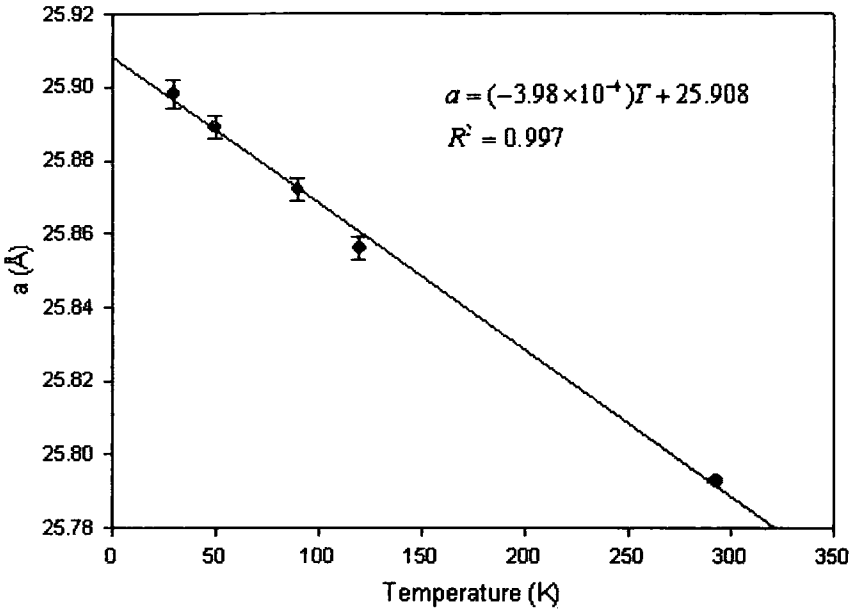

Figure 5.3.1: Plot of unit cell axis length (a) vs. temperature. Data used are from Table 5.3.1. The linear regression equation is given at the top right of the plot.

The NTE behaviour exhibited by the $Zn_4O(BDC)$ framework is not wholly unexpected. In 1993 Baugham *et al.* published theoretical results, suggesting that the presence of bonds in extended structures that can act as 'hinges' could lead to the material demonstrating NTE, and more importantly from an engineering perspective, showing auxetic behaviour.[2] Using a simple chemical model, namely a 3-D network of polyacetylene, the authors showed, by molecular dynamics calculations, that the NTE coefficient for this phase would be $-1.6 \times 10^{-5}\ K^{-1}$. The NTE coefficient determined for the $Zn_4O(BDC)$ framework is of the same order of magnitude as this predicted value. The question that arises, if Baughman's hinge model is appropriate for $Zn_4O(BDC)$, is which bonds are acting as the 'hinge component'?

Under normal circumstances a chemical bond is expected to lengthen with increasing temperature as higher vibration energy levels for the bond become populated. The following three graphs show the change in framework bond lengths as a function of temperature. It is immediately apparent that the estimated standard deviations on the bond lengths are high; this makes interpretation of the change in bond length as a function of temperature somewhat

speculative. Nonetheless, it can be seen from the overall trends in these plots that bond Zn1-O2 is anomalous, in that this bond is longer at lower temperatures. This would suggest that the Zn1-O2 bond has a role to play in the structural reorganisation at lower temperatures that is responsible for the NTE behaviour. Figure 5.3.5 shows a section of the framework structure with atom labels.

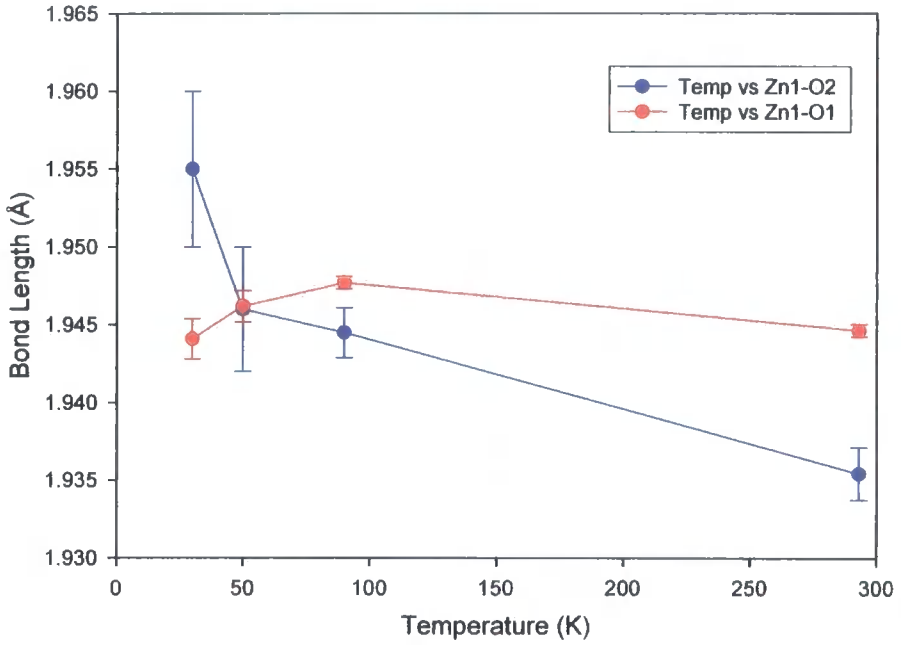

Figure 5.3.2: Plot of Zn-O bond lengths vs. temperature.

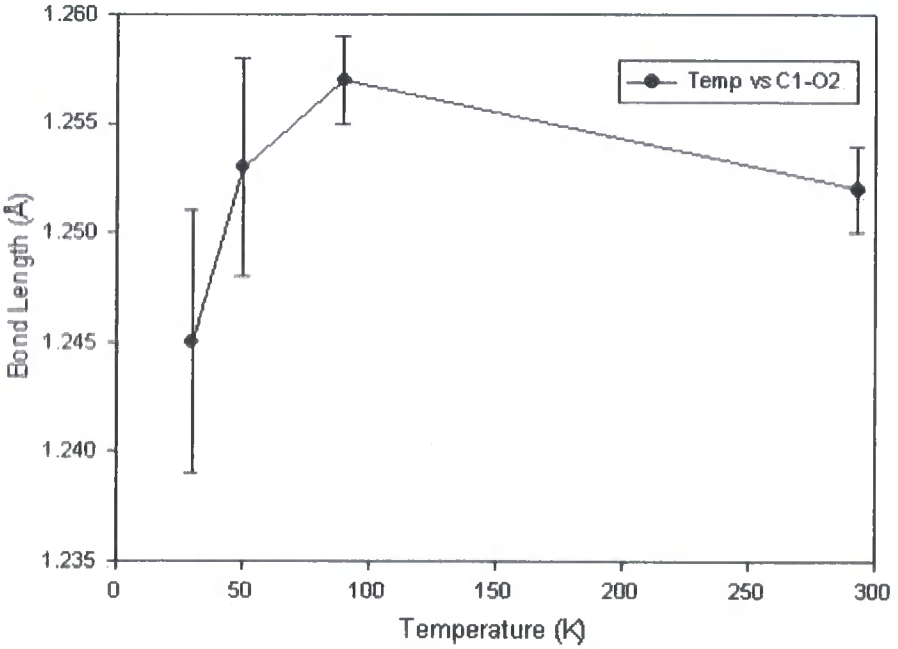

Figure 5.3.3: Plot of C1-O2 bond length vs. temperature.

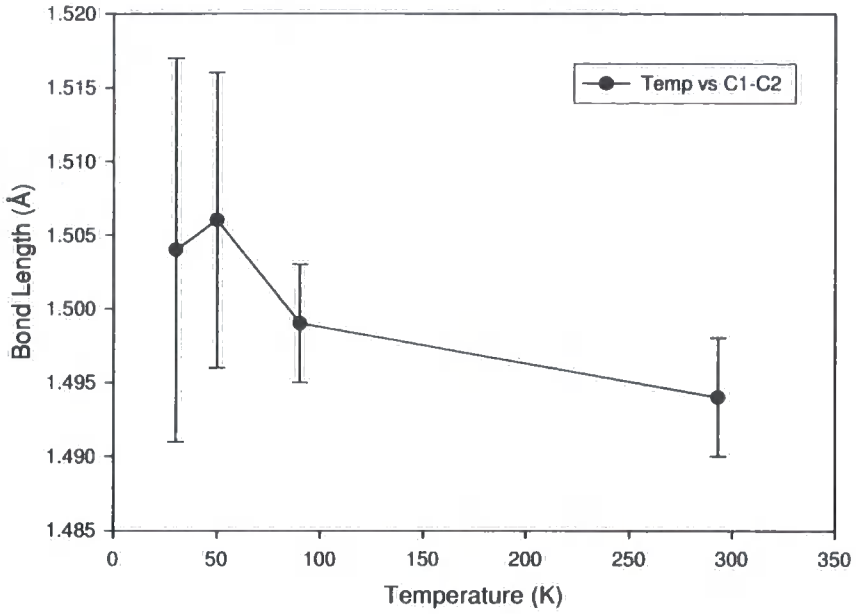

Figure 5.3.4: Plot of C1-C2 bond length vs. temperature.

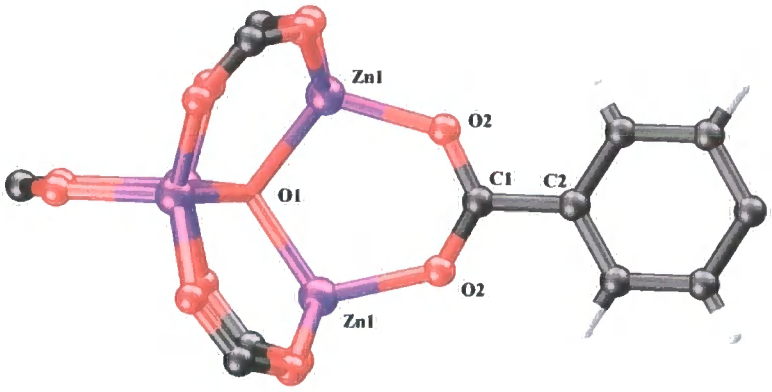

Figure 5.3.5: Section of the framework structure with atom labels.

In conclusion, it is not possible to explain, using the available X-ray data, the structural alterations that result in the NTE behaviour shown by the $Zn_4O(BDC)$ framework. Although the bond length data suggest that the Zn1-O2 bond distortions are important, the large degree of error in all the bond length values means that the temperature dependent bond deformations cannot be described accurately. Moreover, only five data points were used to quantify the NTE coefficient, and only three of these points were below 100K (Fig.5.3.1). Ideally, more data points over a wider temperature range, and at small increments, should be used to explain accurately the trend in NTE behaviour, and to quantify the coefficient of thermal expansion.

For comparison, Lightfoot *et al.* have performed an extensive study of the occurrence of NTE in zeolite materials.[3] Of the seventeen zeolite compounds investigated, fifteen exhibited NTE behaviour (α_v ranges from –35.1 to –3.1 x 10^{-6} $^{o}C^{-1}$). The authors conclude that negative thermal expansivity must be considered the norm rather than the exception in microporous oxides, they also suggested that positive thermal expansion is favoured only by frameworks with high densities, although they do acknowledge that considerably more work is required before any conclusions are drawn. To date, the precise mechanism by which NTE occurs in zeolite compounds remains a matter of speculation.

5.3.2 Nitrogen-loaded $Zn_4O(BDC)$

The refinement of the nitrogen molecules within the framework channels of $Zn_4O(BDC)$ will form the focus of this section. As the physisorbed gas molecules, by their nature, exhibit considerable disorder, care was taken to ensure that the data were interpreted correctly, and to achieve this aim, relevant Fourier maps (with F(000) excluded) were examined rigorously. The absorption of the gas is temperature dependent, with lower temperatures facilitating the greatest gas uptake. The refinement of each dataset of the variable temperature X-ray single crystal study will be discussed in turn. In all cases, the $Zn_4O(BDC)$ framework was refined anisotropically and the gas molecules were refined isotropically.

293K Structure

The framework system is well ordered at 293K, and was successfully refined anisotropically. The asymmetric unit comprises a total of seven independent atoms (one zinc, two oxygen, and three carbon atoms and a single hydrogen atom). At this temperature no nitrogen gas was located in the framework cavities, and the highest residual electron density peak in the difference Fourier map was 0.50 eÅ^3 and is located only 0.10 Å from the zinc atom.

120K Structure

At 120K a single nitrogen molecule of partial occupancy can be observed in the unit cell. Atom N1 resides on a 3*m* symmetry site (see Table 5.3.3 and Fig. 5.3.6 for details), atom N2 is disordered over three positions due to its proximity to the 3-fold axis on which atom N1 sits, subsequently N2 is on a site of mirror symmetry. The N-N bond length was found to be 1.09(2) Å, this is equivalent to the expected bond distance of 1.097 Å.[4] The highest residual electron density peak in the cavity is ~ 0.43 eÅ^3 and is located ~0.35 Å from atom N1.

Table 5.3.3: Atomic parameters for physisorbed nitrogen gas at 120K

Atom	x	y	z	Occupancy	U_{iso}
N1	0.1573(5)	0.3427(5)	0.1573(5)	0.103(2)	0.168(7)
N2	0.1529(9)	0.3481(9)	0.116(1)	0.103(2)	0.25(2)

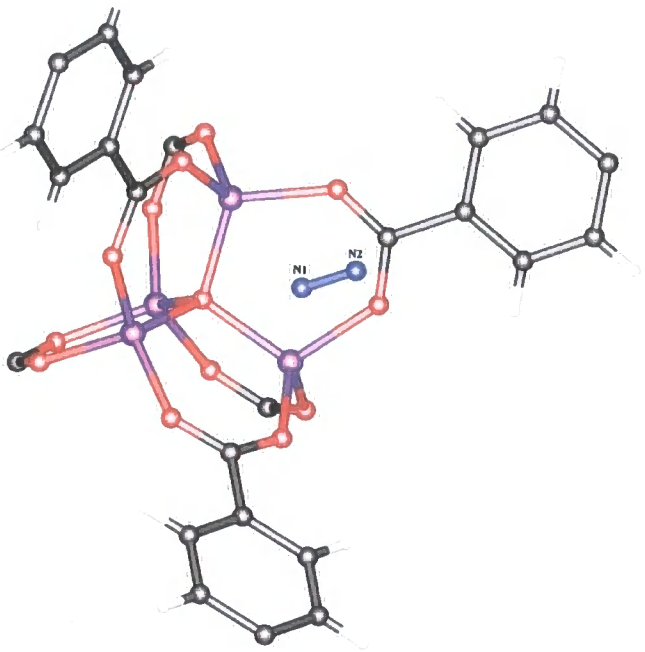

Figure 5.3.6: Location of molecule N1-N2 relative to the $Zn_4O(BDC)$ framework at 120K. (Zn: purple, O: red, C: black, N: blue, H: grey). Only one position of the disordered N2 atom is shown for clarity.

The electron density map given in Figure 5.3.7 provides conclusive evidence pertaining to the presence of nitrogen molecule N1-N2 in the $Zn_4O(BDC)$ structure at 120K. The atoms of the molecule are not well resolved, indeed there is little evidence to support modelling molecule N1-N2 as a diatomic. As the molecule appears to be heavily disordered, a more suitable model would be to treat it as a single body and define the nitrogen atomic structure factor with a Bessel function. However, at the present time the isotropic diatomic model is the best available, and is more realistic than a single atom model. The poor atomic resolution would imply that anisotropic refinement of the nitrogen atoms would produce a thermal displacement model that is essentially meaningless. For this

reason the nitrogen atoms have been modelled in the isotropic state only, albeit with high U_{iso} values (U_{iso} for N2 is 0.25(2) $Å^2$).

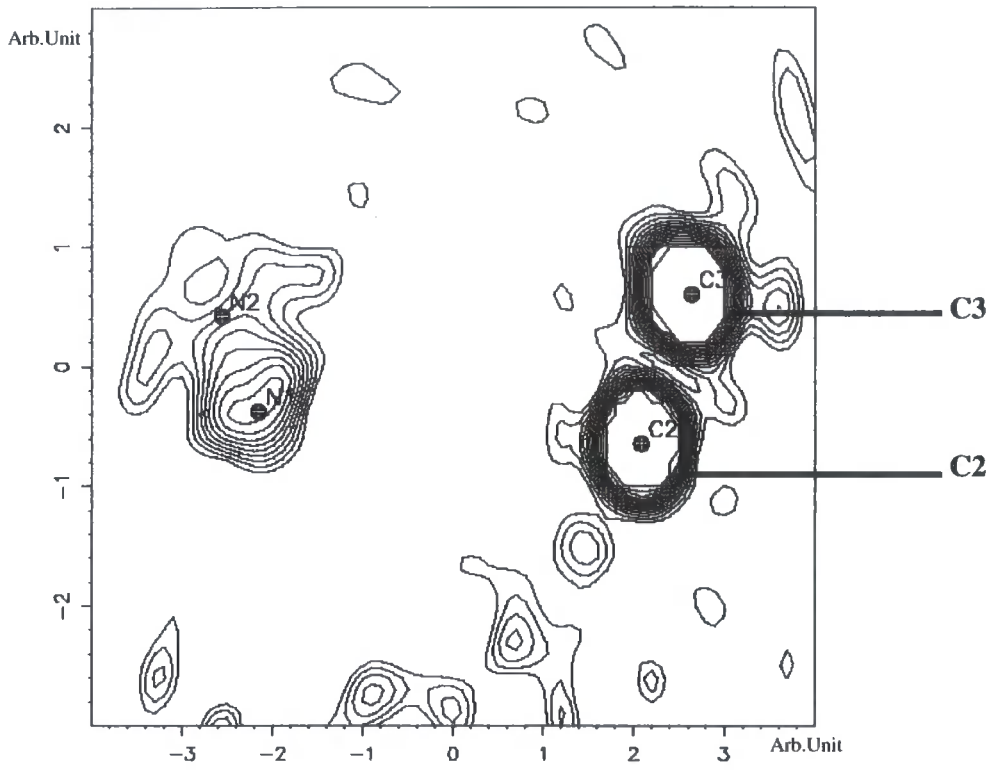

Figure 5.3.7: F_{obs} slant plane Fourier map defined by atoms N1, N2, C2 and C3. The contour range is set to 0-3 $eÅ^3$, and level is 0.1875 $eÅ^3$.

The occupancies of the two nitrogen atoms were constrained to be equal. Attempting to calculate the individual atomic occupancies will result in inaccurate values due to the molecular disorder smearing the electron density that defines the atoms. The final occupancy value was fixed at 62% (best value deduced by SHELX), however due to the high degree of disorder this value must be considered as an approximation only.

Figure 5.3.6 shows the location of the nitrogen molecule in relation to the framework atoms. The van der Waals radii for zinc and nitrogen are 1.39 Å and 1.55 Å, respectively;[5] the sum of the radii is therefore 2.94 Å. The Zn···N1 distance is 3.96(3) Å, which is considerably longer than the sum of the van der Waals radii for these elements, and this precludes the presence of any van der Waals interaction between these atoms. The shortest N···O distances are 3.62(2) Å (O2···N1) and 3.78(4) Å (O2···N2). The van der Waals radius for oxygen is 1.52 Å, and the sum of the radii for oxygen and nitrogen is 3.07 Å; this would suggest the absence of any van der Waals

interaction between the oxygen atoms and the nitrogen molecule. However, although overall the $Zn_4O(BDC)$ framework is electronically neutral, it is likely that there will be a local charge imbalance with the zinc atoms possessing a partial positive charge and the remainder of the framework carrying a negative charge of corresponding magnitude to ensure neutrality. It is therefore possible that coulombic forces that induce polarisation into the N_2 molecule, influencing the location of the nitrogen molecule in the $Zn_4O(BDC)$ cavities i.e. the principal interaction is an induced dipole-dipole interaction reminiscent of a van der Waals contact.

90K Structure

At 90K a nitrogen molecule is located at the site that is occupied at 120K. In addition, a second molecule is present in the framework cavities. Figure 5.3.8 shows the location of these molecules with respect to the $Zn_4O(BDC)$ framework. Atomic parameters for the nitrogen atoms of the gas molecules are provided in Table 5.3.4.

Table 5.3.4: Atomic parameters for physisorbed nitrogen gas at 90K

Atom	x	y	z	Occupancy	U_{iso}
N1	0.3389(3)	0.3389(3)	0.3389(3)	0.151(3)	0.125(5)
N2	0.3615(5)	0.3615(5)	0.3615(5)	0.151(3)	0.35(2)
N3	0.376(8)	0.38(2)	0.124(8)	0.054(7)	0.27(8)

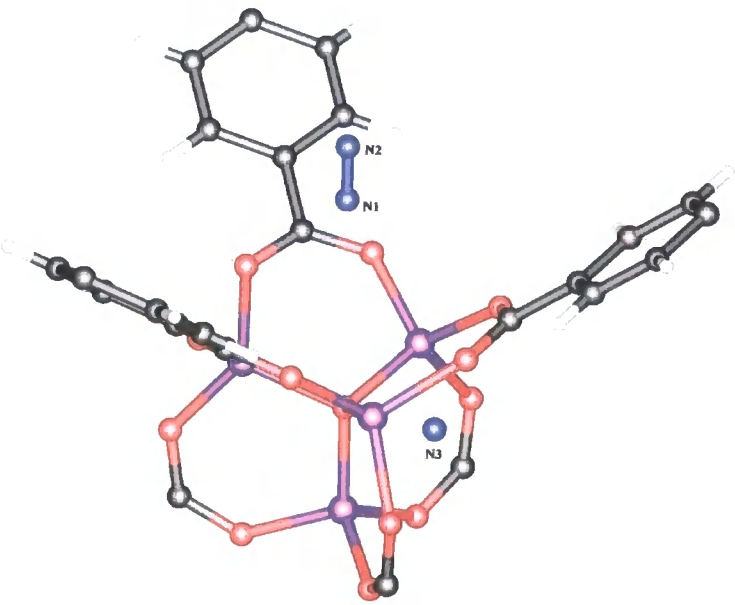

Figure 5.3.8: Location of molecule N1-N2 and N3 relative to the $Zn_4O(BDC)$ framework at 90K. (Zn: purple, O: red, C: black, N: blue, H: grey).

The refined N1-N2 bond length is 0.81(2) Å; this is considerably shorter than the expected 1.097 Å. The reason for this discrepancy is all too apparent from the F_{obs} Fourier map for this molecule (Fig.5.3.9). It can be seen that the atomic position for N2 is poorly defined due to a large degree of molecular motion, the large U_{iso} value 0.35(2) $Å^2$ for atom N2 is easily rationalised in light of this disorder.

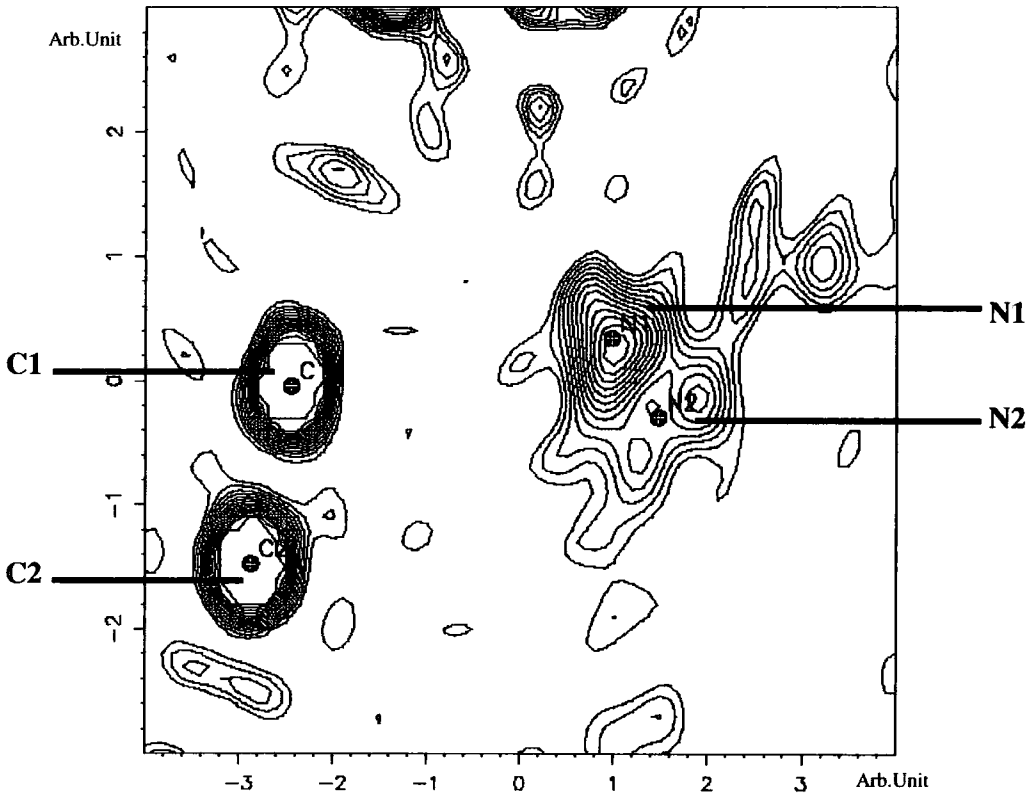

Figure 5.3.9: Slant-plane F_{obs} Fourier map defined by atoms N1, N2, and C1. The contour range is set to 0-5 $eÅ^3$ and the contour level is set to 0.3125 $eÅ^3$.

As the atoms of this molecule are not well resolved in the electron density map the occupancy values determined by SHELX must be expected to be inaccurate. Indeed, un-restrained isotropic refinement of the occupancy values for atoms N1 and N2 give significantly different values of 0.089(5) and 0.244(8), respectively. The latter of these values implies occupancy of greater than 100% for atom N2 (~146%). Ultimately the occupancy values of atoms N1 and N2 were constrained to be 91%. This occupancy was determined by constraining the occupancy values of N1 and N2 to be equal, but allowing this value to be refined as a free variable. Again, the U_{iso}

values for atom N2 is high at 0.35(2) $Å^2$, and this is due to the poor atomic definition in the Fourier map and the uncertainty in the occupancy value.

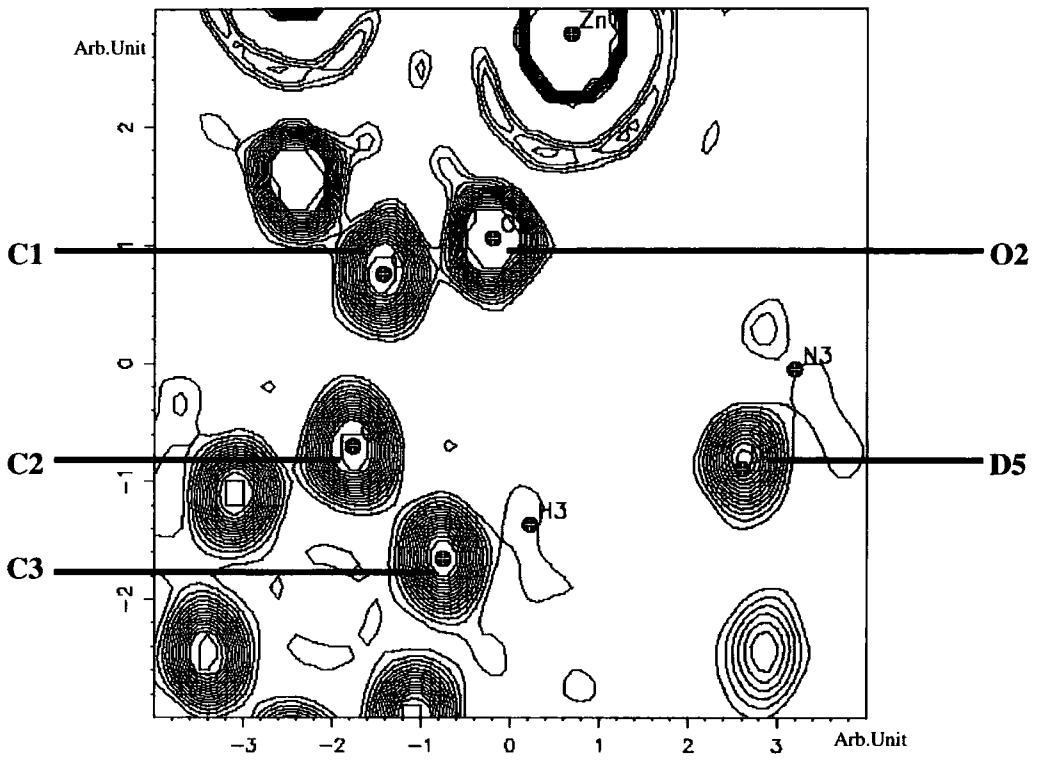

Figure 5.3.10: Slant-plane F_{obs} Fourier map defined by atoms N3, C1, and C2.The contour range is 0-10 $eÅ^3$ and the level is set to 0.635 $eÅ^3$.

Figure 5.3.10 is a slant-plane F_{obs} Fourier map in which N3 features. A significant electron density peak can be seen ~1.0 Å from N3 (flagged as D5). This peak could either represent the second nitrogen atom of the diatomic gas molecule, or a more preferable location for N3. Initially, a second atom, N4, was positioned on this peak, however upon isotropic refinement (with N3 in an isotropic state) this atom became unstable, and was deleted. Atom N3 was then forced to this location. When refined the atom shift slightly but did not return to its original position. The ADP values for the atom were slightly reduced, and the occupancy hardly affected. Figure 5.3.11 displays the Fourier map with atom N3 in its new location. Although the atom N3 still appears to be inadequately located, it should be realised that this is but a single plane through the molecule and provides limited information. Attempts to generate a more informative F_{obs} map failed due to a lack of appropriately positioned atoms to define different slant-planes.

However it should be noted that the presence of significant electron density in the framework cavity at the location marked by atom N3 is indicative of a second nitrogen atom at this site.

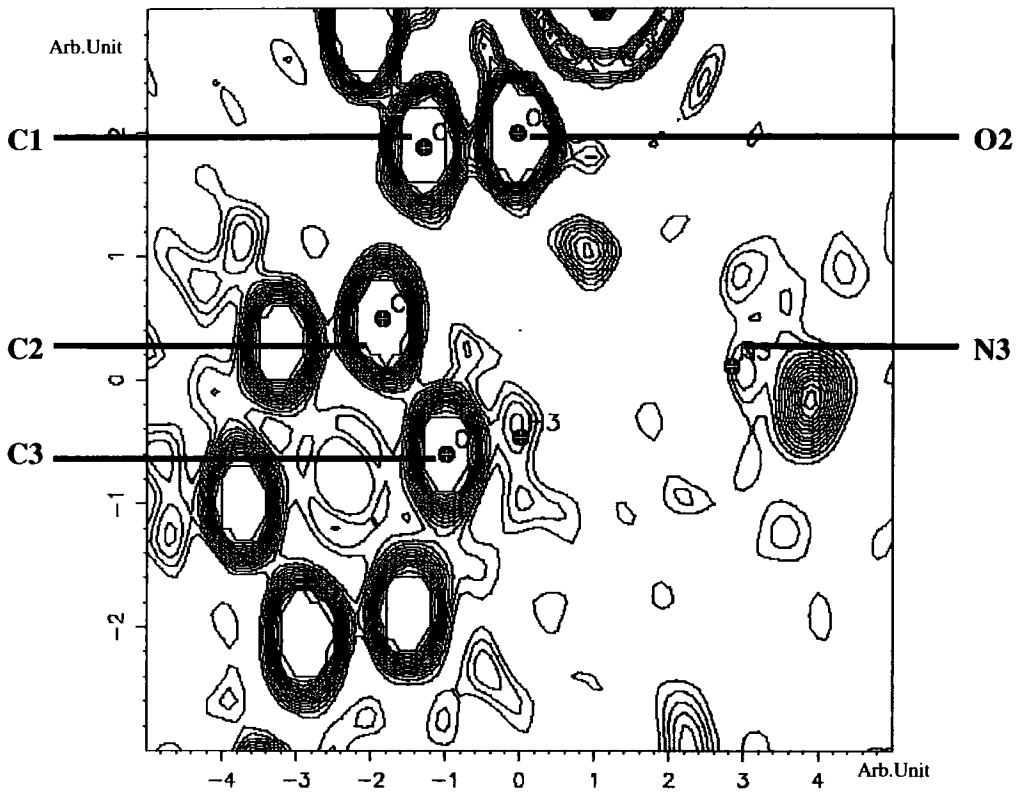

Figure 5.3.11: Slant-plane F_{obs} Fourier map defined by atoms N3, C1, and C2. The contour range is 0-5 eÅ^3 and the level is set to 0.3125 eÅ^3.

Several attempts were made to include the second atom of this molecule into the structural model, on each occasion the refinement of this additional atom became unstable. The Fourier maps indicate that the two atoms of the molecule cannot be resolved, and this would account for the failure of the diatomic model. The best model that can be suggested for this molecule at the present time is the single atom model that has been implemented. This is clearly erroneous, and can only serve as a very poor approximation, and limited reliance can be placed on the occupancy value deduced by SHELX. The final U_{iso} and occupancy values for N3 were determined to be 0.27(8) Å^2 and 0.054(7), respectively. The precise location of molecule N3 is uncertain, and is either on site with *m* or 3*m* symmetry, as such the occupancy is estimated as being between 11-32%.

The shortest contacts between the framework and the gas molecules at 90K are: N3···Zn, 3.83(8) Å; N3···O2, 3.5(2) Å; N3···H, 3.16 Å; N1···Zn, 3.81(1) Å; N1···O1, 3.98(1) Å; N1···O2, 3.513(9) Å. All these values are considerably greater than the sum of the van der Waals radii for the atom pairs, indicating that the induced dipole – dipole interactions that are present between the gas and framework atoms are weak.

50K Structure

Three nitrogen molecules of partial occupancy are located within the cavities of the framework at 50K (Fig. 5.3.12). Atomic parameters for the nitrogen atoms of the gas molecules are given in Table 5.3.5. The first of these molecules, N1-N2, resides over a face of the zinc tetrahedron, and has a bond length of ~0.95 Å. The N5-N6 bond length is ~0.93 Å. In both molecules the bond length is shorter than the expected 1.097 Å. A certain degree of leniency must be given to the refined parameters of the gas molecules, and as these values are not drastically incorrect, they have been retained (as opposed to introducing restraints to the model). However, it was necessary to constrain the occupancy values of atoms of the same diatomic gas molecule to be equivalent.

Table 5.3.5: Atomic parameters for physisorbed nitrogen gas at 50K

Atom	x	y	z	Occupancy	U_{iso}
N1	0.3345(1)	0.3345(1)	0.3345(1)	0.147(2)	0.038(1)
N2	0.3554(3)	0.3554(3)	0.3554(3)	0.147(2)	0.131(4)
N5	0.251(1)	0.4133(7)	0.0867(7)	0.087(5)	0.11(1)
N6	0.286(1)	0.420(1)	0.080(1)	0.087(5)	0.13(1)
N7	0.486(2)	0.346(1)	0.346(1)	0.072(7)	0.15(2)

The third molecule (N7-N7') straddles a two-fold rotation axis, and as such only one atom of the molecule is present in the asymmetric unit. The N7-N7' bond length is 0.7(1) Å. This value is markedly shorter than the expected value for a nitrogen molecule; this combined with the poor accuracy of the bond length suggests that atom N7 may not be ideally positioned. It should be noted that the nitrogen atoms have not been numbered sequentially; this has been done to differentiate between molecules that reside at different locations in the framework cavity e.g. molecule N5-N6 has not been denoted as N3-N4 as this molecule is situated at a site that is

different to molecule 'N3' observed at 90K. The highest residual electron density peak is of ~ 0.66 eÅ^3, this is too low to be considered as a site for a fourth nitrogen molecule.

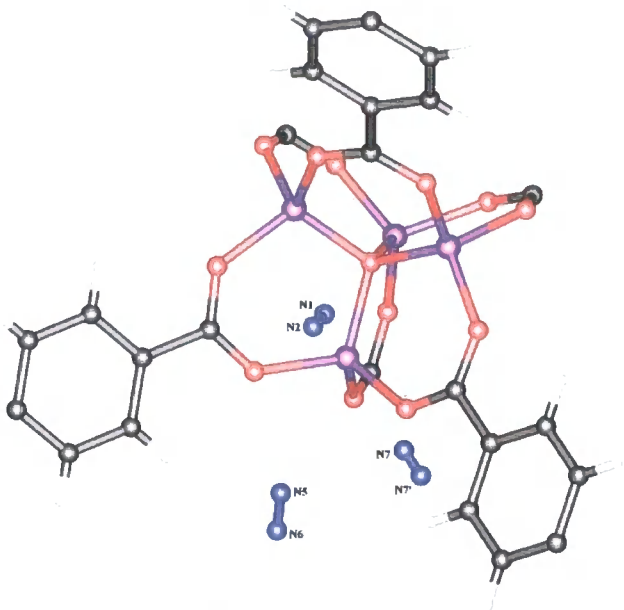

Figure 5.3.12: Location of the three nitrogen molecules absorbed at 50K relative to the $Zn_4O(BDC)$ framework at 50K. (Zn: purple, O: red, C: black, N: blue, H: grey).

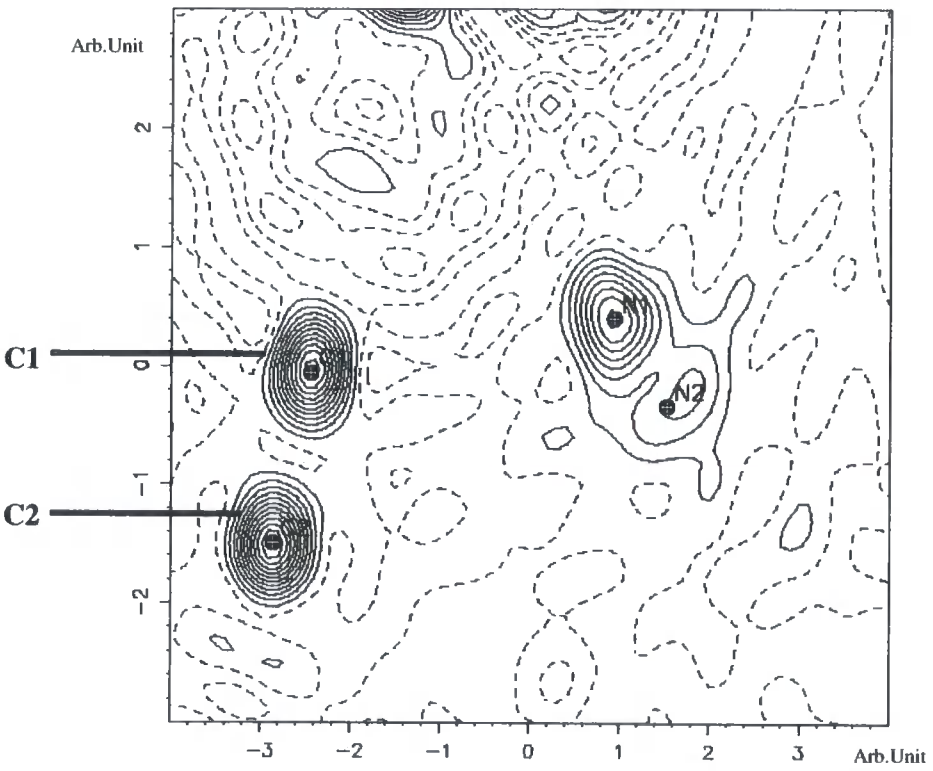

Figure 5.3.13: Slant-plane F_{obs} map defined by atoms N1, N2, and C1. The contour range is set to –3.782-14.344 eÅ^3 and the level 1.1328 eÅ^3.

The evidence for molecule N1-N2 is presented in Figure 5.3.13. Atom N1 is well defined, but the positioning of atom N2 is less clear. This is due to the motion of the atom, which also accounts for the short N1-N2 bond length. Comparison of the peak heights for atoms C1 and N1 suggests that the occupancy of atom N1 is 62%. The SHELX refinement gives a value nearer 100%. The value determined by SHELX should therefore be regarded with caution.

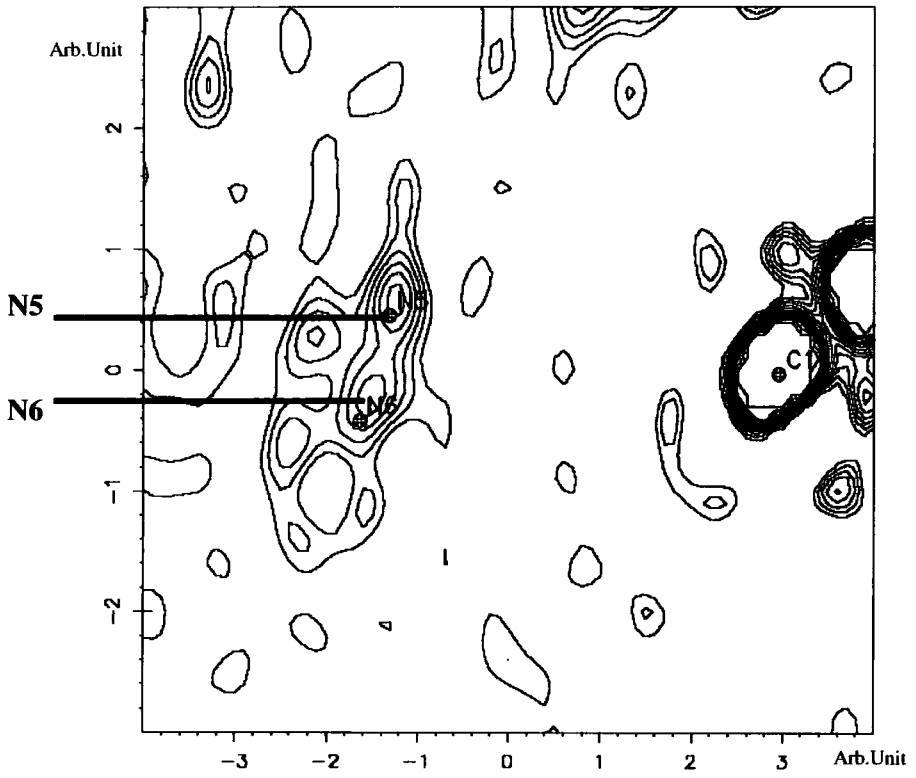

Figure 5.3.14: Slant-plane F_{obs} map defined by atoms C1, N5, and N6. The contour range is set to 0-3 eÅ^3 and the level is set at 0.1875 eÅ^3.

Figure 5.3.14 is a F_{obs} Fourier map in which the nitrogen molecule N5-N6 features. This map provides confirmation for the existence of this molecule within the $Zn_4O(BDC)$ framework at 50K. The extensive disorder displayed by the molecule is clearly evident. A more complex model incorporating a Bessel function will need to be formulated to represent the thermal motion of this molecule more accurately. This molecule is located at a site of mirror symmetry. The final occupancy for this molecule was refined to be ~17%

Figure 5.3.15 shows that there are two density maxima in the Fourier map of the third nitrogen molecule, however they are not well defined. The refined atomic position for N7 is not ideal

because of the inadequate atomic resolution in the F_{obs} map. This explains the short N7-N7' bond length, and its associated high error value. The final occupancy for this molecule was calculated to be ~7%

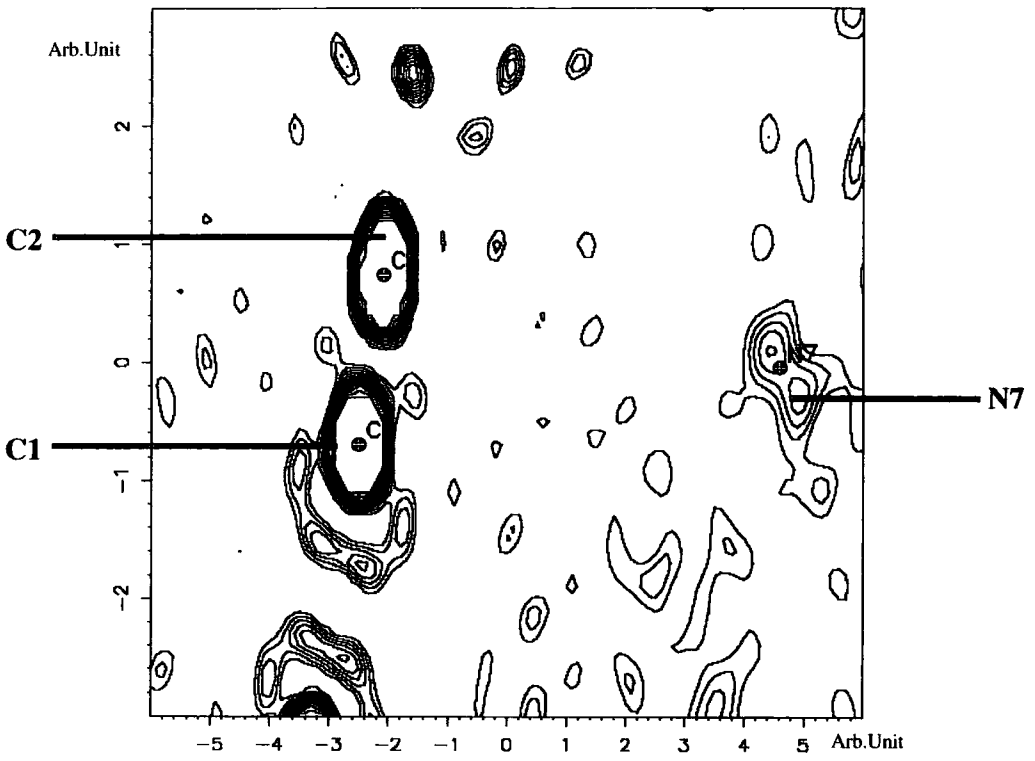

Figure 5.3.15: Slant-plane F_{obs} map defined by atoms C1, C2, and N7. The contour range is set to 0-3 $eÅ^3$ and the level 0.1875 $eÅ^3$.

The shortest nitrogen-framework distances are: N1···O1, 3.787(5) Å; N1···O2, 3.392(3) Å; N1···Zn, 3.635(4) Å; N3···O2, 3.72(2) Å; N5···H3, 3.30 Å; N6···O2, 3.87(3) Å; N6···H, 3.14 Å. These values greatly exceed the sum of the van der Waals radii for these atom pairs indicating that any 'induced' van der Waals forces present are very weak. The distance between the centroid of the N7-N7' bond and the centroid of the phenyl ring of the linker molecule is 3.51 Å. To date, there exists no consensus as to the distance limits for aromatic interactions.[6,7] In addition to this, due to the novel nature of the work presented, there is no precedent for stating that nitrogen molecule N7-N7' is interacting with the phenyl ring of the framework. That said, the positioning of N7-N7' over the ring face, and the relatively close proximity of the ring centroid and the centroid of the N7-N7' triple bond would suggest that some form of intermolecular interaction is stabilising the arrangement.

30K Structure

Three nitrogen gas molecules are found to be absorbed into the $Zn_4O(BDC)$ framework cavities at 30K (Fig. 5.3.16), details of which are listed in Table 5.4.6. The bond lengths between the nitrogen atoms in the gas molecules are in the range of 0.403-1.001 Å. In the final crystallographic model the distance between these atoms were restrained to be 1.09(2) Å. Furthermore, it was necessary to constrain the occupancy values for atoms of the same gas molecule to be equal.

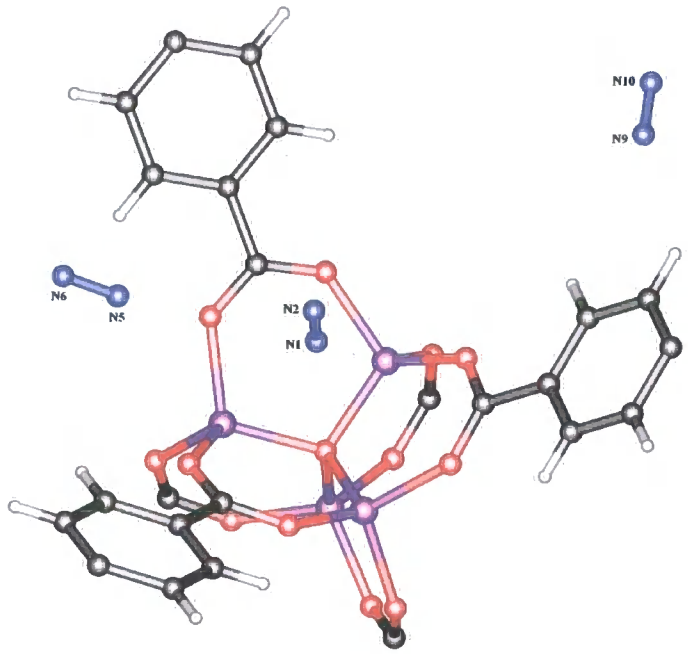

Figure 5.3.16: Location of the three nitrogen molecules absorbed at 30K relative to the $Zn_4O(BDC)$ framework (Zn: purple, O: red, C: black, N: blue, H: grey).

Table 5.3.6: Atomic parameters for physisorbed nitrogen gas at 30K

Atom	x	y	z	Occupancy	U_{iso}
N1	0.3337(1)	0.3337(1)	0.3337(1)	0.16667	0.0292(9)
N2	0.3568(2)	0.3568(2)	0.3568(2)	0.16667	0.091(3)
N5	0.256(1)	0.412(1)	0.088(1)	0.081(6)	0.088(8)
N6	0.274(4)	0.439(2)	0.061(2)	0.081(6)	0.27(4)
N9	0.384(1)	0.5	0.116(1)	0.039(5)	0.08(1)
N10	0.414(2)	0.5	0.086(2)	0.039(5)	0.32(7)

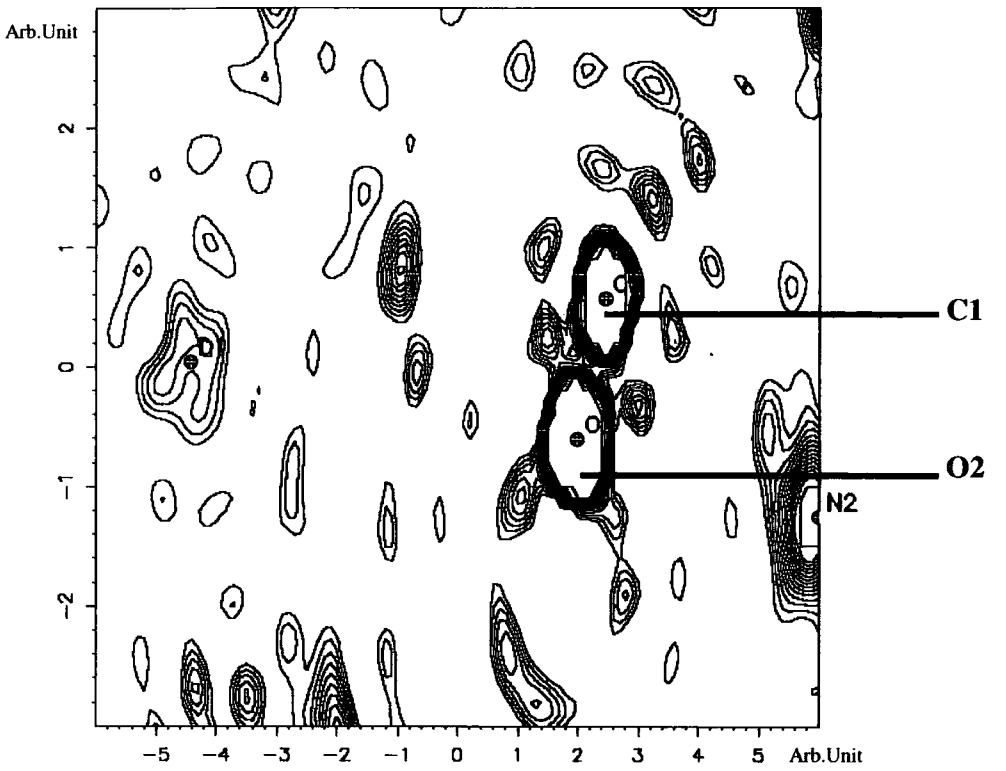

Figure 5.3.17: Slant plane F_{obs} map defined by atoms D1, C1, and O2. The contour range is set to 0-3 eÅ^3, and the level 0.1875 eÅ^3.

The highest residual peak reported by SHELX is ~0.84 eÅ^3 at x, y, 0. Atom D1 (arbitrary label) was assigned to this position and refined isotropically. The occupancy refined to 0.027(4) and U_{iso} to 0.03(1) Å^2, this corresponds to a percentage occupancy of ~5%. SHELX identified a second atom site 0.610 Å from D1; this peak was only 0.54 eÅ^3 in height. A second atom was placed here and refined; this resulted in its atomic coordinates becoming unstable. This is not surprising as this is far too low a residual to be considered as a genuine atom position. Figure 5.3.17 is a F_{obs} map that displays 'atom' D1. The difficultly in assigning the second nitrogen atom to the 'molecule' can now be understood, as only one peak maximum is evident in the Fourier map. It maybe possible that this site is a real gas molecule position, but the low electron density and poor definition in the Fourier makes this unlikely. No gas molecule was assigned at this position in the final structural model.

The N1-N2 molecule was well defined in the F_{obs} Fourier map, and the occupancy of the molecule was fixed at 100% (refinement gave 105%). Figure 5.3.18 provides evidence for the presence of the second gas molecule N5-N6 in the framework cavities at 50K. The position of

atom N5 appears to be relatively well defined in this map. More than one density maximum can be identified in Fourier map, which supports the case for modelling the second atom of the molecule, namely N6.

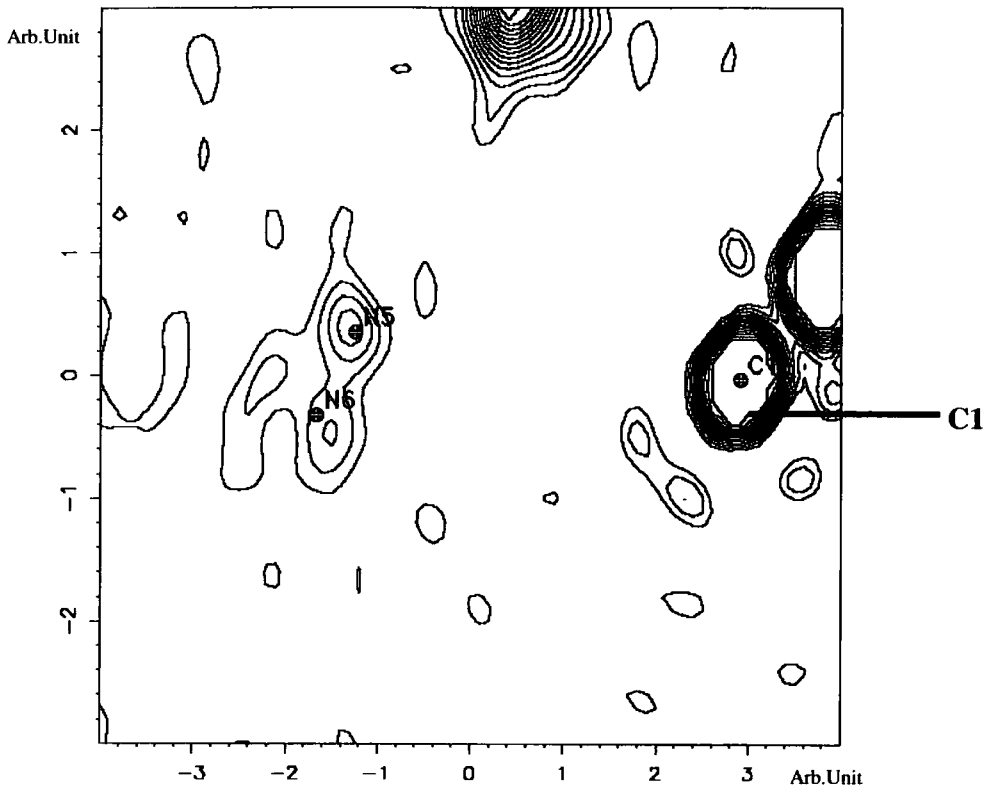

Figure 5.3.18: Slant plane F_{obs} map defined by atoms C1, N5, and N6. The contour range is set to 0-5 eÅ^3, and the level 0.3125 eÅ^3.

It is apparent from the Fourier map that the location of atom N6 is poorly defined. This is not surprising as the electron density in this region is rather 'smeared'. This would account for the N5-N6 bond length being foreshortened to 0.796 Å. The electron density of this molecule is dumbbell shaped with the individual atoms not fully resolved, this makes evaluation of the occupancies of the individual atoms subject to some error. The poor atomic resolution, and difficulty in determining accurately the atomic occupancy values, accounts for the large U_{iso} value of 0.27(4) Å^2 for N6 (occupancy values for atoms N5 and N6 were fixed at 17.4%). A preferable model for the nitrogen molecule N5-N6 would be to treat the molecule as a single entity, not as two discrete atoms, and apply a suitable structure factor model i.e. Bessel function.

The Fourier map shown in Figure 5.3.19 displays the region in which the nitrogen molecule N9-N10 is located. The electron density associated with this molecule is very diffuse in nature. It is

likely that there is significant thermal motion associated with this molecule. However in the map more than one density maximum can be observed, implying that modelling this density as a diatomic molecule is appropriate.

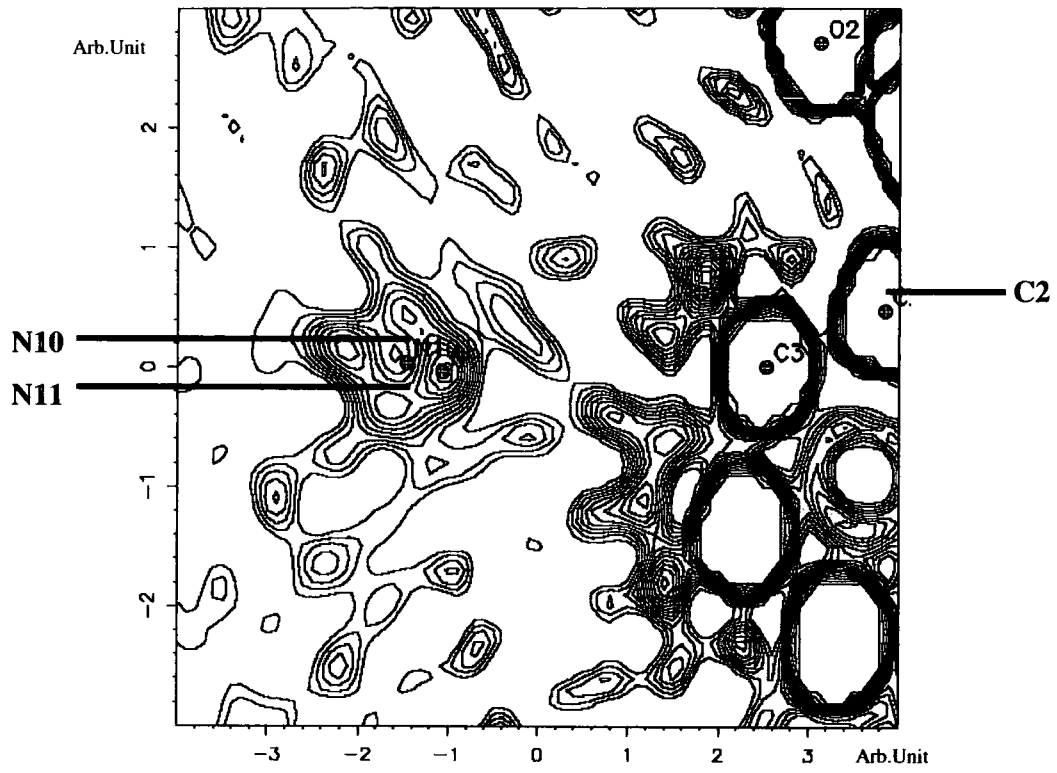

Figure 5.3.19: Slant plane F_{obs} map defined by atoms C3, N9, and N10. The contour range is set to 0-2 eÅ^3, and the level 0.125 eÅ^3.

Critical examination of the map presented in Figure 5.3.19 indicates that atom N10 does not seem to be well placed. Obtaining a realistic atom model for this molecule is not easy, as a certain degree of 'molecular tumbling' is clearly apparent. Again, modelling the molecule as a single entity may be preferable. A more immediate solution is to attempt to 'shift' atom N10 to a more realistic location because at present the N9-N10 bond length is only 0.403 Å. The distance between atoms N9-N10 was restrained to be 1.09(2) Å, and upon refinement the distance increased to a more reasonable value of 1.10(2) Å, with atom N10 shifting to the peak maximum to the left of the atom flag in Figure 5.319. The final occupancy for this molecule was determined to be 16%.

Several close framework–nitrogen contacts can be observed at 30K, these include: N5···H, 3.24 Å; N6···H, 3.59 Å; N9···H, 3.10 Å. The sum of the van der Waals radii for nitrogen and

hydrogen is 2.75 Å. This would suggest that weak hydrogen bond interactions are present between the polarised nitrogen molecules and the 1,4-benzenedicarboxylate linker molecules. Other contacts include: N1···O1, 3.754(5) Å; N1···O2, 3.372(3) Å; N1···Zn, 3.606(4) Å; N5···H, 3.24. All of these contacts exceed the sum of the van der Waals radii for the atom pairs, and as such should be considered as very weak interactions.

5.3.3 Summary for the refinement of nitrogen-loaded Zn_4O(BDC) structures

In Section 5.3.2 of this chapter the refinement of nitrogen-loaded Zn_4O(BDC) was discussed. Five symmetry unique absorption sites were identified. The modelling of the gas molecules within the framework cavities is non-trivial and the models proposed for the nitrogen molecules in the final structural models must be considered as an approximation; a simple model for a complex problem. As the models are not ideal, the refined free variables, in particular the occupancy values, must be regarded as circumspect, and care taken not to over interpret their significance. That said, by direct examination of the Fourier maps based on the observed structure factors clear evidence pertaining to the existence of the nitrogen molecules can be seen. In addition, the refinement of the gas molecules was performed carefully, with all atomic parameters (x, y, z, occupancy and U_{iso} values) and their associated error values scrupulously evaluated.

Many of the nitrogen molecules exhibit considerable disorder, such as molecular tumbling, and would benefit from being modelled as single entities as opposed to as diatomic molecules comprising two discrete atoms. The electron density for such a molecule could be approximated to a sphere. Subsequently, diffraction from this sphere can be modelled by altering the atomic structure factors for the atoms involved using a Bessel function (i.e. the structure factor for the N_2 molecule), which mathematically defines the diffraction from a spherical aperture, and from consideration of Babinet's theorem, diffraction from a spherical aperture is equivalent to diffraction from a sphere (see Appendix 3).

5.3.4 Argon-loaded Zn_4O(BDC)

The same philosophy used in the analysis of nitrogen-loaded Zn_4O(BDC) (Section 5.3.2) was applied to the refinement of argon-loaded Zn_4O(BDC). As argon is a mono-atomic gas, in many respects the refinement of the argon gas within the framework cavities is less complex than for the refinement of the nitrogen gas systems. The individual datasets will now be reviewed in turn.

In all cases the non-hydrogen atoms of the framework system were refined anisotropically, and the gas atoms were refined isotropically unless stated otherwise.

293K Structure

At 293K the cavities of the $Zn_4O(BDC)$ framework were found to be fully evacuated. The highest residual electron density in the Fourier difference map is 0.519 $eÅ^3$ and is located at ~1.59 Å from C1. The unit cell parameters for the nitrogen- and argon-loaded systems recorded at 293K are in reasonable agreement (Tables 5.3.1 and 5.3.2). The framework is well ordered and all the non-hydrogen atoms were refined anisotropically.

90K Structure

At 90K four argon atoms with partial occupancy are located in the $Zn_4O(BDC)$ framework cavities, Table 5.3.7 summarises the atomic parameters for these atoms. Figure 5.3.20 shows the position of the gas absorption sites relative to the framework. To support the atom assignments the relevant Fourier maps based on F_{obs} have been evaluated.

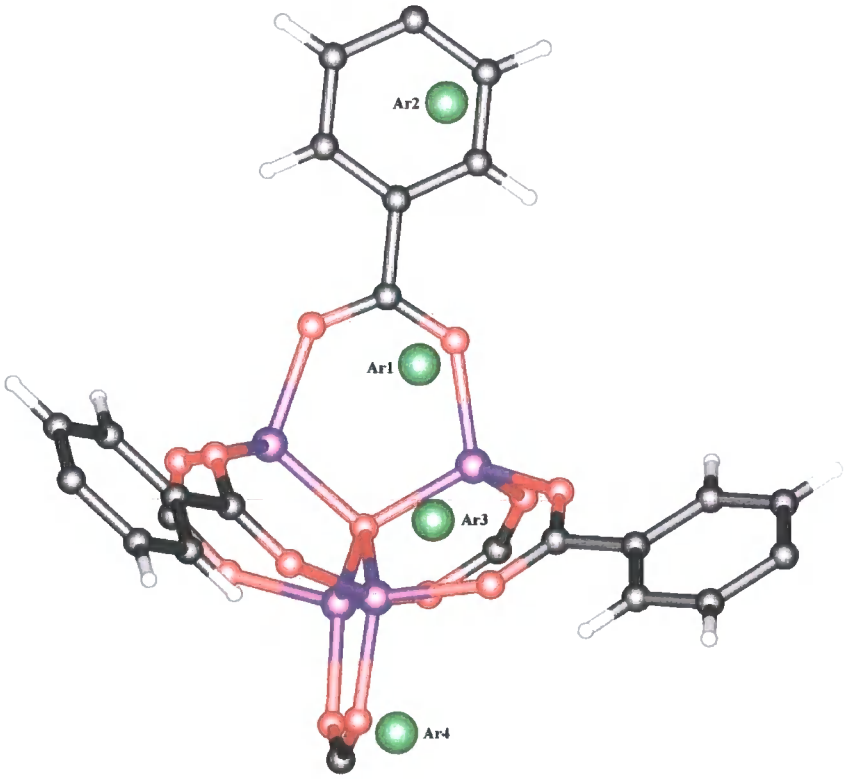

Figure 5.3.20: Location of the four argon gas atoms relative to the $Zn_4O(BDC)$ framework at 90K. (Zn: purple, O: red, C: black, Ar: green, H: grey).

Table 5.3.7: Atomic parameters for physisorbed argon gas at 90K

Atom	x	y	z	Occupancy	U_{iso}
Ar1	0.15623(8)	0.34377(8)	0.15623(8)	0.123(1)	0.081(1)
Ar2	0.152(1)	0.5	0.152(1)	0.028(2)	0.17(2)
Ar3	0.2522(7)	0.4147(5)	0.0853(5)	0.087(3)	0.163(8)
Ar4	0.3777(4)	0.3777(4)	0.1223(4)	0.031(1)	0.090(6)

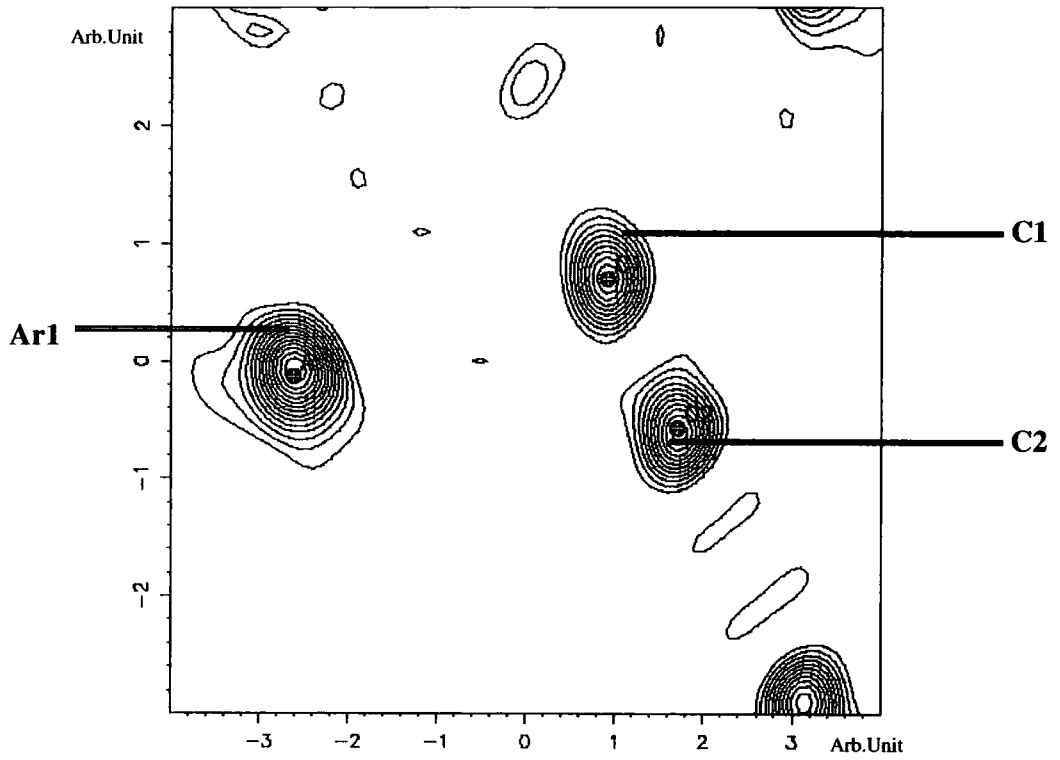

Figure 5.3.21: Slant-plane F_{obs} Fourier map defined by atoms Ar1, C1, and C2. Contour range is set to 0-17.44 eÅ^3 and the contour level is set to 1.09 eÅ^3.

Figure 5.3.21 provides conclusive evidence of presence of atom Ar1 in the $Zn_4O(BDC)$ framework cavities. The atom is reasonably well defined in the F_{obs} map and as such an attempt was made to deduce the atom occupancy directly from the map. The relative heights of the carbon (C2) and argon peaks were evaluated; these were found to be 13.04 eÅ^3 and 17.44 eÅ^3, respectively, this gives a peak ratio of 1.34. Accounting for the difference in atomic numbers (Z),

and including the reduction in occupancy due to Ar1 being located on a special position (3*m* point symmetry - 32*f*), the final occupancy of Ar1 was calculated to be 0.0743. This is 60% of the occupancy value of 0.123(1) determined by the isotropic SHELX refinement. Once the reduction due to symmetry has been corrected for, this equates to an occupancy value of 74% for atom Ar1.

The discrepancy between the occupancy values calculated manually from the Fourier maps and those calculated by SHELX, highlights the need for caution when considering the refined occupancy values. There are several sources of error that maybe responsible for the difference between the two values:

1. The SHELX occupancy values are inaccurate; this is reflected by the relatively high error values associated with the refined occupancy values.

2. The determination of the total electron density from the Fourier maps is not particularly accurate. This problem is two-fold; firstly, the electron density of the gas atoms tends to be rather diffuse making quantification of the electron density difficult. The use of dummy atoms can only partially resolve this problem (see discussion of atom Ar3 for an example). Secondly, because of the diffuse nature of the atoms the plane defining the Fourier map is not easily determined, this may result in a distorted view of the density and inaccuracy in the measurements.

3. The differences in the SHELX refinement values and the values derived from the Fourier map may be a result of the combination of the above sources of error.

To check the reproducibility of the SHELX refinement, the Ar1 occupancy was fixed at 0.0743, and U_{iso} refined. Once U_{iso} had reached a constant value it was fixed and the occupancy was allowed to refine. An increase of ~10% was observed in the occupancy value upon refinement. Both parameters were then allowed to refine together. Interestingly, when the occupancy was refined with the thermal parameters it returned to the original value of 0.1223(1). In conclusion, the exact value for the occupancy of atom Ar1 is difficult to determine. Although the SHELX refinement value does seem to be stable, adding support to the use of this value, it is by no means conclusive, and care should be taken not to over interpret the values calculated, for this, or any other gas atom.

The refinement of argon atom Ar2 (which is situated on a site of *mm*2 symmetry) proved to be a very good example of the necessity of cautious evaluation of the Fourier maps for the gas atoms in this structure. The Fourier map for this atom is shown in Figure 5.3.22, and is defined by atoms Ar2, C2 and the dummy atom D2. Atom D2 was included to allow the slant-plane to be defined more easily, at no point was it included in the refinement. Dummy atoms D6 and D7 were included in the structural model to help quantify the electron density associated with atom Ar2. These atoms were included in the structural refinement (x, y, z parameters were not refined) to incorporate their phase information into the Fourier calculation. Their positional coordinates were deduced from the Fourier map.

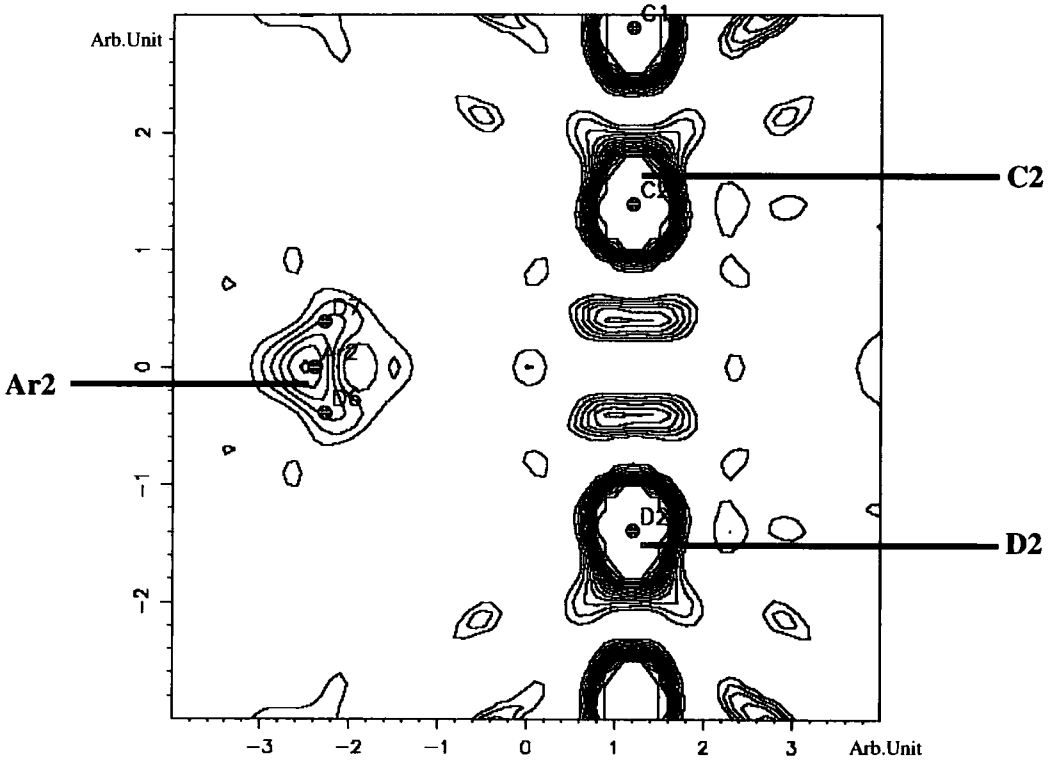

Figure 5.3.22: Slant-plane F_{obs} map. Atoms C2, D2, and Ar2 define the plane. The contour level is set to 0.3636 eÅ^3 and the range is 0-4 eÅ^3.

From examination of the Fourier map it appears that atom Ar2 is 'librating'. However, when the dummy atoms D6 and D7 were refined, the occupancy for atom D7 became negative, and the U_{iso} value for D6 became an unrealistic 2.0(0.5) Å^2, and as such both 'atoms' were deleted. Therefore the limbs of libration indicated by the Fourier map (locations of D7 and D6) are

unlikely to be genuine electron density associated with atom Ar2, but rather a spurious artefact of the high symmetry of the system (the high symmetry increases the *residual* electron density peaks artificially increasing their prominence). The occupancy of atom Ar2 was calculated from the Fourier map to be 0.0108 (4%). The occupancy value determined by the isotropic SHELX refinement was 0.028(2) (11%). Once again inconsistencies between the SHELX and Fourier map calculated occupancies are noticeable.

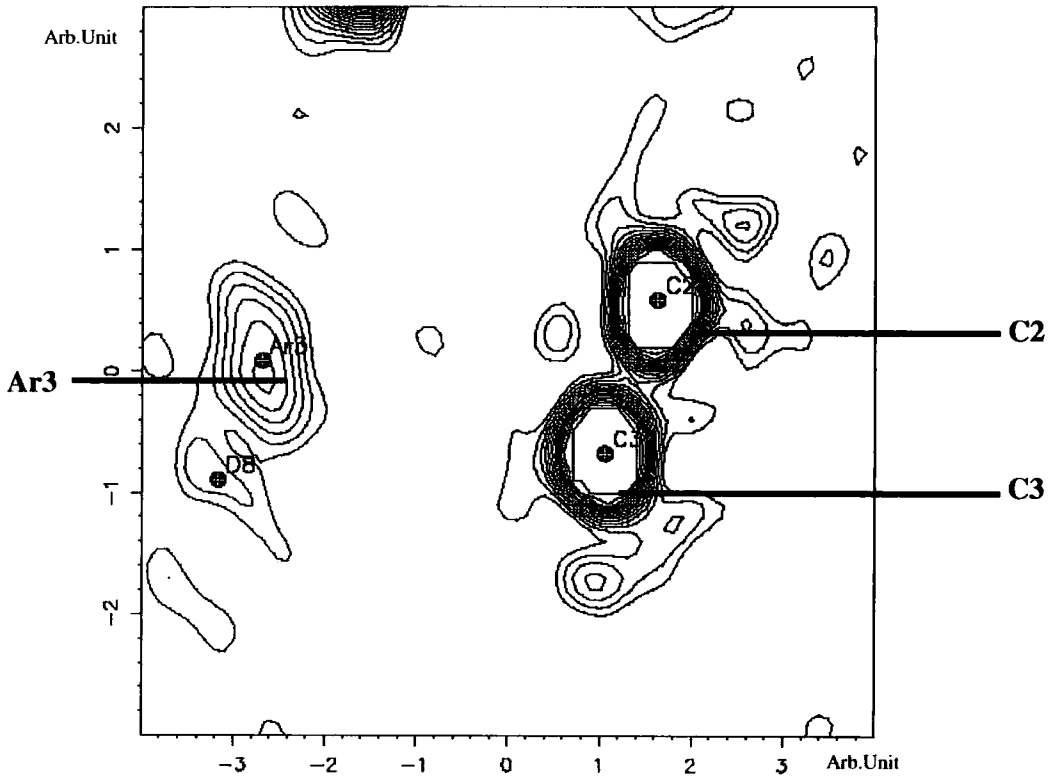

Figure 5.3.23: Slant-plane F_{obs} Fourier map defined by atoms C2, C3, and Ar3. The contour level is set to 0.25 eÅ^3 and the range is 0-4 eÅ^3.

Figure 5.3.23 provides evidence as to the presence of atom Ar3 in the cavities of $Zn_4O(BDC)$ at 90K. This atom resides on a site of mirror symmetry (position 96*k*). The calculation of the occupancy for atom Ar3 from the Fourier map is not a trivial matter; it can be seen clearly from Figure 5.3.22 that the electron density for this atom is not well defined, and that significant low-level residual density is apparent. There is a relatively large area of electron density just below atom Ar3 in Figure 5.3.23; it is possible that this is a second position for Ar3, albeit with low occupancy. To test this theory a dummy atom, D8, was positioned here and refined. The co-ordinates of D8 were inferred by examination of the Fourier map. Upon refinement the final

occupancy of D8 became 0.01(1) and U_{iso} became 0.63(0.55) $Å^2$. These figures and their respective error values indicate that D8 cannot be regarded as a genuine atom position, nor can it be used to evaluate the electron density of atom Ar3.

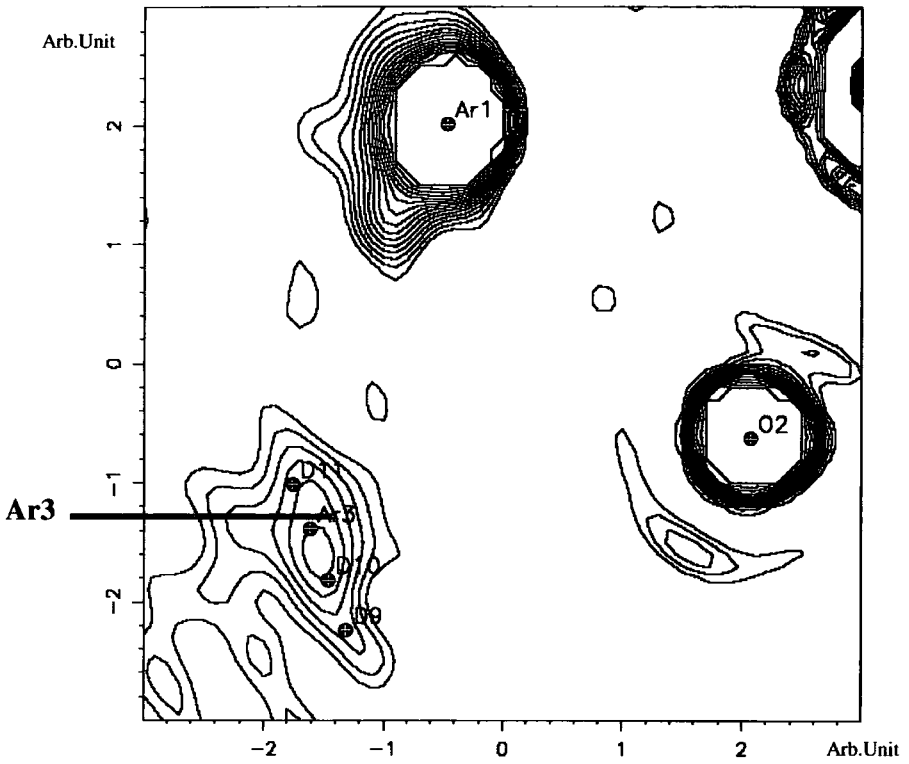

Figure 5.3.24: Slant-plane Fourier map defined by atoms Ar3, Ar1, and O2. This diagram shows the relative positions of the dummy atoms D9, D10 and D11. The contour level is set to 0.3636 $eÅ^3$ and the range is 0-4 $eÅ^3$.

Due to the difficulty in analysing the electron density associated with atom Ar3 from the Fourier map given in Figure 5.3.23, a second plane through atoms Ar3, Ar1 and O2 was investigated (Fig. 5.3.24). Dummy atoms D9, D10, and D11 were added to the model; the coordinates of these atoms were deduced from the Fourier map. However, when D10 was refined it gave a negative occupancy and a U_{iso} value of ~0.00 $Å^2$, and as such was deleted. The total occupancy of the Ar3 atom (including the density contributions from D9 and D11) based on the Fourier map was 0.0504 (10%). The total occupancy based on the isotropic SHELX refinement (sum of Ar3, D9 and D11 occupancies) is 0.108(9) (22%). The occupancy of Ar3 determined by the isotropic SHELX refinement is 0.087(3) (17%). Again, clear differences in the occupancy for Ar3 determined from the SHELX refinements and from examination of the Fourier map are evident.

Both atoms Ar2 and Ar3 exhibit a high degree of inaccuracy in their refined U_{iso} values (0.17(2) $Å^2$ and 0.162(8) $Å^2$ respectively) this can be rationalised by the diffuse nature of the electron density defining these atoms (Figures 5.3.22 and 5.3.23). An anisotropic refinement with second-order tensors was attempted for both Ar2 and Ar3, the resultant occupancy and U_{ij} values are given in Table 5.3.8. The refined occupancy values for atoms Ar2 and Ar3 equate to 16% and 19%, respectively.

Table 5.3.8: Occupancy and U_{ij} values (second-order tensor) for atoms Ar2 and Ar3 at 90K.

Atom	Occupancy	U_{11}	U_{22}	U_{33}	U_{23}	U_{13}	U_{12}
Ar2	0.04(1)	0.33(4)	0.15(2)	0.33(4)	0.000	-0.25(4)	0.0000
Ar3	0.095(3)	0.31(2)	0.139(7)	0.139(7)	-0.017(8)	-0.04(1)	-0.04(1)

Several of the U_{ij} values for atom Ar2 (in particular the U_{33} and U_{13}) are rather high, and for this reason the tensor model was extended to incorporate fourth-order terms (as the atom resides on a centrosymmetric site, the 3-D density probability function for the ADP values must reflect this symmetry. This cannot be achieved using third-order terms alone, and hence the need to included the fourth-order tensor terms in the refinement). The refinement of the ADP values using the forth-order model failed because stable values could not be obtained for several of the cross-delta terms.[†]

A third-order tensor model was applied to the ADP values for atom Ar3, although the refinement was successfully completed, the final gamma terms were not significantly greater than their associated error values. It can be concluded therefore that a second-order tensor model is preferable for atom Ar3.

Atom Ar4 is located on a site of 3*m* point symmetry (position 32*f*). The electron density for this atom is relatively well defined (Fig. 5.3.25). Atom D4 is a dummy atom included in the model to allow the plane of the Fourier map to be defined. The occupancy of atom Ar4 was calculated from the Fourier map, and was found to be 0.033. This is in agreement with the value of 0.031(1) obtained from the SHELX refinement. Once the reduction due to symmetry has been corrected for, this equates to occupancy of 19% for atom Ar4. Interestingly, in spite of the diffuse nature of

[†] All higher-rank (greater than second-order) tensor analyses were performed using the in-house program UPALS written by Dr. G. J. McIntyre (Institut Laue-Langevin, France).

the electron density, no dummy atoms were required to determine the total electron density of atom Ar4.

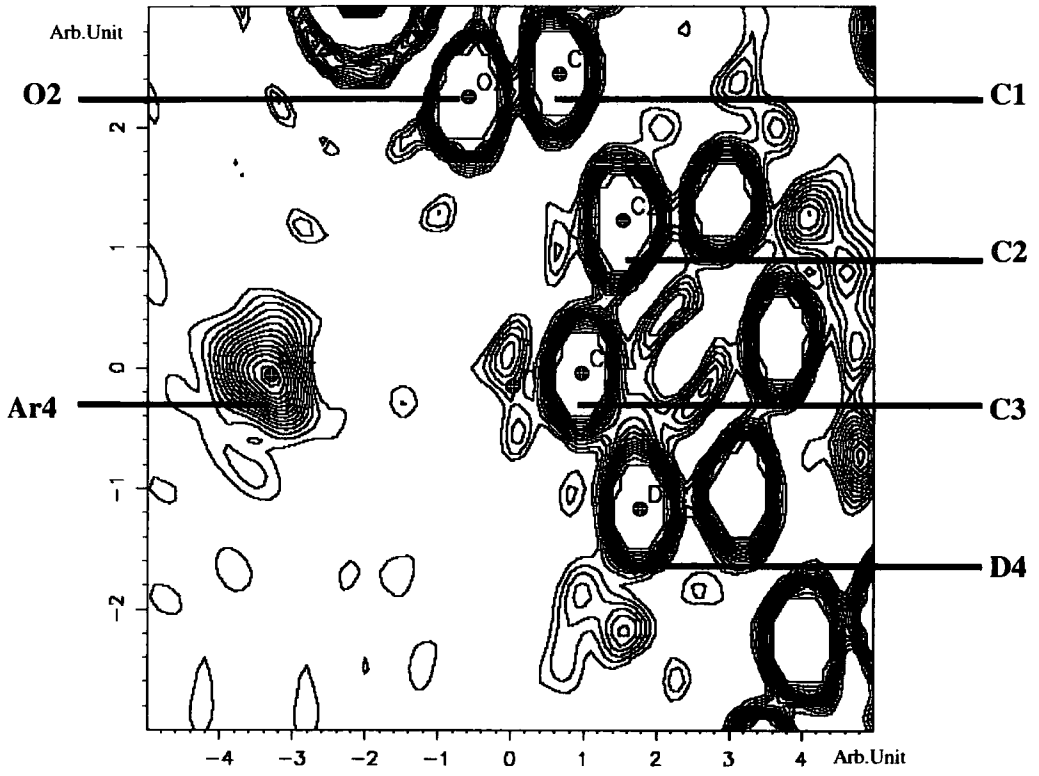

Figure 5.3.25: Slant-plane F_{obs} Fourier map defined by atoms Ar4, C2, and D4. The contour level is set to 0.3636 eÅ^3 and the contour range is 0-4 eÅ^3.

The shortest framework-gas interactions are as follows: Ar4···Zn, 3.78(2) Å; Ar1···Zn, 4.001(3) Å; Ar4···O2, 3.57(1) Å; Ar3···O1, 3.76(2) Å; Ar1···O2, 3.658(3) Å; Ar4···H, 3.32 Å; Ar3···H, 3.32 Å. The van der Waals radius for argon is 1.88 Å; therefore the sum of the van der Waals radii for the atom pairs involved in these 'contacts' are 3.40 Å (Ar-O) and 3.08 Å (Ar-H). This would suggest that any induced van der Waals interactions that are present are weak. The distance from atom Ar2 and the centroid of the benzene ring of the linker molecule is 3.578 Å. This may indicate the presence of a weak interaction between the polarisable electron density of the argon atom and the π-electron density of the benzene ring system.

50K Structure

At 50K six absorption sites have been identified; these are shown in Figure 5.3.26. Atomic parameters for these gas atoms are given in Table 5.3.9.

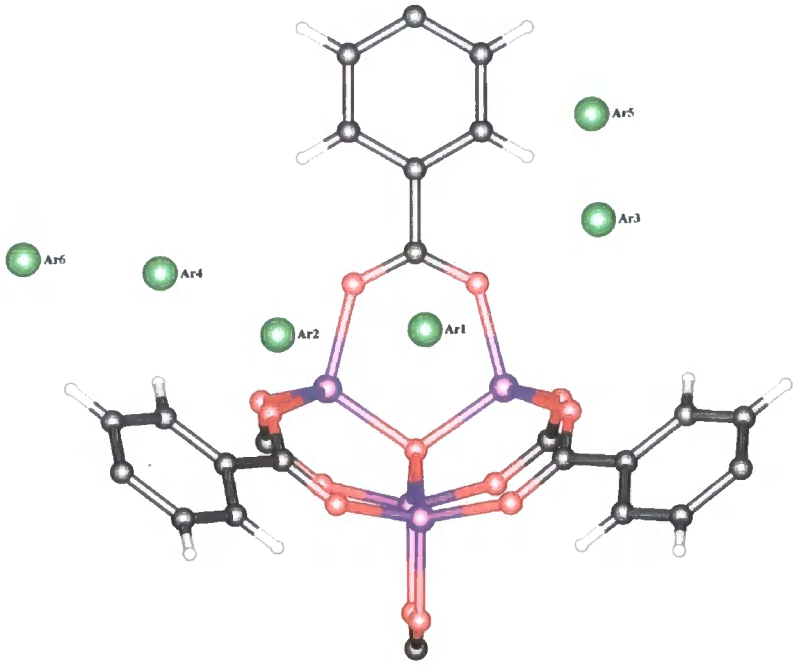

Figure 5.3.26: Location of the six argon atoms absorbed at 50K relative to the $Zn_4O(BDC)$ framework (Zn: purple, O: red, C: black, Ar: green, H: grey).

Table 5.3.9: Atomic parameters for physisorbed argon gas at 50K

Atom	x	y	z	Occupancy	U_{iso}
Ar1	0.34270(9)	0.34270(9)	0.34270(9)	0.148(2)	0.039(1)
Ar2	0.3471(5)	0.5	0.3471(5)	0.060(3)	0.074(6)
Ar3	0.4179(4)	0.4179(4)	0.2462(6)	0.105(5)	0.079(6)
Ar4	0.3750(6)	0.3750(6)	0.1250(6)	0.055(3)	0.11(1)
Ar5	0.5	0.5	0.344(2)	0.013(2)	0.07(2)
Ar6	0.5	0.390(1)	0.110(1)	0.036(4)	0.12(2)

Figure 5.3.27 is an F_{obs} Fourier map through the plane defined by atoms C1, C2, and Ar1. It can be seen that atom Ar1 is well defined. The occupancy of the gas atom Ar1 can be approximated from the relative heights of the Ar1 and C1 peaks in the Fourier map. The ratio of the relative intensities of the two peaks was found to be 2.76. As the total occupancy of C1 is 100% (after correction for reduction due to symmetry) this ratio implies that Ar1 has occupancy of 92%. The

isotropic SHELX refinement suggested an occupancy value of 89% (after correction for a six-fold reduction due to the atom being located on a site of 3*m* symmetry).

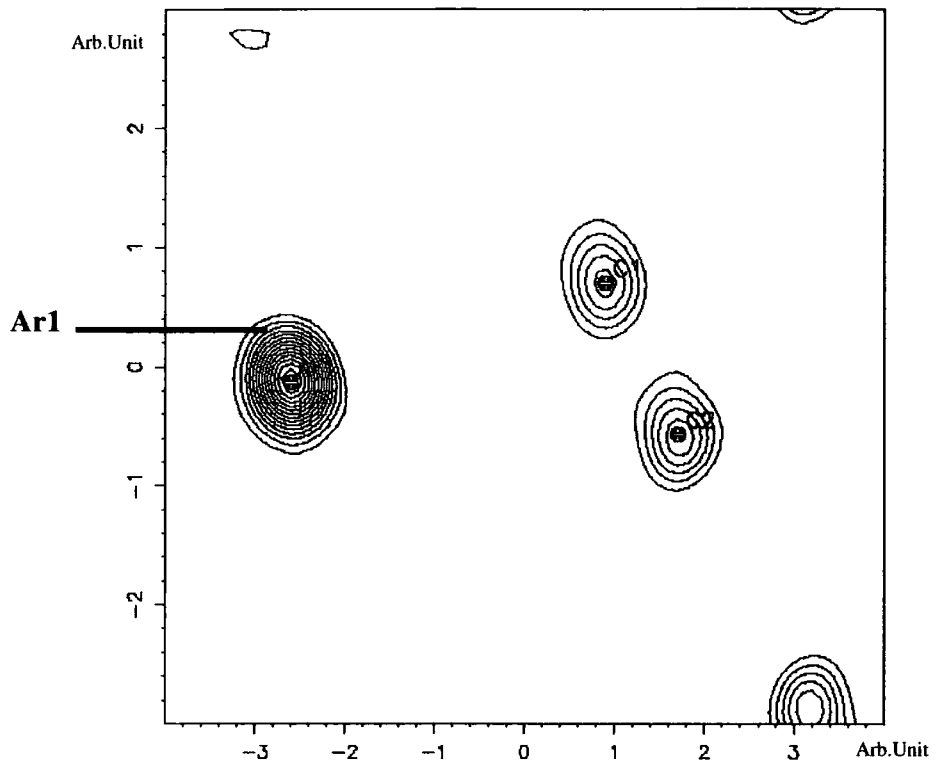

Figure 5.3.27: Slant-plane Fourier map defined by atoms Ar1, C1, and C2. The contour range is 0-38.14 eÅ^3, and contour level is set to 2.3835 eÅ^3.

Figure 5.3.28 is a representation of the Fourier map of the plane characterised by atoms Ar2, C2, and C3. As in the case of atom Ar1, argon atom Ar2 appears to be well ordered with its atomic position clearly defined. The occupancy of atom Ar2 was assessed by comparison of the relative intensities of the C3 and Ar2 peaks in the F_{obs} map. Using this technique the occupancy was found to be 16%. This is in contrast to the 24% calculated by SHELX (isotropic refinement). Both these figures have been corrected to account for the positioning of argon atom Ar2 on the special position x, ½, x (point symmetry *mm*2 – 48*i*). Although some low-level diffuse electron density can be seen surrounding atom Ar2, it was not deemed necessary to incorporate dummy atoms into the model to determine the total electron density for this atom.

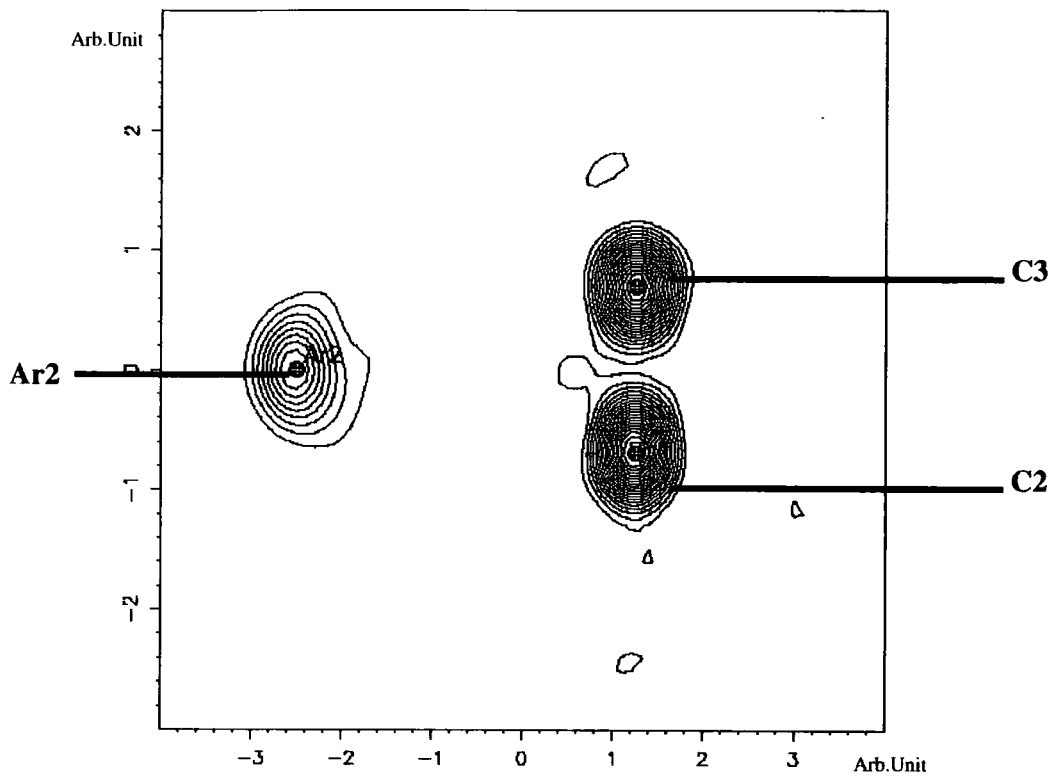

Figure 5.3.28: Slant-plane F_{obs} Fourier map defined by atoms Ar2, C2, and C3. The contour range is set to 0-14.88 eÅ^3, and contour level to 0.7085 eÅ^3.

Figure 5.3.29 shows a slant-plane F_{obs} Fourier maps in which atom Ar3 features. The atom location is relatively well defined. The ratio of peak heights for atoms Ar3 and C3 is 0.329. This equates to an occupancy value of 11% for atom Ar3. The isotropic SHELX refinement calculates the occupancy to be 21%.

The aspherical nature of argon atom Ar4 is clearly apparent in Figure 5.3.30. Dummy atoms needed to be employed so a reasonable estimate of the total electron density of atom Ar4 could be deduced from the F_{obs} Fourier map. The original SHELX refinement (isotropic) of argon atom Ar4 gave an occupancy value of 22%. The total electron density for this atom, including contributions from the dummy atoms was found to be 10.24 eÅ^3; this equates to an occupancy value of 25%. It should be stated that the coordinates of the dummy atoms D5, D6 and D7 (Figure 5.3.30) were deduced from the Fourier map. SHELX calculates the *total* occupancy (sum of Ar4, D5, D6 and D7 occupancies) to be 37%.

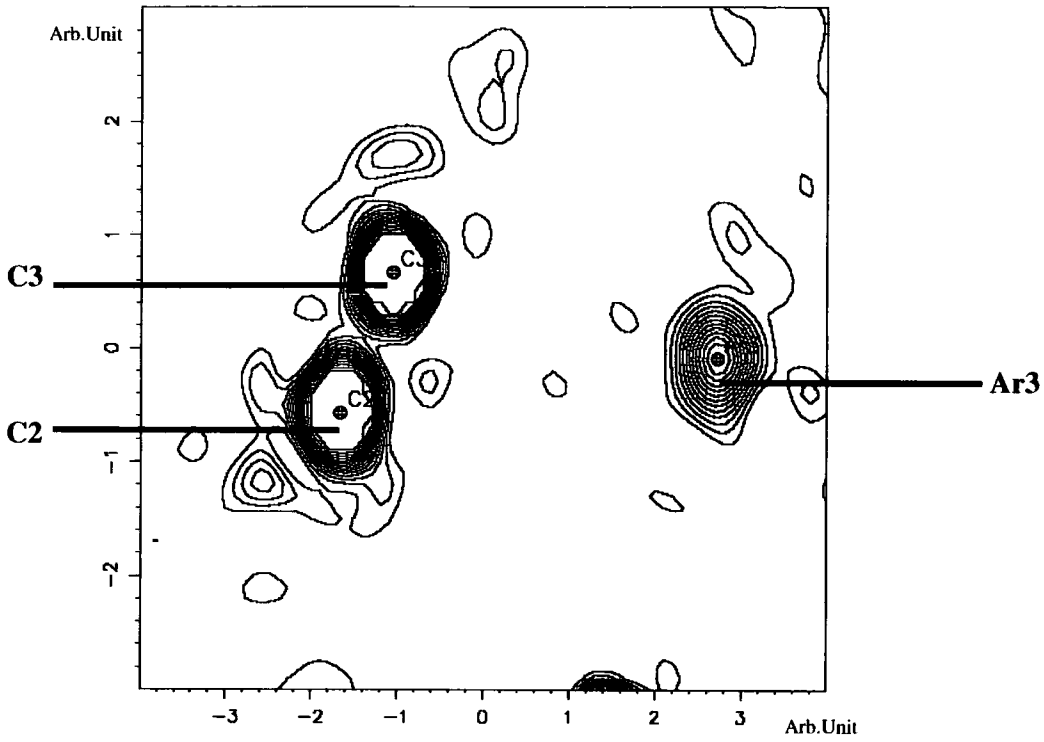

Figure 5.3.29: Slant-plane F_{obs} Fourier map defined by atoms Ar3, C2, and C3. The contour range is set to 0-5 eÅ^3, and contour level to 0.3125 eÅ^3.

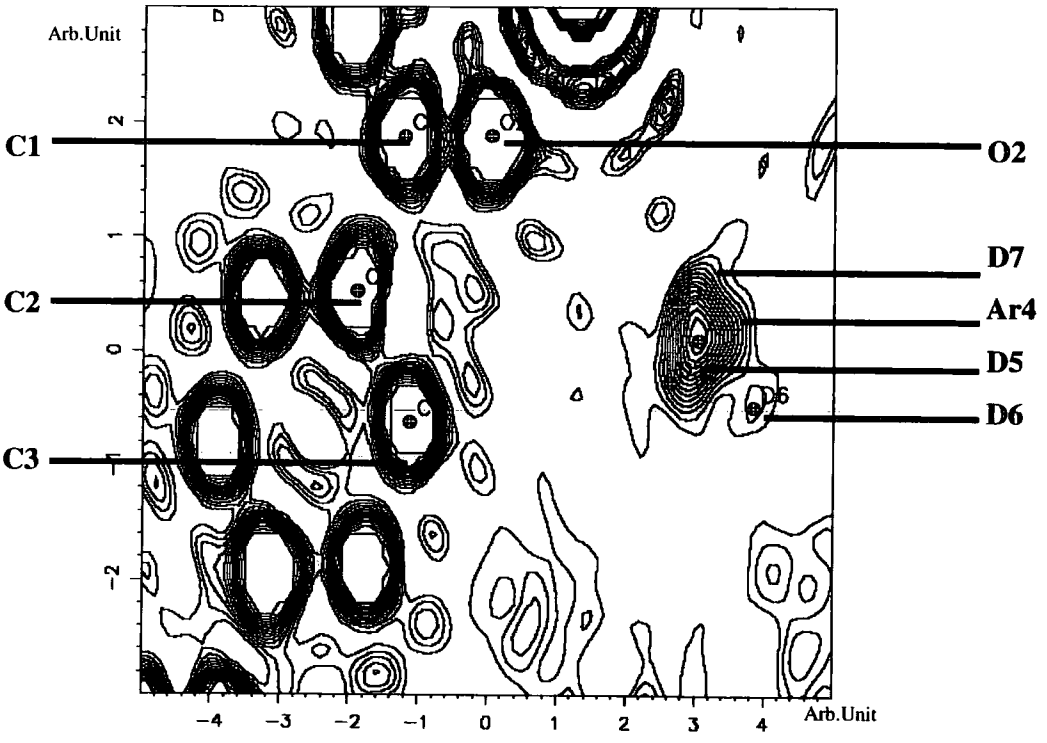

Figure 5.3.30: Slant-plane F_{obs} Fourier map defined by atoms Ar4, C2, and C3. The contour range is set to 0-5 eÅ^3, and contour level to 0.3125 eÅ^3.

The U_{iso} value for atom Ar4 is rather high (0.11(1) $Å^2$), so a second-order tensor model was applied to this atom; the results of this analysis are given in Table 5.3.10. The percentage occupancy value is 33% for atom Ar4 under this refinement strategy.

Table 5.3.10: Occupancy and U_{ij} values (second-order tensor) for atoms Ar4 and Ar6 at 50K.

Atom	Occupancy	U_{11}	U_{22}	U_{33}	U_{23}	U_{13}	U_{12}
Ar4	0.055(3)	0.12(1)	0.12(1)	0.12(1)	0.20(7)	0.20(7)	-0.20(7)
Ar6	0.037(4)	0.13(4)	0.12(2)	0.12(2)	0.05(3)	0.000	0.000

Figure 5.3.31 is a F_{obs} Fourier map showing atom Ar5. The final occupancy determined by the isotropic SHELX refinement, after correction for an eight-fold reduction due to the atom's location on a site of 4*mm* symmetry (24*e*), is 11%. Comparison of the relative peak heights of atoms Ar5 and C1 in the F_{obs} map gives the occupancy of Ar5 as 8%.

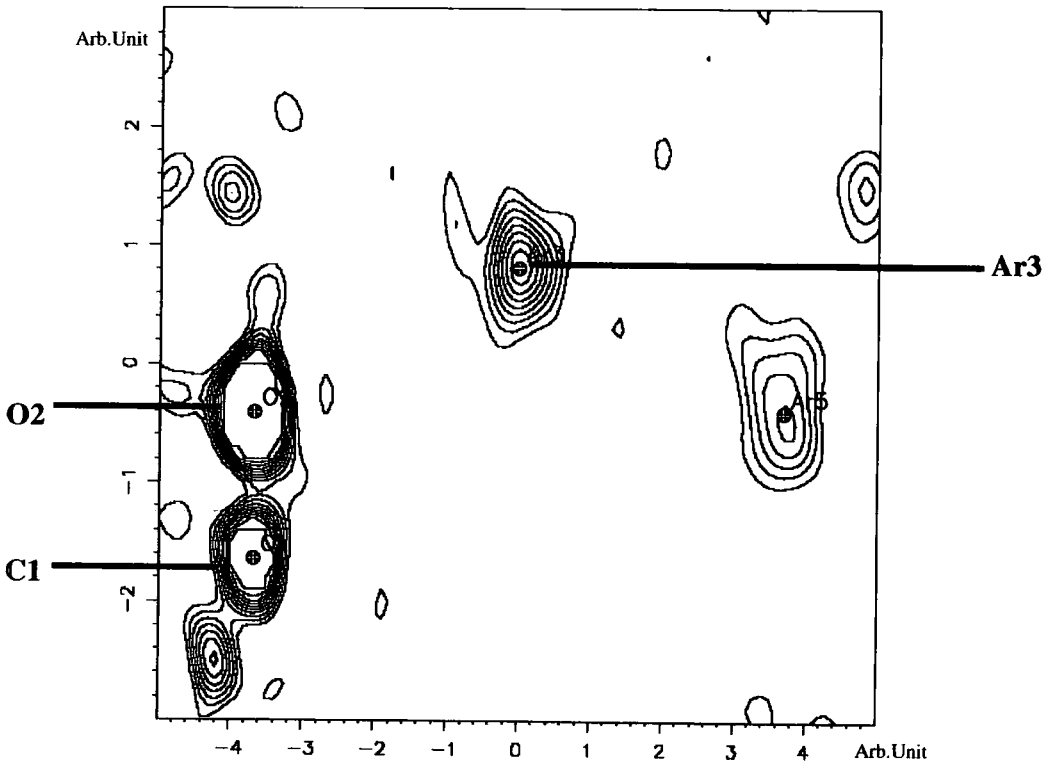

Figure 5.3.31: Slant-plane F_{obs} Fourier map defined by atoms O2, Ar3, and Ar5. The contour range is 0-5 $eÅ^3$, and the contour level set to 0.4545 $eÅ^3$

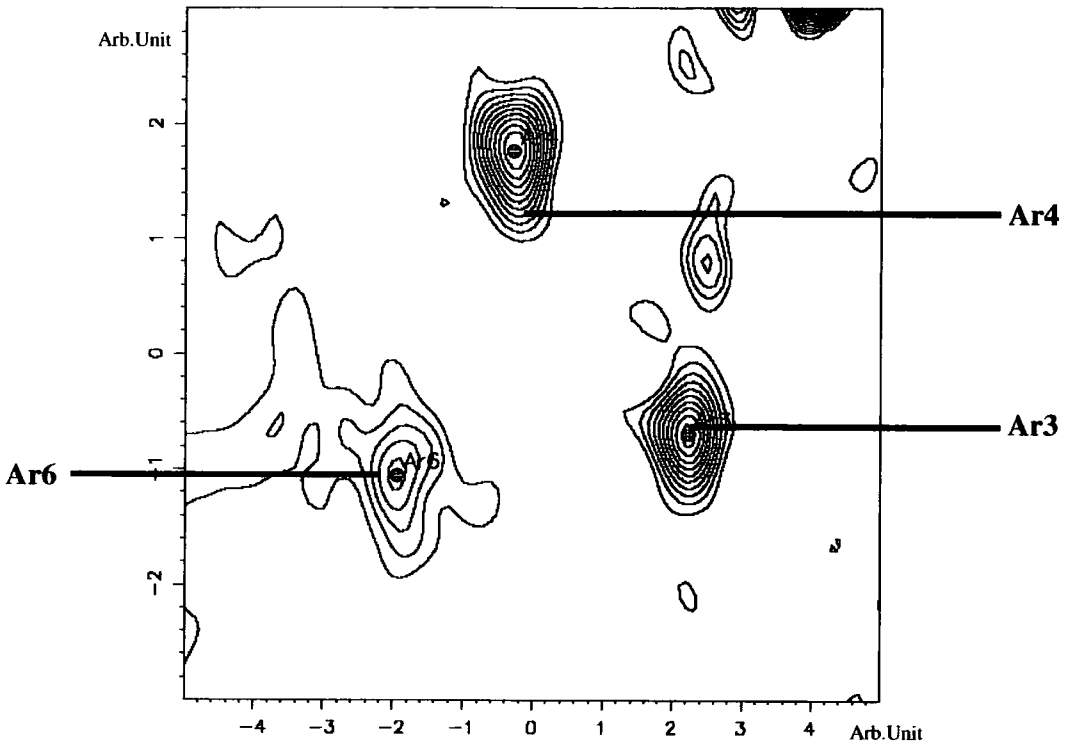

Figure 5.3.32: Slant-plane F_{obs} Fourier map defined by atoms Ar3, Ar4 and Ar6. The contour range is 0-6.153 eÅ^3, and the contour level set to 0.3845 eÅ^3

Argon atom Ar6 is located on a site of *mm*2 symmetry (48*h*). The F_{obs} Fourier map shown in Figure 5.3.32 shows this atom in the framework cavities at 50K. There is considerable low level diffuse electron density surrounding this atom, and calculation of the atom occupancy from the Fourier map is impossible. However, the isotropic SHELX refinement suggests that the occupancy of this atom is 15% (U_{iso} = 0.12(2) Å^2), this is a reasonably large occupancy value, and would suggest that atom Ar6 is genuine. Under anisotropic refinement using a second-order tensor model the occupancy remained at 15% (Table 5.3.10)

The shortest argon-framework distances are: Ar1···Zn, 3.958(3) Å; Ar4···Zn, 3.67(2) Å; Ar1···O2, 3.624(3) Å; Ar3···O2, 3.860(2) Å; Ar4···O2, 3.47(2) Å; Ar3···H, 3.34 Å; Ar4···H, 3.29 Å; Ar6···H, 3.31 Å. These distances imply that the interactions between the framework and gas atoms are weak, as would be expected for physisorption. The distance been atom Ar2 and the centroid of the benzene ring of the linker molecule is only 3.554 Å, this is strongly suggestive of an Ar2···π interaction.

30K Structure

At 30K, eight partially occupied argon absorption sites were identified. The details of the atoms at these sites are provided in Table 5.3.11. The location of these sites in relation to the $Zn_4O(BDC)$ framework is shown in Figure 5.3.33.

Table 5.3.11: Atomic parameters for physi-absorbed argon gas at 30K

Atom	x	y	z	Occupancy	U_{iso}
Ar1	0.34191(8)	0.34191(8)	0.34191(8)	0.163(3)	0.029(1)
Ar2	0.3418(7)	0.5	0.3418(7)	0.038(3)	0.042(7)
Ar3	0.4159(7)	0.4159(7)	0.246(1)	0.096(7)	0.10(1)
Ar4	0.376(1)	0.376(1)	0.124(1)	0.048(5)	0.16(3)
Ar5	0.5	0.5	0.327(1)	0.022(3)	0.05(1)
Ar6	0.381(3)	0.5	0.103(3)	0.040(5)	0.12(3)
Ar7	0.4273(8)	0.4273(8)	0.4273(8)	0.019(3)	0.03(1)
Ar8	0.5	0.5	0.0	0.03(1)	0.05(4)

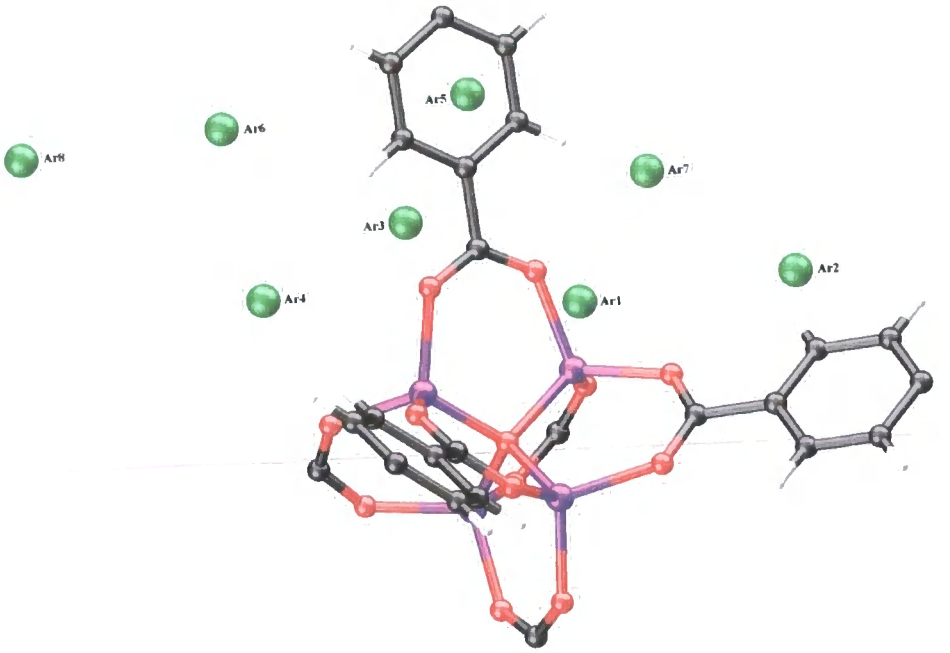

Figure 5.3.33: Location of the eight argon atoms absorbed at 30K relative to the $Zn_4O(BDC)$ framework. (Zn: purple, O: red, C: black, Ar: green, H: grey).

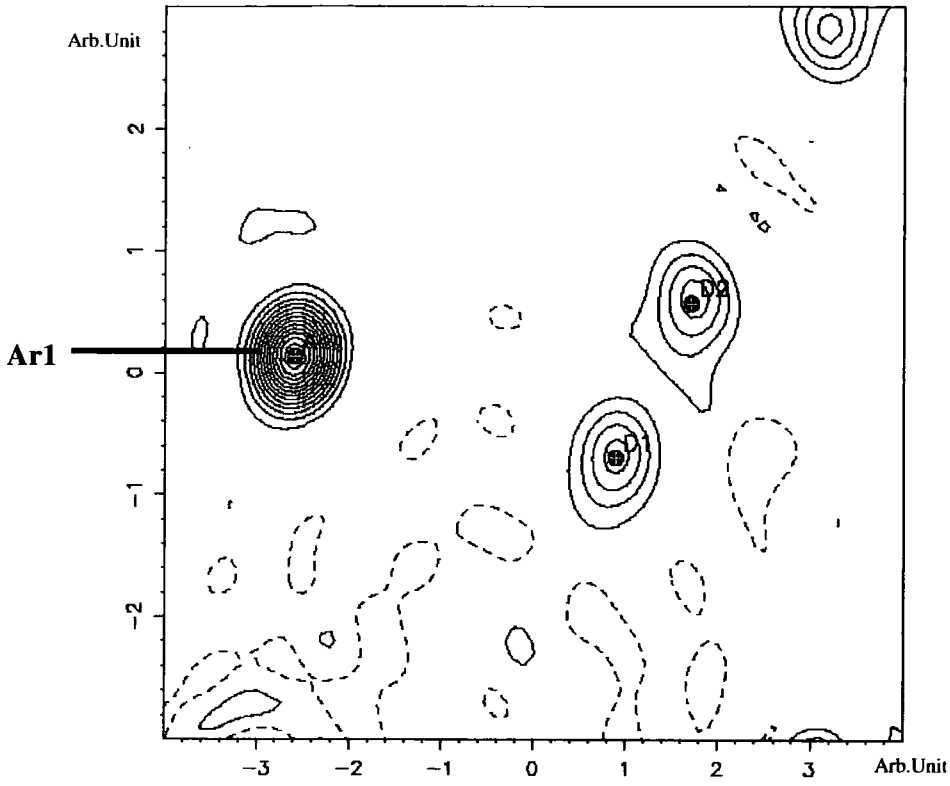

Figure 5.3.34: Slant-plane F_{obs} Fourier map. Atoms D1, D2, and Ar1 define the plane of the map. The contour range is –5.639-49.077 eÅ^3, and the contour level is set to 3.4197 eÅ^3.

Figure 5.3.34 is an F_{obs} Fourier map displaying atom Ar1. The dummy atoms D1 and D2 are symmetry equivalents of carbon atoms C1 and C2; they have been included in the structural model (but not refined) to allow the slant-plane to be defined. From the Fourier map it can be seen that argon atom Ar1 is exceptionally well defined. SHELX calculates the occupancy of atom Ar1 to be 98%. Comparison of the peak heights of atoms Ar1 and D1 gives an estimate of the occupancy to be 100%. On this occasion the calculated and observed values are in relatively good agreement. The low U_{iso} value of 0.029(1) Å^2 indicates that isotropically modelling the thermal behaviour of this atom is crystallographically reasonable.

The electron density for atom Ar2 is shown in Figure 5.3.35 and the reasonably low U_{iso} value of 0.042(7) Å^2 suggests that an isotropic model for this atom is suitable. The occupancy of argon atom Ar2 as determined from the Fourier map by comparison of the relative peak heights for atoms C2 and Ar2 is 14%. This value is in agreement with the SHELX calculated value of 15%.

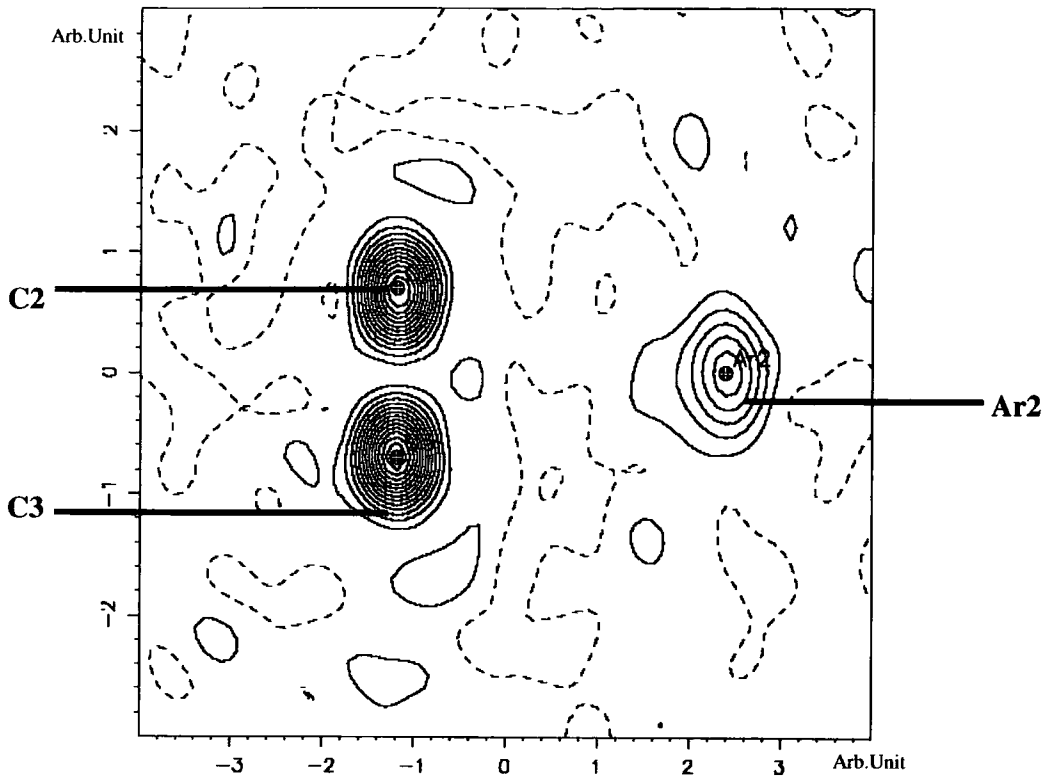

Figure 5.3.35: Slant-plane F_{obs} Fourier map. Atoms C2, C3, and Ar2 define the plane of the map. The contour range is -1.514-14.982 eÅ^3, and the contour level is set to 1.0309 eÅ^3.

Figure 5.3.36 shows an F_{obs} Fourier map in which atom Ar3 features. The relative peak heights of atoms Ar3 and C1 suggest an occupancy value of 9% for Ar3. The isotropic SHELX refinement calculates the occupancy for this atom to be 19%. The U_{iso} value was 0.10(1) Å^2, and the aspherical nature of the electron density associated with atom Ar3, would suggest that this atom would benefit from being modelled with higher-order tensors. An anisotropic refinement of atom Ar3 using a second-order tensor was attempted (Table 5.3.12), but the U_{12} term indicated that this was not a suitable model; therefore an isotropic model is more appropriate for atom Ar3.

Table 5.3.12: Occupancy and U_{ij} values (second-order tensor) for atoms Ar3, Ar4, and Ar6 at 30K.

Atom	Occupancy	U_{11}	U_{22}	U_{33}	U_{23}	U_{13}	U_{12}
Ar3	0.092(6)	0.073(8)	0.073(8)	0.14(2)	-0.03(1)	-0.03(1)	0.01(1)
Ar4	0.045(5)	0.16(2)	0.16(2)	0.16(2)	0.04(1)	0.04(1)	-0.04(1)
Ar6	0.042(5)	0.06(3)	0.21(7)	0.07(3)	0.000	-0.03(3)	0.000

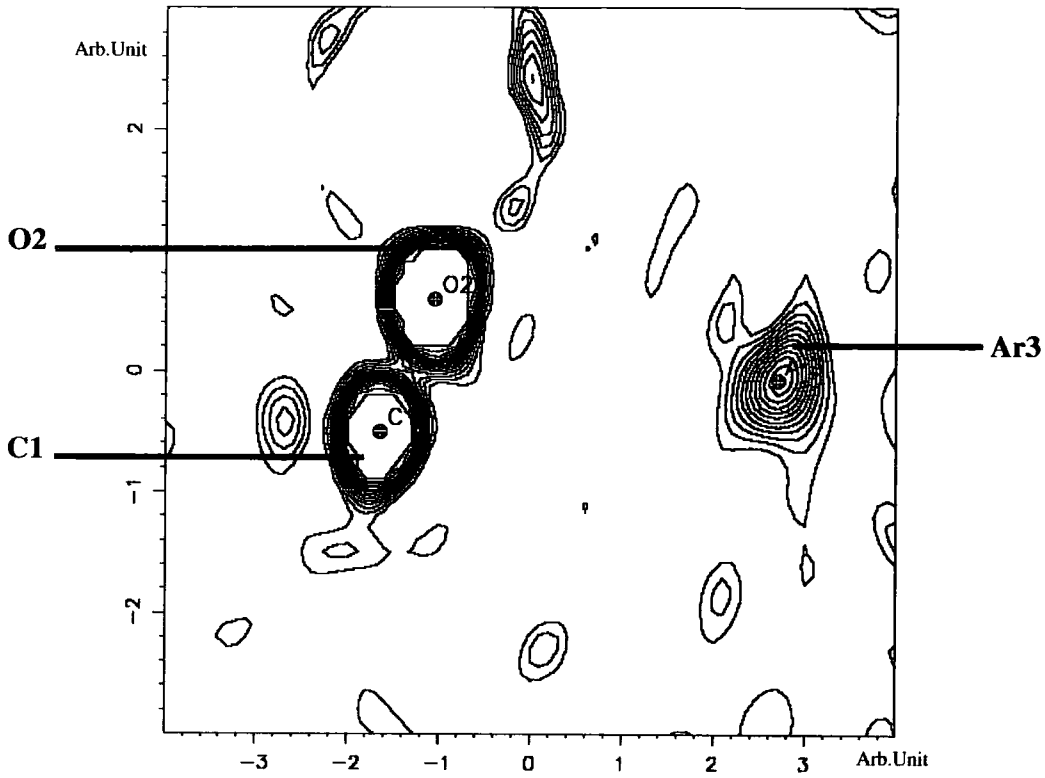

Figure 5.3.36: Slant-plane F_{obs} Fourier map. Atoms C1, O2, and Ar3 define the plane of the map. The contour range is 0-5 eÅ^3, and the contour level is set to 0.3125 eÅ^3.

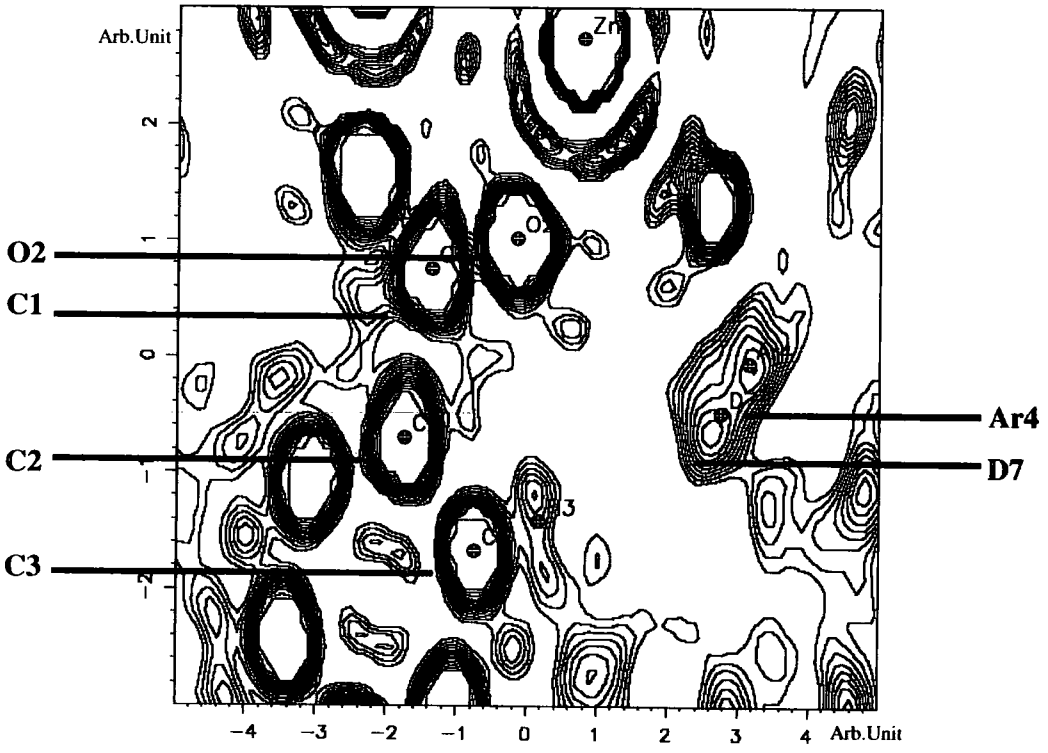

Figure 5.3.37: Slant-plane F_{obs} Fourier map. Atoms C1, C2, and Ar4 define the plane of the map. The contour range is 0-5 eÅ^3, and the contour level is set to 0.3125 eÅ^3.

The Fourier map for atom Ar4 (Fig. 5.3.37) indicates that this atom maybe better modelled with a split-atom model (more than one density maxima can be observed in the map). An atom was positioned on the second density maxima (D7) and was refined isotropically with atom Ar4. When an attempt was made to refine the occupancy and ADP values concurrently the refinement became unstable. A non-split atom model will have to suffice for atom Ar4.

The isotropic SHELX refinement calculated the occupancy of atom Ar4 to be 29%. The atomic coordinates of D7 and Ar4 were fixed to force the refinement to proceed to allow the electron density of atom Ar4 to be determined from the Fourier map. Using the total electron density of atom Ar4, and by comparing it with the density for atom C2, the occupancy of argon atom Ar4 was calculated to be 10%. The disagreement between the calculated and observed values is not surprising considering the disorder apparent in the Fourier map. This atom can be modelled reasonably well using a second-order tensor (Table 5.3.12). Doing so alters the occupancy to 27%.

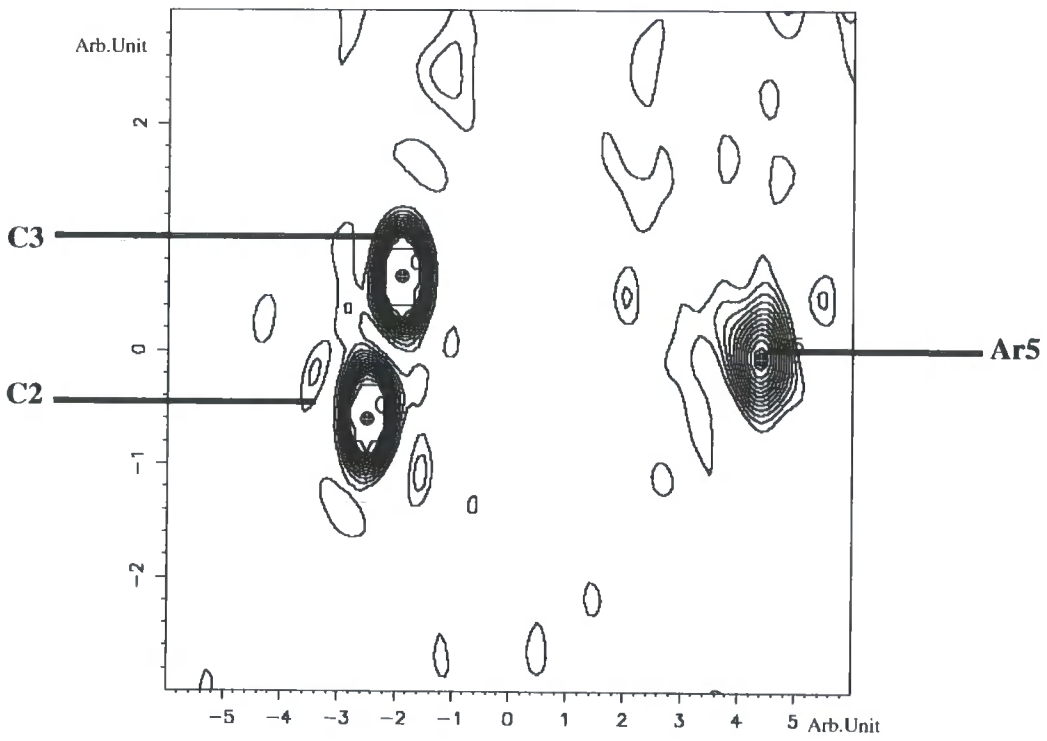

Figure 5.3.38: Slant-plane F_{obs} Fourier map. Atoms C2, C3, and Ar5 define the plane of the map. The contour range is 0-7 $eÅ^3$, and the contour level is set to 0.4375 $eÅ^3$.

Argon atom Ar5 is located on a site of 4*mm* symmetry (24*e*). Figure 5.3.38 displays an F_{obs} Fourier map in which argon atom Ar5 features. It can been seen that atom Ar5 is relatively well defined, although an area of low-level diffuse electron density can be seen surrounding it. Comparison of the peak heights of atoms C3 and Ar5 suggests that the occupancy of atom Ar5 is 14%. This is akin to the value of 18% calculated by SHELX. The U_{iso} value of 0.05(1) $Å^2$ for Ar5 implies that the isotropic modelling of this atom is ideal.

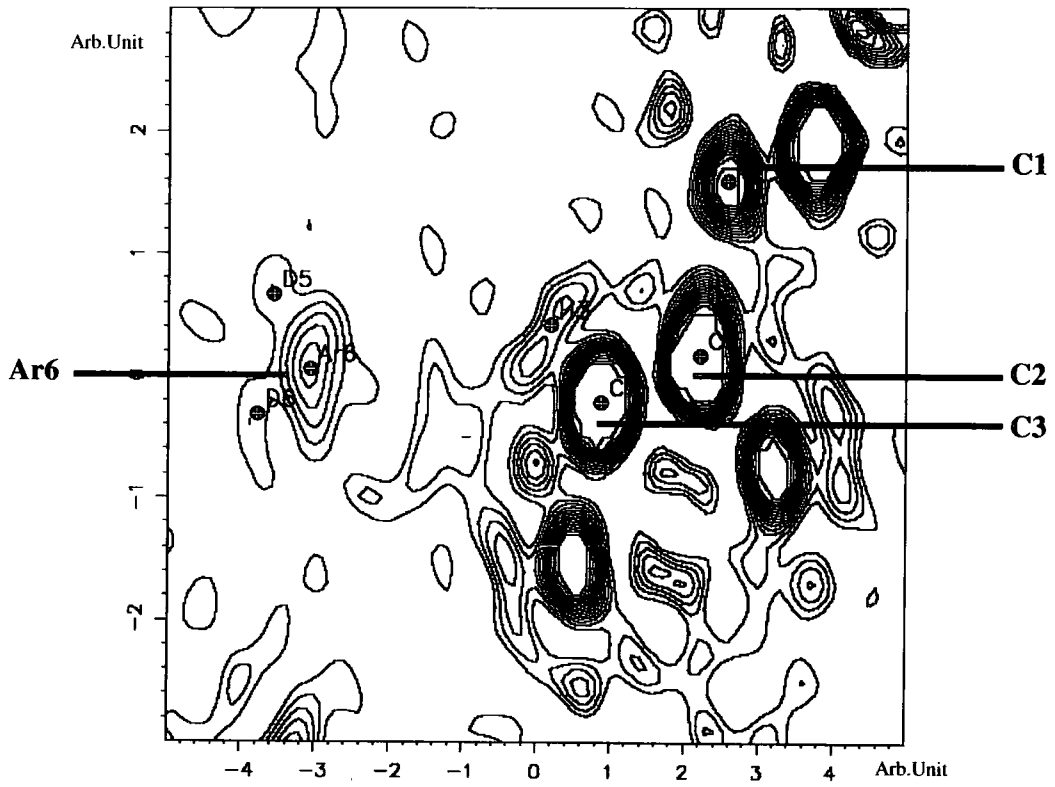

Figure 5.3.39: Slant-plane F_{obs} Fourier map. Atoms C2, C3 and Ar6 define the plane of the map. The contour range is 0-5 $eÅ^3$, and the contour level is set to 0.3125 $eÅ^3$.

It is clear from Figure 5.3.39 that there is a certain amount of low-level electron density surrounding atom Ar6. SHELX calculates the occupancy of this atom to be 8%. Dummy atoms D5 and D6 were added to the structural model to aid in the quantification of the electron density of atom Ar6. Upon isotropic refinement D5 recorded a negative occupancy value and was subsequently removed from the model. The total electron density for Ar6 including the contribution from D6 is 2.51 $eÅ^3$, when compared to atom C2, this equates to an occupancy value of 6%. This is in reasonable agreement with the value calculated from the SHELX refinement. The high U_{iso} value of 0.12(3) $Å^2$ suggests that the thermal displacement parameters

for atom Ar6 may benefit from modelling with a second-order tensor. This analysis has been performed (Table 5.3.12) and is clear from the U_{ij} values and their associated error values, that an isotropic model is more realistic for this atom.

Figure 5.3.40 is an F_{obs} Fourier map showing argon atom Ar7. The electron density for the atom is reasonably well defined, although a smear of electron density can be seen stretching between Ar7 and Ar1 (atom located at the top of the map). Examination of the relative peak heights of atoms C2 and Ar7 gives atom Ar7 an occupancy value of 12%; this is in agreement with the isotropic refinement value of 11% calculated by SHELX. The relatively low U_{iso} value of 0.03(1) $Å^2$ suggests that this atom is adequately modelled when refined isotropically.

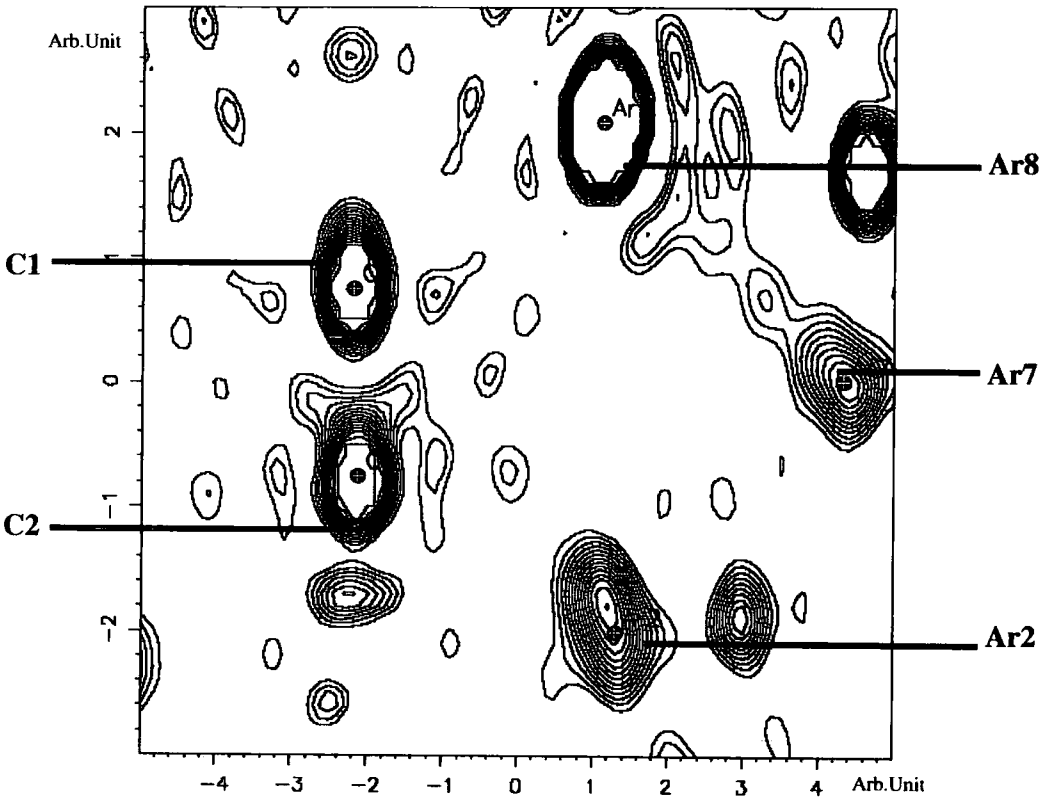

Figure 5.3.40: Slant-plane F_{obs} Fourier map. Atoms C1, C2, and Ar7 define the plane of the map. The contour range is 0-7 $eÅ^3$, and the contour level is set to 0.4375 $eÅ^3$.

The final argon atom to be located in the $Zn_4O(BDC)$ at 30K, Ar8, is positioned on a site of m-3m symmetry (4*a*). The Fourier map presented in Fig. 5.3.41 indicates that atom Ar8 is relatively well ordered. The isotropic SHELX refinement gave an occupancy value of 14% for

atom Ar8. The ratio of the peak heights of atoms Ar6 and O2 is 0.252, this equates to an occupancy figure of ~11% for atom Ar8.

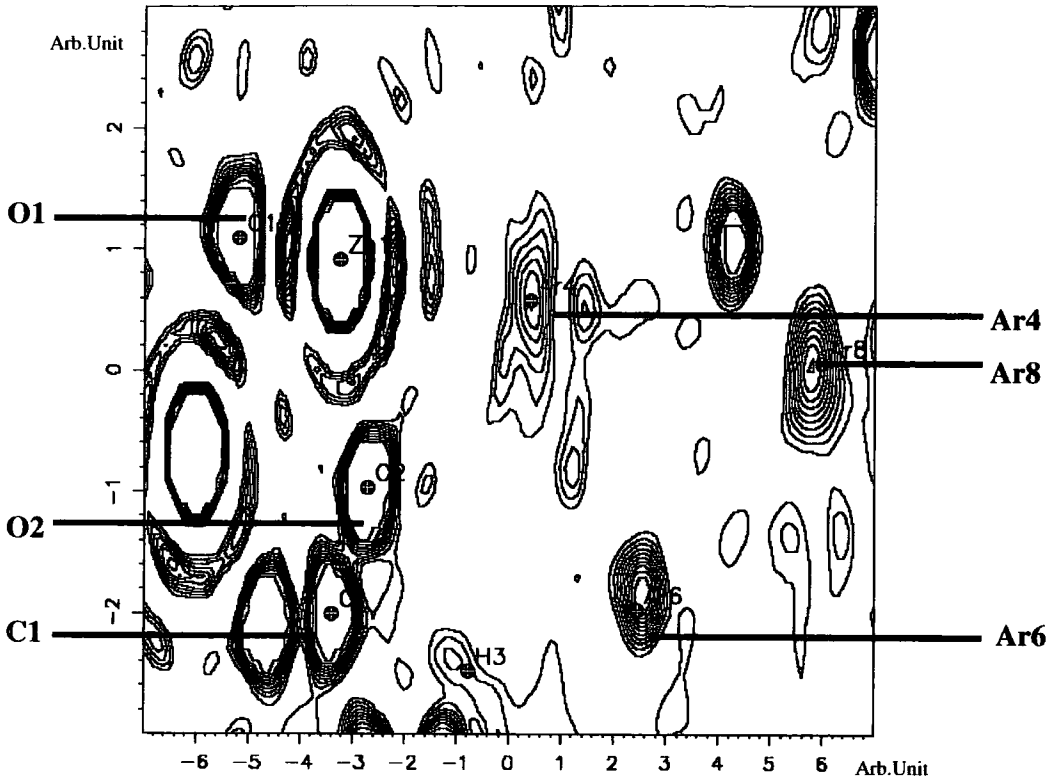

Figure 5.3.41: Slant-plane F_{obs} Fourier map. Atoms Zn1, O2, and Ar8 define the plane of the map. The contour range is 0-5 eÅ^3, and the contour level is set to 0.4545 eÅ^3.

Atom Ar2 is positioned over the benzene ring of the linker molecule, the Ar2···centroid distance is 3.360 Å and this indicates the presence of a strong Ar2···π interaction. Figure 5.3.33 suggests the presence of an Ar5···π contact, however, this is due to the perspective of the diagram, and no such interaction exists. Several weak gas-framework interactions can be noted for this structure, these include the following: Ar1···Zn, 3.927(8) Å; Ar4···Zn, 3.68(8) Å; Ar1···O2, 3.601(7) Å; Ar3···O2, 3.77(4) Å; Ar4···O2, 3.49(7) Å; Ar3···H, 3.31 Å; Ar4···H, 3.28 Å; Ar6···H, 3.28 Å.

5.3.5 Summary for the refinement of argon-loaded $Zn_4O(BDC)$ structures

In Section 5.3.4 of this chapter the refinement of the argon-loaded $Zn_4O(BDC)$ structures in the temperature range of 293-30K was discussed. The same technique that was developed for the refinement of nitrogen-loaded $Zn_4O(BDC)$ was extended to this work. This necessitated the

calculation and cautious evaluation of a variety of F_{obs} Fourier maps in which the gas atoms feature. Using this method, a total of eight unique gas absorption sites have been identified. The five absorption sites identified in the nitrogen-loaded $Zn_4O(BDC)$ structure analyses (Section 5.3.2) are all occupied at 30K by argon gas in the argon-loaded $Zn_4O(BDC)$ structure. Atom Ar1 resides on the equivalent site as N1-N2, Ar4 on the N3 site, Ar3 on the N5-N6 site, Ar2 on the site of N7-N7', and atom Ar6 is located on the N9-N10 gas site.

5.4 Conclusion

The primary objective of this study was to identify the absorption sites in gas-loaded single crystals of $Zn_4O(BDC)$ using low-temperature X-ray diffraction. The results presented in this chapter provide irrefutable evidence that this objective has been achieved. In the case of the nitrogen-loaded system a total of four different sites have been identified. For the argon-loaded crystal, eight absorption sites were located in the framework cavities.

The principal sites of interaction between the gas atoms/molecules are situated in the vicinity of the ZnO_4 clusters located at the nodes of the framework structure. Secondary sites have been found over the benzene rings of the 1,4-benzenedicarboxylate linker molecules, and close to the hydrogen atoms of the ring systems. Lower occupancy sites have also been located, and are situated deeper into the cavities, further away from the framework atoms. It should be borne in mind that in some cases the poor atomic resolution in the Fourier maps prohibits the accurate determination of the gas atom coordinates (as indicated by the high e.s.d. values), subsequently, the calculation of the intermolecular distances are subject to error, and should be regarded with caution. Equally, for the same reason, prudence should be exercised when interpreting the refined occupancy and thermal displacement parameters of the gas atoms.

Ultimately, the aim is to use the information gained from this study to optimise the framework architecture for the storage of hydrogen gas. In the work presented in this chapter, argon and nitrogen gases were used, as these gas species have sufficient electron density to allow their locations in the framework cavities to be identified using laboratory X-ray diffraction. Ideally, this analysis should be performed on a hydrogen-loaded single crystal of $Zn_4O(BDC)$ to obtain information of direct relevance to the gas storage issue. For this, a different 'probe' is required to find the physically absorbed hydrogen molecules within the $Zn_4O(BDC)$ cavities, namely

neutrons. The single crystal neutron diffraction study of hydrogen-loaded $Zn_4O(BDC)$ is the subject of the next chapter.

5.5 References

All Fourier maps were generated with WinGX (version 1.64.05): Farrugia LJ, *J. Appl. Cryst.*, **32**, 837 (1999).

[1] Evans JSO, *J. Chem. Soc., Dalton Trans.*, 3317 (1999).

[2] Baughman RH, Galvão DS, *Nature*, **365**, 735 (1993).

[3] Lightfoot P, Woodcock DA, Maple MJ, Villaescusa LA, Wright PA, *J. Mater. Chem.*, **11**, 212 (2001).

[4] Lide DR, *Handbook of Chemistry and Physics 62nd Ed*, CRC press, 1981-1982.

[5] Bondi A, *J. Phys. Chem.*, **68**, 441 (1964).

[6] Hunter CA, Lawson KR, Perkins J, Urch CJ, *J. Chem. Soc., Perkin Trans. 2*, 651 (2001).

[7] Desiraju GR, Steiner T, '*The Weak Hydrogen Bond in Structural Chemistry and Biology*', IUCr Monograph, Oxford University Press 1999.

Chapter 6

Single Crystal Neutron Diffraction Study of Hydrogen-Loaded Zn_4O(1,4-benzenedicarboxylate)

6.1 Introduction

This study was continuation of the work presented in Chapter 5. The aim of this project was to locate the gas absorption sites within hydrogen-loaded Zn_4O(1,4-benzenedicarboxylate) (Zn_4O(BDC)) using low-temperature single crystal neutron diffraction. Chapter 4 contains a review of the literature that is relevant to the work to be reported in this chapter.

6.2 Experimental

The samples used in this investigation was a colourless cubic crystal of hydrogen-loaded Zn_4O(1,4-benzenedicarboxylate) with the following dimensions: 0.4 x 0.6 x 0.6 cm. The crystal was sealed in a Lindermann capillary filled with hydrogen under an approximate pressure of approximately 1.0 atm. Prior to hydrogen filling all air and solvent had been evacuated from the crystal and capillary.

All neutron data were collected with the Very Intense Vertical Axis Laue DIfractometer (VIVALDI)[1-4] at the Institut Laue-Langevin (Grenoble, France). A white beam of thermal neutrons covering a wavelength range of 0.8-5.2 Å was utilised. Neutron-sensitive image plates, covering a total of 63% of the full solid angle, were employed to record the Laue images. A standard ILL Orange cryostat was used to control the sample temperature.[5]

Data were recorded at the following temperatures: 300K, 150K, 120K, 50K, 30K and 5K. At each temperature three or four Laue images were recorded, each at a different setting of φ, the

rotation about an axis perpendicular to the incident beam, within the range of $-120 < \varphi < -20^{\circ}$ ($\Delta \varphi = 20^{\circ}$). The exceptions being the 5K data collection, for which eight images were recorded ($-120 < \varphi < 20^{\circ}$ [$\Delta \varphi = 20^{\circ}$]), and the 300K data collection, for which five Laue images were recorded ($-120 < \varphi < -20^{\circ}$ [$\Delta \varphi = 20^{\circ}$]). The exposure time for each image was approximately 4.5 h.

The diffraction images were indexed with the program LAUEGEN,[6,7] and the reflections were integrated with a modified two-dimensional version of the algorithm formulated by Wilkinson et al and Prince et al.[8,9] The data were normalised, to account for the incident wavelength spectrum, by comparison of recurring and equivalent reflections, this was performed with the program LAUENORM.[10] Only data that were within the wavelength band 0.95-3.0 Å with $d \geq 0.95$ Å (the resolution limit of the Laue images), and had $I > 3\sigma I$ were included in this procedure. Data that did not satisfy these criteria were rejected. The absorption by the capillary, the cryostat heat shields, and the sample was estimated to be approximately 0.7-1.0 %. This negligible degree of absorption would have been mostly accounted for during the empirical normalisation procedure, and as such no additional absorption correction was deemed necessary. Full-matrix least-squares structure refinement was carried out with SHELXTL.[11]

6.3 Results & Discussion

6.3.1 Hydrogen-loaded $Zn_4O(BDC)$

Data collected at 120K, 150K and 300K showed an absence of hydrogen gas within the framework cavity, therefore the following discussion will be confined to a consideration of data collected at 120K, 50K, 30K and 5K. Table 6.3.1 lists the refinement statistics obtained from the analysis of these datasets (see supplementary data for further details). All Laue patterns exhibited the expected face centred cubic symmetry, and were indexed with a = 25.8Å, a value that is in agreement with the X-ray data reported in Chapter 5. As a starting model for the refinement of the neutron structures, the framework atomic coordinates were taken from the argon-loaded $Zn_4O(BDC)$ structure (30K X-ray data) (see Chapter 5). The possibility of anisotropic refinement was investigated for all structures but was found to be unsuitable, presumably due to the limited amount data collected; therefore, all structures have been refined isotropically.

Table 6.3.1: Refinement statistics for the VT analysis of H_2 loaded $Zn_4O(BDC)$.

	120K	50K	30K	5K
Collected reflections	5693	4701	6281	12468
Unique reflections	417	411	416	434
Omitted reflections	6	6	7	4
Data/parameter ratio	417 / 17	411 / 19	416 / 22	434 / 24
R(int) / R(σ)	0.4189 / 0.2161	0.3606 / 0.2033	0.3826 / 0.1722	0.3922 / 0.1345
Goof (S)	2.272	1.996	2.130	3.117
R_1 [I>2σ(I)]	0.2721	0.2154	0.2304	0.2444
wR_2 [I>2σ(I)]	0.2585	0.2314	0.2834	0.2476

All Fourier maps presented in this chapter are based on the observed data (F_{obs}) with F(000) excluded.

120K Structure

At this temperature the framework cavities are devoid of hydrogen gas, and the $Zn_4O(BDC)$ framework was refined isotropically with no difficulty. No abnormalities were observed in the framework structure.

50K Structure

At 50K the framework cavities are each occupied by a hydrogen molecule. As the individual atoms of this molecule could not be resolved, a single hydrogen 'atom' was positioned at this site (denoted H1) and carefully refined. Table 6.3.2 provides the atomic parameters for this 'atom', and it can be seen that H1 is located on a site of 3m symmetry (32*f*) with 100% occupancy. Figure 6.3.1 shows the location of this molecule in relation to the framework structure.

Table 6.3.2: Atomic parameters for hydrogen molecule 'H1' at 50K.

Atom	x	y	z	Occupancy	U_{iso}
H1	0.3378(8)	0.1622(8)	0.1622(8)	0.16667	0.09(1)

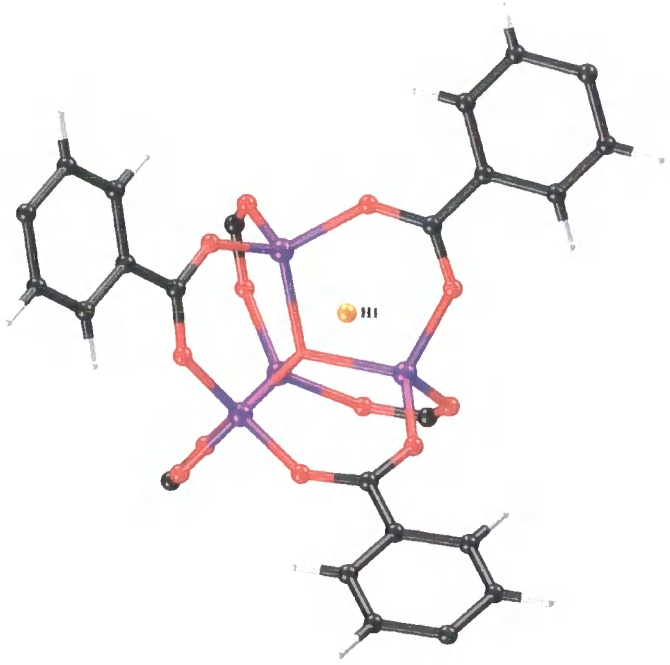

Figure 6.3.1: Diagram showing the location of H1 relative to the framework atoms at 50K. Zn: purple; O: red; C: black; framework hydrogen: grey; absorbed hydrogen: yellow.

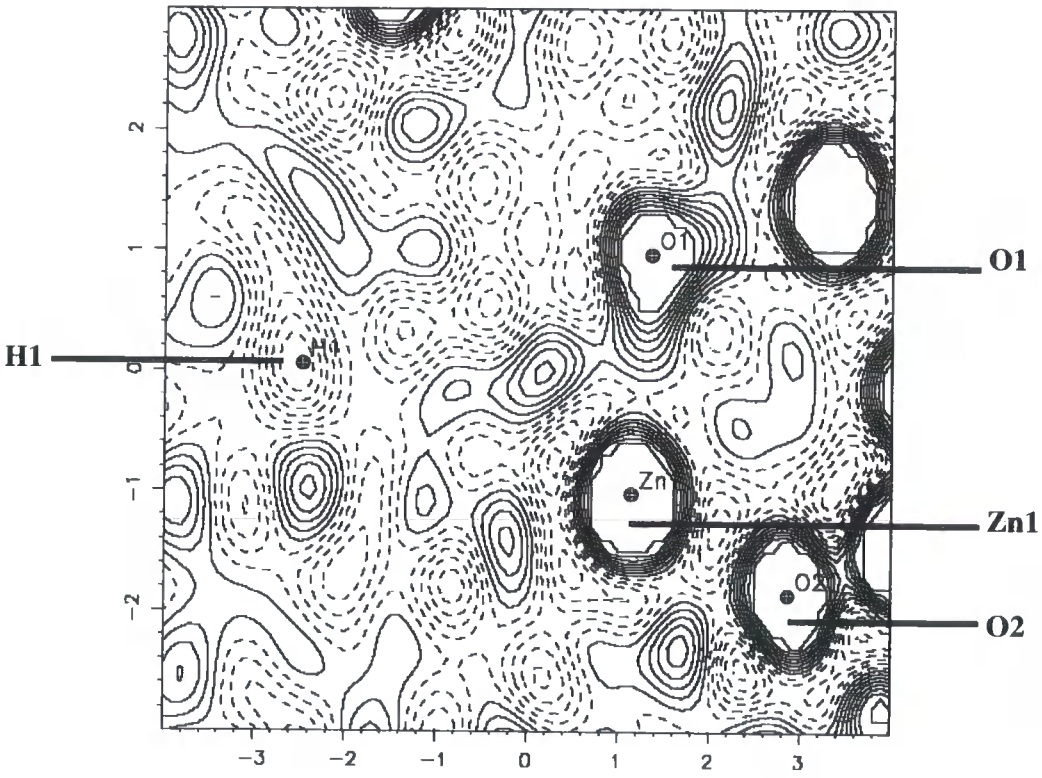

Figure 6.3.2: Slant plane neutron $F_{(obs)}$ map defined by atoms H1, O1, and Zn1. The contour range is 5.0 – (-5.109) cmÅ^2, and the level is set to 0.6318 cmÅ^2.

Figure 6.3.2 is a contour Fourier map in which H1 features. The difficulty in locating the second atom of this molecule can now be understood, no clearly defined second hole of significant depth can be found in the vicinity of H1. It is worth noting however that this is only one plane, several different planes passing through the same of volume of space were examined, but none indicated a possible site for the second atom of the molecule.

H1 is positioned over the shared vertex of the ZnO_4. The shortest gas–framework distances are Zn···H, 3.75(6) Å; O1···H, 3.91(7) Å; O2···H, 3.46(4) Å (see Fig.6.3.3 for atom labels). For comparison the sum of the van der Waals radii for the atom pairs are Zn/H, 2.59 Å, and O/H 2.72 Å.[12] As the gas–framework distances are significantly longer than the sum of the van der Waals radii, the interaction between the hydrogen gas and the framework is very weak, as expected for physical absorption.

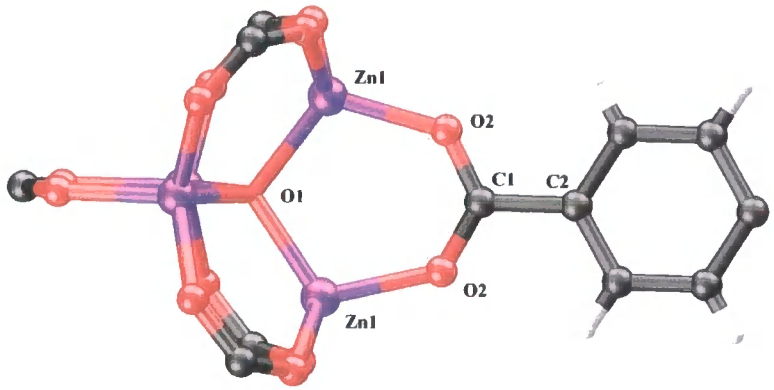

Figure 6.3.3: Section of the framework structure with atom labels.

30K Structure

Table 6.3.3 lists the atomic parameters obtained for the physisorbed gas at 30K. The gas molecule site occupied at 50K is also occupied at 30K; additionally, the second atom of the hydrogen molecule has been resolved at this temperature. The occupancy of this molecule was found to be 100% (based on H1). Atom H2 is located on a site of mirror symmetry (96*k*). The refined occupancy for this atom is given in Table 6.3.3, it should be noted that this value is ~1/3 of the expected 0.5, this arises due to the atom's proximity to the 3-fold axis on which H1 resides, consequently H2 is 'disordered' over three positions (see Fig. 6.3.4). The H1-H2

distance was refined to 0.7247(1) Å (see Appendix 3). This is in reasonable agreement with the expected distance of 0.7414Å.[13]

Table 6.3.3: Atomic parameters for the hydrogen molecule in the $Zn_4O(BDC)$ cavities at 30K.

Atom	x	y	z	Occupancy	U_{iso}
H1	0.332(1)	0.168(1)	0.168(1)	0.16667	0.10(2)
H2	0.332(1)	0.168(1)	0.140(2)	0.1667	0.04(2)

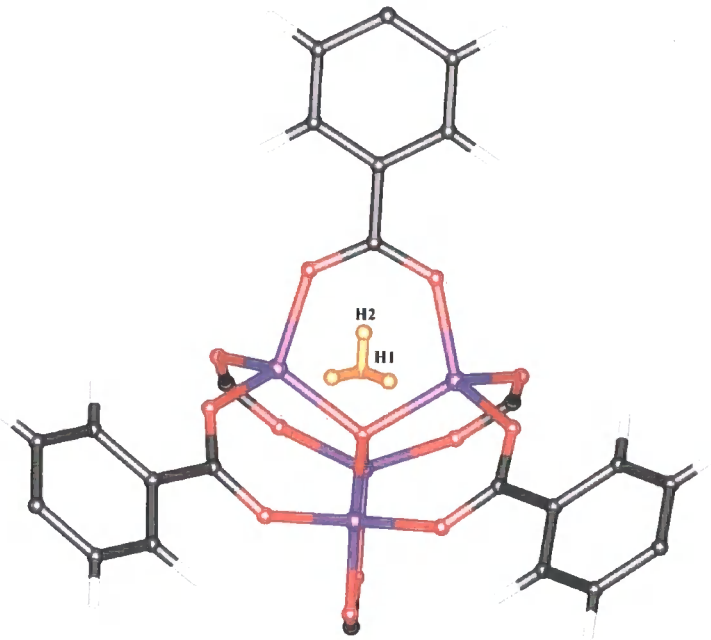

Figure 6.3.4: Diagram showing the location of molecule H1-H2 relative to the framework atoms at 50K. Zn: purple; O: red; C: black; framework hydrogen: grey; absorbed hydrogen: yellow. Only one position of the disordered H2 atom is labelled for clarity.

A contour representation of a neutron F_{obs} Fourier map displaying the H1-H2 molecule is shown in Figure 6.3.5. The 'smear' of nuclear density above atom H1 is the location of 1/3 of the H2 atom, the remaining 2/3 of the atom are located outside the plane of this map. It is to be expected that H2 will not be ideally placed in the model due to the disorder caused by the 3-fold axis (as discussed above) and indeed this is evident in the Fourier map (Fig.6.3.5). Attempts to 'force' the atom to the density minima above the H2 label in Figure 6.3.4 gave an unrealistically long H1-H2 bond length. The best crystallographic strategy is to leave atom H2 at its refined position.

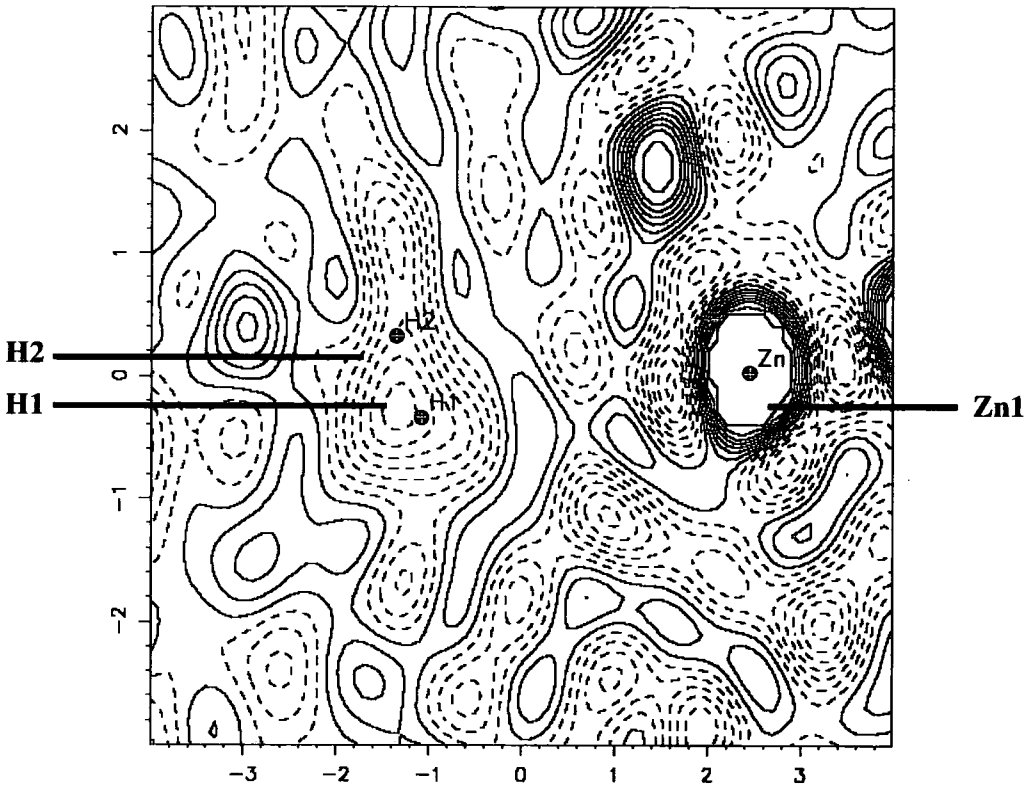

Figure 6.3.5: Slant plane neutron Fourier map defined by atoms H1, H2, and Zn1. The contour range is 5.0 – (-4.957) cmÅ^2, and the level is set to 0.6223 cmÅ^2.

The shortest gas–framework distances at 30K are Zn···H1, 3.55(6) Å; O1···H1, 3.69(7) Å; O2···H1, 3.34(4) Å; Zn···H2, 3.82(5) Å; O2···H2, 3.22(5) Å

5K Structure

At 5K, the disordered H1-H2 molecule can be readily located in the framework pore (100% occupancy) and an additional gas molecule site can be identified (denoted as H4). Unfortunately the individual atoms of this second molecule cannot be resolved. Figure 6.3.6 shows the location of these molecules in relation to the framework structure. Crystallographic details for the gas atoms are given in Table 6.3.4.

Table 6.3.4: Atomic parameters for hydrogen gas in the $Zn_4O(BDC)$ framework cavities at 5K.

Atom	x	y	z	Occupancy	U_{iso}
H1	0.334(1)	0.166(1)	0.166(1)	0.16667	0.09(2)
H2	0.333(1)	0.167(1)	0.139(2)	0.16667	0.05(2)
H4	0.125(1)	0.125(1)	0.125(1)	0.16412	0.18(3)

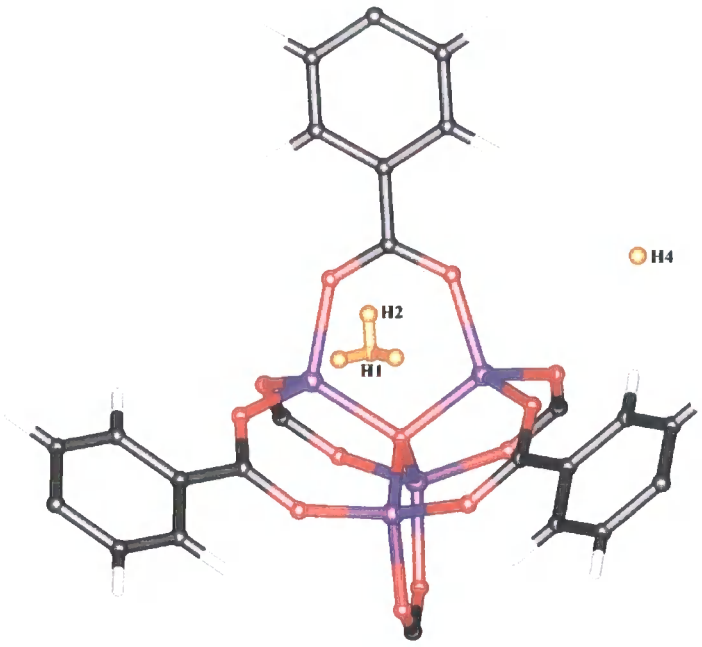

Figure 6.3.6: Diagram showing the location of the hydrogen molecules relative to the framework atoms at 5K. Zn: purple; O: red; C: black; framework hydrogen: grey; absorbed hydrogen: yellow. Only one position of the disordered H2 atom is labelled for clarity.

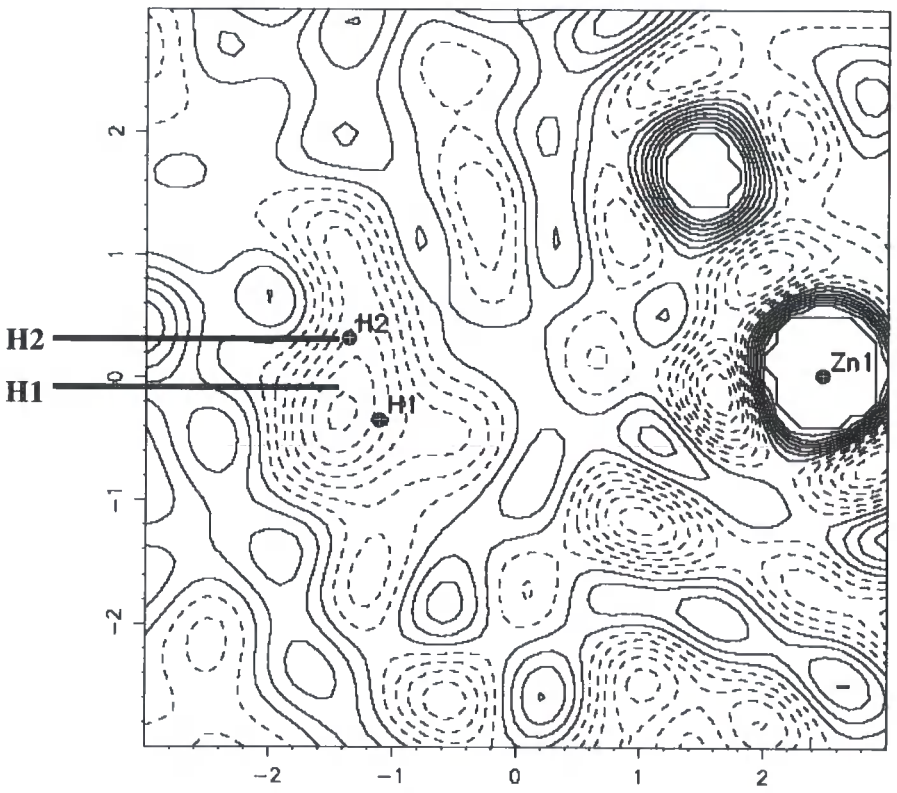

Figure 6.3.7: Slant plane neutron Fourier map defined by atoms H1, H2, and Zn1. The contour range is 5.0 – (-5.392) cmÅ^2, and the level is set to 0.6495 cmÅ^2.

The Fourier map of molecule H1-H2 shown in Figure 6.3.7 is very similar to Figures 6.3.5, which displays the F_{obs} Fourier map for the same molecule at 30K. At 5K, the H1-H2 bond length refined to 0.6998(1) Å. Again, the atoms of the molecule do not appear to be well placed, this will be due to the molecular disorder.

'Atom' H4 is located on a site of 3m symmetry (32*f*) and after cautious refinement was found to have an occupancy value of 98%, although the isotropic temperature facture for this 'atom' is rather high, so care must be taken not to place too much reliance on this occupancy value. Two slant-plane Fourier maps showing H4 are provided below in Figures 6.3.8 and 6.3.9. These maps show that the second atom of this molecule cannot be resolved. It is likely that the molecule is subject to considerable molecular motion, and this explains the high U_{iso} value for 'atom' H4.

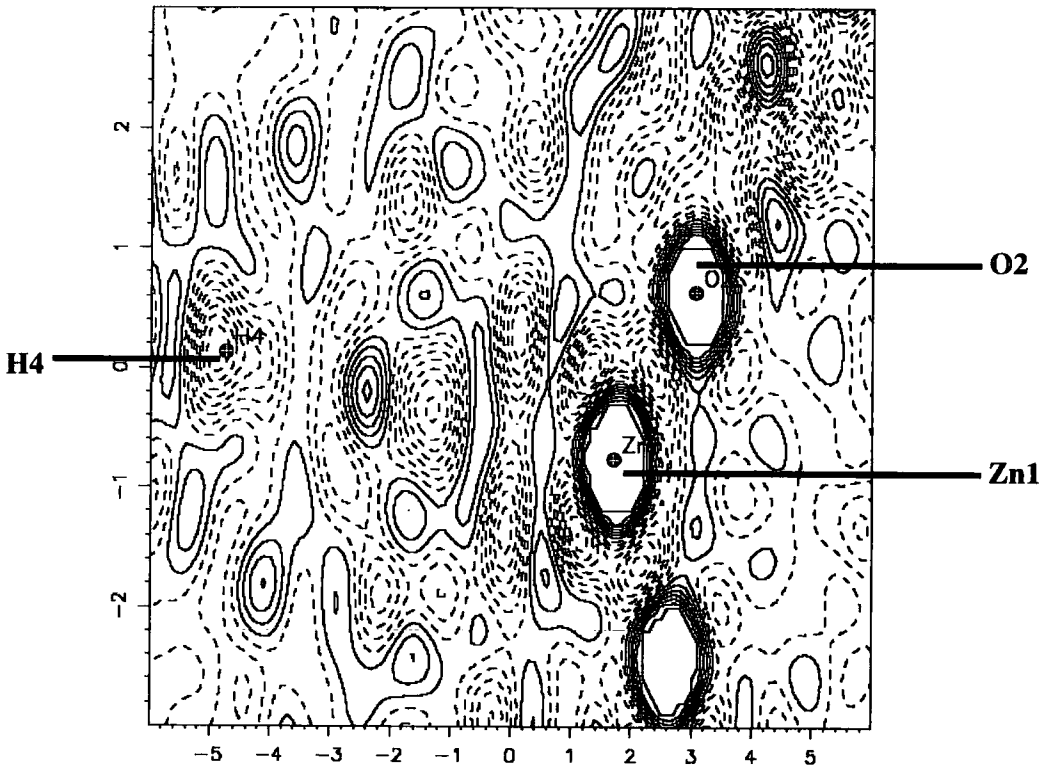

Figure 6.3.8: Slant plane neutron Fourier map defined by atoms H4, O2, and Zn1. The contour range is 5.0 – (-5.927) cmÅ^2, and the level is set to 0.6829 cmÅ^2.

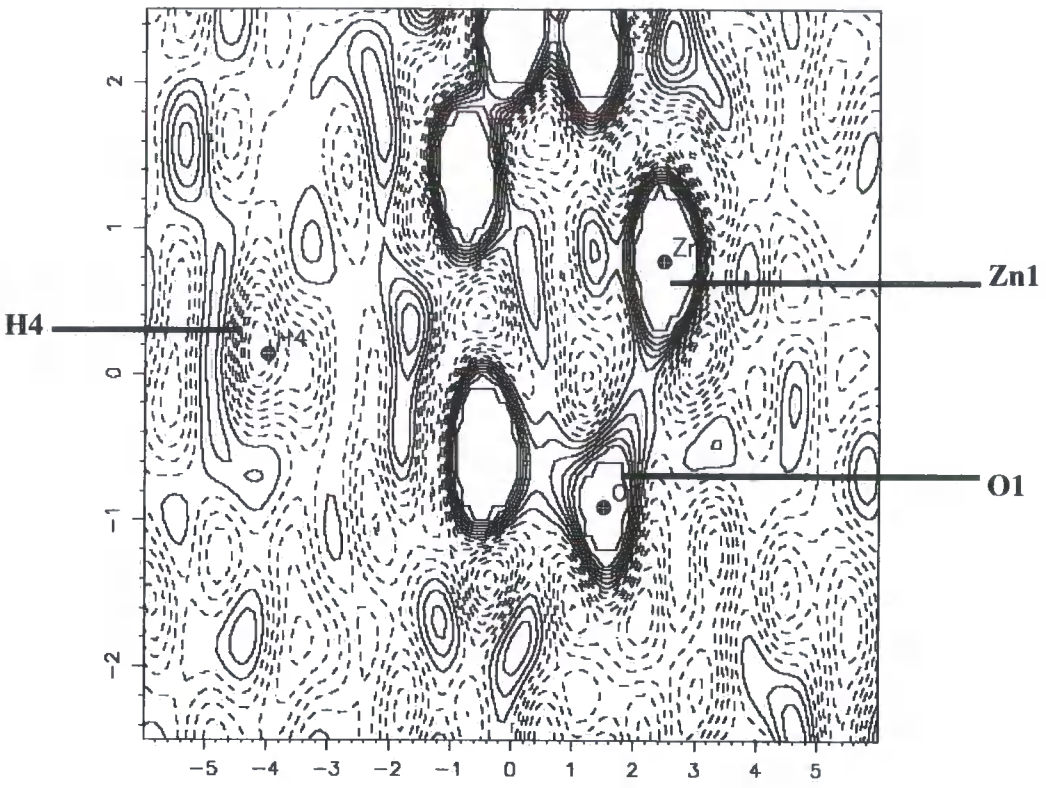

Figure 6.3.9: Slant plane neutron Fourier map defined by atoms H4, O1, and Zn1. The contour range is 5.0 – (-5.961) cmÅ^2, and the level is set to 0.6850 cmÅ^2.

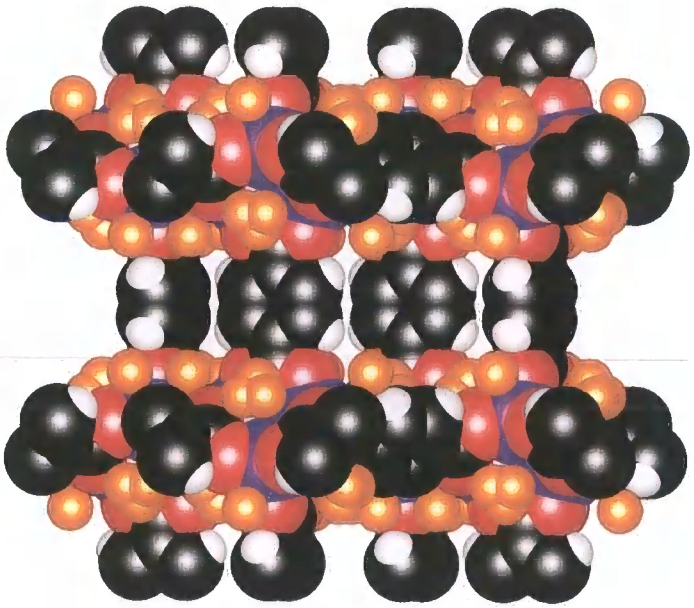

Figure 6.3.10: A space-filling representation of a single framework cavity for hydrogen-loaded $Zn_4O(BDC)$ at 5K. Zn: purple; O: red; C: black; framework hydrogen: grey; absorbed hydrogen: yellow.

At 5K, the gas–framework distances are O1···H1, 3.75(6) Å; O2···H1, 3.37(3) Å; Zn···H1, 3.61(5) Å; O2···H2, 3.23(5) Å; Zn···H2, 3.84(5) Å; O2···H4, 3.45(5) Å; Zn···H4, 3.64(6) Å. It is immediately apparent from a space-filling diagram of one of the framework cavities at 5K (Fig.6.3.10) that the hydrogen gas congregates in the vicinity of the framework nodes. At 120K, the evacuated framework contains ~77% of void space that is accessible to the hydrogen gas, and at 5K the physisorbed hydrogen gas occupies approximately 12% of this volume.

6.3.2 Summary for the refinement of hydrogen-loaded $Zn_4O(BDC)$ structures

The relationship between the gas sites identified in this study and those highlighted in the Ar/N_2 loaded $Zn_4O(BDC)$ X-ray diffraction study (Chapter 5) can easily be recognised. Molecule H1-H2 resides at the principal absorption site over a face of the tetrahedron of zinc atoms that forms part of the framework node (location of Ar1 / N1-N2). Hydrogen 'atom' H4 is positioned over a face of the ZnO_4 tetrahedra (location of Ar4 / N3).

It should be appreciated that the refinement of the neutron structures presented herein have been performed using only ~400 unique reflections. The availability of so few Fourier components inevitably leads to significant termination errors contributing to the background 'noise' in the calculated neutron F_{obs} Fourier maps. The maps used to aid the refinement of these structures have been meticulously examined to ensure that the gas absorption sites identified in this study are genuine, and not just artefacts caused by the low data completeness.

6.3.3 Comparison of the neutron results with other studies.

Using second-order Møller-Plesset perturbation theory, Sagara *et al.* calculated a binding energy of 6.86 $kJmol^{-1}$ for the interaction between the physisorbed hydrogen gas and the nodel regions of the $Zn_4O(BDC)_3$ architecture.[14] A lower binding energy of approximately 5.27 $kJmol^{-1}$ was estimated for the interaction between hydrogen gas and a fully protonated 1,4-benzenedicarboxylic acid molecule, a model which can be considered as a simple representation of the linker sections of the $Zn_4O(BDC)$ framework. The grand canonical Monte Carlo simulations executed by the same authors indicated that the absorption sites surrounding the metal clusters become saturated at 78K and 4800 kPa, at 300K the hydrogen gas was predicted to reside not only on sites located adjacent to nodes, but also near the BDC links.

The neutron diffraction results are in partial agreement with these theoretical findings. As predicted, the relatively high-energy absorption sites situated near to the metal clusters were

found to be fully occupied at low temperature (5K). However, no evidence of hydrogen gas residing in the framework channels was seen at 300K, and at none of the temperatures investigated was there any hydrogen gas located in the vicinity of the BDC linker molecules. That said, we do acknowledge that the neutron data are weak especially at higher temperatures. Additionally, the neutron data were collected at ~1 atm, and as such the amount of gas loaded into the framework will be reduced with respect to the Monte Carlo simulations. Both these factors may account for our inability to observe nuclear density at the lower energy sites that are theoretically predicted to be occupied at higher temperatures.

Rosi *et. al.* identified two distinct hydrogen absorption sites within the $Zn_4O(BDC)_3$ cavities using inelastic neutron scattering spectroscopy at 10K.[15] The authors concluded that one site was associated with the hydrogen gas interacting with the zinc atoms of the framework nodes, and the second site with the BDC linker molecules. Later, Rowsell *et al.* re-analysed these INS data and postulated that both the hydrogen gas absorption sites are connected with the ZnO_4 nodal clusters.[16] The first of these sites was said to be located over the shared vertex of the ZnO_4 units that is situated at the centre of the node, the neutron results presented herein concur with this assignment (site of molecule H1-H2). However, the authors speculated that the second site is located over an edge of the ZnO_4 tetrahedra; this is at odds with the model derived from the neutron diffraction data in which the second site is positioned over the face of the ZnO_4 tetrahedra (site of 'H4') (Fig.6.3.6).

6.4 Conclusion

The structural refinements of hydrogen-loaded $Zn_4O(BDC)$ based on Laue neutron diffraction data collected at 120K, 50K, 30K and 5K have been presented in this chapter. It has been shown that at $\geq$ 120K the framework cavities are devoid of hydrogen gas. At 50K and 30K a single gas molecule site was located, and shown to be 100% occupied. At 5K an additional site, with 98% occupancy was identified. Fourier maps based on the observed data (F_{obs}) have been presented as evidence for the existence of these hydrogen molecules within framework cavities. The work presented in this chapter is the first example of the use of neutron diffraction for the elucidation of hydrogen gas absorption sites within a host structure.

6.5 References

[1] Wilkinson C, Lehmann MS, *Nucl. Instr. and Meth.*, **A310**, 411 (1991).

[2] Cipriani F, Castagna J-C, Lehmann MS, Wilkinson C, *Physica B*, **213** & **214**, 975 (1995)

[3] Cipriani F, Castagna J-C, Wilkinson C, Oleinek P, Lehmann MS, *J. Neutron Res.*, **4**, 79 (1994)

[4] Cole JC, McIntyre GJ, Lehmann MS, Myles DAA, Wilkinson C, Howard JAKH, *Acta Cryst.*, **A57**, 429 (2001)

[5] http://www.ill.fr/YellowBook/

[6] Campbell JW, *J. Appl. Cryst.*, **28**, 228 (1995)

[7] Campbell JW, Hao Q, Harding MM, Nguti ND, Wilkinson C, *J. Appl. Cryst.*, **31**, 496 (1998)

[8] Wilkinson C, Khamis HW, Stansfield RFD, McIntyre GJ, *J. Appl. Cryst.*, **21**, 471 (1998)

[9] Prince E, Wilkinson C, McIntyre GJ, *J. Appl. Cryst.*, **30**, 133 (1997)

[10] Campbell JW, Habash J, Helliwell JR, Moffat K, *Q. Protein Crystallogr.*, **18**, 23 (1996)

[11] Sheldrick GM (2000). SHELXTL/PC. Version 6.10 for Windows NT. Bruker AXS Inc. Madison. Wisconsin. USA.

[12] Bondi A, *J. Phys. Chem.*, **68**, 441 (1964).

[13] Lide DR, *CRC Handbook of Chemistry and Physics*, 74th Ed. (1994)

[14] T. Sagara, J. Klassen, E. Ganz, *J. Chem. Phys.*, **121**(24), 12543 (2004).

[15] N. L. Rosi, J. Eckert, M. Eddaoudi, D. T. Vodak, J. Kim, M. O'Keeffe, O. M. Yaghi, *Science*, **300**, 1127 (2003).

[16] J. L. C. Rowsell, J. Eckert, O. M. Yaghi, *J. Am. Chem. Soc.*, Submitted (2005)

Appendix 1

Future Perspectives

In this appendix future research based on the work presented in this thesis is suggested. The research proposed is based solely on the literature and experimental studies reported in Chapters 4-6.

A1.1 Further Refinement of the Gas-Loaded Zn_4O(BDC) Structures

In Chapter 5 the refinements of nitrogen-loaded Zn_4O(BDC) were discussed in detail, and it was noted that in many cases the diatomic gas molecules that are located within the framework cavities are highly disordered, and in some cases the individual atoms of the gas molecules could not be resolved. Subsequently, it was concluded that modelling the disordered nitrogen gas molecules as diatomic molecules is not necessarily the best crystallographic strategy. A more appropriate model would be to assume that the electron density of one or both of the atoms of the diatomic is distributed isotropically about a centre of mass; this would require the structure factor of the atoms that are distributed in this manner to incorporate a Bessel function (see Appendix 3). Future work would involve the implementation of this model for the gas into the crystallographic models for the nitrogen-loaded Zn_4O(BDC) structures.

A1.2 Investigation into the Catalytic Activity of 2-D and 3-D Coordination Polymers

The purpose of the research proposed in this section is to further our understanding of the catalytic activity of coordination polymer (CP) materials by utilising single-crystal X-ray and neutron diffraction techniques to obtain structural information of CPs loaded with reaction substrates in attempted to gain valuable insight into the mechanism by which they function.

The gas absorption properties of transition metal carboxylates with the general formula $M_2(O_2CR)_4L_2$ have been well documented by Takamizawa, Mori and co-workers.[1-6] These

researchers have hypothesised that these materials comprise lantern-like metal clusters (see Fig.A1.2.1) linked by the dicarboxylate species into 2-D sheets that subsequently stack. The additional organic ligand (L), which is not always present, may in some cases act as a 'pillar' ligand and covalently bond adjacent layers (see Chapter 4 for more details).[1] The structural characterisation of this class of compounds has been confined to spectroscopic, magnetic and gas sorption measurements and theoretical simulations. Astonishingly, very few single crystal and powder diffraction studies have been performed on these materials.

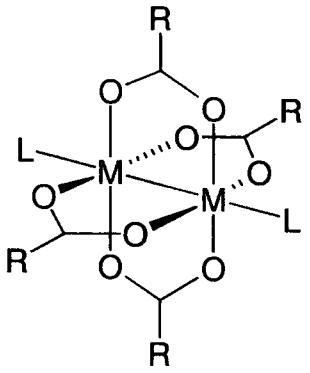

Figure A1.2.1: Lantern-like metal cluster suggested to be the major structural motif in $M_2(O_2CR)_4L_2$ coordination polymers. M = metal centre, L = additional ligand bound to the metal, R = dicarboxylate species.

The same authors have also shown that this class of CPs are capable of efficiently catalysing the hydrogenation of olefins at 200K.[7-9] It was also noted that the catalytic activity of the CP decreased over consecutive runs. It was suggested that the build up of hydrocarbons caused this poisoning of the catalysis. The proposed project work, listed below, can be regarded as an extension to the work presented in Chapters 5 and 6. The ultimate aim of this project being to understand the hydrogenation reaction mechanism and to determine the role played by the CP catalysis:

(1) Several different $M_2(O_2CR)_4L_2$ complexes with know catalytic properties should be synthesised. A crystallisation experiment should then be carried out in attempt to grow single crystals suitable for neutron analysis.

(2) The most promising candidate(s) identified from the crystallisation experiment should then be thoroughly characterised, and the catalytic properties of the material assessed. Evacuated, hydrogen-loaded, and olefin-loaded single crystals should be prepared. These systems can then be analysed by a combination of X-ray and neutron diffraction to identify the location of the reactants within the framework cavities.

(3) Additional samples containing a H_2 /olefin mixture (in different ratios) can be analysed. The use of low-temperature X-ray and neutron crystallography would be essential, as the reaction must be slowing down sufficiently to enable data to be obtained to give an insight into the behaviour of the mixture of reactant gases within the cavities (the hydrogenation reaction occurs at ~200K). Before commencing this ambitious work, the rate of the hydrogenation reaction as a function of temperature will need to be measured.

(4) To elucidate the nature of the catalysis poisoning, a *post*-reaction single-crystal should be analysed, in the hope that any species, in particular hydrocarbons, can be identified. From this information it maybe possible to tailor the CP to reduce the poisoning and improve the catalytic efficiency.

A1.3 References

[1] Mori W, Takamizawa S, *J. Solid State Chem.*, **152**, 120 (2000).

[2] Seki K, Mori W, *J. Phys. Chem. B*, **106**, 1380 (2002).

[3] Mori W, Inoue F, Yoshida K, Nakayama H, Takamizama S, Kihita M, *Chem. Lett.*, 1219 (1997).

[4] Seki K, Takamizawa S, Mori W, *Chem. Lett.*, 122 (2001).

[5] Takamizama S, Yamaguchi K, Mori W, *Inorg. Chem. Comm.*, **1**, 177 (1998).

[6] Takamizama S, Mori W, Furihata M, Takeda S, Yamaguchi K, *Inorg. Chim. Acta*, **283**, 268 (1998).

[7] Naito S, Tanibe T, Saito E, Miyao T, Mori W, *Chem. Lett.*, 1178 (2001).

[8] Ohmura, Mori W, Hiraga H, Ono M, Nishimoto Y, *Chem. Lett.*, **32**, 468 (2003).

[9] Mori W, Takamizawa S, Kato CN, Ohmura T, Sato T, *Mircopor. Mesopor. Mater.*, **73**, 31 (2004).

Appendix 2

Secondary Interactions and Graph-Set Analysis

This appendix has been included to provide the reader with a concise introduction to the key types of secondary interactions discussed in this thesis (primarily in Chapter 2). Additionally, in Section A2.2 the fundamental concepts of graph-set theory required for the analysis of hydrogen bond patterns will be presented.

A2.1 Secondary Interactions

Many of the crystal structures presented in Chapter 2 displayed complex networks of weak hydrogen bonds and $\pi\cdots\pi$ interactions. In this section these two types of secondary interactions will be introduced briefly. It is not the intention of this Appendix to evaluate the literature concerned with this extensive topic, but to enable the basic concepts and terminology associated with this branch of structural analysis to be defined. The discussion of aromatic interactions will be confined to $\pi\cdots\pi$ interactions between phenyl rings.

A2.1.1 Hydrogen bonds

No precise definition of the term 'hydrogen bond' has been agreed amongst the scientific community, and the subject remains controversial.[1,2] For the purposes of this thesis the definition proposed by Pimentel and McClellan in 1960 has been accepted. Therefore a hydrogen bond A-H···B is said to exist if the following criteria are fulfilled: (i) there is evidence of bond formation (association or chelation); (ii) there is evidence that this new bond linking A-H and B specifically involves the hydrogen atom already bonded to A.

The Pimentel-McClellan definition has been adopted as is does not presume to name atoms A and B. This allows for the possibility of C-H···B and A-H···π type interactions to be classed as

hydrogen bonds, and as significant evidence for existence these forms of secondary interactions is given in Chapter 2, this is the most appropriate definition of a hydrogen bond given to date.

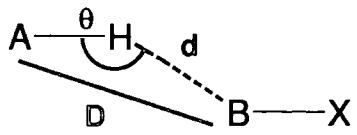

Figure A2.1.2: Schematic showing the geometric parameters for a hydrogen bond.

Table A2.1.1 summarises the properties of the three main classes of hydrogen bonds (strong, moderate and weak). Figure A2.1.2 illustrates the terms D, d and θ.

Table A2.1.1: Hydrogen bond properties.

	Strong	Moderate	Weak
Bond energy ($kJmol^{-1}$)	60-190	20-60	< 20
D range (Å)	2.2-2.5	2.5-3.0	3.0-4.0
d range (Å)	1.2-1.5	1.5-2.2	2.2-3.0
θ range (°)	175-180	130-180	90-180
Bond lengths	B-H ≈ A-H	B···H > A-H	B···H >> A-H
Example	[F···H···F]$^-$	O-H···O=C	C-H···O

A2.1.2 Aromatic interactions

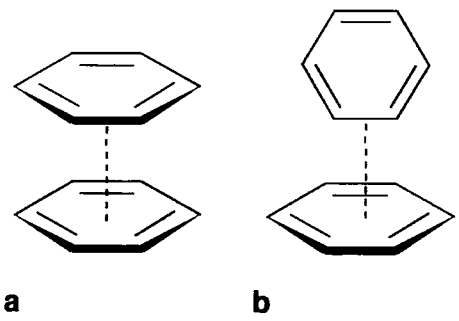

Figure A2.1.3: The two principal types of aromatic interactions (a) face-to-face stacking, (b) edge-to-face.

Aromatic contacts are predominantly a combination of van der Waals and electrostatic interactions with a 'bond energy' of 5-10 kJ mol^{-1}. A simplistic representation of an aromatic ring is to consider the carbon atoms as a positive framework (overlapped carbon σ-orbitals) sandwiched between two negatively charged electron π-clouds.[3] The two key types of π···π

interactions are shown in Figure A2.1.3. Of these two, the edge-to-face arrangement (Fig. A2.1.3b), in which the rings are orientated perpendicular to each other, is energetically favourable. This is because the repulsive interaction between the π-clouds is minimised, while the attractive framework–electron cloud interactions are maximised. The most energetically unstable situation is shown in Figure A2.1.3a in which, although the van der Waals forces are maximised, there is a strong repulsive interaction between the electron π-clouds of the stacked rings. The off-stacked arrangement shown in Figure A2.1.4 is an adaptation on this arrangement, and reduces the electron-cloud interaction and therefore is considerably more energetically favourable.

As in the case of weak hydrogen bonds, no consensus has been reached as to a cut-off limit for 'd' (Fig. A2.1.4), above which no π···π interaction would be considered feasible. The sum of van der Waals radii for a carbon-carbon contact is 3.40 Å,[4] so for the purposes of the analyses discussed in this thesis the upper limit for 'd' was set as 4.0 Å.

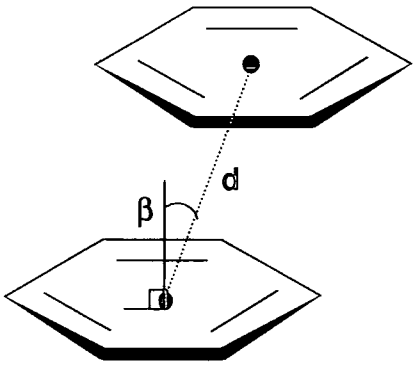

Figure A2.1.4: Diagram to illustrate the geometrical parameters associated with π···π interactions. The β-angle gives an indication as to the degree of ring slippage from the totally eclipsed arrangement, and 'd' is the distance between ring centroids.

A2.2 Graph-Set Analysis

By applying graph-set theory to the analysis of the hydrogen bond patterns seen in the crystal packing of a given compound, the most important hydrogen bond motifs can be readily identified, and the overall patterns to which they contribute can be characterised with relative ease. This allows for the hydrogen bond patterns observed in a structure to be evaluated systematically, and for comparisons to be made between different crystals structures. A glossary of graph-set terms is given in Table A2.2.1; these are the definitions that have been applied in

Chapter 2. For a more detailed appraisal of graph-set theory for hydrogen bond pattern recognition see references [5] and [6].

Table A2.2.1: Glossary of graph-set terms (adapted from Bernstein *et al.*).[5]

Term	**Definition**
Motif	A hydrogen pattern constructed with only one type of hydrogen bond.
Degree of a pattern (**n**)	The number of atoms in the pattern
Designator of a pattern (**B**)	One of the four letters **C** (chain), **R** (ring), **D** (discrete) or **S** (intramolecular), used to describe the type of pattern.
Descriptor [$\mathbf{B}_d^a(\mathbf{n})$]	Notation for fully describing a hydrogen bond pattern. **B** is the designator, a and d are the number of acceptor and donor atoms in the pattern, respectively. If a and d are omitted then it is assumed that they are equal to one. **n** is the degree of the pattern.
Unitary graph-set ($\mathbf{N_1}$)	A list of all descriptors for the motifs in a structure.
Binary graph-set ($\mathbf{N_2}$)	A descriptor in which two types of hydrogen bonds contribute to the pattern. This can be extended to tertiary for three types, quaternary for four types etc.
Basic / complex graph-set	For a particular set of hydrogen bonds the basic graph-set is the one with the lowest degree, in some cases it is possible to assign a descriptor with a higher degree and this is known at a complex graph-set.

The most effective method of explaining of graph-set analysis is by example. Figure A2.2.1 illustrates the method for graph-set assignment using simple hydrogen bond motifs for demonstration purposes. More complex examples are given in Figure A2.2.2.

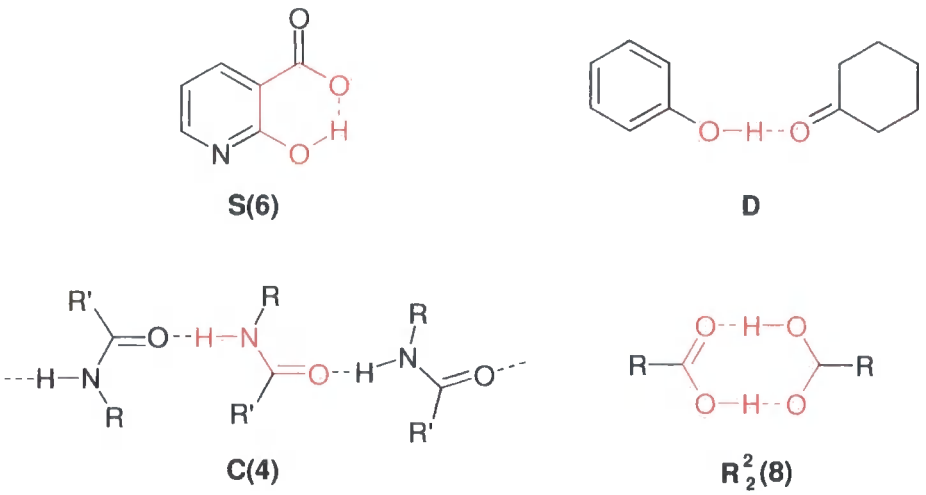

Figure A2.2.1: Simple hydrogen bond motifs with their graph-set assignments.

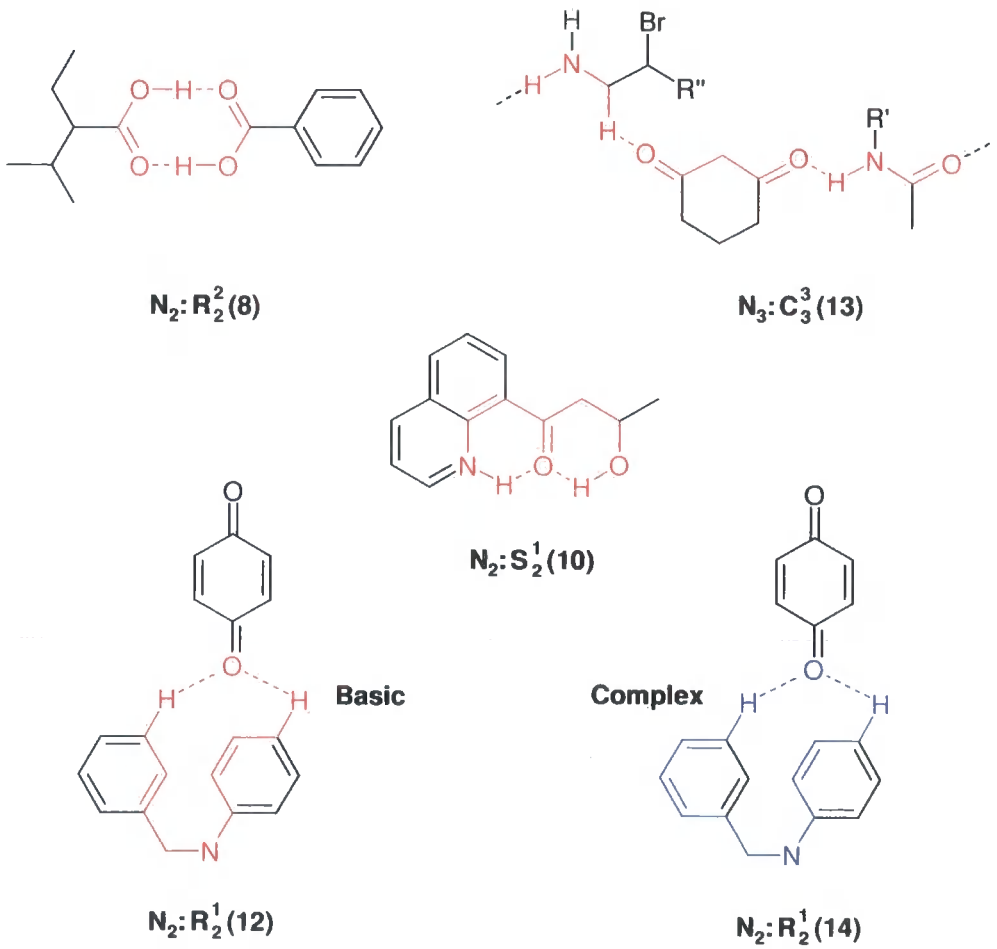

Figure A2.2.2: Complex hydrogen bond patterns with their higher-level graph-set assignments.

A1.3 References

[1] Aakeröy CB, Seddon KR, *Chem. Soc. Rev.*, 397 (1993).

[2] Desiraju GR, Steiner T, '*The Weak Hydrogen Bond in Structural Chemistry and Biology*', IUCr Monograph, Oxford University Press 1999.

[3] Hunter CA, Lawson KR, Perkins J, Urch CJ, *J. Chem. Soc., Perkin Trans. 2*, 651 (2001).

[4] Bondi A, *J.Phys.Chem.*, **68,** 441 (1964).

[5] Bernstein J, Davis RE, Shimoni L, Chang N-L, *Angew. Chem. Int. Ed.*, **34**, 1555 (1995).

[6] Etter MC, *Acc. Chem. Res.*, **23**, 120 (1990).

Appendix 3

Spherical Models for Disordered Diatomic Molecules

A3.1 Spherical Models

In Chapters 5 and 6 the diatomic gas molecules that were physically absorbed within the $Zn_4O(BDC)$ framework cavities exhibited varying degrees of molecular disorder, and subsequently modelling them as diatomic molecules is not crystallographically reasonable. However, there are two spherical models that are more appropriate, and these are shown pictorially in Figure A3.1.1.

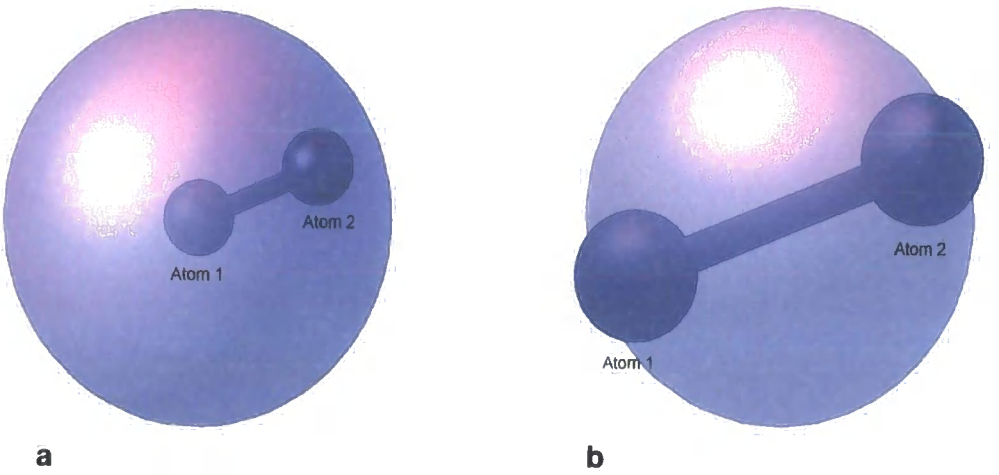

Figure A3.1.1: Two spherical models for disordered diatomic molecules. The large transparent blue spheres represent the 'smears' of electron density that are created by the molecular disorder. The atoms situated on these spheres cannot be regarded as discrete entities, in effect their electron density is disturbed evenly over the surface of the sphere.

Figure A3.1.1a shows a spherical model (model **A**) in which one atom of a diatomic molecule (atom 2) is assumed to be isotropically distributed about the second atom

(atom 1), creating a sphere of electron density surrounding the central pivot atom, the centre of mass in this case is positioned at atom 1. In the second model (model **B**), the molecule is oscillating about the centre of mass located at the middle of the bond between atoms 1 and 2 creating a sphere of electron density about this point (Fig.A3.1.1b).

To implement either of these models it is necessary to alter the contribution of atoms located on the surface of the sphere (atom 2 in model **A**, and both atoms 1 and 2 in model **B**, Fig.A3.1.1) to the structure factor for all reflections. Assuming that both atoms 1 and 2 are of type *i*, the contribution of an atom on the sphere to a structure factor is given by Expression A3.1.1.[1,2] In this expression, f_i is the atomic scattering factor, r is the radius of the sphere, s is equal to $\sin\theta/\lambda$, B_i is the temperature factor for atom(s) i ($B = 8\pi^2 U_{iso}$), $\bar{r}_c$ is the vector that defines the centre of mass for the disordered molecule, and $\bar{h}$ is the scattering vector.

$$f_i \cdot \left(\frac{\sin 4\pi rs}{4\pi rs} \right) \exp\left(-B_i s^2\right) \exp\left(-2\pi . \bar{r}_c . \bar{h}\right)$$

Expression A3.1.1: Contribution of atoms of type *i* positioned on the sphere in models **A** and **B**.

The sine term in Expression A3.1.1 is a mathematical function, known as a Bessel function that modifies the atomic scattering factor of atom *i* in such away so that it represents scattering from a sphere with a radius *r*. In the case of model **A**, *r* is equal to the A1-A2 bond length, and in model **B** *r* equals half the A1-A2 bond length. Figure A3.1.2 demonstrate the consequence of multiplying the atomic scattering factor by the Bessel function, in this example, the diatomic is assumed to be a nitrogen gas molecule (N_2), where $r = 1.097$ Å for model **A**, and $r = 0.5485$ Å for model **B**.

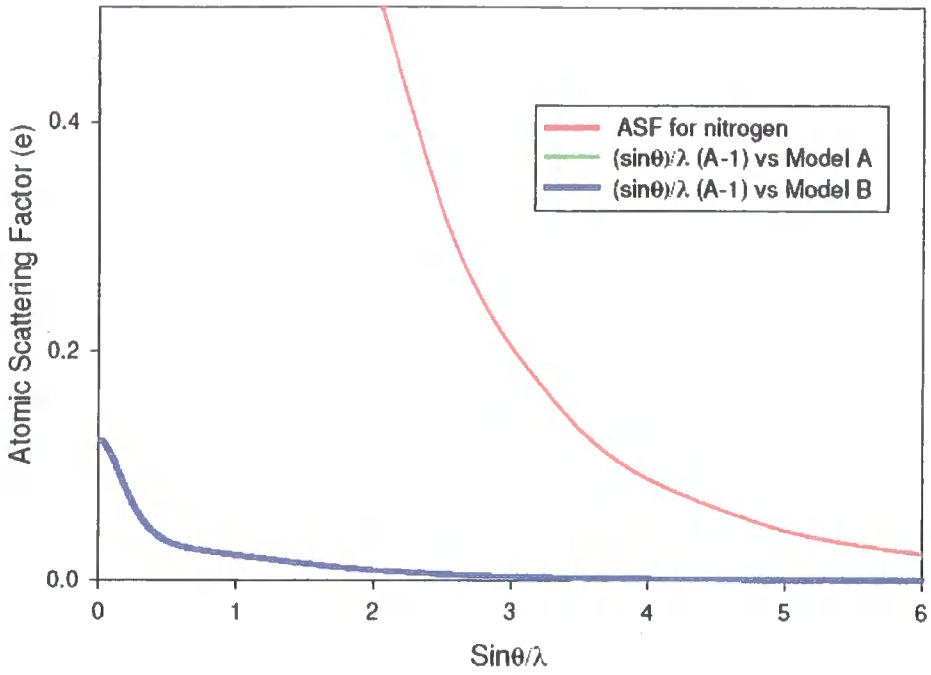

Figure A3.1.2: Graph showing the effect of multiplying the atomic scattering factor (ASF) for nitrogen by a Bessel function. The ASF for models A and B overlay each other, and for this reason their graphs cannot be resolved.

For the disordered nitrogen and hydrogen molecules discussed in Chapters 5 and 6 respectively, it is exceptionally difficult to determine which of the models presented above would most accurately portray the molecular disorder. The model should be selected only after careful examination of the relevant F_{obs} Fourier maps, however, it likely that there will still remain some degree of ambiguity as to the most appropriate model.

A3.2 References

[1] Smith HG, Levy HA, *Acta Cryst.*, **15**, 1201 (1962).

[2] Lundgren J-O, *Acta Cryst.*, **B35**, 1027 (1979).

Appendix 4

Calculation of Bond Lengths and Errors

In Chapter 6 the variable temperature neutron diffraction analysis of hydrogen-loaded $Zn_4O(BDC)$ was discussed in detail, the structures reported in this chapter were refined using standard SHELTX software (see Chapter 1). The bond lengths for the hydrogen molecules, and their associated estimated standard deviations (e.s.d.), are not calculated by SHELX. Subsequently, it has been necessary for these figures to be computed manually, the method employed for these calculations is explained in this Appendix.

A4.1 Calculation of Bond Lengths

The bond length (r) between two atoms A and B, can be calculated with Equation A4.1.1, where a, b, c, α, β, and γ are the unit cell parameters, and Δx, Δy, and Δz are the differences between the x, y, z coordinates of atoms A and B, respectively.[1]

$$r = \left[(a\Delta x)^2 + (b\Delta y)^2 + (c\Delta z)^2 + 2ab\cdot\cos\gamma\cdot\Delta x\Delta y + 2ac\cdot\cos\beta\cdot\Delta x\Delta z + 2bc\cdot\cos\alpha\cdot\Delta y\Delta z\right]^{1/2}$$

Equation A4.1.1

In the case of the diatomic hydrogen molecules absorbed within cubic $Zn_4O(BDC)$ $\alpha = \beta = \gamma = 90^o$ and Equation A4.1.1 simplifies to

$$r = \left[(a\Delta x)^2 + (b\Delta y)^2 + (c\Delta z)^2\right]^{1/2}$$

Equation A4.1.2.

For example, the atomic coordinates for constituent atoms of the H1-H2 molecule at 30K are given in Table A4.1.1.

Table A4.1.1: Atom coordinates for atoms H1 and H2 at 30K.

	x	y	z
H1	0.332(1)	0.168(1)	0.168(1)
H2	0.332(1)	0.168(1)	0.140(1)

By substituting the values in Table A3.1.1 into Equation A3.1.2 the bond distance between atoms H1 and H2 can be calculated:

$$r = \left[(25.8821\times 0)^2 + (25.8821\times 0)^2 + (25.8821\times 0.028)^2\right]^{1/2}$$

$$\boldsymbol{r = 0.7247\ \text{Å}}$$

Repeating this procedure for H1-H2 at 5K:

Table A4.1.2: Atom coordinates for atoms H1 and H2 at 5K.

	x	y	z
H1	0.334(1)	0.166(1)	0.166(1)
H2	0.333(1)	0.167(1)	0.139(2)

Substituting the values in Table A4.1.2 into Equation A4.1.2 to calculate the bond distance between atoms H1 and H2 at 5K:

$$r = \left[(25.8821\times 0.001)^2 + (25.8821\times 0.001)^2 + (25.8821\times -0.027)^2\right]^{1/2}$$

$$\boldsymbol{r = 0.6998\ \text{Å}}$$

A4.2 Calculation of Estimated Standard Deviations

The estimated standard deviation values (σ) for bond lengths calculated in the last section can be determined with Equation A4.2.1.[1]

$$\sigma_r = \left[\begin{array}{l} \left(\sigma_{x1}^2 + \sigma_{x2}^2\right)\left(\frac{\Delta x + \Delta y \cdot \cos\gamma + \Delta z \cdot \cos\beta}{r}\right)^2 + \left(\sigma_{y1}^2 + \sigma_{y2}^2\right)\left(\frac{\Delta y + \Delta x \cdot \cos\gamma + \Delta z \cdot \cos\alpha}{r}\right)^2 \\ + \left(\sigma_{z1}^2 + \sigma_{z2}^2\right)\left(\frac{\Delta z + \Delta x \cdot \cos\beta + \Delta y \cdot \cos\alpha}{r}\right)^2 \end{array} \right]^{1/2}$$

Equation A4.2.1

In Equation A4.2.1 the terms a, b, c, α, β, and γ are the unit cell parameters, and Δx, Δy, and Δz are the differences between the x, y, z coordinates of atoms H1 and H2, respectively, and the sigma terms are the esd values for the atomic coordinates e.g. σ_{x1} is the esd for the x-coordinate of atom H1. However, as $\alpha = \beta = \gamma = 90^\circ$ Equation A4.2.1 simplifies to Equation A4.2.2.

$$\sigma_r = \left[\left(\sigma_{x1}^2 + \sigma_{x2}^2\right)\left(\frac{\Delta x}{r}\right)^2 + \left(\sigma_{y1}^2 + \sigma_{y2}^2\right)\left(\frac{\Delta y}{r}\right)^2 + \left(\sigma_{z1}^2 + \sigma_{z2}^2\right)\left(\frac{\Delta z}{r}\right)^2 \right]^{1/2}$$

Equation A4.2.2

Substituting the esd values reported in Table A4.1.1 into Equation A4.2.1 gives

$$\sigma_r = \left[\begin{array}{l} \left(0.001^2 + 0.001^2\right)\left(\frac{0}{0.7247}\right)^2 + \left(0.001^2 + 0.001^2\right)\left(\frac{0}{0.7247}\right)^2 \\ + \left(0.001^2 + 0.002^2\right)\left(\frac{0.028}{0.7247}\right)^2 \end{array} \right]^{1/2}$$

σ_r = **0.0001** (to 4 d.p.)

Therefore the H1-H2 bond length AT 30K is 0.7247(1) Å. Repeating the above calculation for H1-H2 at 5K gives an esd value of 0.0001 (to 4 d.p.), thus the H1-H2 bond length at 5K is 0.6998(1) Å.

A4.3 References

[1] Glusker JP, Lewis M, Rossi M, 'Crystal Structure Analysis for Chemists and Biologists', Wiley-VCH 1994.

Appendix 5

List of Publications

---

[1] E. C. Spencer, M. B. Mariyatra, J. A. K. Howard, K. Panchanatheswaran, *Acta Cryst.*, **C60**, o839 (2004).

[2] D. R. Turner, E. C. Spencer, J. A. K. Howard, D. A. Tocher, J. W. Steed, *Chem. Commun.*, 1352 (2004).

[3] D. R. Turner, B. Smith, E. C. Spencer, A. E. Goeta, I. Radosavljevic Evans, D. A. Tocher, J. A. K. Howard, J. W. Steed, *New J. Chem.*, **29**, 90 (2005).

[4] L. K. Thompson, T. L. Kelly, L. N. Dawe, H. Grove, M. T. Lemaire, J. A. K. Howard, E. C. Spencer, C. J. Matthews, S. T. Onions, *Inorg. Chem.*, **43**(24), 7605 (2004).

[5] E. C. Spencer, B. Kalyanasundari, M. B. Mariyatra, J. A. K. Howard, K. Panchanatheswaran, *Inorg. Chem. Acta*, Submitted (2005).

[6] E. C. Spencer, M. B. Mariyatra, J. A. K. Howard, K. Panchanatheswaran, *J. Organomet. Chem.*, Submitted (2005).

[7] E. C. Spencer, J. A. K. Howard, G. J. McIntyre, J. L. C. Rowsell, O. M. Yaghi, *Chem. Commun.*, In preparation (2005).

In addition to the papers listed above, twelve articles have been published in the electronic journal Acta Cryst. Section E (see Chapter 2 Section 2.5, and Chapter 3 Section 3.5).

Appendix 6

Conferences, Seminars and Courses Attended

A6.1 Conferences Attended

[1] British Crystallography Association Autumn Meeting (London)
13th November 2002

[2] Physical Chemistry Group Winter Meeting (Edinburgh)
11th December 2002

[3] Materials for Energy Production and Storage Conference
(Rutherford Appleton Laboratory)

[4] British Crystallography Association Spring Meeting (York)
15th-17th April 2003

[5] British Crystallography Association Spring Meeting (Loughborough)
12th-14th April 2005

[6] American Crystallographic Association Annual Meeting
(Orlando, USA) 27th May – 2nd June 2005

A6.2 Departmental Seminars Attended

[1] Gideon Davis, *'Structural Enzymology of Glycosyl Transfer'*, 1st October 2002

[2] Jinqui Qui, *'New Design Approaches for Non-linear Optical Chromophores and Molecular Conductive Magnets'*, 9th October 2002

[3] Jack Dunitz, *'Are Crystal Structures Predictable?'*, 10th October 2002

[4] Paul Raithby, *'Adventures in Organometallic Polymer Chemistry'*,
12th February 2003

[5] Tony Ryan, *'Introducing Soft Nanotechnology'*, 19th February 2003

A6.3 Courses Attended

[1] BCA/CCG Intensive teaching school on X-ray structural analysis. (Durham) 7^{th} –15^{th} April 2003

[2] Oxford School on Neutron Scattering (Oxford) 8^{th} – 18^{th} September 2003

[3] HERCULES (Grenoble) 22^{nd} February – 2^{nd} April 2004

[4] Erice International School of Crystallography: Electron Crystallography (Erice) 10^{th} – 19^{th} June 2005

Supplementary Data Tables for Chapter 2

Compound 1: 3-Nitrobenzenesulphonyl chloride.

Table S.2.1: Atomic coordinates ($x10^4$) and U_{eq}($Å^2$ x 10^3) for 3-Nitrobenzenesulphonyl Chloride.

Atom	x	y	z	U_{eq}
S1	1052(1)	3052(1)	4951(1)	21(1)
Cl1	3231(1)	4303(1)	5377(1)	37(1)
C1	2439(3)	-821(2)	4223(2)	20(1)
C2	3410(3)	-1353(2)	5311(2)	24(1)
C3	3635(3)	-513(2)	6308(2)	27(1)
C4	2911(3)	838(2)	6199(2)	25(1)
C5	1983(3)	1340(2)	5083(2)	19(1)
C6	1716(3)	529(2)	4071(2)	19(1)
N1	2148(3)	-1732(2)	3177(2)	25(1)
O1	3023(3)	-2819(2)	3273(2)	36(1)
O2	1028(3)	-1359(2)	2269(2)	39(1)
O3	254(2)	3270(2)	5861(2)	32(1)
O4	94(3)	3315(2)	3754(2)	41(1)

Compound 2: Phenyl 3-nitrobenzenesulphonate.

Table S.2.2: Atomic coordinates ($x10^4$) and U_{eq}($Å^2$ x 10^3) for Phenyl 3-nitrobenzenesulphonate.

Atom	x	y	z	U_{eq}
S1	2629(1)	-1124(1)	3236(1)	19(1)
C1	1125(2)	630(2)	7016(6)	18(1)
C2	1132(2)	1622(2)	5871(5)	20(1)
C3	1590(2)	1769(2)	3843(5)	22(1)
C4	2041(2)	918(2)	3034(6)	18(1)
C5	2032(2)	-61(2)	4260(5)	16(1)
C6	1573(2)	-239(2)	6291(5)	16(1)
C7	3791(2)	97(2)	4286(6)	18(1)
C8	3694(2)	896(2)	6005(6)	21(1)
C9	4058(2)	1882(2)	5661(6)	23(1)
C10	4499(2)	2057(2)	3633(6)	22(1)
C11	4594(2)	1234(2)	1933(6)	23(1)
C12	4241(2)	234(2)	2258(6)	21(1)
N1	621(1)	485(2)	9160(4)	24(1)
O1	218(1)	1259(2)	9769(4)	31(1)
O2	636(1)	-394(2)	10221(4)	29(1)
O3	2373(1)	-2141(1)	4141(3)	25(1)
O4	2761(1)	-970(1)	710(3)	25(1)
O5	3412(1)	-918(1)	4680(3)	20(1)

Compound 3: 2-Nitrophenyl 3-nitrobenzenesulphonate.

Table S.2.3: Atomic coordinates ($x10^4$) and U_{eq}($Å^2$ x 10^3) for 2-Nitrophenyl 3-nitrobenzenesulphonate.

Atom	x	y	z	U_{eq}
S1	2595(1)	4436(1)	5057(1)	22(1)
C1	1010(1)	5951(2)	7938(5)	23(1)
C2	976(1)	6856(2)	6474(5)	26(1)
C3	1454(1)	7034(2)	4570(5)	29(1)
C4	1954(1)	6292(2)	4122(5)	27(1)
C5	1964(1)	5381(2)	5619(4)	22(1)
C6	1500(1)	5189(2)	7576(4)	21(1)
C7	3551(1)	5718(2)	6233(4)	21(1)
C8	3403(1)	6644(2)	7508(5)	25(1)
C9	3754(1)	7551(2)	6868(5)	28(1)
C10	4228(1)	7535(2)	4901(6)	26(1)
C11	4375(1)	6609(2)	3604(5)	24(1)
C12	4041(1)	5700(2)	4328(4)	20(1)
N1	513(1)	5783(1)	10011(4)	26(1)
N2	4253(1)	4710(2)	3104(4)	25(1)
O1	78(1)	6456(1)	10301(4)	35(1)
O2	561(1)	4990(1)	11363(3)	32(1)
O3	2808(1)	4529(1)	2416(3)	29(1)
O4	2400(1)	3452(1)	6120(3)	28(1)
O5	3192(1)	4806(1)	6923(3)	23(1)
O6	4279(1)	3924(1)	4488(3)	33(1)
O7	4408(1)	4734(1)	786(3)	34(1)

Compound 4: 2,4-Dinitrophenyl 3-nitrobenzenesulphonate.

Table S.2.4: Atomic coordinates ($x10^4$) and U_{eq}($Å^2$ x 10^3) for 2,4-Dinitrophenyl 3-nitrobenzenesulphonate.

Atom	x	y	z	U_{eq}
S1	6809(1)	4785(1)	4324(1)	17(1)
C1	6394(1)	8435(4)	1180(2)	18(1)
C2	6787(1)	10065(4)	840(2)	22(1)
C3	7193(1)	10039(5)	1583(2)	24(1)
C4	7203(1)	8437(4)	2661(2)	19(1)
C5	6799(1)	6855(4)	2976(2)	15(1)
C6	6390(1)	6804(4)	2241(2)	18(1)
C7	6181(1)	6853(4)	5886(2)	15(1)
C8	5801(1)	8235(4)	5321(2)	18(1)
C9	5353(1)	8283(4)	5895(2)	19(1)
C10	5298(1)	6906(4)	7008(2)	17(1)
C11	5668(1)	5508(4)	7602(2)	18(1)
C12	6108(1)	5526(4)	7013(2)	16(1)
N1	5962(1)	8425(4)	387(2)	23(1)
N2	6517(1)	4156(4)	7654(2)	20(1)
N3	4824(1)	6976(4)	7639(2)	24(1)
O1	5928(1)	10242(3)	-417(2)	30(1)
O2	5658(1)	6588(4)	569(2)	28(1)
O3	7293(1)	4132(3)	4616(1)	25(1)
O4	6447(1)	2683(3)	4223(2)	21(1)
O5	6646(1)	6961(3)	5408(1)	18(1)
O6	6711(1)	2177(3)	7149(2)	34(1)
O7	6622(1)	5114(3)	8673(1)	30(1)
O8	4530(1)	8714(3)	7298(2)	32(1)
O9	4755(1)	5267(4)	8462(2)	44(1)

Compound 5: 8-Quinolyl 3-nitrobenzenesulphonate.

Table S.2.5: Atomic coordinates ($x10^4$) and U_{eq}($Å^2$ x 10^3) for 8-Quinolyl 3-nitrobenzenesulphonate.

Atom	x	y	z	U_{eq}	Atom	x	y	z	U_{eq}
S1	9973(1)	3980(1)	7311(1)	17(1)	S2	3483(1)	6529(1)	7100(1)	19(1)
C1	8324(2)	5101(1)	9047(1)	20(1)	C16	5212(2)	7546(1)	5227(1)	19(1)
C2	8705(2)	4588(1)	8639(1)	19(1)	C17	4825(2)	7058(1)	5701(1)	18(1)
C3	9590(2)	4625(1)	7899(1)	16(1)	C18	4096(2)	7139(1)	6504(1)	17(1)
C4	10103(2)	5155(1)	7595(1)	20(1)	C19	3763(2)	7690(1)	6814(1)	20(1)
C5	9710(2)	5659(1)	8039(2)	23(1)	C20	4171(2)	8168(1)	6312(2)	23(1)
C6	8800(2)	5638(1)	8764(2)	23(1)	C21	4916(2)	8102(1)	5514(2)	21(1)
C7	11130(2)	3093(1)	8301(1)	16(1)	C22	5123(2)	5586(1)	7229(1)	17(1)
C8	11748(2)	2713(1)	7727(1)	18(1)	C23	4424(2)	5222(1)	7792(1)	21(1)
C9	11678(2)	2115(1)	7913(2)	21(1)	C24	4464(2)	4620(1)	7632(2)	23(1)
C10	10995(2)	1921(1)	8666(1)	20(1)	C25	5221(2)	4399(1)	6935(2)	22(1)
C11	10341(2)	2311(1)	9268(1)	18(1)	C26	5992(2)	4771(1)	6362(1)	18(1)
C12	9632(2)	2133(1)	10064(1)	21(1)	C27	6815(2)	4572(1)	5630(1)	22(1)
C13	9016(2)	2539(1)	10597(1)	22(1)	C28	7512(2)	4959(1)	5101(1)	23(1)
C14	9088(2)	3126(1)	10339(1)	21(1)	C29	7367(2)	5553(1)	5284(1)	21(1)
C15	10388(2)	2917(1)	9083(1)	16(1)	C30	5937(2)	5379(1)	6496(1)	16(1)
N1	7359(2)	5067(1)	9829(1)	27(1)	N3	5998(2)	7468(1)	4375(1)	24(1)
N2	9749(2)	3322(1)	9616(1)	18(1)	N4	6610(2)	5769(1)	5952(1)	19(1)
O1	6934(2)	5522(1)	10153(1)	41(1)	O6	6573(2)	7895(1)	4050(1)	31(1)
O2	7048(2)	4586(1)	10109(1)	41(1)	O7	6027(2)	6977(1)	4038(1)	35(1)
O3	8600(2)	3622(1)	7162(1)	21(1)	O8	2436(2)	6181(1)	6425(1)	25(1)
O4	10718(2)	4120(1)	6504(1)	25(1)	O9	3003(2)	6715(1)	7976(1)	29(1)
O5	11258(2)	3696(1)	8139(1)	18(1)	O10	5116(1)	6191(1)	7385(1)	19(1)

Compound 6: Methyl 4-(3-nitrobenzenesulphonyloxy)benzoate.

Table S.2.6: Atomic coordinates ($x10^4$) and U_{eq}($Å^2$ x 10^3) for Methyl 4-(3-nitrobenzenesulphonyloxy)benzoate.

Atom	x	y	z	U_{eq}
S1	2669(1)	2209(1)	-1161(1)	19(1)
C1	4645(2)	1007(2)	1189(1)	23(1)
C2	5587(2)	1936(2)	1213(2)	30(1)
C3	5641(2)	2951(2)	477(2)	33(1)
C4	4761(2)	3041(2)	-263(2)	26(1)
C5	3828(1)	2087(2)	-259(1)	20(1)
C6	3758(2)	1051(2)	460(1)	20(1)
C7	1638(1)	4140(2)	-78(1)	16(1)
C8	1867(2)	4224(2)	946(1)	19(1)
C9	1749(2)	5498(2)	1411(1)	19(1)
C10	1420(1)	6660(2)	852(1)	17(1)
C11	1258(1)	6551(2)	-189(1)	17(1)
C12	1357(1)	5278(2)	-663(1)	16(1)
C13	1171(2)	7958(2)	1422(1)	21(1)
C14	728(2)	10335(2)	1321(2)	25(1)
N1	4580(2)	-84(2)	1966(1)	31(1)
O1	5336(1)	-65(2)	2642(1)	43(1)
O2	3775(1)	-945(2)	1893(1)	41(1)
O3	2273(1)	862(1)	-1429(1)	26(1)
O4	2992(1)	3189(1)	-1914(1)	27(1)
O5	1580(1)	2794(1)	-515(1)	18(1)
O6	1051(1)	8006(1)	2326(1)	33(1)
O7	1057(1)	9061(1)	816(1)	20(1)

Compound 7: Methyl 4-tosyloxybenzoate.

Table S.2.7: Atomic coordinates ($x10^4$) and U_{eq}($Å^2$ x 10^3) for Methyl 4-tosyloxybenzoate.

Atom	x	y	z	U_{eq}
S1	5265(1)	3467(1)	1894(1)	24(1)
C1	10938(3)	6111(2)	1054(2)	35(1)
C2	9518(2)	5459(1)	1270(1)	27(1)
C3	9799(2)	4511(2)	1812(1)	28(1)
C4	8510(2)	3897(2)	2014(1)	26(1)
C5	6911(2)	4240(1)	1663(1)	23(1)
C6	6595(2)	5185(2)	1124(1)	30(1)
C7	7900(2)	5789(2)	930(1)	31(1)
C8	5713(2)	1878(1)	752(1)	21(1)
C9	5910(2)	958(1)	1322(1)	24(1)
C10	6771(2)	89(1)	1046(1)	24(1)
C11	7394(2)	143(1)	211(1)	21(1)
C12	7180(2)	1078(1)	-347(1)	23(1)
C13	6335(2)	1960(1)	-72(1)	23(1)
C14	8218(2)	-845(1)	-76(1)	24(1)
C15	9092(3)	-1745(2)	-1349(2)	34(1)
O1	5823(2)	2756(1)	2679(1)	30(1)
O2	3877(2)	4149(1)	1883(1)	33(1)
O3	4716(1)	2753(1)	950(1)	23(1)
O4	8645(2)	-1608(1)	440(1)	33(1)
O5	8398(2)	-791(1)	-987(1)	31(1)

Compound 8: 2-Naphthyl 4-toluenesulphonate.

Table S.2.8: Atomic coordinates ($x10^4$) and U_{eq}($Å^2$ x 10^3) for 2-Naphthyl 4-toluenesulphonate.

Atom	x	y	z	U_{eq}	Atom	x	y	z	U_{eq}
S1	3310(1)	9187(1)	6220(1)	27(1)	S2	9699(1)	5820(1)	10564(1)	20(1)
C1	9502(4)	9530(1)	1037(5)	32(1)	C18	3206(4)	5482(1)	5314(6)	31(1)
C2	7955(3)	9451(1)	2330(5)	23(1)	C19	4829(3)	5561(1)	6635(5)	23(1)
C3	8098(3)	9260(1)	4410(5)	26(1)	C20	6370(4)	5425(1)	5829(5)	23(1)
C4	6674(3)	9171(1)	5620(5)	22(1)	C21	7874(3)	5499(1)	7032(4)	21(1)
C5	5103(3)	9286(1)	4700(5)	24(1)	C22	7821(3)	5708(1)	9063(4)	18(1)
C6	4923(3)	9493(1)	2658(5)	23(1)	C23	6300(3)	5840(1)	9924(5)	20(1)
C7	6353(4)	9570(1)	1487(5)	25(1)	C24	4813(3)	5766(1)	8703(5)	24(1)
C8	2725(3)	8340(1)	5049(5)	24(1)	C25	9723(3)	6656(1)	9072(5)	21(1)
C9	3566(3)	8136(1)	3416(5)	25(1)	C26	9920(3)	6960(1)	10728(5)	21(1)
C10	4719(4)	7420(1)	1904(5)	29(1)	C27	9356(4)	7736(1)	12172(5)	27(1)
C11	4966(4)	6957(1)	2046(6)	35(1)	C28	8630(4)	8156(1)	11897(6)	35(1)
C12	4414(4)	6707(1)	3860(6)	35(1)	C29	7676(4)	8266(1)	9956(5)	34(1)
C13	3616(4)	6926(1)	5505(5)	33(1)	C30	7493(4)	7959(1)	8314(5)	30(1)
C14	2474(4)	7644(1)	7044(5)	29(1)	C31	8066(4)	7179(1)	6864(5)	25(1)
C15	2160(4)	8102(1)	6890(5)	28(1)	C32	8800(3)	6756(1)	7110(5)	25(1)
C16	3889(3)	7654(1)	3555(5)	24(1)	C33	9165(3)	7407(1)	10508(5)	22(1)
C17	3324(3)	7410(1)	5395(5)	26(1)	C34	8242(3)	7510(1)	8527(4)	24(1)
O1	2236(3)	9577(1)	6089(5)	41(1)	O4	10857(3)	5452(1)	10349(4)	30(1)
O2	3813(3)	8992(1)	8286(4)	36(1)	O5	9319(3)	5990(1)	12672(3)	28(1)
O3	2264(2)	8809(1)	4804(3)	24(1)	O6	10545(2)	6225(1)	9197(3)	22(1)

Supplementary Data Tables for Chapter 3

Compound 1: Benzoylmethylenetriphenylphosphorane & Terephthalic Acid Co-crystal

Table S.3.1: Atomic coordinates (x 10^4) and equivalent isotropic displacement parameters ($Å^2$x 10^3)for Benzoylmethylenetriphenylphosphorane & Terephthalic Acid Co-crystal.

Atom	x	y	z	U_{eq}	Atom	x	y	z	U_{eq}
P1	926(1)	544(1)	7101(1)	17(1)	C18	-3030(2)	1435(1)	5774(1)	26(1)
C1	3340(2)	1323(1)	4908(1)	19(1)	C19	-2031(2)	1224(1)	5141(1)	24(1)
C2	3734(2)	2025(1)	4579(1)	22(1)	C20	-833(2)	965(1)	5553(1)	21(1)
C3	4558(2)	2096(1)	3763(1)	26(1)	C21	637(2)	-435(1)	7331(1)	18(1)
C4	5004(2)	1471(1)	3265(1)	29(1)	C22	-529(2)	-781(1)	6986(1)	22(1)
C5	4632(2)	768(1)	3589(1)	28(1)	C23	-673(2)	-1548(1)	7088(1)	26(1)
C6	3803(2)	694(1)	4400(1)	22(1)	C24	343(2)	-1963(1)	7538(1)	26(1)
C7	2406(2)	1272(1)	5770(1)	19(1)	C25	1498(2)	-1621(1)	7893(1)	25(1)
C8	2170(2)	595(1)	6236(1)	19(1)	C26	1652(2)	-859(1)	7795(1)	22(1)
C9	1325(2)	966(1)	8320(1)	19(1)	C27	4662(2)	503(1)	749(1)	26(1)
C10	2330(2)	1502(1)	8393(1)	23(1)	C28	5418(2)	735(1)	-53(1)	24(1)
C11	2624(2)	1846(1)	9317(1)	26(1)	C29	5753(2)	230(1)	-803(1)	28(1)
C12	1937(2)	1656(1)	10171(1)	29(1)	C30	5897(2)	1522(1)	-137(1)	26(1)
C13	944(2)	1123(1)	10103(1)	27(1)	O1	1831(1)	1865(1)	6058(1)	22(1)
C14	640(2)	776(1)	9185(1)	24(1)	O2	5638(1)	1927(1)	669(1)	29(1)
C15	-621(2)	930(1)	6603(1)	18(1)	O3	6457(2)	1752(1)	-866(1)	44(1)
C16	-1622(2)	1154(1)	7239(1)	23(1)					
C17	-2825(2)	1400(1)	6820(1)	27(1)					

Compound 2: Benzoylmethylenetriphenylphosphorane & Fumaric Acid Co-crystal

Table S.3.2: Atomic coordinates (x 10^4) and equivalent isotropic displacement parameters ($Å^2$x 10^3)for Benzoylmethylenetriphenylphosphorane & Fumaric Acid Co-crystal.

Atom	x	y	z	U_{eq}	Atom	x	y	z	U_{eq}
P1	1558(1)	2949(1)	1169(1)	19(1)	C16	2240(1)	5108(2)	379(1)	27(1)
C1	3639(1)	739(1)	2765(1)	21(1)	C17	2762(1)	6331(2)	334(1)	31(1)
C2	3774(1)	492(2)	3546(1)	25(1)	C18	3216(1)	7034(2)	993(1)	32(1)
C3	4465(1)	-516(2)	3895(1)	30(1)	C19	3135(1)	6529(2)	1700(1)	28(1)
C4	5033(1)	-1270(2)	3473(1)	32(1)	C20	2609(1)	5317(2)	1752(1)	24(1)
C5	4920(1)	-1013(2)	2702(1)	31(1)	C21	418(1)	3230(1)	1560(1)	20(1)
C6	4228(1)	-16(2)	2348(1)	25(1)	C22	-58(1)	4506(2)	1544(1)	22(1)
C7	2876(1)	1811(1)	2395(1)	20(1)	C23	-1033(1)	4618(2)	1735(1)	25(1)
C8	2398(1)	1690(1)	1631(1)	22(1)	C24	-1532(1)	3460(2)	1927(1)	27(1)
C9	1065(1)	2326(1)	215(1)	21(1)	C25	-1050(1)	2193(2)	1954(1)	28(1)
C10	1759(1)	1766(2)	-193(1)	28(1)	C26	-73(1)	2079(2)	1775(1)	24(1)
C11	1393(1)	1323(2)	-937(1)	30(1)	C27	3963(1)	4935(2)	4050(1)	26(1)
C12	341(1)	1449(2)	-1274(1)	28(1)	C28	4707(1)	5417(2)	4752(1)	26(1)
C13	-355(1)	1986(2)	-873(1)	28(1)	O1	2675(1)	2803(1)	2804(1)	24(1)
C14	8(1)	2426(2)	-125(1)	25(1)	O2	3984(1)	3610(1)	3951(1)	32(1)
C15	2169(1)	4583(1)	1091(1)	21(1)	O3	3398(1)	5731(1)	3634(1)	35(1)

Compound 3: Benzoylmethylenetriphenylphosphonium Picrate

Table S.3.3: Atomic coordinates (x 10^4) and equivalent isotropic displacement parameters ($Å^2$x 10^3)for Benzoylmethylenetriphenylphosphonium Picrate.

Atom	x	y	z	U_{eq}	Atom	x	y	z	U_{eq}
P1	5203(1)	1024(1)	7601(1)	14(1)	C22	2346(2)	345(1)	7120(1)	21(1)
C1	894(2)	2065(1)	7327(1)	16(1)	C23	1168(2)	-51(1)	7303(1)	22(1)
C2	682(2)	2235(1)	6401(1)	18(1)	C24	1317(2)	-277(1)	8180(1)	21(1)
C3	-822(2)	2528(1)	6036(1)	22(1)	C25	2626(2)	-102(1)	8892(1)	21(1)
C4	-2110(2)	2653(1)	6597(1)	22(1)	C26	3824(2)	293(1)	8721(1)	18(1)
C5	-1895(2)	2492(1)	7522(1)	21(1)	C27	3476(2)	1121(1)	3072(1)	18(1)
C6	-400(2)	2197(1)	7891(1)	18(1)	C28	4499(2)	1085(1)	2292(1)	16(1)
C7	2445(2)	1738(1)	7765(1)	16(1)	C29	6099(2)	1333(1)	2247(1)	16(1)
C8	3900(2)	1603(1)	7178(1)	18(1)	C30	6904(2)	1624(1)	3016(1)	17(1)
C9	6843(2)	1164(1)	8600(1)	15(1)	C31	6074(2)	1683(1)	3802(1)	17(1)
C10	6620(2)	1574(1)	9220(1)	19(1)	C32	4461(2)	1435(1)	3832(1)	16(1)
C11	7921(2)	1657(1)	9994(1)	21(1)	O1	2567(2)	1583(1)	8567(1)	23(1)
C12	9417(2)	1331(1)	10153(1)	21(1)	O2	1952(2)	943(1)	3067(1)	25(1)
C13	9646(2)	926(1)	9536(1)	20(1)	O3	2836(2)	396(1)	1553(1)	28(1)
C14	8369(2)	842(1)	8758(1)	17(1)	O4	4010(2)	963(1)	696(1)	30(1)
C15	6367(2)	817(1)	6664(1)	15(1)	O5	9164(2)	1898(1)	2224(1)	29(1)
C16	7428(2)	1190(1)	6280(1)	19(1)	O6	9290(2)	2141(1)	3665(1)	34(1)
C17	8365(2)	1041(1)	5568(1)	21(1)	O7	3944(2)	1970(1)	5051(1)	28(1)
C18	8243(2)	526(1)	5230(1)	23(1)	O8	2673(2)	1198(1)	4935(1)	27(1)
C19	7215(2)	155(1)	5613(1)	24(1)	N1	3724(2)	797(1)	1458(1)	20(1)
C20	6281(2)	299(1)	6335(1)	19(1)	N2	8559(2)	1899(1)	2968(1)	21(1)
C21	3684(2)	513(1)	7835(1)	16(1)	N3	3634(2)	1539(1)	4652(1)	19(1)

Compound 4: Benzoylmethylenetriphenylphosphonium Maleate

Table S.3.4: Atomic coordinates (x 10^4) and equivalent isotropic displacement parameters ($Å^2$x 10^3)for Benzoylmethylenetriphenylphosphonium Maleate.

Atom	x	y	z	U_{eq}	Atom	x	y	z	U_{eq}
P1	793(1)	818(1)	6680(1)	22(1)	C18	1259(2)	2563(1)	7927(1)	39(1)
C1	1254(2)	-570(1)	7964(1)	24(1)	C19	2059(2)	2525(1)	7476(1)	38(1)
C2	2078(2)	-599(1)	8415(1)	35(1)	C20	1915(2)	2004(1)	7086(1)	31(1)
C3	1894(2)	-1068(1)	8836(1)	39(1)	C21	2124(1)	727(1)	6221(1)	25(1)
C4	886(2)	-1521(1)	8808(1)	37(1)	C22	2226(2)	1184(1)	5776(1)	31(1)
C5	62(2)	-1495(1)	8359(1)	38(1)	C23	3218(2)	1116(1)	5400(1)	38(1)
C6	235(2)	-1020(1)	7938(1)	32(1)	C24	4086(2)	597(1)	5463(1)	38(1)
C7	1498(1)	-51(1)	7530(1)	23(1)	C25	3981(2)	138(1)	5897(1)	39(1)
C8	503(2)	59(1)	7084(1)	23(1)	C26	2997(2)	198(1)	6280(1)	33(1)
C9	-559(2)	946(1)	6237(1)	27(1)	C27	10060(2)	2178(1)	4810(1)	38(1)
C10	-781(2)	472(1)	5815(1)	39(1)	C28	8718(2)	2163(1)	4620(1)	33(1)
C11	-1790(2)	566(1)	5454(1)	48(1)	C29	8182(2)	1867(1)	4180(1)	33(1)
C12	-2565(2)	1130(1)	5513(1)	48(1)	C30	8744(2)	1424(1)	3735(1)	31(1)
C13	-2350(2)	1596(1)	5929(1)	51(1)	O1	2467(1)	289(1)	7523(1)	30(1)
C14	-1346(2)	1511(1)	6296(1)	39(1)	O2	10891(1)	1801(1)	4556(1)	51(1)
C15	965(2)	1520(1)	7158(1)	26(1)	O3	10356(1)	2546(1)	5200(1)	56(1)
C16	155(2)	1563(1)	7613(1)	38(1)	O4	8086(1)	1287(1)	3326(1)	41(1)
C17	317(2)	2085(1)	7998(1)	44(1)	O5	9878(1)	1196(1)	3799(1)	42(1)

Compound 5: α-acetyl-α-benzoylmethylenetriphenylphosphorane.

Table S.3.5: Atomic coordinates (x 10^4) and equivalent isotropic displacement parameters ($Å^2$x 10^3)for α-acetyl-α-benzoylmethylenetriphenylphosphorane.

Atom	x	y	z	U_{eq}	Atom	x	y	z	U_{eq}
P1	6635(1)	6193(1)	4267(1)	18(1)	P2	8252(1)	9253(1)	971(1)	16(1)
C1	7382(5)	5646(1)	3700(5)	19(1)	C29	7685(5)	9849(1)	1380(4)	15(1)
C2	6584(5)	5544(1)	2186(4)	21(1)	C30	7004(5)	9890(1)	2442(4)	18(1)
C3	7130(5)	5161(1)	1577(5)	24(1)	C31	6704(5)	10346(2)	2885(5)	25(1)
C4	8461(5)	4870(2)	2470(5)	27(1)	C32	7079(5)	10761(2)	2281(5)	28(1)
C5	9250(5)	4964(2)	3993(5)	27(1)	C33	7828(5)	10723(1)	1283(5)	27(1)
C6	8735(5)	5353(1)	4593(5)	23(1)	C34	8126(5)	10267(1)	820(4)	22(1)
C7	8160(5)	6667(1)	4417(4)	19(1)	C35	8053(5)	9221(1)	-917(4)	19(1)
C8	9868(5)	6552(2)	4916(5)	23(1)	C36	7047(5)	9538(1)	-2014(4)	20(1)
C9	11092(5)	6912(2)	5233(5)	27(1)	C37	6884(5)	9482(2)	-3467(5)	23(1)
C10	10630(6)	7396(2)	5065(5)	28(1)	C38	7675(5)	9102(2)	-3839(5)	26(1)
C11	8921(6)	7522(2)	4569(5)	25(1)	C39	8672(5)	8775(2)	-2747(5)	23(1)
C12	7693(5)	7158(2)	4254(5)	24(1)	C40	8860(5)	8834(1)	-1276(5)	21(1)
C13	6769(5)	6184(2)	6148(4)	19(1)	C41	6635(5)	8826(1)	935(4)	18(1)
C14	7444(5)	5801(2)	7151(5)	24(1)	C42	4970(5)	8980(1)	439(5)	21(1)
C15	7596(6)	5846(2)	8594(5)	31(1)	C43	3673(5)	8648(2)	235(5)	25(1)
C16	7066(5)	6258(2)	9069(5)	28(1)	C44	4074(5)	8160(2)	505(5)	26(1)
C17	6346(6)	6636(2)	8075(5)	27(1)	C45	5719(5)	8003(1)	966(4)	24(1)
C18	6208(5)	6598(2)	6627(5)	23(1)	C46	7005(5)	8334(1)	1187(4)	19(1)
C19	4565(5)	6344(1)	3027(4)	18(1)	C47	10328(5)	9095(1)	2246(4)	16(1)
C20	3389(5)	6005(1)	3179(5)	20(1)	C48	11601(5)	9391(1)	2053(5)	21(1)
C21	1498(5)	5999(2)	2258(5)	26(1)	C49	13391(5)	9415(2)	3208(5)	25(1)
C22	4293(5)	6658(1)	1766(4)	19(1)	C50	10500(5)	8843(1)	3575(4)	18(1)
C23	2636(5)	6925(1)	1027(4)	20(1)	C51	12113(5)	8576(1)	4458(4)	18(1)
C24	1807(5)	7121(1)	1845(5)	23(1)	C52	12804(5)	8588(2)	6011(5)	23(1)
C25	304(6)	7382(2)	1158(5)	30(1)	C53	14271(5)	8327(2)	6808(5)	29(1)
C26	-358(6)	7447(2)	-366(5)	31(1)	C54	15062(6)	8053(2)	6113(5)	31(1)
C27	455(6)	7260(2)	-1209(5)	28(1)	C55	14368(5)	8039(2)	4577(5)	29(1)
C28	1971(6)	7006(1)	-503(4)	24(1)	C26	12906(5)	8306(1)	3752(5)	22(1)
O1	3982(4)	5668(1)	4131(3)	28(1)	O3	11198(4)	9656(1)	930(3)	26(1)
O2	5424(4)	6732(1)	1314(3)	24(1)	O4	9322(3)	8815(1)	4002(3)	24(1)

Compound 6: Carbethoxymethylenetriphenylphosphorane.

Table S.3.6: Atomic coordinates (x 10^4) and equivalent isotropic displacement parameters ($Å^2$x 10^3)for Carbethoxymethylenetriphenylphosphorane.

Atom	x	y	z	U_{eq}
P1	6328(1)	343(1)	3260(1)	18(1)
C1	7158(2)	406(1)	2128(1)	20(1)
C2	6347(2)	546(1)	1121(1)	23(1)
C3	6977(2)	641(1)	247(1)	29(1)
C4	8403(2)	596(1)	379(1)	29(1)
C5	9216(2)	448(1)	1376(1)	28(1)
C6	8592(2)	350(1)	2251(1)	24(1)
C7	7350(1)	-482(1)	4140(1)	19(1)
C8	7737(2)	-1311(1)	3736(1)	24(1)
C9	8428(2)	-1974(1)	4416(1)	30(1)
C10	8720(2)	-1827(1)	5500(1)	29(1)
C11	8335(2)	-1009(1)	5906(1)	27(1)
C12	7663(2)	-330(1)	5233(1)	22(1)
C13	6533(2)	1445(1)	3925(1)	20(1)
C14	7510(2)	2085(1)	3736(1)	22(1)
C15	7656(2)	2919(1)	4278(1)	27(1)
C16	6829(2)	3118(1)	5002(1)	28(1)
C17	5851(2)	2484(1)	5193(1)	27(1)
C18	5701(2)	1650(1)	4661(1)	23(1)
C19	4595(2)	117(1)	2952(1)	21(1)
C20	4137(2)	-761(1)	2575(1)	21(1)
C21	2199(2)	-1795(1)	2286(1)	25(1)
C22	906(2)	-1885(1)	2733(2)	33(1)
O1	4843(1)	1379(1)	2294(1)	27(1)
O2	2737(1)	882(1)	2533(1)	25(1)

Compound 7: Bis(benzoylmethylenetriphenylphosphorane)-dinitratodioxouranium (VI).

Table S.3.7: Atomic coordinates (x 10^4) and equivalent isotropic displacement parameters ($Å^2$x 10^3) for bis(benzoylmethylenetriphenylphosphorane-dinitratodioxouranium (VI). Solvent atoms are italicised. Table continued on following page.

Atom	x	y	z	U_{eq}	Atom	x	y	z	U_{eq}
U1	2487(1)	7510(1)	2505(1)	12(1)	C27	4661(4)	9217(3)	1922(3)	15(1)
P1	-1980(1)	8341(1)	3765(1)	14(1)	C28	4009(4)	9611(3)	2737(3)	19(1)
P2	6906(1)	6684(1)	1298(1)	14(1)	C29	3739(4)	10591(4)	2775(3)	23(1)
O1	617(3)	7434(2)	2755(2)	18(1)	C30	4091(4)	11181(4)	2000(4)	26(1)
O2	4342(2)	7617(2)	2274(2)	16(1)	C31	4715(4)	10798(4)	1184(4)	25(1)
O3	1338(3)	7008(3)	4115(2)	24(1)	C32	5004(4)	9815(3)	1145(3)	18(1)
O4	1836(3)	6936(3)	5268(2)	34(1)	C33	5054(4)	8165(3)	1885(3)	13(1)
O5	2929(3)	7324(3)	3918(2)	28(1)	C34	6190(4)	7852(3)	1448(3)	16(1)
O6	3010(3)	6282(2)	2346(2)	18(1)	C35	6759(4)	5909(3)	2314(3)	18(1)
O7	1966(3)	8737(2)	2661(2)	18(1)	C36	5716(4)	5678(3)	2833(3)	20(1)
O8	3671(3)	7921(2)	891(2)	22(1)	C37	5595(4)	5090(4)	3611(3)	26(1)
O9	3221(3)	7894(3)	-270(2)	28(1)	C38	6502(5)	4733(4)	3882(4)	33(1)
O10	2047(3)	7663(3)	1094(2)	24(1)	C39	7534(5)	4970(4)	3376(4)	36(1)
N1	2034(3)	7079(3)	4459(3)	21(1)	C40	7671(4)	5553(4)	2591(4)	27(1)
N2	2984(3)	7837(3)	543(3)	19(1)	C41	8373(4)	6761(3)	768(3)	17(1)
C1	305(4)	5832(3)	3035(3)	15(1)	C42	8785(4)	7387(4)	1067(3)	22(1)
C2	910(4)	5469(3)	2201(3)	20(1)	C43	9901(4)	7465(4)	669(4)	25(1)
C3	1176(4)	4496(4)	2133(3)	25(1)	C44	10615(4)	6920(4)	-31(4)	26(1)
C4	866(4)	3880(4)	2894(4)	28(1)	C45	10216(4)	6285(4)	-325(3)	25(1)
C5	297(4)	4232(4)	3729(4)	26(1)	C46	9101(4)	6205(3)	72(3)	20(1)
C6	10(4)	5207(3)	3801(3)	19(1)	C47	6554(4)	6104(3)	575(3)	16(1)
C7	-96(4)	6883(3)	3111(3)	14(1)	C48	6812(4)	5116(3)	572(3)	21(1)
C8	-1236(4)	7182(3)	3542(3)	14(1)	C49	6634(4)	4687(4)	-51(4)	26(1)
C9	-1885(4)	9168(3)	2786(3)	18(1)	C50	6183(4)	5233(4)	-663(3)	26(1)
C10	-836(4)	9319(3)	2190(3)	22(1)	C51	5902(4)	6209(4)	-644(3)	23(1)
C11	-761(5)	9957(4)	1440(3)	27(1)	C52	6095(4)	6649(3)	-32(3)	19(1)

C12	-1733(5)	10456(4)	1295(4)	30(1)	*C100*	*8156(5)*	*9342(4)*	*8468(4)*	*30(1)*
C13	-2772(5)	10303(4)	1889(4)	36(1)	*Cl1*	*7780(1)*	*9806(1)*	*9509(1)*	*41(1)*
C14	-2854(4)	9658(4)	2630(4)	28(1)	*Cl2B*	*8472(6)*	*8089(5)*	*8464(5)*	*61(2)*
C15	-1600(4)	8863(3)	4515(3)	18(1)	*Cl2A*	*8323(3)*	*8079(2)*	*8685(2)*	*27(1)*
C16	-1934(4)	9836(3)	4614(3)	22(1)	*C101*	*6800(6)*	*5727(5)*	*6690(5)*	*49(2)*
C17	-1686(4)	10218(4)	5231(3)	25(1)	*Cl3B*	*6333(4)*	*6896(3)*	*6698(3)*	*79(1)*
C18	-1102(4)	9637(4)	5737(3)	26(1)	*Cl3A*	*5541(4)*	*6567(3)*	*7171(3)*	*72(1)*
C19	-771(4)	8680(4)	5636(3)	25(1)	*Cl4B*	*7168(4)*	*5754(4)*	*5550(3)*	*49(1)*
C20	-1023(4)	8284(3)	5031(3)	20(1)	*Cl4A*	*7302(2)*	*5313(2)*	*5587(2)*	*38(1)*
C21	-3433(4)	8233(3)	4309(3)	17(1)	*C102*	*1428(7)*	*7308(6)*	*7460(6)*	*78(3)*
C22	-4127(4)	8650(4)	5100(3)	29(1)	*Cl5*	*1184(2)*	*8430(1)*	*6922(1)*	*51(1)*
C23	-5236(5)	8523(5)	5502(4)	41(2)	*Cl6B*	*2757(8)*	*7163(7)*	*7660(6)*	*132(3)*
C24	-5651(4)	8000(4)	5110(4)	31(1)	*Cl6A*	*2671(3)*	*7048(2)*	*7669(2)*	*18(1)*
C25	-4966(4)	7603(4)	4313(4)	27(1)					

Compound 8: Bis(α-acetyl-α-benzoylmethylenetriphenylphosphorane)-dinitratodioxouranium (VI).

Table S.3.8: Atomic coordinates (x 10^4) and equivalent isotropic displacement parameters ($Å^2$x 10^3) for Bis(α-acetyl-α-benzoylmethylenetriphenylphosphorane) - dinitratodioxouranium (VI). Solvent atoms are italicised.

Atom	x	y	z	U_{eq}	Atom	x	y	z	U_{eq}
U1	0	0	5000	17(1)	C14	-2061(4)	2648(2)	4786(3)	32(1)
P1	1093(1)	2092(1)	3106(1)	19(1)	C15	-925(4)	2879(2)	5017(3)	30(1)
N1	-2476(3)	161(2)	4347(2)	24(1)	C16	45(4)	2677(2)	4539(2)	27(1)
O1	470(2)	1695(2)	1193(2)	30(1)	C17	1059(3)	2911(2)	2408(2)	23(1)
O2	720(2)	586(2)	3790(2)	21(1)	C18	64(4)	3387(2)	2365(3)	30(1)
O3	-134(2)	938(1)	5433(2)	22(1)	C19	44(4)	4006(3)	1825(3)	37(1)
O4	-1587(2)	241(2)	3873(2)	30(1)	C20	994(4)	4155(2)	1315(3)	33(1)
O5	-3495(3)	293(2)	4121(2)	35(1)	C21	1998(4)	3680(2)	1346(3)	32(1)
O6	-2231(2)	-54(2)	5088(2)	25(1)	C22	2031(4)	3061(2)	1893(2)	27(1)
C1	1866(4)	681(2)	1178(2)	23(1)	C23	2480(3)	2158(2)	3678(2)	20(1)
C2	2898(4)	403(3)	1544(3)	31(1)	C24	2916(3)	2891(2)	3913(2)	28(1)
C3	3673(4)	-59(3)	1091(3)	39(1)	C25	3922(4)	2939(3)	4420(3)	33(1)
C4	3408(5)	-255(3)	279(3)	43(1)	C26	4508(4)	2279(3)	4676(3)	33(1)
C5	2383(5)	15(3)	-87(3)	42(1)	C27	4106(3)	1558(3)	4426(2)	29(1)
C6	1619(4)	484(2)	349(3)	34(1)	C28	3090(3)	1497(2)	3922(2)	23(1)
C7	1045(3)	1232(2)	1609(2)	21(1)	*C50*	*6992(6)*	*2462(4)*	*1389(3)*	*67(2)*
C8	988(3)	1216(2)	2535(2)	19(1)	*C51*	*7395(4)*	*1737(3)*	*1481(3)*	*48(1)*
C9	765(3)	552(2)	2992(2)	21(1)	*C52*	*6812(6)*	*1229(4)*	*1977(3)*	*63(2)*
C10	484(4)	-221(2)	2593(3)	30(1)	*C53*	*5830(5)*	*1406(4)*	*2388(3)*	*60(2)*
C11	-125(3)	2240(2)	3822(2)	19(1)	*C54*	*5379(5)*	*2107(4)*	*2296(3)*	*61(2)*
C12	-1263(3)	1996(2)	3587(2)	23(1)	*C55*	*5926(7)*	*2683(4)*	*1815(4)*	*95(3)*
C13	-2221(4)	2196(2)	4076(3)	29(1)					

Compound 9: Carbethoxymethyltriphenylphosphonium triacetatouranylate(VI).

Table S.3.9: Atomic coordinates (x 10^4) and equivalent isotropic displacement parameters ($Å^2$x 10^3) for carbethoxymethyltriphenylphosphonium triacetatouranylate(VI).

Atom	x	y	z	U_{eq}	Atom	x	y	z	U_{eq}
P1	832(1)	3106(1)	3995(1)	15(1)	C20	-404(5)	4755(4)	2975(5)	22(1)
O1	-720(4)	5036(3)	3953(4)	31(1)	C21	-1634(5)	6005(5)	1966(5)	24(1)
O2	-883(4)	5103(3)	1896(3)	22(1)	C22	-1970(6)	6334(4)	691(6)	34(1)
C1	-879(5)	2751(3)	4444(5)	16(1)	U1	6988(1)	890(1)	9230(1)	16(1)
C2	-1239(6)	2816(4)	5644(5)	21(1)	O3	7500(4)	2236(3)	10604(4)	26(1)
C3	-2592(6)	2574(4)	5935(6)	27(1)	O4	5979(4)	2489(3)	9086(4)	27(1)
C4	-3551(6)	2273(4)	5019(6)	32(2)	O5	5206(3)	1032(3)	7488(3)	20(1)
C5	-3177(6)	2216(4)	3831(6)	33(1)	O6	6283(4)	-329(2)	7672(3)	21(1)
C6	-1844(6)	2441(4)	3520(6)	23(1)	O7	8073(4)	-666(3)	9624(3)	22(1)
C7	1723(5)	2117(4)	3349(5)	18(1)	O8	8836(4)	502(3)	10790(3)	24(1)
C8	1431(6)	1208(4)	3741(5)	24(1)	O9	8303(3)	1229(2)	8234(3)	23(1)
C9	2207(7)	456(4)	3337(6)	30(1)	O10	5660(4)	558(2)	10219(3)	22(1)
C10	3251(6)	616(4)	2533(6)	30(2)	C23	6613(6)	2764(4)	10064(5)	23(1)
C11	3525(6)	1516(4)	2138(6)	26(1)	C24	6274(7)	3715(4)	10576(6)	36(2)
C12	2779(5)	2277(4)	2545(5)	24(1)	C25	5416(5)	199(4)	7096(5)	21(1)
C13	1888(5)	3506(4)	5291(5)	17(1)	C26	4652(6)	-140(4)	5944(5)	30(1)
C14	2705(5)	2834(4)	5950(5)	22(1)	C27	8918(5)	-349(4)	10462(5)	21(1)
C15	3480(6)	3102(4)	7008(5)	24(1)	C28	10002(7)	-1000(5)	11066(6)	38(2)
C16	3433(5)	4021(4)	7424(5)	24(1)					
C17	2644(7)	4694(4)	6772(6)	28(1)					
C18	1868(6)	4434(4)	5727(6)	22(1)					
C19	622(5)	3967(4)	2775(5)	22(1)					

Compound 10: Benzoylmethylenetriphenylphosphonium trinitratouranylate(VI).

Table S.3.10: Atomic coordinates (x 10^4) and equivalent isotropic displacement parameters ($Å^2$x 10^3) for benzoylmethylenetriphenylphosphonium trinitratouranylate (VI). Table continued on following page.

Atom	x	y	z	U_{eq}	Atom	x	y	z	U_{eq}
U1	2655(1)	9411(1)	10848(1)	18(1)	C15	3658(2)	5401(2)	9147(2)	22(1)
U2	2202(1)	10567(1)	9178(1)	17(1)	C16	3626(2)	5487(3)	9811(2)	23(1)
O3	2142(1)	10692(2)	11559(1)	22(1)	C17	3378(2)	4722(3)	10154(2)	32(1)
O4	2269(1)	10752(2)	12603(1)	27(1)	C18	3155(2)	3895(3)	9841(2)	33(1)
O5	2777(1)	9633(2)	12067(1)	25(1)	C19	3176(2)	3825(3)	9182(2)	33(1)
O6	3197(1)	8067(2)	11532(1)	24(1)	C20	3434(2)	4570(2)	8831(2)	25(1)
O7	3757(2)	6841(2)	11164(1)	41(1)	C21	4586(2)	5887(2)	8130(2)	19(1)
O8	3197(1)	7838(2)	10515(1)	28(1)	C22	5150(2)	5310(2)	8369(2)	25(1)
O9	3533(1)	9908(2)	10851(1)	25(1)	C23	5644(2)	4952(3)	7961(2)	29(1)
O10	1805(1)	8853(2)	10902(1)	26(1)	C24	5575(2)	5160(3)	7311(2)	26(1)
O11	2599(1)	9224(2)	9749(1)	25(1)	C25	5012(2)	5714(3)	7069(2)	28(1)
O12	2196(1)	10722(2)	10277(1)	25(1)	C26	4524(2)	6091(3)	7480(2)	26(1)
O13	3067(1)	11099(2)	9176(1)	26(1)	P2	982(1)	3635(1)	1357(1)	16(1)
O14	1318(1)	10090(2)	9114(1)	25(1)	O2	2236(1)	2696(2)	862(1)	23(1)
O15	1655(1)	12140(2)	9498(1)	31(1)	C27	3037(2)	2535(2)	1787(2)	20(1)
O16	1196(2)	13194(2)	8832(1)	46(1)	C28	3180(2)	2708(2)	2436(2)	24(1)
O17	1744(1)	11946(2)	8487(1)	24(1)	C29	3828(2)	2426(3)	2740(2)	29(1)
O18	2145(1)	10356(2)	7955(1)	23(1)	C30	4333(2)	1950(3)	2393(2)	33(1)
O19	2688(1)	9244(2)	7439(1)	26(1)	C31	4193(2)	1768(3)	1743(2)	32(1)
O20	2761(1)	9298(2)	8481(1)	22(1)	C32	3554(2)	2067(2)	1438(2)	25(1)
N1	2392(1)	10377(2)	12097(1)	19(1)	C33	2341(2)	2786(2)	1441(2)	18(1)
N2	3398(2)	7552(2)	11070(1)	24(1)	C34	1738(2)	3155(2)	1835(2)	18(1)
N3	1519(2)	12459(2)	8936(1)	27(1)	C35	377(2)	4130(2)	1912(2)	17(1)
N4	2539(1)	9617(2)	7939(1)	19(1)	C36	503(2)	4041(3)	2568(2)	24(1)
P1	3964(1)	6370(1)	8671(1)	17(1)	C37	27(2)	4448(3)	2982(2)	26(1)
O1	2620(1)	7258(2)	9104(1)	24(1)	C38	-578(2)	4913(3)	2735(2)	25(1)
C1	1910(2)	7420(2)	8123(2)	20(1)	C39	-710(2)	5012(3)	2080(2)	29(1)
C2	1378(2)	7948(2)	8404(2)	27(1)	C40	-234(2)	4624(3)	1669(2)	26(1)
C3	770(2)	8235(3)	8040(2)	36(1)	C41	1285(2)	4594(2)	874(2)	19(1)

C4	675(2)	7973(3)	7407(2)	35(1)	C42	1494(2)	5435(2)	1188(2)	24(1)
C5	1188(2)	7436(3)	7122(2)	30(1)	C43	1769(2)	6171(3)	840(2)	32(1)
C6	1813(2)	7167(2)	7478(2)	24(1)	C44	1828(2)	6085(3)	190(2)	31(1)
C7	2573(2)	7177(2)	8519(2)	19(1)	C45	1616(2)	5251(3)	-121(2)	31(1)
C8	3222(2)	6846(2)	8171(2)	19(1)	C46	1353(2)	4489(3)	220(2)	23(1)
C9	4389(2)	7257(2)	9179(2)	21(1)	C47	532(2)	2745(2)	869(2)	19(1)
C10	4128(2)	8182(2)	9173(2)	27(1)	C48	-6(2)	2997(3)	407(2)	28(1)
C11	4438(2)	8850(3)	9582(2)	41(1)	C49	-371(2)	2291(3)	55(2)	36(1)
C12	5024(2)	8606(3)	9993(2)	43(1)	C50	-209(2)	1352(3)	163(2)	39(1)
C13	5298(2)	7696(3)	9990(2)	37(1)	C51	338(2)	1102(3)	616(2)	40(1)
C14	4978(2)	7018(3)	9590(2)	29(1)	C52	705(2)	1793(2)	965(2)	27(1)

Compound 11: Dibromobis(carbethoxymethylenetriphenylphosphorane) dimercury (II).

Table S.3.11: Atomic coordinates (x 10^4) and equivalent isotropic displacement parameters (Å^{2}x 10^3) for dibromobis(carbethoxymethylenetriphenylphosphorane) dimercury (II). Solvent atoms are italicised.

Atom	x	y	z	U_{eq}	Atom	x	y	z	U_{eq}
Hg1	1001(1)	3427(1)	10412(1)	16(1)	C13	4168(5)	3004(5)	8360(5)	11(1)
P1	3027(1)	1990(1)	8320(1)	8(1)	C14	4723(6)	3925(6)	7387(5)	17(1)
Br1	1136(1)	3184(1)	12461(1)	20(1)	C15	5625(6)	4685(6)	7415(6)	22(1)
Br2	-1680(1)	4260(1)	10665(1)	19(1)	C16	5968(6)	4537(6)	8399(6)	25(1)
O1	2779(4)	460(4)	10742(3)	16(1)	C17	5405(7)	3650(6)	9361(6)	26(2)
O2	615(4)	129(4)	11133(3)	17(1)	C18	4505(6)	2868(6)	9359(5)	18(1)
C1	3918(5)	514(5)	8075(5)	11(1)	C19	1561(5)	1765(5)	9599(4)	8(1)
C2	3177(6)	-486(6)	8225(5)	18(1)	C20	1745(5)	731(5)	10534(5)	12(1)
C3	3853(7)	-1605(6)	7998(6)	24(1)	C21	714(6)	-866(6)	12096(5)	22(1)
C4	5242(7)	-1734(5)	7637(5)	21(1)	C22	1501(8)	-2019(7)	11673(7)	36(2)
C5	5972(6)	-736(6)	7486(6)	21(1)	*C100*	*7813(10)*	*2429(11)*	*4275(9)*	*31(2)*
C6	5309(6)	401(5)	7708(5)	15(1)	*C101*	*7980(50)*	*1990(60)*	*4470(50)*	*33(13)*
C7	2455(5)	2648(5)	7112(4)	10(1)	*Cl1*	*8143(2)*	*2583(2)*	*5511(2)*	*42(1)*
C8	2845(6)	2075(5)	6154(5)	14(1)	*Cl2A*	*7992(3)*	*818(3)*	*4216(3)*	*66(1)*
C9	2358(6)	2567(6)	5242(5)	20(1)	*Cl2B*	*9160(20)*	*297(19)*	*5028(17)*	*73(6)*
C10)	1494(7)	3615(6)	5279(5)	23(1)	*Cl3A*	*6166(3)*	*3000(2)*	*4403(2)*	*46(1)*
C11	1116(7)	4191(6)	6218(5)	25(1)	*Cl3B*	*6870(20)*	*1190(20)*	*4440(20)*	*88(7)*
C12	1584(6)	3713(6)	7144(5)	18(1)					

Compound 12: Dichlorobis(carbethoxymethylenetriphenylphosphorane) dimercury (II).

Table S.3.12: Atomic coordinates (x 10^4) and equivalent isotropic displacement parameters (Å^{2}x 10^3) for dichlorobis(carbethoxymethylenetriphenylphosphorane) dimercury (II). Solvent atoms are italicised.

Atom	x	y	z	U_{eq}	Atom	x	y	z	U_{eq}
Hg1	4287(1)	4916(1)	1579(1)	32(1)	C16	2920(12)	5012(13)	6103(11)	67(4)
Hg2	3797(8)	2593(7)	369(6)	37(2)	C17	1840(30)	4960(30)	5690(30)	58(9)
P1	3043(2)	2896(2)	3170(2)	27(1)	C17A	1960(20)	5330(20)	5440(20)	42(7)
Cl1	6549(2)	4917(2)	533(2)	35(1)	C18	1880(20)	4360(20)	4770(20)	32(6)
Cl2	3735(3)	6818(3)	2110(3)	58(1)	C18A	2030(20)	4680(20)	4540(20)	35(6)
O1	5929(7)	2412(7)	2981(6)	48(2)	C19	4193(9)	3102(8)	1994(8)	29(2)
O2	6010(6)	2020(6)	1190(6)	40(2)	C20	5453(9)	2473(8)	2128(8)	31(2)
C1	1602(9)	3252(9)	2644(7)	29(2)	C21	7314(10)	1484(12)	1179(12)	60(3)
C2	1234(10)	4325(9)	2023(9)	42(3)	C22	7872(15)	1256(18)	97(14)	107(6)
C3	134(10)	4562(10)	1592(9)	45(3)	*C23*	*767(14)*	*8271(12)*	*3152(13)*	*72(4)*
C4	-600(11)	3754(11)	1748(10)	54(3)	*C24*	*3163(11)*	*2204(12)*	*-1100(9)*	*52(3)*
C5	-260(12)	2700(12)	2340(12)	65(4)	*Cl3*	*125(8)*	*7238(7)*	*2763(8)*	*96(2)*
C6	835(10)	2450(10)	2799(10)	49(3)	*Cl4*	*277(8)*	*9619(8)*	*2612(8)*	*98(2)*
C7	3254(8)	1404(8)	3730(8)	30(2)	*Cl5*	*615(8)*	*8222(8)*	*4684(8)*	*110(3)*
C8	3676(10)	561(9)	2988(10)	42(3)	*Cl3A*	*-115(9)*	*7127(9)*	*3463(9)*	*75(3)*
C9	3810(10)	-629(10)	3429(11)	50(3)	*Cl4A*	*-150(18)*	*9325(16)*	*2229(17)*	*66(5)*
C10	3526(11)	-916(11)	4546(13)	61(4)	*Cl5A*	*423(13)*	*9117(13)*	*4294(12)*	*115(4)*
C11	3097(14)	-79(11)	5287(11)	67(4)	*Cl4B*	*610(30)*	*9400(30)*	*1780(30)*	*141(11)*
C12	2962(11)	1086(10)	4880(9)	51(3)	*Cl6*	*4254(4)*	*1223(4)*	*-447(4)*	*85(1)*
C13	3000(9)	3771(9)	4297(7)	30(2)	*Cl6A*	*3970(70)*	*930(70)*	*-1380(70)*	*80(20)*
C14	4090(20)	3856(19)	4677(18)	32(5)	*Cl7*	*3082(5)*	*1667(6)*	*-2373(5)*	*73(2)*
C14A	3890(20)	3480(20)	5020(20)	50(7)	*Cl7A*	*3099(11)*	*2279(11)*	*-2458(10)*	*58(3)*
C15	4040(20)	4540(20)	5580(20)	46(6)	*Cl8*	*1769(4)*	*2389(4)*	*-239(3)*	*91(1)*
C15A	3890(20)	4080(20)	5890(20)	50(7)					

Compound 13: Diiodobis(carbethoxymethylenetriphenylphosphorane) dimercury (II).

Table S.3.13: Atomic coordinates (x 10^4) and equivalent isotropic displacement parameters ($Å^2$x 10^3) for diiodobis(carbethoxymethylenetriphenylphosphorane) dimercury (II). Solvent atoms are italicised.

Atom	x	y	z	U_{eq}	Atom	x	y	z	U_{eq}
Hg1	4696(1)	3218(1)	1257(1)	23(1)	C8	-483(7)	5916(7)	2335(8)	36(2)
Hg2	3084(7)	5533(6)	598(6)	41(2)	C9	-1197(8)	7268(8)	1730(9)	49(2)
I1	5454(1)	5253(1)	1577(1)	27(1)	C10	-648(8)	8109(8)	730(8)	39(2)
I2	6675(1)	750(1)	2044(1)	26(1)	C11	628(7)	7569(7)	333(8)	36(2)
I3	1581(14)	8206(14)	-255(19)	78(5)	C12	1362(7)	6214(7)	943(7)	31(2)
P1	1735(2)	3605(2)	2788(2)	20(1)	C13	2769(6)	3585(6)	3898(6)	19(1)
O1	3113(4)	608(4)	3141(4)	24(1)	C14	2476(6)	4729(7)	4265(6)	24(1)
O2	3292(5)	960(5)	1038(4)	29(1)	C15	3263(7)	4701(7)	5131(7)	29(2)
C1	575(6)	2727(6)	3690(6)	22(1)	C16	4314(6)	3540(7)	5647(6)	25(2)
C2	-368(7)	2658(7)	3018(8)	35(2)	C17	4610(7)	2390(7)	5290(6)	24(1)
C3	-1302(7)	2051(8)	3692(9)	42(2)	C18	3843(6)	2401(6)	4426(6)	21(1)
C4	-1304(7)	1499(8)	5002(9)	45(2)	C19	2682(6)	2896(6)	1631(6)	23(1)
C5	-354(7)	1559(8)	5652(8)	39(2)	C20	3037(6)	1386(6)	2042(6)	20(1)
C6	574(7)	2187(7)	4996(7)	31(2)	C21	3823(7)	-530(7)	1337(7)	32(2)
C7	783(6)	5374(6)	1948(6)	22(1)	C22	2836(12)	-1233(12)	1811(12)	89(4)

Supplementary Data Tables for Chapter 5

Data Set 1: Nitrogen-loaded Zn_4O(1,4-benzenedicarboxylate) at 293K.

Table S.5.1: Atomic coordinates ($x10^4$) and $U_{eq}(Å^2 \times 10^3)$ for N_2-loaded Zn_4O(BDC) at 293K

Atom	x	y	z	U_{eq}
Zn(1)	2935(1)	2935(1)	2065(1)	27(1)
O(1)	2500	2500	2500	27(1)
O(2)	2805(1)	3663(1)	2195(1)	57(1)
C(1)	2500	3885(1)	2500	44(1)
C(2)	2500	4464(1)	2500	49(1)
C(3)	2823(1)	4734(1)	2177(1)	77(1)

Data Set 2: Nitrogen-loaded Zn_4O(1,4-benzenedicarboxylate) at 120K.

Table S.5.2: Atomic coordinates ($x10^4$) and $U_{eq}(Å^2 \times 10^3)$ for N_2-loaded Zn_4O(BDC) at 120K

Atom	x	y	z	U_{eq}
Zn(1)	2934(1)	2934(1)	2066(1)	13(1)
O(1)	2500	2500	2500	14(1)
O(2)	2806(1)	3663(1)	2194(1)	26(1)
C(1)	2500	3885(1)	2500	22(1)
C(2)	2500	4463(1)	2500	24(1)
C(3)	2827(1)	4733(1)	2173(1)	36(1)
N(1)	1564(5)	3436(5)	1564(5)	168(7)
N(2)	1519(8)	3481(8)	1148(8)	248(24)

Data Set 3: Nitrogen-loaded Zn_4O(1,4-benzenedicarboxylate) at 90K.

Table S.5.3: Atomic coordinates ($x10^4$) and U_{eq}($Å^2$ x 10^3) for N_2-loaded Zn_4O(BDC) at 90K

Atom	x	y	z	U_{eq}
Zn(1)	2934(1)	2934(1)	2066(1)	11(1)
O(1)	2500	2500	2500	12(1)
O(2)	2807(1)	3663(1)	2193(1)	21(1)
C(1)	2500	3885(1)	2500	17(1)
C(2)	2500	4463(1)	2500	19(1)
C(3)	2828(1)	4733(1)	2172(1)	29(1)
N(1)	3385(2)	3385(2)	3385(2)	125(5)
N(2)	3594(3)	3594(3)	3594(3)	355(21)
N(3)	3737(12)	3930(20)	1263(12)	272(80)

Data Set 4: Nitrogen-loaded Zn_4O(1,4-benzenedicarboxylate) at 50K.

Table S.5.4: Atomic coordinates ($x10^4$) and U_{eq}($Å^2$ x 10^3) for N_2-loaded Zn_4O(BDC) at 50K

Atom	x	y	z	U_{eq}
Zn(1)	2934(1)	2934(1)	2066(1)	9(1)
O(1)	2500	2500	2500	10(1)
O(2)	2807(1)	3663(1)	2193(1)	15(1)
C(1)	2500	3885(1)	2500	12(1)
C(2)	2500	4462(1)	2500	14(1)
C(3)	2830(1)	4732(1)	2171(1)	19(1)
N(1)	3350(1)	3350(1)	3350(1)	38(1)
N(2)	3560(1)	3560(1)	3560(1)	131(4)
N(5)	2553(11)	4149(6)	851(6)	109(10)
N(6)	2910(11)	4192(9)	808(9)	126(13)
N(7)	4900(110)	3463(7)	3463(7)	147(21)

Data Set 5: Nitrogen-loaded Zn_4O(1,4-benzenedicarboxylate) at 30K.

Table S.5.5: Atomic coordinates ($x10^4$) and U_{eq}($Å^2$ x 10^3) for N_2-loaded Zn_4O(BDC) at 30K

Atom	x	y	z	U_{eq}
Zn(1)	2933(1)	2933(1)	2067(1)	7(1)
O(1)	2500	2500	2500	9(1)
O(2)	2807(1)	3663(1)	2193(1)	12(1)
C(1)	2500	3886(1)	2500	11(1)
C(2)	2500	4462(1)	2500	11(1)
C(3)	2831(1)	4731(1)	2169(1)	14(1)
N(1)	3337(1)	3337(1)	3337(1)	29(1)
N(2)	3568(2)	3568(2)	3568(2)	91(3)
N(5)	2557(14)	4123(10)	877(10)	88(8)
N(6)	2740(40)	4394(15)	606(15)	274(42)
N(9)	3838(14)	5000	1162(14)	85(12)
N(10)	4137(15)	5000	863(15)	320(75)

Data Set 6: Argon-loaded Zn_4O(1,4-benzenedicarboxylate) at 293K.

Table S.5.6: Atomic coordinates ($x10^4$) and U_{eq}($Å^2$ x 10^3) for Ar-loaded Zn_4O(BDC) at 293K

Atom	x	y	z	U_{eq}
Zn(1)	2935(1)	2935(1)	2065(1)	27(1)
O(1)	2500	2500	2500	27(1)
O(2)	2805(1)	3663(1)	2195(1)	57(1)
C(1)	2500	3885(1)	2500	44(1)
C(2)	2500	4464(1)	2500	49(1)
C(3)	2822(1)	4734(1)	2178(1)	77(1)

Data Set 7: Argon-loaded Zn_4O(1,4-benzenedicarboxylate) at 90K.

Table S.5.7: Atomic coordinates ($x10^4$) and U_{eq}($Å^2$ x 10^3) for Ar-loaded Zn_4O(BDC) at 90K

Atom	x	y	z	U_{eq}
Zn(1)	2934(1)	2934(1)	2066(1)	10(1)
O(1)	2500	2500	2500	13(1)
O(2)	2806(1)	3663(1)	2194(1)	21(1)
C(1)	2500	3884(1)	2500	17(1)
C(2)	2500	4463(1)	2500	18(1)
C(3)	2828(1)	4733(1)	2172(1)	27(1)
Ar(1)	1562(1)	3438(1)	1562(1)	81(1)
Ar(2)	1514(7)	5000	1514(7)	174(19)
Ar(3)	2526(8)	4145(4)	853(5)	163(8)
Ar(4)	3777(4)	3777(4)	1223(4)	90(6)

Data Set 8: Argon-loaded Zn_4O(1,4-benzenedicarboxylate) at 50K.

Table S.5.8: Atomic coordinates ($x10^4$) and U_{eq}($Å^2$ x 10^3) for Ar-loaded Zn_4O(BDC) at 50K

Atom	x	y	z	U_{eq}
Zn(1)	2934(1)	2934(1)	2066(1)	10(1)
O(1)	2500	2500	2500	12(2)
O(2)	2805(1)	3663(1)	2195(1)	16(1)
C(1)	2500	3883(3)	2500	14(1)
C(2)	2500	4465(3)	2500	14(1)
C(3)	2827(2)	4730(2)	2173(2)	19(1)
Ar(1)	3427(1)	3427(1)	3427(1)	39(1)
Ar(2)	3471(5)	5000	3471(5)	74(6)
Ar(3)	4179(4)	4179(4)	2462(6)	79(6)
Ar(4)	3750(6)	3750(6)	1250(6)	114(10)
Ar(5)	5000	5000	3443(22)	68(18)
Ar(6)	5000	390(1)	110(1)	123(20)

Data Set 9: Argon-loaded Zn_4O(1,4-benzenedicarboxylate) at 30K.

Table S.5.9: Atomic coordinates ($x10^4$) and U_{eq}($Å^2$ x 10^3) for Ar-loaded Zn_4O(BDC) at 30K

Atom	x	y	z	U_{eq}
Zn(1)	2934(1)	2934(1)	2066(1)	10(1)
O(1)	2500	2500	2500	12(2)
O(2)	2805(1)	3663(1)	2195(1)	16(1)
C(1)	2500	3883(3)	2500	14(1)
C(2)	2500	4465(3)	2500	14(1)
C(3)	2827(2)	4730(2)	2173(2)	19(1)
Ar(1)	3419(1)	3419(1)	3419(1)	29(1)
Ar(2)	3418(7)	5000	3418(7)	42(7)
Ar(3)	41591(7)	41591(7)	246(1)	99(10)
Ar(4)	376(1)	376(1)	124(1)	165(26)
Ar(5)	5000	5000	327(1)	50(10)
Ar(6)	381(3)	5000)	103(3)	117(31)
Ar(7)	4273(8)	4273(8)	4273(8)	34(10)
Ar(8)	5000	5000	0000	54(38)

Supplementary Data Tables for Chapter 6

Data Set 1: Nitrogen-loaded Zn_4O(1,4-benzenedicarboxylate) at 120K.

Table S.6.1: Atomic coordinates ($x10^4$) and U_{eq}($Å^2$ x 10^3) for H_2-loaded Zn_4O(BDC) at 120K

Atom	x	y	z	U_{eq}
Zn(1)	2933(4)	2933(4)	2067(4)	21(4)
O(1)	2500	2500	2500	26(9)
O(2)	2805(3)	3657(4)	2195(3)	37(3)
C(1)	2500	3892(3)	2500	24(3)
C(2)	2500	4458(5)	2500	28(3)
C(3)	2826(3)	4730(3)	2174(3)	31(2)
H(3)	1934(7)	494(9)	1934(7)	67(6)

Data Set 2: Nitrogen-loaded Zn_4O(1,4-benzenedicarboxylate) at 50K.

Table S.6.2: Atomic coordinates ($x10^4$) and U_{eq}($Å^2$ x 10^3) for H_2-loaded Zn_4O(BDC) at 50K

Atom	x	y	z	U_{eq}
Zn(1)	2946(3)	2946(3)	2054(3)	14(4)
O(1)	2500	2500	2500	27(8)
O(2)	2806(3)	3661(4)	2194(3)	29(3)
C(1)	2500	3894(4)	2500	20(3)
C(2)	2500	4449(4)	2500	12(3)
C(3)	2828(2)	4733(3)	2171(2)	16(2)
H(3)	1931(5)	475(7)	1931(5)	48(5)
H(1)	3378(8)	1622(8)	1622(8)	9(1)

Data Set 3: Nitrogen-loaded Zn_4O(1,4-benzenedicarboxylate) at 30K.

Table S.6.3: Atomic coordinates ($x10^4$) and U_{eq}($Å^2$ x 10^3) for N_2-loaded Zn_4O(BDC) at 30K

Atom	x	y	z	U_{eq}
Zn(1)	2936(3)	2936(3)	2064(3)	15(4)
O(1)	2500	2500	2500	16(8)
O(2)	2808(3)	3667(3)	2192(3)	24(3)
C(1)	2500	3895(5)	2500	16(3)
C(2)	2500	4458(5)	2500	16(3)
C(3)	2828(2)	4736(3)	2172(2)	19(2)
H(3)	3071(5)	4515(7)	1929(5)	43(5)
H(1)	3323(15)	1677(15)	1677(15)	101(23)
H(2)	3323(14)	1677(14)	1401(24)	41(20)

Data Set 4: Nitrogen-loaded Zn_4O(1,4-benzenedicarboxylate) at 5K.

Table S.6.4: Atomic coordinates ($x10^4$) and U_{eq}($Å^2$ x 10^3) for N_2-loaded Zn_4O(BDC) at 5K

Atom	x	y	z	U_{eq}
Zn(1)	2934(3)	2934(3)	2067(3)	13(4)
O(1)	2500	2500	2500	22(8)
O(2)	2807(2)	3661(3)	2193(3)	23(3)
C(1)	2500	3895(4)	2500	13(3)
C(2)	2500	4452(5)	2500	14(2)
C(3)	2831(2)	4736(3)	2169(2)	17(2)
H(3)	1923(5)	478(7)	1923(5)	42(4)
H(1)	3337(13)	1663(13)	1663(13)	88(19)
H(2)	3328(145	1672(15)	1389(24)	53(22)
H(4)	1254(13)	1254(13)	1254(13)	179(29)